Picosecond and Femtosecond Coherent Multidimensional Spectroscopy of Colloidal PbSe Quantum Dot Structure and Dynamics

By

Stephen Benjamin Block

A Dissertation submitted in partial fulfillment of

the requirements for the degree of

Doctor of Philosophy

(Chemistry)

at the

University of Wisconsin-Madison

2012

Date of final oral examination: June 27, 2012

The dissertation is approved by the following members of the Final Oral Committee:
John Wright, professor, Chemistry
Mark Ediger, professor, Chemistry
Robert Hamers, professor, Chemistry
Randall Goldsmith, assistant professor, Chemistry
Deniz Yavuz, associate professor, Physics

Abstract

Multiresonant coherent multidimensional spectroscopy (MR-CMDS) is a fully coherent mixed frequency/time domain technique that selectively characterizes vibrational and electronic energetic structure and dynamics. The work reported here describes technique development with 1-picosecond pulses on model vibrational systems, application of this technique to PbSe quantum dots, and recent adaptation to include use of 50-femtosecond pulses. An overview of the quantum mechanical theory behind experimental design and interpretation, with an emphasis on the perturbative limit, is included. A record of the instrumentation and optical component selection associated with both laser systems is provided, which is particularly important for the development of the femtosecond laser table. Initial experiments on the femtosecond system revealed environmental artifacts that have now been identified and characterized. Picosecond pulses are not a good match for studying PbSe quantum dots with MR-CMDS because the pulses are too long to isolate coherence lifetimes and fully coherent processes. Frequency domain results previously acquired on the picosecond system revealed coherence lifetimes near 50fs, which directed the selection of a more appropriate laser system. Experiments with femtosecond pulses are now confirmed to directly measure coherence lifetimes and selectively emphasize spectral signatures from fully coherent processes that were not visible with longer pulses. These confirmations reveal that the flexibility of MR-CMDS techniques, as developed on the model vibrational systems, is available for quantum-confined semiconductor structures. Future directions include laser system improvements and suggestions of samples that may better inform dye-sensitized solar cell core charge transfer events.

Table of Contents

Abstract i

List of Figures v

List of Tables ix

Acknowledgements x

Introduction 1

I.1. Quantum-Confined Structures and Solar Applications 1

I.2. Ultrafast Spectroscopy of Quantum-Confined Semiconductor Systems 4

Chapter 1: Non-Linear Spectroscopy Theory Overview 15

1.1. Steady-State Limit 20

1.2. Isolating Particular Light-Matter Interactions 22

1.3. Incorporating Inhomogeneous Broadening 27

1.4. Interference from Non-Resonant Background 29

Chapter 2: Picosecond Instrumentation 35

2.1. System Adaptations for Near-Infrared Quantum Dot Experiments 38

Chapter 3: Femtosecond Instrumentation 42

3.1. Optical Component Selection 42

3.2. Initial Arrangement and Calibration 45

3.3. Later Table Developments 49

Chapter 4: Experimental Design 56

4.1. Sample Preparation 56

4.2. Experimental Parameters 58

4.3. Technique Development and Overview 62

Chapter 5: Review of Picosecond Experimental Capabilities 79

5.1. Crossed-Polarization Studies 81

Chapter 6: Femtosecond Experimental Results and Discussion 103

6.1. Early Results and Exploration 103

6.2. Artifacts of the System 106

6.3. Fast Dynamics Around Zero Delay 111

6.4. General Femtosecond System Experimental Capabilities 116

Chapter 7: Outlook and Future Directions 160

7.1. Future Directions 161

Appendix A: Frequency Domain Simulations 164

Appendix B: Phase Matching Near Absorptive Features 174

Appendix C: Daily Calibration Routine 180

Appendix D: Power Measurement With “The Pig” 209

Appendix E: Fluence Calculations 211

Appendix F: Ultrafast Coherent Multidimensional Spectroscopy of Quantum Dots for a Non-Technical Audience 214

List of Figures

Figure I.1 Depiction and Effects of Quantum Confinement 12

Figure I.2 Illustrations of Dye-Sensitized Solar Cell Cores 13

Figure I.3 Semiconductor Heterostructures 14

Figure 1.1 WMEL Diagrams For Each MR-CMDS Pulse Sequence 31

Figure 1.2 Common Depictions of Four-Wave Mixing Processes 32

Figure 1.3 WMEL Pathways as Seen in a Two-Dimensional Delay Scan 33

Figure 1.4 WMEL Diagrams of Representative $\chi^{(5)}$ Processes 34

Figure 2.1 Photo-Damaged Quantum Dot Samples 41

Figure 3.1 Picosecond and Femtosecond Laser Table Diagram 53

Figure 3.2 Zero Delay Value Drift and Fluctuation 54

Figure 3.3 Laboratory Temperature Fluctuation 55

Figure 4.1 Absorption Spectrum of RDC Stretching Modes 69

Figure 4.2 Absorption Spectrum of Octane Stretching Modes 70

Figure 4.3 MR-CMDS Frequency Scan Cross-Section of Octane 71

Figure 4.4 Appearance of Coherence Transfer In An RDC Monochromator Scan 72

Figure 4.5 Appearance of Population Relxation in RDC Delay Scans 73

Figure 4.6 Two-Dimensional Frequency Scan of RDC 74

Figure 4.7 Two-Dimensional Frequency Scan of RDC at High Laser Power 75

Figure 4.8 Two-Dimensional Delay Scan of an RDC Cross-Peak 76

Figure 4.9 Two-Dimensional Delay Scan of RDC With Coherence Transfer 77

Figure 4.10 Octane Wigner Plot 78

Figure 5.1 Absorption Spectrum of PbSe Quantum Dots for Picosecond Experiments 87

Figure 5.2 Picosecond Delay Scans of PbSe 1S Exciton 88

Figure 5.3 Picosecond Frequency Scans of PbSe 1S and 1P Excitons 89

Figure 5.4 Picosecond Frequency Scan of PbSe 1P Exciton Diagonal Peak 90

Figure 5.5 1P Exciton Population Lifetime 91

Figure 5.6 Two-Dimensional Frequency Scans of PbSe—Data and Simulations 92

Figure 5.7 TEM Images of Infrared-Scattering Nanoparticles 93

Figure 5.8 PbSe Absorption Profile Shift Over Time 94

Figure 5.9 PbSe Population Decay Profiles With Erratic Heterodyne Scatter 95

Figure 5.10 Comparison of Population Decay Profiles From Different Pulse Sequences 96

Figure 5.11 Two-Dimensional Delay Scan With Parallel Polarized Excitation Fields 97

Figure 5.12 Two-Dimensional Delay Scan With Cross Polarized Excitation Fields 98

Figure 5.13 Population Decay Profiles With Cross Polarized Excitation Fields 99

Figure 5.14 Two-Dimensional Frequency Scan With Parallel Polarized Electric Fields 100

Figure 5.15 Two-Dimensional Frequency Scan With Cross Polarized Electric Fields 101

Figure 5.16 Frequency Scans With All Pathway Contributions vs. Only Pathway 1/ 3 102

Figure 6.1 Linear Absorption Profiles of PbSe Samples For Femtosecond Studies 123

Figure 6.2 Early Two-Dimensional Delay Scan Results 124

Figure 6.3 Early Population Lifetime Scan Results 125

Figure 6.4 Power Dependence of Population Lifetime Scans 126

Figure 6.5 Two-Dimensional Delay Scan of Deteriorated Sample at Low Power 127

Figure 6.6 PbSe Absorption Profile Shift With Damage Over Time 128

Figure 6.7 Two-Dimensional Delay Scans Showing System Artifacts 129

Figure 6.8 Frequency Scan Showing Ambient Temperature Fluctuation Effects 130

Figure 6.9 Two-Dimensional Delay Scans Showing Pulse Reflection 131

Figure 6.10 Delay Scan of Silicon Wafer Showing Pulse Reflection 132

Figure 6.11 Population Lifetime Scans Showing Delay Stage Pitch/Yaw Impacts 133

Figure 6.12 Pitch/Yaw Modulation Frequency Invariant Under Changing Frequencies 134

Figure 6.13 Pitch/Yaw Modulation Phase Invariant Under Changing Frequencies 135

Figure 6.14 Pitch/Yaw Modulation Phase Change With Alignment 136

Figure 6.15 Inhomogeneous Broadening Effects in Two-Dimensional Delay Scans 138

Figure 6.16 Population Behavior With Inhomogeneous Broadening 139

Figure 6.17 Non-Resonant Background Contributions to Two-Dimensional Delay Scan 140

Figure 6.18 Non-Resonant Background Contributions to Population Lifetime Scans 141

Figure 6.19 Frequency Scan Interference Effects From Non-Resonant Background 142

Figure 6.20 Two-Dimensional Delay Scans With Varying Background Intensity 143

Figure 6.21 Population Decay Profiles With Varying Background Intensity 144

Figure 6.22 PbSe Population Decay Profiles With Strong and Weak Resonant Signal 145

Figure 6.23 PbSe Wigner Plot Near 1S Exciton Transition With $\omega_1 = \omega_2 = \omega_m$ 146

Figure 6.24 PbSe Wigner Plot With $\omega_1 > \omega_{1S}$ 147

Figure 6.25 PbSe Wigner Plot With $\omega_1 < \omega_{1S}$ 148

Figure 6.26 Fitting a 1S Exciton Population Decay Profile 149

Figure 6.27 Fitting a 1P-to-1S Exciton Population Relaxation Profile 150

Figure 6.28 Fitting a Two-Dimensional Delay Scan for Coherence Lifetimes 151

Figure 6.29 Two-Dimensional Delay Scan Fit For Population Lifetimes 152

Figure 6.30 Off-Diagonal Two-Dimensional Delay Scan and Fit 153

Figure 6.31 Two-Dimensional PbSe Frequency Scan and Fit 154

Figure 6.32 Unexplained Division of Two-Dimensional Frequency Scan Features 156

Figure 6.33 Two-Dimensional PbSe Frequency Scan With 1P Exciton Features 157

Figure 6.34 Pathway 1/3 Two-Dimensional Frequency Scan 158

Figure 6.35 Fully Coherent Pathway Contributions to a Two-Dimensional Frequency Scan 159

List of Tables

Table 6.1 Time-Domain Simulation Parameters 137

Table 6.2 Frequency-Domain Simulation Parameters 155

Acknowledgements

It is well known and commonly observed that no one acquires a graduate degree alone. Indeed, I owe credit for whatever may be deemed my success in graduate school to a great many people. I will only even briefly recognize a small collection of these individuals, but I hope that these few words will hint to the reader of the extent to which I am indebted to the communities around me.

This thesis explains results from the three eras of spectroscopic investigation in the research group of John Wright for which I was a member. The first period focused on technique development on molecules with vibrational modes of interest. Drs. Mark Rickard, Kathryn Kornau, Nathan A. Mathew, and Andrei Pakoulev led those investigations. In the process, these four, and in particular Kate and Nathan, trained me in the use of the picosecond laser system. In many ways, those two established the first environment and character of the research group I experienced.

After Kate and Nathan graduated, the research group focus shifted toward the study of quantum dot properties. A collaboration between the groups of John Wright, Song Jin, and Bob Hamers made this shift possible. In particular, Dr. Rachel Selinsky allowed us to study quantum dots by setting aside her own research progress to synthesize and characterize PbSe quantum dot batches for our use. Her patience as we learned to study these samples was remarkable, particularly when our first investigations involved destroying her samples by using too much laser power.

I co-led the quantum dot project with Dr. Lena Yurs. Lena joined the research group within a week of me doing so, and we worked closely for most of the following four and a half

years. She taught me a great deal about the importance of partnership in frequently-frustrating research endeavors, often by demonstrating the perseverance and hope required to surmount the presented obstacles. It was my pleasure to work with her for as long as I was able to do so.

It eventually became clear that the picosecond laser system was not the correct tool to study PbSe quantum dots in the way we wished. Lena worked-up the results from the picosecond system and graduated. While she did so, Schuyler Kain, Andei, and Dr. Igor Stiopkin worked to construct a femtosecond laser system. As the quantum dot project shifted to that system, I looked to carry the insights from earlier experiments into the initial use of the new laser. Skye took on the thoroughly unenviable task of writing LabView code to integrate and control all of the new equipment used. As experiments began, he promptly and seemingly-tirelessly addressed the bugs and glitches we discovered. Ultrafast laser systems require precise control that is not always built-in to the component parts. Skye's efforts allowed us to make full use of the marvelous laser system we had constructed.

Experiments on the new system coincided with the increased availability of Dan Kohler. Many of the newest results shown in this dissertation are a product of his efforts and collaboration. He also learned how to synthesize quantum dots from Rachel, and so supplied our group with the samples studied on the new laser system.

The names mentioned above are those most directly responsible for the research results presented in this document. Our research group is phenomenal at providing analysis, instrumentation troubleshooting, and morale support. Erin Boyle and Paul Hebert, as officemates and friends, were chief in this regard among those not already discussed. Over the course of my time in the group, however, Sam Penwell, Ross Lovely, Blaise Thompson, Eric

Hagee, Matt Rowley, and Kyle Czech helped establish and maintain the community culture of the research group.

All of my comments thus far have focused on the students of the group, when my deepest gratitude and admiration is felt for my advisor, Dr. John Wright. The man balances an excellent research career, professional and personal life guidance, and a devoted family life as well as anyone I have ever heard of. He provides scientific insights that are simple, deep, and/or completely novel, according to need. Were it not for his style of leadership and his inspiring passion for science, it is difficult to imagine where I would find myself today.

The members of the University of Wisconsin Chemistry department taught me a lot about academic and professional communities. Department members like Teresa Knudsen, Kyle Roux, Dr. Chad Wilkenson, Dr. Rob McClain and Bill Goebel established a culture of familiarity around the building, facilitating and adding enjoyment to daily efforts. The collaborative atmosphere of the department provided many friends who in turn shared scientific insights and perspective. This department has offered an almost ideal environment for a graduate career.

There are two friendships that developed out of the Chemistry department that deserve special recognition, and more than I can provide here. Drs. Benjamin Bratton and Andrew Berke were brothers of mine for the years I spent in the program. Our weekly breakfast gatherings refreshed motivation and made it all but impossible to ever feel as though I was working alone. Their absence in Madison is felt acutely, but I consider the time I had with them to be one of the greatest blessings of this stage of my life.

For all of the support I experienced from the department, the communities from outside the department may have characterized my graduate career with every bit as much strength.

Bible study groups that developed over time, church families in Madison and at home, and the graduate chapter of Intervarsity were steady encouraging presences. A list of friends who invested in my well-being would be almost painfully long if generated. These friends include people from home, fellow graduate students in other programs, and long-time friends from multiple church families. From the first week I arrived in Madison, I have never lacked for incredible people in my life.

I have seen many thesis dedications directed toward spouses and family. For all that I have learned about community over the past few years, the past few months have also begun to teach me the powerful reasoning behind those dedications. Joy Johnson has been a steady comfort, exhortative ally, and delightful distraction from dissertation work. My every hope is that she will be employed in such efforts as they evolve for a long time to come.

There have been no stronger supporters and no better teachers than my parents. Aside from the particulars like editing papers and providing the equivalent of professional counseling, they continue to teach me about motivation, priorities, dedication, and the love of God. I have marveled at their persistent belief in my abilities and delight in my identity. Graduate school can have some painful lows. My parents never allowed those lows to exist without strong counterpoint. If I were to dedicate this thesis, I can think of no party more deserving than my parents.

Lastly, before I allow the reader to enjoy some fine scientific text, it feels incomplete to offer so much praise of so many important people without also drawing attention to the Author and Creator of a world that has been made capable of and interesting to study. Science owes its beauty and allure to one responsible party. My mortal gratitude can never match the gift given.

Introduction

Steve Lee began the first series of experiments on what is now called coherent multidimensional spectroscopy following a group experiment that used two nitrogen-pumped dye lasers for multiresonant nonlinear spectroscopy.[1] A recent subset of these techniques, collectively called multiresonant coherent multidimensional spectroscopy (MR-CMDS) has been developed through the study of systems with prominent or interesting vibrational modes.[2, 3, 4, 5] MR-CMDS uses ultrafast laser pulses to selectively create and observe sequences of coherent superposition wavefunction states. By varying frequencies and pulse time-orderings, this technique can study molecular energetic structure and dynamics simultaneously with great specificity. Explorations on model systems confirmed that MR-CMDS can detect and measure potential well energetic structure, coupling between states, coherent and incoherent energy transfer, and some photochemistry.[6, 7, 8, 9, 10, 11] The model systems used for the fundamental studies built MR-CMDS capabilities to the point of shifting the focus of further technique development to materials of interest for direct application.

I.1. Quantum-Confined Structures and Solar Applications

The energetic structure of semiconductor systems has allowed them to become ubiquitous in modern computing and electronic technologies of all kinds. When the physical size of the semiconductor material is decreased to a certain threshold, the energetic properties undergo a qualitative change.[12] The threshold is determined by the native exciton size characteristic of the particular material.[13]

When energy is added to a semiconductor (usually in the form of an applied voltage or incident light) in excess of its bandgap, an electron is promoted from the molecularly-localized valence band to the delocalized conduction band, leaving a vacancy in the valence band called a hole. The positive charge of the hole and the negative charge of the electron experience Coulombic attraction that defines their range of separation. This attraction, combined with the molecular orbital structure, determines the effective size (Bohr radius) of the electron, hole, and exciton as a whole. If the lattice of atoms comprising the semiconductor material occupies a volume (or, in fact, even space in a single dimension) that is smaller than the exciton diameter (see Figure 1a for an illustration of a system confined in all three dimensions), the system is said to be quantum-confined. As the degree of confinement becomes more extreme the electron and hole are forced to occupy less than their optimal volume, increasing the energy of the excited state.[14, 15] Lattice size reduction decreases the density of conduction band states until the band edge states come to be resolvable as single (or at least collections of very few) state, as illustrated in Figure 1b. Further, the delocalized electron and hole become forced into the shape of the containing structure. The container shape, then, determine the nature of these quantum-confined excited states. For example, quantum-confined semiconductor spheres, called quantum dots, have excitonic states that can be characterized by the spherical harmonics (1S, 1P, etc.). Figure 1c shows a series of absorption plots for quantum-confined PbSe quantum dots. As the diameter of the dots decreases, the energy of the absorption features increase, allowing a certain amount of transition energy tunability.

There are few technological needs that are greater for a world that is undergoing rapid modernization than the availability of abundant, clean energy sources. There is no currently-accessible source of energy more abundant than solar radiation. The properties of quantum-confined semiconductors have led to some attempts to incorporate these structures into existing photovoltaic cell designs.[16,17,18,19] Figure 2a shows a conceptual diagram of a dye-sensitized solar cell. Here a chromophore absorbs incident radiation, then transfers charge through a molecular structure, required to retain electrical contact between components, to a charge acceptor. The charge accepting states are usually in the conduction band of a large bandgap semiconductor (see Figure 2b), such as TiO_2, which then conduct the charge through a circuit before replenishing the chromophore. Quantum dots are appealing dyes for these types of cells because their absorptive cross-sections are high, they can be synthesized to absorb light in any wavelength range, and they can be grown directly onto the surface of the charge-accepting material. High absorptive cross-sections diminish the required material thickness, allowing conducting electrons easier access to donor/acceptor interfaces. Wavelength range absorption can be adjusted to better align with the band edge of the acceptor or to access a region with greater spectral irradiance. The ability to grow a chromophore directly on the surface of a charge acceptor eliminates the need for any bridging molecules, increasing the probability and rate of transfer, and therefore also the efficiency. Here the small length scale is critical so that the two different semiconductor materials can be in contact without the mismatch of their respective lattices becoming significant. When the lattices are well-aligned, the native exciton radius could extend into the acceptor material, as illustrated in Figure 3a, enabling the possibility of ultrafast charge transfer.

Advances in nanostructure synthetic technique have made possible creation of complex morphologies that can serve as tailored scaffolding for quantum-confined materials that would serve as chromophores. Incorporation of chromophore material into customized structures[20,21] (Figure 3b) in various ways (Figure 3c) can allow a system to be optimized according to optical path length and donor/acceptor interaction. The possibility of using inexpensive, non-toxic, earth-abundant materials adds appeal to the use of nanomaterials for these types of cells. For example, Figure 3d shows an Fe_2O_3 (hematite) nanowire decorated with PbSe quantum dots.[22]

The synthetic capabilities are increasingly available, but much remains unknown about how to characterize the energetic and dynamic properties of these heterostructure systems and their charge transfer processes. For example, the role and identity of interfacial states in charge transfer phenomena are difficult to study. Without characterization of the processes and identification of critical features, it is impossible to meaningfully guide synthetic efforts and development.

I.2. Ultrafast Spectroscopy of Quantum-Confined Semiconductor Systems

Spectroscopy offers promise to help answer the questions that are critical to informing the development of improved photovoltaic devices. Many projects have developed an understanding of incoherent quantum dot and quantum well relaxation dynamics by transient absorption and pump-probe techniques.[23, 24, 25, 26] Some work has directly studied the lifetimes of various multiexcitonic coherences in quantum wells.[27, 28, 29] Other reports indicated significant formation of multiexciton states from single high energy photon absorption,[30, 31, 32] but the importance of this phenomenon has been strongly questioned.[33] These studies have provided extensive insight into the behavior of various quantum confined states on a femtosecond timescale, even to the point of watching incoherent electron injection into TiO_2 nanocrystals.[34] The fastest and most efficient energy transportation will occur by processes that can only be described quantum mechanically and observed by techniques that preserve coherent information.[35]

MR-CMDS has demonstrated the capability to identify the states involved in coherent energy transfer and incoherent energy transfer and distinguish between the two types of effects. The complete picture provided by the full use of these methods can also inform synthetic developments by measuring rates of charge transfer, reporting the states involved in transfer processes, and characterizing the changes in electronic structure resulting from incorporation of nanocrystals into various heterostructures. To achieve these goals, the technique must be adapted to fit the structural and dynamical properties of the system of interest.

Initial experiments in this project altered the laser system used to study vibrational modes and behavior.[36, 37, 38] The alterations primarily revolved around shifting instrumentation from producing and detecting mid-infrared frequencies to doing so with near-infrared radiation. Changes in sample handling and pulse fluence were also important. These adaptations allowed the study of incoherent dynamics and basic quantum dot excitonic structure. The 1-picosecond pulses used were too long to distinguish between or directly measure coherent phenomena, eliminating some of the unique strengths of MR-CMDS.

Once it became clear that the coherence lifetimes of quantum-confined semiconductor materials were too short to be accessed by picosecond pulses, a laser system with sub-50 femtosecond pulses was assembled to complete the transfer from vibrational system studies to these electronic systems. This document provides an overview of the theoretical framework behind the spectroscopic techniques used, details the instrumentation used and developed for this project, and reports and evaluates the preliminary studies resulting from the use of femtosecond pulses for the application of MR-CMDS methodologies to PbSe quantum dot electronic structure and coherent dynamics.

Works Cited

1. Lee, S. H.; Steehler, J. K.; Nguyen, D. C.; Wright, J. C. Site-Selective Nonlinear Four-Wave Mixing by Multiply Enhanced Nonparametric and Parametric Spectroscopy. *Applied Spectroscopy* **1985,** *39* (2), 243-253.
2. Meyer, K. A. *Frequency-Scanned Ultrafast Spectroscopic Techniques Applied to Infrared Four-Wave Mixing Spectroscopy;* PhD Thesis; University of Wisconsin-Madison: Madison, WI, 2004.
3. Rickard, M. A. *Fundamental Studies of Triply Vibrationally Enhanced Four-Wave Mixing Spectroscopy;* PhD Thesis; University of Wisconsin-Madison: Madison, WI, 2008.
4. Kornau, K. M. *Triply Vibrationally Enhanced Four-Wave Mixing Spectroscopy;* PhD Thesis; University of Wisconsin-Madison: Madison, WI, 2009.
5. Mathew, N. A. *Mixed Frequency/Time Domain Coherent Multidimensional Spectroscopy;* PhD Thesis; University of Wisconsin-Madison: Madison, WI, 2010.
6. Rickard, M. A.; Pakoulev, A. V.; Kornau, K.; Mathew, N. A.; Wright, J. C. Interferometric Coherence Transfer Modulations in Triply Vibrationally Enhanced Four-Wave Mixing. *Journal of Physcal Chemistry A* **2006,** *110* (40), 11384-11387.
7. Pakoulev, A. V.; Rickard, M. A.; Kornau, K. M.; Mathew, N. A.; Yurs, L. A.; Block, S. B.; Wright, J. C. Mixed Frequency-/Time-Domain Coherent Multidimensional Spectroscopy: Research Tool or Potential Analytical Method? *Accounts of Chemical Research* **2009,** *42* (9), 1310-1321.
8. Mathew, N. A.; Rickard, M. A.; Kornau, K. M.; Pakoulev, A. V.; Block, S. B.; Yurs, L. A.;

Wright, J. C. Coherent Multidimensional Vibrational Spectroscopy of Representative N-Alkanes. *Journal of Physical Chemistry A* **2009,** *113* (36), 9792-9803.

9. Mathew, N. A.; Yurs, L. A.; Block, S. B.; Pakoulev, A. V.; Kornau, K. M.; Sibert, E. L.; Wright, J. C. Fully and Partially Coherent Pathways in Multiply Enhanced Odd-Order Wave-Mixing Spectroscopy. *Journal of Physical Chemistry A* **2010,** *114* (2), 817-832.
10. Kornau, K. M.; Rickard, M. A.; Mathew, N. A.; Pakoulev, A. V.; Wright, J. C. Multiresonant Coherent Multidimensional Vibrational Spectroscopy of Aromatic Systems: Pyridine, a Model System. *Journal of Physical Chemistry A* **2011,** *115* (16), 4054-4062.
11. Penwell, S. B.; Wright, J. C. Multiresonant Coherent Multidimensional Spectroscopy of the Vibrationally Induced Decarboxylation of AOT: Deuterium Oxide Reverse Micelles. *Journal of Physical Chemistry B* **2011,** *115* (18), 5564-5573.
12. Selinsky, R. S. *Synthesis and Characterization of Inorganic Semiconducting Nanocrystals for Solar and Spintronics Applications;* PhD Thesis; University of Wisconsin-Madison: Madison, WI, 2012.
13. Wise, F. W. Lead Salt Quantum Dots: the Limit of Strong Quantum Confinement. *Accounts of Chemical Research* **2000,** *33* (11), 773-780.
14. Murray, C. B.; Norris, D. J.; Bawendi, M. G. Synthesis and Characterization of Nearly Monodisperse CdE (E = S, Se, Te) Semiconductor Nanocrystallites. *Journal of the American Chemical Society* **1993,** *115* (19), 8706-8715.
15. Alivisatos, A. P. Semiconductor Clusters, Nanocrystals, and Quantum Dots. *Science* **1996,** *271* (5251), 933-937.

16. Plass, R.; Pelet, S.; Krueger, J.; Gratzel, M. Quantum Dot Sensitization of Organic-Inorganic Hybrid Solar Cells. *Journal of Physical Chemistry B* **2002,** *106* (31), 7578-7580.

17. Wang, P.; Wang, L.; Ma, B.; Li, B.; Qiu, Y. TiO2 Surface Modification and Characterization with Nanosized PbS in Dye-Sensitized Solar Cells. *Journal of Physical Chemistry B* **2006,** *110* (29), 14406-14409.

18. Kramer, I. J.; Pattantyus-Abraham, A. G.; Barkhouse, A. R.; Wang, X.; Konstantatos, G.; Debnath, R.; Levina, L.; Raabe, I.; Nazeeruddin, M. K.; Gratzel, M.; Sargent, E. H. Advances in Colloidal Quantum Dot Solar Cells: The Depleted-Heterojunction Device. *Thin Solid Films* **2011,** *519,* 7351-7355.

19. Gratzel, M. Solar Energy Conversion by Dye-Sensitized Photovoltaic Cells. *Inorganic Chemistry* **2005,** *44* (20), 6841-6851.

20. Yao, W.-T.; Yu, S.-H.; Liu, S.-J.; Chen, J.-P.; Liu, X.-M.; Li, F.-Q. Architectural Control Synthesis of CdS and CdSe Nanoflowers, Branched Nanowires, and Nanotrees via Solvothermal Approach in a Mixed Solution and Their Photocatalytic Property. *Journal of Physical Chemistry B* **2006,** *110* (24), 11704-11710.

21. Bierman, M. J.; Lau, Y. K. A.; Kvit, A. V.; Schmitt, A. L.; Jin, S. Dislocation-Driven Nanowire Growth and Eshelby Twist. *Science* **2008,** *320,* 1060-1063.

22. Selinsky, R. S.; Shin, S.; Lukowski, M. A.; Jin, S. Epitaxial Heterostructures of Lead Selenide Quantum Dots on Hematite Nanowires. *Journal of Physical Chemistry Letters* **2012,** *3,* 1649-1656.

23. Wehrenberg, B. L.; Wang, C.; Guyot-Sionnest, P. Interband and Intraband Optical Studies of

PbSe Colloidal Quantum Dots. *Journal of Physical Chemistry B* **2002,** *106* (41), 10634-10640.

24. Cho, B.; Peters, W. K.; Hill, R. J.; Courtney, T. L.; Jonas, D. M. Bulklike Hot Carrier Dynamics in Lead Sulfide Quantum Dots. *Nano Letters* **2010,** *10,* 2498-2505.
25. Harbold, J. M.; Du, H.; Krauss, T. D.; Cho, K.-S.; Murray, C. B. Time-Resolved Intraband Relaxation of Strongly Confined Electrons and Holes in Colloidal PbSe Nanocrystals. *Physical Review B* **2005,** *72* (19), 195312(6).
26. Cooney, R. R.; Sewall, S. L.; Dias, E. A.; Sagar, D. M.; Anderson, K. E. H.; Kambhampati, P. Unified Picture of Electron and Hole Relaxation Pathways in Semiconductor Quantum Dots. *Physical Review B* **2007,** *75* (24), 245311-241-14.
27. Turner, D. B.; Nelson, K. A. Coherent Measurements of High-Order Electronic Correlations in Quantum Wells. *Nature* **2010,** *466,* 1089-1092.
28. VanEngen Spivey, A. G.; Borca, C. N.; Cundiff, S. T. Correlation Coefficient for Dephasing of Light-Hole Excitons and Heavy-Hole Excitons in GaAs Quantum Wells. *Solid State Communications* **2008,** *145,* 303-307.
29. Stone, K. W.; Turner, D. B.; Gundogdu, K.; Cundiff, S. T.; Nelson, K. A. Exciton-Exciton Correlations Revealed by Two-Quantum, Two-Dimensional Fourier Transform Optical Spectroscopy. *Accounts of Chemical Research* **2009,** *42* (9), 1452-1461.
30. Schaller, R. D.; Klimov, V. I. High Efficiency Carrier Multiplication in PbSe Nanocrystals: Implications for Solar Energy Conversion. *Physical Review Letters* **2004,** *92* (18), 186601-1861-4.

31. Schaller, R. D.; Sykora, M.; Pietryga, J. M.; Klimov, V. I. Seven Excitons at a Cost of One: Redefining the Limits for Conversion Efficiency of Photons into Charge Carriers. *Nano Letters* **2006,** *6* (3), 424-429.
32. Murphy, J. E.; Beard, M. C.; Norman, A. G.; Ahrenkiel, S. P.; Johnson, J. C.; Yu, P.; Micic, O. I.; Ellingson, R. J.; Nozik, A. J. PbTe Colloidal Nanocrystals: Synthesis, Characterization, and Multiple Exciton Generation. *Journal of the American Chemical Society* **2006,** *128,* 3241-3247.
33. McGuire, J. A.; Sykora, M.; Joo, J.; Pietryga, J. M.; Klimov, V. I. Apparent Versus True Carrier Multiplication Yields in Semiconductor Nanocrystals. *Nano Letters* **2010,** *10,* 2049-2057.
34. Tisdale, W. A.; Williams, K. J.; Timp, B. A.; Norris, D. J.; Aydil, E. S.; Zhu, X.-Y. Hot-Electron Transfer from Semiconductor Nanocrystals. *Science* **2010,** *8,* 1543-1547.
35. Engel, G. S.; Calhoun, T. R.; Read, E. L.; Ahn, T.-K.; Mancal, T.; Cheng, Y.-C.; Blankenship, R. E.; Fleming, G. R. Evidence for Wavelike Energy Transfer Through Quantum Coherence in Photosynthetic Systems. *Nature* **2007,** *446,* 782-786.
36. Yurs, L. A.; Block, S. B.; Pakoulev, A. V.; Selinsky, R. S.; Jin, S.; Wright, J. C. Multiresonant Coherent Multidimensional Electronic Spectroscopy of Colloidal PbSe Quantum Dots. *Journal of Physical Chemistry C* **2011,** *115* (46), 22833-22844.
37. Yurs, L. A. *Multiresonant Coherent Multidimensional Spectroscopy of Quantum-Confined Nanomaterials;* PhD Thesis; University of Wisconsin-Madison: Madison, WI, 2011.
38. Yurs, L. A.; Block, S. B.; Pakoulev, A. V.; Selinsky, R. S.; Jin, S.; Wright, J. C. Spectral

Isolation and Measurement of Surface-Trapped State Multidimensional Nonlinear Susceptibility in Colloidal Quantum Dots. *Journal of Physical Chemistry C* **2012,** *116* (9), 5546-5553.

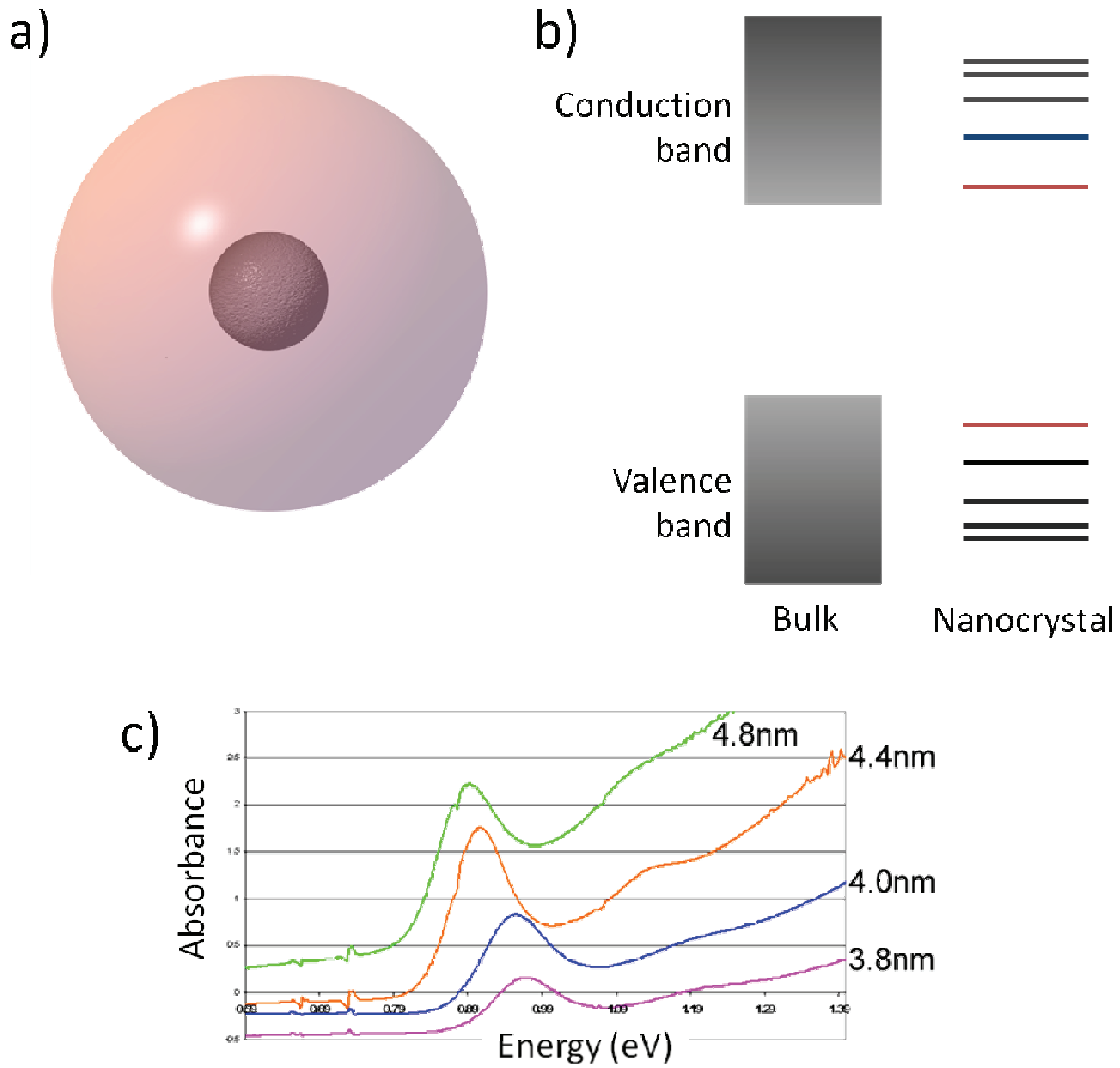

Figure 1—Depiction and effects of quantum confinement. (a) A quantum dot (small sphere) compared to the native exciton size (larger sphere) in a case of strong confinement. (b) The effects of quantum confinement on semiconductor band structure. The density of energy levels decreases to the point of becoming discrete states. Further, as the degree of confinement grows stronger, the separation between the band-edge states (shown in red) increases. (c) Near-infrared absorption spectra of PbSe quantum dots of the sizes indicated. Samples were synthesized and diameters determined by TEM by Rachel Selinsky. Absorption profiles are artificially offset to more clearly show the blue shift in the 1S exciton peak as dot diameter decreases.

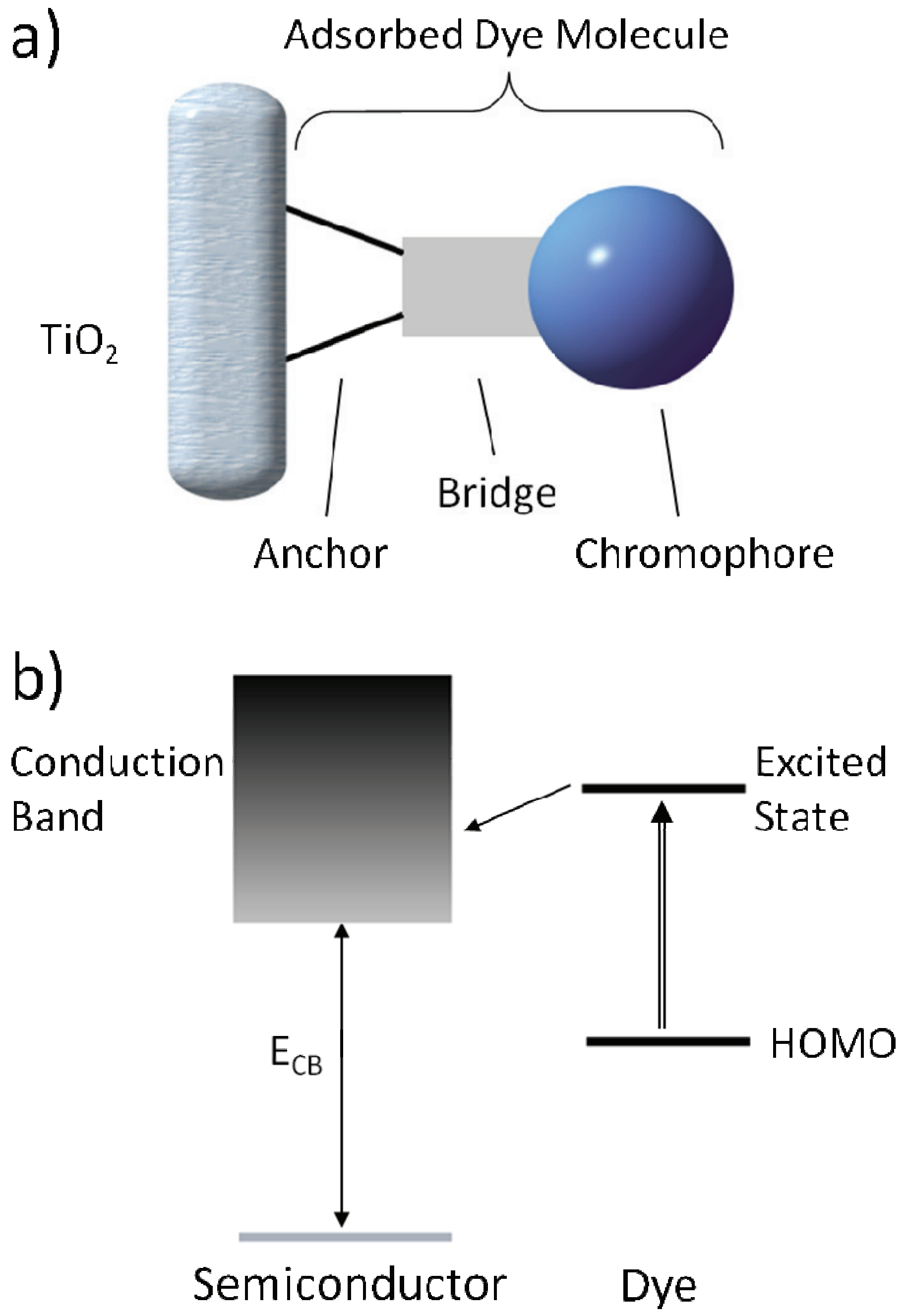

Figure 2—Illustrations of dye-sensitized solar cell cores. (a) The physical structure of this type of solar cell involves a chromophore, some molecular structure to keep it in electrical contact with the receptor, and the electron acceptor (shown here as TiO_2). (b) An energy level diagram of the donor-acceptor system. The double arrow shows absorption of a photon, promoting the dye to an excited electronic state. The excited state then relaxes by transferring an electron into the conduction band of the neighboring semiconductor. A large-bandgap (E_{CB}) material is usually chosen to minimize direct relaxation to the semiconductor valence band. The conduction band is placed in contact with a circuit running through a device and back to a redox couple that replenished the HOMO of the dye.

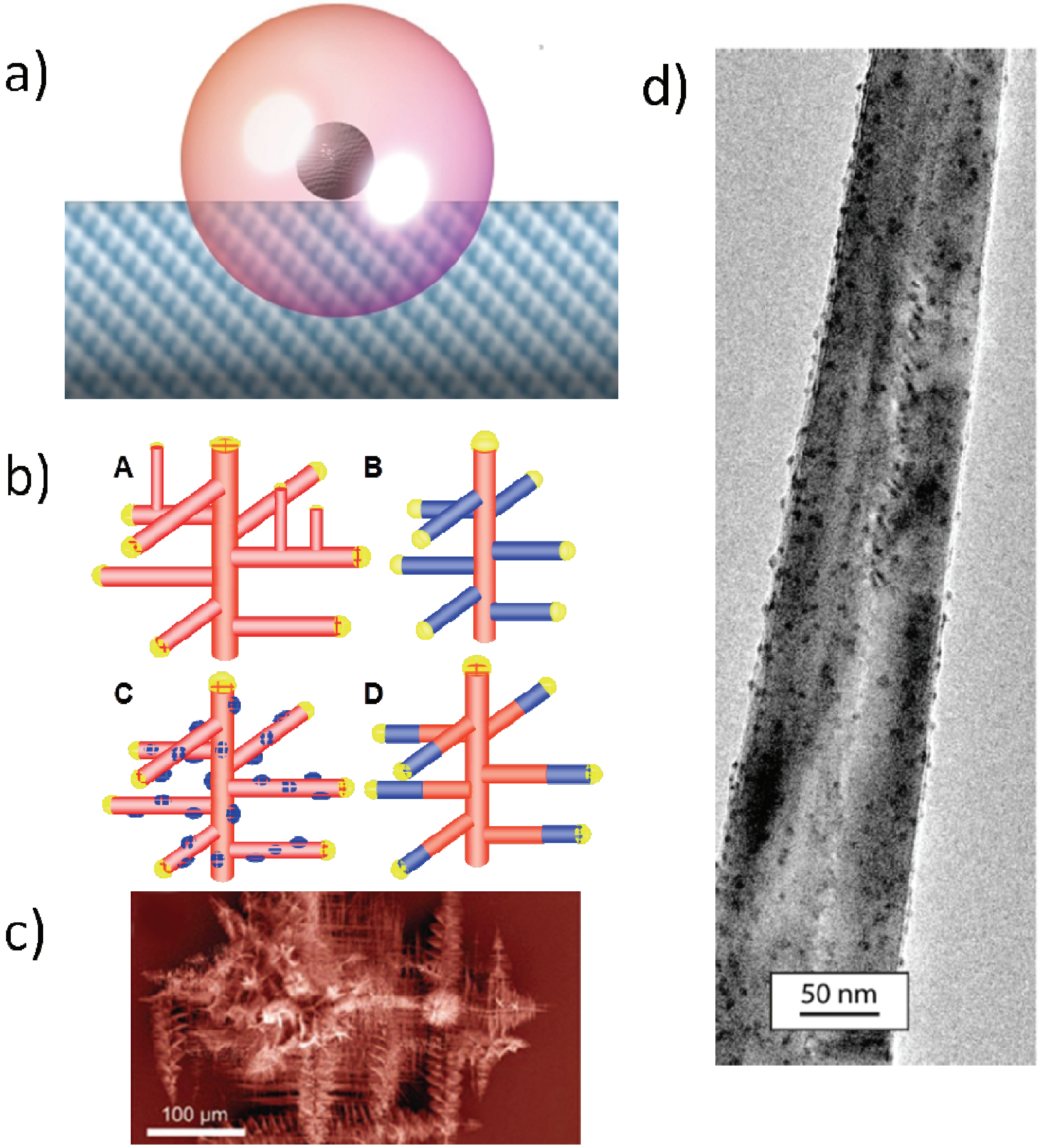

Figure 3—Semiconductor heterostructures. (a) An illustration of a quantum dot resting on the surface of an electron acceptor. No lattice matching is shown. The native exciton size of the quantum dot is included as a reminder; given minimal interfacial barrier, the exciton will already overlap with the charge acceptor. (b) Illustrations of various potential acceptor scaffolding/donor decoration systems. Here the acceptor is shown in red and the dye-substitute is shown in blue. (c) A TEM image of a hyper-branched PbS "pine tree". (d) A TEM image of an Fe_2O_3 nanowire decorated with PbSe quantum dots. System synthesized by Mark Lukowski and Rachel Selinky.

Chapter 1: Non-Linear Spectroscopy Theory Overview

Discussion of MR-CMDS techniques requires an understanding of light-matter interactions at a quantum mechanical level. This section explains the theory and terminology required for understanding the rest of this work.

The techniques highlighted regard light as a perturbation to a system wavefunction that creates or manipulates a linear combination of component time-independent wave states. A two-state system demonstrates the reasoning, but data interpretation calculations expand the wavefunction to include as many states as are needed.

$$\Psi = \sum_i c_i \psi_i = c_g\psi_g + c_e\psi_e \tag{1}$$

Here Ψ is taken to be the total wavefunction, the c_i are the contributions to the total wavefunction provided by component states ψ_i, and the subscripts g and e denote the ground state and an arbitrary excited state. This approach isolates all time-dependence on the constants c_i so that the eigenfunctions are unchanged by the applied perturbations.

In most experiments of interest, the only perturbation to the system is that of the oscillating laser electric field. The time-dependent Schrodinger equation is

$$\frac{\partial\Psi}{\partial t} = -\frac{i}{\hbar}\hat{\mathrm{H}}\Psi = -\frac{i}{\hbar}(\hat{\mathrm{H}}_0\Psi + \hat{\mathrm{V}}\Psi) = -\frac{i}{\hbar}\left(\hat{\mathrm{H}}_0\Psi - \vec{\mu}\cdot\vec{\mathrm{E}}\Psi\right) \tag{2}$$

where $\hat{\mathrm{H}}$ is the Hamiltonian operator, $\hat{\mathrm{H}}_0$ is the time-independent portion of the Hamiltonian, $\hat{\mathrm{V}}$ is the perturbation from the electric field ($\vec{\mathrm{E}}$), and $\vec{\mu}$ is the transition dipole moment. All subsequent explanations will treat the transition dipole and electric field as parallel ($\vec{\mu}\cdot\vec{\mathrm{E}} = |\vec{\mu}||\vec{\mathrm{E}}| \equiv \mu\mathrm{E}$). This treatment is an excellent approximation for the spherical symmetry of quantum dots, and is still instructive when compared to the rigorous case of an ensemble average over all relative orientations. Using the two-state wavefunction described in (1) and recalling that all temporal dependence in the wavefunction exists in the weighting constants,

$$\frac{\partial \Psi}{\partial t} = \frac{\partial c_g}{\partial t}\psi_g + \frac{\partial c_e}{\partial t}\psi_e = -\frac{i}{\hbar}\left(c_g E_g \psi_g + c_e E_e \psi_e\right) + \frac{i}{\hbar}\left(\mu \mathrm{E} c_g \psi_g + \mu \mathrm{E} c_e \psi_e\right) \tag{3}$$

The terms that now need to be isolated in order to characterize the change in the system brought about by the incident radiation are $\frac{\partial c_g}{\partial t}$ and $\frac{\partial c_e}{\partial t}$. Isolation of either one is accomplished by multiplying the entire relation (3) by the complex conjugate of one of the component wavefunctions and integrating over all space. Using the orthonormality of the component wavefunctions and noting that $\int \psi_g^* \mu \mathrm{E} \psi_g d\tau = 0$,

$$\int (\psi_g^* \frac{\partial c_g}{\partial t}\psi_g + \psi_g^* \frac{\partial c_e}{\partial t}\psi_e)\, d\tau = \frac{\partial c_g}{\partial t}\int \psi_g^*\, \psi_g d\tau + \frac{\partial c_e}{\partial t}\int \psi_g^*\, \psi_e d\tau = \frac{\partial c_g}{\partial t} * 1 + 0 = \frac{\partial c_g}{\partial t} =$$

$$= -\frac{i}{\hbar}\int \psi_g^*\, c_g E_g \psi_g d\tau - \frac{i}{\hbar}\int \psi_g^*\, c_e E_e \psi_e d\tau + \frac{i}{\hbar}\int \psi_g^*\, \mu \mathrm{E} c_g \psi_g d\tau + \frac{i}{\hbar}\int \psi_g^*\, \mu \mathrm{E} c_e \psi_e d\tau =$$

$$= -i c_g \omega_g \int \psi_g^*\, \psi_g d\tau - i c_e \omega_e \int \psi_g^*\, \psi_e d\tau + \frac{i}{\hbar} c_g \int \psi_g^*\, \mu \mathrm{E} \psi_g d\tau + \frac{i}{\hbar} c_e \int \psi_g^*\, \mu \mathrm{E} \psi_e d\tau =$$

$$= -i c_g \omega_g + 0 + 0 + \frac{i}{\hbar} c_e \int \psi_g^*\, \mu \mathrm{E} \psi_e d\tau \equiv -i c_g \omega_g - \frac{i}{\hbar} c_e V_{ge} \tag{4}$$

where ω_i is the frequency of state *i*. Therefore,

$$\frac{\partial c_g}{\partial t} = -i c_g \omega_g - \frac{i}{\hbar} c_e V_{ge} \text{ and, similarly, } \frac{\partial c_e}{\partial t} = -i c_e \omega_e - \frac{i}{\hbar} c_g V_{eg} \tag{5}$$

Equations (5) neglect all perturbations other than those of interest, i.e. those introduced by the incident electric field and those inherent to the system. Because of interactions with the surrounding environment, there will always be some loss of quantum mechanical information. Though there are constructs for rigorously addressing these fluctuating interactions,[1] the treatment presented here will add this term phenomenologically under the Markovian limit. And so,

$$\frac{\partial c_g}{\partial t} = -ic_g\omega_g - \frac{i}{\hbar}c_eV_{ge} - \Gamma_g c_g \tag{6}$$

As the total wavefunction is perturbed from its initial stationary state, it becomes a simultaneous superposition of multiple eigenstates. The superposition state oscillates at frequencies determined by the difference between pairs of contributing eigenstates. If the transition dipole between those two states is non-zero, the oscillations will emit an electric field. Before considering observables, it is instructive first to consider the state itself in the form of a probability distribution.

$$\Psi^*\Psi = \sum_i\sum_j c_i^*\, c_j\psi_i^*\psi_j \;=\; c_g^*c_g\psi_g^*\psi_g \;+\; c_e^*c_e\psi_e^*\psi_e \;+\; c_e^*c_g\psi_e^*\psi_g \;+\; c_g^*c_e\psi_g^*\psi_e \tag{7}$$

This product has two types of terms: those for which the two wavefunctions are adjoints and those for which they represent different wave states. When *i* ≠ *j*, the term describes a coherence. When *i* = *j*, the term describes a population. These terms are often described using density matrix elements,

$$\begin{bmatrix} c_g^*c_g & c_g^*c_e \\ c_e^*c_g & c_e^*c_e \end{bmatrix} \equiv \begin{bmatrix} \rho_{gg} & \rho_{eg} \\ \rho_{ge} & \rho_{ee} \end{bmatrix} = \boldsymbol{\rho} \tag{8}$$

To describe the observable changes in a system, then, the goal becomes the calculation of $\frac{\partial\rho}{\partial t}$. Consider first an element that describes a coherence:

$$\frac{\partial\rho_{eg}}{\partial t} = \frac{\partial}{\partial t}c_g^*c_e = \frac{\partial c_g^*}{\partial t}c_e + c_g^*\frac{\partial c_e}{\partial t} =$$

$$= \left(ic_g^*\omega_g + \frac{i}{\hbar}c_e^*V_{ge} - \Gamma_g c_g^*\right)c_e + \left(-ic_e\omega_e - \frac{i}{\hbar}c_gV_{eg} - \Gamma_e c_e\right)c_g^* =$$

$$= \left(i\omega_g \rho_{eg} + \frac{i}{\hbar} V_{ge} \rho_{ee} - \Gamma_g \rho_{eg}\right) + \left(-i\omega_e \rho_{eg} - \frac{i}{\hbar} V_{eg} \rho_{gg} - \Gamma_e \rho_{eg}\right) = \qquad (9)$$

$$= \rho_{eg}(i\omega_g - i\omega_e - \Gamma_g - \Gamma_e) - \frac{i}{\hbar}(V_{eg}\rho_{gg} - V_{ge}\rho_{ee}) \equiv \rho_{eg}(i\omega_{ge} - \Gamma_{eg}) - \frac{i}{\hbar}(V_{eg}\rho_{gg} - V_{ge}\rho_{ee})$$

Notice from this expression that the changes in time produced by the electric field (any term with V_{eg} or V_{ge}) involve feeding the coherence from populations. Additionally, the changes in coherence magnitude produced by the electric field acting to change a gg population to an eg coherence are of an opposite sign to the changes produced by an interaction with an ee population. A change from gg to eg, indicating an alteration to the non-complex conjugate side (or ket-side when using Dirac bra-ket terminology) then affects the opposite change to the magnitude of the coherence as that affected by an interaction with the complex conjugate (or bra) side.

The terms of (9) that do not involve the electric field reveal other properties of a coherence. The loss term added phenomenologically leads to decay. Additionally, the real part of the coherence feeds the imaginary part, and vice versa, via the $i\omega_{ge}\rho_{eg}$ term. Solution of just this part of (9) (or for the entirety of it, if there is no perturbing electric field and we ignore the dephasing rate, Γ_{eg}) reveals that a coherence oscillates at the difference frequency between its two composing states (ω_{ge}). When discussing any observations pertaining to coherences, it is important to realize that the decay experienced by a coherence can come from losses either of the component state magnitudes or of phase memory. Interactions with the surrounding environment will disrupt the memory that a coherence has of its phase in the past, even if the values of the density matrix are unchanged. This additional loss of memory is usually called pure dephasing, Γ_{eg}^{*}, and then $\Gamma_{eg} = \Gamma_e + \Gamma_g + \Gamma_{eg}^{*}$.

The changes in the populations can be determined in a similar manner.

$$\frac{\partial \rho_{ee}}{\partial t} = \frac{\partial}{\partial t} c_e^* c_e = \frac{\partial c_e^*}{\partial t} c_e + c_e^* \frac{\partial c_e}{\partial t} =$$

$$= \left(i c_e^* \omega_e + \frac{i}{\hbar} c_g^* V_{eg} - \Gamma_e c_e^* \right) c_e + \left(-i c_e \omega_e - \frac{i}{\hbar} c_g V_{eg} - \Gamma_e c_e \right) c_e^* =$$

$$= \left(i \omega_e \rho_{ee} + \frac{i}{\hbar} V_{eg} \rho_{eg} - \Gamma_e \rho_{ee} \right) + \left(-i \omega_e \rho_{ee} - \frac{i}{\hbar} V_{eg} \rho_{ge} - \Gamma_e \rho_{ee} \right) =$$

$$= -\frac{i}{\hbar} \left(V_{eg} \rho_{ge} - V_{eg} \rho_{eg} \right) - 2\Gamma_e \rho_{ee} \equiv -\frac{i}{\hbar} \left(V_{eg} \rho_{ge} - V_{eg} \rho_{eg} \right) - \Gamma_{ee} \rho_{ee} \qquad (10)$$

Here again characteristics of populations become clear. Note that coherences feed populations when they interact with an electric field and that populations also experience decay. Again electric field interactions with the bra- and ket-side of a system produce opposing changes. As populations do not oscillate (revealed here by the absence of a high frequency feeding term), there will be no pure dephasing, so $\Gamma_{ee} = \Gamma_e + \Gamma_e$.

Each of these interactions with light induces a polarization in the exposed material. The relationship between the electric field and the macroscopic polarization created in the sample is a proportionality constant called the electric susceptibility. The polarized sample in turn launches its own electric fields. In general, the relationship can be written as a Taylor expansion,

$$\vec{\mathrm{P}} = \chi^{(1)} \vec{\mathrm{E}} + \chi^{(2)} \vec{\mathrm{E}}^2 + \ \ldots \qquad (11)$$

Where $\vec{\mathrm{P}}$ is the polarization, $\vec{\mathrm{E}}$ is the electric field, and $\chi^{(n)}$ is the corresponding nth-order susceptibility tensor. In an isotropic sample, all even terms cancel out because of inversion symmetry. In a four-wave mixing experiment, the signal measured corresponds to the polarization created cooperatively by three excitation beams, so the lowest-order term observed is $\chi^{(3)} \mathrm{E}_1 \mathrm{E}_2 \mathrm{E}_3$. Higher order terms (such as $\chi^{(5)} \mathrm{E}_1 \mathrm{E}_2^3 \mathrm{E}_3$) will also contribute to the measured signal, but in general $\chi^{(n)} \gg \chi^{(n+2)}$,[2] so the electric fields must be very strong for these contributions to be significant.

1.1. Steady-State Limit

In MR-CMDS experiments, electric fields produce a sequence of coherences and populations. Coherences, as oscillating charges, produce detectable electric fields when the transition dipole between the two states in the superposition is nonzero. The amplitudes of these electric fields are directly proportional to the magnitudes of the coherences that produce them. As such, it is desirable to isolate the factors leading to an increase or decrease in the magnitude of the observed coherence. An informative conditionality is the steady state limit, in which the applied electric field lasts considerably longer than the coherence dephasing rate. Under these conditions, the coherences are always forced to oscillate in time at the driving frequency, ω, instead of their native frequency, ω_{eg}, and oscillate in space according to the driving wave vector $\vec{k}$ (where $|\vec{k}| = \mathrm{n}\omega/c$ and n is the index of refraction). The coherence can then be characterized as $\rho_{eg} = \widetilde{\rho_{eg}} e^{-i\omega t - ikz}$, where $\widetilde{\rho_{eg}}$ is the magnitude of the coherence. Then the expression for the variation of a coherence in time (9) becomes

$$\frac{\partial \rho_{eg}}{\partial t} = \frac{\partial \widetilde{\rho_{eg}}}{\partial t} e^{-i\omega t - ikz} - i\omega \widetilde{\rho_{eg}} e^{-i\omega t - ikz} =$$

$$= \widetilde{\rho_{eg}} e^{-i\omega t - ikz}\left(-i\omega_{eg} - \Gamma_{eg}\right) - \frac{i}{\hbar}\left(V_{eg}\rho_{gg} - V_{ge}\rho_{ee}\right) \tag{12}$$

Isolating the change of the magnitude of the coherence yields

$$\frac{\partial \widetilde{\rho_{eg}}}{\partial t} = \widetilde{\rho_{eg}}\left[-i\left(\omega_{eg} - \omega\right) - \Gamma_{eg}\right] - \frac{i}{\hbar}\left(V_{eg}\rho_{gg} - V_{ge}\rho_{ee}\right) e^{i\omega t + ikz} \tag{13}$$

Magnitudes of coherences driven by pulsed electric fields can still be calculated using this approximation by changing the electric field profile. If the pulse is short in time relative to the dephasing rate, however, the intensity of the driven signal will be low relative to the native free induction decay oscillations, which are most easily calculated by treating the electric field as an instantaneous perturbation. When the applied electric field is a continuous wave, $V_{eg} = -\mu_{eg}\mathrm{E}_0\cos(\omega t + kz)$ and $V_{eg} = V_{ge}$. Expressing the cosine term as a sum of exponents changes (13) to

$$\frac{\partial\widetilde{\rho_{eg}}}{\partial t} = \widetilde{\rho_{eg}}\left[-i\left(\omega_{eg} - \omega\right) - \Gamma_{eg}\right] + \frac{i\mu_{eg}\mathrm{E}_0}{2\hbar}\left(e^{-i\omega t - ikz} + e^{i\omega t + ikz}\right)\left(\rho_{gg} - \rho_{ee}\right)e^{i\omega t + ikz} \quad (14)$$

If the light pulse is long relative to the frequency of oscillation, then the rotating wave approximation asserts that the fast oscillations ($e^{2i\omega t + 2ikz}$) produce effects that average out. (14) can then be simplified to

$$\frac{\partial\widetilde{\rho_{eg}}}{\partial t} = \widetilde{\rho_{eg}}\left[-i\left(\omega_{eg} - \omega\right) - \Gamma_{eg}\right] + \frac{i\mu_{eg}\mathrm{E}_0}{2\hbar}\left(\rho_{gg} - \rho_{ee}\right) \quad (15)$$

As soon as the system has reached the steady state, $\frac{\partial\widetilde{\rho_{eg}}}{\partial t} = 0$, so

$$\widetilde{\rho_{eg}} = \frac{i\mu_{eg}\mathrm{E}_0}{2\hbar}\frac{-(\rho_{gg} - \rho_{ee})}{\left[-i\left(\omega_{eg} - \omega\right) - \Gamma_{eg}\right]} = \frac{\mu_{eg}\mathrm{E}_0}{2\hbar}\frac{(\rho_{gg} - \rho_{ee})}{(\omega_{eg} - \omega - i\Gamma_{eg})} \quad (16)$$

This expression reveals that the magnitude of a driven coherence is highest when the driving frequency is resonant with the transition ($\omega_{eg} = \omega$), the electric field is strong, and the transition dipole moment is large.

The procedure for deriving $\widetilde{\rho_{gg}}$, $\widetilde{\rho_{ge}}$, and $\widetilde{\rho_{ee}}$ is analogous to the one shown above. Because a new population can only be created after two interactions with light, the incident electric fields are shown as ω and ω_2.

$$\widetilde{\rho_{gg}} = \frac{\mu_{eg}\mathrm{E}_0}{2\hbar}\frac{(\rho_{eg} - \rho_{ge})}{(\omega_{gg} - \omega_2 + \omega - i\Gamma_{gg})} \tag{17}$$

$$\widetilde{\rho_{ge}} = \frac{\mu_{eg}\mathrm{E}_0}{2\hbar}\frac{(\rho_{ee} - \rho_{gg})}{(\omega_{eg} - \omega + i\Gamma_{eg})} \tag{18}$$

$$\widetilde{\rho_{ee}} = \frac{\mu_{eg}\mathrm{E}_0}{2\hbar}\frac{(\rho_{ge} - \rho_{eg})}{(\omega_{ee} - \omega_2 + \omega - i\Gamma_{ee})} \tag{19}$$

1.2. Isolating Particular Light-Matter Interactions

As described above, an interaction with light allows populations to feed coherences and vice versa. Four-wave mixing techniques select a sequence of three light-matter interactions to observe the energetic and dynamical properties of the system. If there were no restrictions placed on the interactions, interpretation of data would require extensive effort to isolate the processes that provide information about states and properties of interest. Two experimental parameters reduce the number of processes observed—temporal sequencing of the electric field interactions and spatial isolation of light produced by particular field interactions.

Suppose the excitation fields used have different frequencies. It has already been demonstrated that electric fields with frequencies that are not resonant with transitions produce coherences and populations with less efficiency than resonant fields. If one field is resonant with a transition fundamental and another field with the corresponding overtone (assuming that the system is anharmonic), one sequence of interactions will be doubly-resonant and the other sequence will not be resonant at all. A situation of this kind occurs with the experiment labeled IVα in Figure 1, to be described shortly. This kind of response to pulse time ordering may then reveal the existence of combination bands or overtones in a manner that would be obscured if the sequence of the electric field interactions was unclear.

The expressions derived above (equations (16)-(19)) report that a final state can be fed by a transition from multiple initial states. An extension of this observation reveals that a single initial state evolves into multiple final states when the electric field is observed to interact with the complex conjugate side (bra) of the density matrix element describing the initial state or the non-complex conjugate side (ket). An increase in the energy of the ket-side of a state requires a transfer of energy from the electric field to the system (as evidenced by an increase in the frequency of the final state; $\omega_{eg} > \omega_{gg}$). This process of energy removal from the electric field can be observed as a change in the momentum of the electric field equal to the momentum of a single photon, $\hbar\vec{k}$. An increase in the energy of the bra-side of a state involves the addition of energy from the electric field, as well, but from the component of the field that is propagating with opposite phase. Similarly, the change in momentum has the opposite direction. Thus for every electric field interaction, there is a corresponding transfer of momentum from the excitation field to the polarization of the system. Each positive interaction can add energy to the ket side of the state or stimulate the decrease of energy from the bra side; each negative interaction can perform the parallel actions. These capabilities appear in the derivations of (16)-(19) as the fast oscillating terms that average out according to the rotating wave approximation—the component of the electric field oscillating as $-\vec{k}$ averages out of the feeding term for $\widetilde{\rho_{eg}}$ and the $+\vec{k}$ averages out of the feeding term for $\widetilde{\rho_{ge}}$. After three successive electric field interactions, then, the final momentum of the driven oscillator polarization is $\vec{k}_{out} = \pm\vec{k}_1 \pm \vec{k}_2 \pm \vec{k}_3$. If all excitation beams enter the sample parallel to each other, the final output coherence will emit in the same direction, regardless of how it interacted with each pulse. By changing the angles of the incoming beams, $\vec{k}_{out}$ will have different directions for each combination of interactions.

Even when resonant, not all outputs will have identical intensities. In any experiment, energy must be conserved. If a system interacts with the three fields such that $\omega_{final} = \omega_1 - \omega_2 + \omega_3$, then the light emitted by this polarization has momentum characteristic of its frequency—$\vec{k}_{final}$. The intensity of this beam is dependent on the coherent build-up of light from an entire array of such oscillators. If the light from each polarized oscillator is out of phase with others, the intensity of the output will be low. As each oscillator is polarized by the laser electric fields ($\vec{k}_1$, $\vec{k}_2$, and $\vec{k}_3$), the output direction is defined by $\vec{k}_{out}$. The intensity losses due to the mismatch of phase between polarizations created in one part of the ensemble and those created others is $\mathrm{I} = \mathrm{I}_0 \operatorname{sinc}^2(\Delta \vec{k} l)$, where I and I_0 are the observed and maximum possible output intensities, l is the sample pathlength, and $\Delta\vec{k} = \vec{k}_{final} - \vec{k}_{out}$ is the phase-mismatch. Appendix B shows an example calculation pertaining to this consideration.

As explained further in Experimental Design, the experiments discussed in this work all made use of the phase-matching condition $\vec{k}_{out} \equiv \vec{k}_1 - \vec{k}_{-2} + \vec{k}_{2'}$. $\vec{k}_{-2}$ and $\vec{k}_{2'}$ are labeled as such because the pulses to which they correspond are generated from the same optical parametric amplifier (see Instrumentation) and hence have equal frequencies. By choosing a pulse sequence, then, an experiment can isolate particular sets of interactions. These interactions are shown from left to right as they occur in time in Wave-Mixing Energy Level (WMEL) diagrams in Figure 1. The relationship between a WMEL diagram and the corresponding Feynman diagram and Liouville representation are shown for reference in Figure 2. In WMEL diagrams, solid arrows show ket-side transitions; dashed arrows show bra-side transitions, and the final coherence output is shown by the dark double arrow. The positive k-vectors (from $\vec{k}_1$ and $\vec{k}_{2'}$) show donation of energy to the system by either increasing the energy of the ket-state or decreasing the energy of the bra-state, and the negative k-vector ($\vec{k}_{-2}$) is shown doing so in the opposite manner. Pathways labeled I through VI pertain to each possible pulse time-ordering. Figure 3 shows a plot of the relative timing of the pulses in which these six pathways are labeled.

The expression for the magnitude of a coherence created by a single four-wave mixing process in the steady state limit appears as a product of the individual interaction terms in equations (16)-(19). Consider, for example, the sequence labeled pathway IIIα in Figure 1. If the system begins in the ground state, $\rho_{gg} = 1$, then all other density elements are zero. By specifying this pathway, only the ρ_{ge}calculated from the first electric field interaction is important when calculating $\rho_{e'e}$, so the ρ_{ge} term effectively becomes the numerator for $\rho_{e'e}$.

$$\widetilde{\rho_{e'e}} = \left[\frac{\mu_{eg}\mathrm{E}_0}{2\hbar}\frac{(0-1)}{(\omega_{eg}-\omega_2+i\Gamma_{eg})}\right]\left[\frac{\mu_{e'g}\mathrm{E}_0}{2\hbar}\frac{1}{(\omega_{e'e}-(\omega_2-\omega_1)-i\Gamma_{e'e})}\right] \tag{20}$$

Similarly, only the $\rho_{e'e}$created by the first two interactions is important for the creation of the final output $\rho_{e'g}$ coherence, so substituting (20) for ρ_{ee} in (16) gives

$$\widetilde{\rho_{e'g}} = \left(\frac{\mathrm{E}_0}{2\hbar}\right)^3\left[\frac{-\mu_{eg}}{(\omega_{eg}-\omega_2+i\Gamma_{eg})}\right]\left[\frac{\mu_{e'g}}{(\omega_{e'e}-(\omega_2-\omega_1)-i\Gamma_{e'e})}\right]\left[\frac{-\mu_{eg}}{(\omega_{e'g}-\omega_1-i\Gamma_{e'g})}\right] \tag{21}$$

Confining experiments to low electric field intensities and a set phase-matching condition eliminates processes not shown in Figure 1. Specific pulse sequences select certain pathways within that experimental space. The only ways to observe α-pathways and not β-pathways require a difference between an accessed fundamental transition and the corresponding combination band. If a narrow band source cannot be resonant with the fundamental and the combination band, as in pathway IVα, then the detuning will decrease the contributions from that process. Similarly, if coupling separates the energies of output light generated by α and β processes, spectral resolution of the output can distinguish between the processes. Further, signal from α and β pathways destructively interfere. (21) shows the magnitude of the coherence created by pathway IIIα. When each incident field is resonant with the corresponding transition, (21) becomes

$$\widetilde{\rho_{e'g}} = \left(\frac{\mathrm{E}_0}{2\hbar}\right)^3 \left[\frac{-\mu_{eg}}{(i\Gamma_{eg})}\right]\left[\frac{\mu_{e'g}}{(-i\Gamma_{e'e})}\right]\left[\frac{-\mu_{eg}}{-i\Gamma_{e'g})}\right] = \left(\frac{\mathrm{E}_0}{2\hbar}\right)^3 \frac{-\mu_{eg}\mu_{e'g}\mu_{eg}}{i\Gamma_{eg}\Gamma_{e'e}\Gamma_{e'g}} \qquad (22)$$

The coherence created at the end of pathway IIIβ has a magnitude (23):

$$\widetilde{\rho_{e'+e,e'}} = \left(\frac{\mathrm{E}_0}{2\hbar}\right)^3 \left[\frac{-\mu_{eg}}{(\omega_{eg} - \omega_2 + i\Gamma_{eg})}\right]\left[\frac{\mu_{e'g}}{(\omega_{e'e} - (\omega_2 - \omega_1) - i\Gamma_{e'e})}\right]\left[\frac{\mu_{e'+e,e'}}{(\omega_{e'+e,e} - \omega_1 - i\Gamma_{e'+e,e})}\right]$$

When each excitation field is resonant for this pathway, (23) becomes

$$\widetilde{\rho_{e'+e,e'}} = \left(\frac{\mathrm{E}_0}{2\hbar}\right)^3 \left[\frac{-\mu_{eg}}{(i\Gamma_{eg})}\right]\left[\frac{\mu_{e'g}}{(-i\Gamma_{e'e})}\right]\left[\frac{\mu_{e'+e,e'}}{(-i\Gamma_{e'+e,e})}\right] = \left(\frac{\mathrm{E}_0}{2\hbar}\right)^3 \frac{\mu_{eg}\mu_{e'g}\mu_{e'+e,e'}}{i\Gamma_{eg}\Gamma_{e'e}\Gamma_{e'+e,e}} \qquad (24)$$

which clearly shows an absence of the additional factor of -1.

In some cases, pulse fluences are high enough to allow a system to interact with the electric field multiple times. In most cases, these multiple interactions result in output beams that are directed away from the optical path isolated for the desired signal beam. However, in certain cases it is possible to generate an output that overlaps in space with the intended observed light. For example, if the ω_1 pulse is allowed to interact three times, then $\vec{k}_{out} = \vec{k}_1 - \vec{k}_1 + \vec{k}_1 - \vec{k}_{-2} + \vec{k}_{2'}$, can describe the phase-matching for a process that accesses higher overtones or that interferes with other processes yielding output at fundamental transition frequencies, as shown in Figure 4. The direction of this k-vector is the same as $\vec{k}_{out} \equiv \vec{k}_1 - \vec{k}_{-2} + \vec{k}_{2'}$, so spatial isolation will not distinguish between the two. The destructive interference between the first process shown in Figure 4 and pathway IIIα becomes clear when magnitude calculations are juxtaposed as between (22) and (24). If all transitions are resonant, this higher order process produces a final coherence $\widetilde{\rho_{e'g}}$ with magnitude

$$\widetilde{\rho_{e'g}} = \left(\frac{\mathrm{E}_0}{2\hbar}\right)^5 \frac{-\mu_{eg}}{i\Gamma_{eg}} \frac{\mu_{e'g}}{-i\Gamma_{e'e}} \frac{-\mu_{e'g}}{i\Gamma_{eg}} \frac{\mu_{e'g}}{-i\Gamma_{e'e}} \frac{-\mu_{eg}}{-i\Gamma_{e'g}} = \left(\frac{\mathrm{E}_0}{2\hbar}\right)^5 \frac{\mu_{eg}\mu_{e'g}\mu_{e'g}\mu_{e'g}\mu_{eg}}{i\Gamma_{eg}\Gamma_{e'e}\Gamma_{eg}\Gamma_{e'e}\Gamma_{e'g}} \tag{25}$$

As discussed earlier, these additional interferences only become important when electric field strengths are high enough to overcome the disparity in magnitudes between $\chi^{(3)}$ and $\chi^{(5)}$.

1.3. Incorporating Inhomogeneous Broadening

Synthesis of colloidal quantum dots always yields a distribution of particle sizes. As exciton energies depend directly on the extent of the confinement, this distribution of sizes results in a broadening of the observed sample transition. To appropriately model data, it is important to represent the effects of this inhomogeneous broadening. Although the Central Limit Theorem predicts a Gaussian distribution of quantum dot sizes, the calculations performed here approximate the distribution as Lorenzian in order to arrive at a closed-form solution. This broadening is incorporated into calculations by setting the transition frequency to $\omega_{eg} + \xi$ and integrating over ξ, which is the independent variable in the Lorenzian distribution. Ignoring constants, (21) becomes

$$\tilde{\rho}_{e'g} = \left[\frac{1}{(\omega_{eg} + \xi - \omega_2 + i\Gamma_{eg})}\right]\left[\frac{1}{(\omega_{e'e} - (\omega_2 - \omega_1) - i\Gamma_{e'e})}\right]\left[\frac{1}{(\omega_{e'g} + \xi - \omega_1 - i\Gamma_{e'g})}\right] \tag{26}$$

This expression assumes that *e* and *e*' are perfectly and positively correlated, meaning that the shift ξ for each is identical. The total $\tilde{\rho}_{e'g}$ is found by integrating across the distribution with width parameter σ.

$$\int_{-\infty}^{\infty} \tilde{\rho}_{e'g} \frac{\sigma}{\xi^2 + \sigma^2} \mathrm{d}\xi \tag{27}$$

This integral can be solved using the Cauchy Residue Theorem. According to this theorem, an integral across the real numbers is related to the contour integral around either half of the complex plane bound by the real axis. The value of this integral is found using the sum of the residues for each pole encompassed by that contour.

$$\int_{-\infty}^{\infty} \tilde{\rho}_{e'g} \frac{\sigma}{\xi^2 + \sigma^2} \mathrm{d}\xi = 2\pi i \sum_n R_n \tag{28}$$

where the R_n are the residues corresponding to the nth pole. A residue is the value of a function evaluated at a pole without diverging factor. The integral above, then, has a total of four poles (each defined as a ξ_n), and there is a residue for each.

$$\xi_1 = \omega_2 - \omega_{eg} - i\Gamma_{eg} \tag{29}$$

$$\xi_2 = \omega_1 - \omega_{e'g} + i\Gamma_{e'g} \tag{30}$$

$$\xi_{3,4} = \pm i\sigma \tag{31}$$

For this integral, there are two poles with positive and two with negative imaginary contributions, and either pair may be used. Arbitrarily choosing those in the positive half of the plane (ξ_2 and ξ_3) directs the calculation to two residues:

$$R_2 = \left[\frac{1}{(\omega_{eg} + \xi_2 - \omega_2 + i\Gamma_{eg})}\right]\left[\frac{1}{(\omega_{e'e} - (\omega_2 - \omega_1) - i\Gamma_{e'e})}\right]\left[\frac{\sigma}{\xi_2^2 + \sigma^2}\right] \quad \text{(32) and (33 ↓)}$$

$$R_3 = \left[\frac{1}{(\omega_{eg} + \xi_3 - \omega_2 + i\Gamma_{eg})}\right]\left[\frac{1}{(\omega_{e'e} - (\omega_2 - \omega_1) - i\Gamma_{e'e})}\right]\left[\frac{1}{(\omega_{e'g} + \xi_3 - \omega_1 - i\Gamma_{e'g})}\right]\left[\frac{\sigma}{2i\sigma}\right]$$

Finally, then, for pathway IIIα,

$$\int_{-\infty}^{\infty} \tilde{\rho}_{e'g} \frac{\sigma}{\xi^2 + \sigma^2} \mathrm{d}\xi = 2\pi i(R_2 + R_3) \tag{34}$$

Complete expressions for all of the pathways can be calculated in similar ways. Frequency domain spectra for the most common pathway contributions are calculated and discussed further in Appendix A—Frequency Domain Simulations.

1.4. Interference from Non-Resonant Background

Electronic transitions tend to have fast dephasing rates and large transition dipole moments. As excitation frequencies used in experiments increase, the non-linear signal originating from the tails of these broad transitions becomes more significant. Though these contributions can make data more difficult to interpret on inspection, they can also serve as a standard reference if their source is a common solvent.[3, 4] Carbon tetrachloride was used as the solvent for all near-IR experiments described in this work. CCl_4 both has a strong third-order susceptibility and is a well-characterized material.[3] In earlier work, when narrow-band excitation sources were used, CCl_4 Raman contributions were significant.[5, 6] For experiments with femtosecond pulses, the broad background resulting from electronic transitions (from the solvent or the analyte) was more significant, and could be treated as invariant with excitation frequency over the ranges used in experiments. In simple calculations, the contribution can then be treated by adding a complex constant to the magnitude of the electric field created by the near-resonant non-linear polarizations of the analyte. This constant can then be related back to the known properties of to CCl_4 provide quantitative information about the analyte polarizability. Appendix A demonstrates and discusses the qualitative effects of non-resonant background on frequency domain spectra.

Works Cited

1. Skinner, J. L.; Hsu, D. Pure Dephasing of a Two-Level System. *Journal of Physical Chemistry* **1986,** *90* (21), 4931-4938.

2. Mathew, N. A. *Mixed Frequency/Time Domain Coherent Multidimensional Spectroscopy;* PhD Thesis; University of Wisconsin-Madison: Madison, WI, 2010.

3. Levenson, M. D.; Bloembergen, N. Dispersion of the Nonlinear Optical Susceptibilities of Organic Liquids and Solutions. *Journal of Chemical Physics* **1974,** *60* (4), 1323-1327.

4. Lascola, R.; Wright, J. C. Measurement of the Second Order Molecular Hyperpolarizability of C60- by Nondegenerate Four-Wave Mixing. *Chemical Physics Letters* **1997,** *269,* 79-84.

5. Yurs, L. A.; Block, S. B.; Pakoulev, A. V.; Selinsky, R. S.; Jin, S.; Wright, J. C. Spectral Isolation and Measurement of Surface-Trapped State Multidimensional Nonlinear Susceptibility in Colloidal Quantum Dots. *Journal of Physical Chemistry C* **2012,** *116* (9), 5546-5553.

6. Yurs, L. A. *Multiresonant Coherent Multidimensional Spectroscopy of Quantum-Confined Nanomaterials;* PhD Thesis; University of Wisconsin-Madison: Madison, WI, 2011.

7. Meyer, K. A. *Frequency-Scanned Ultrafast Spectroscopic Techniques Applied to Infrared Four-Wave Mixing Spectroscopy;* PhD Thesis; University of Wisconsin-Madison: Madison, WI, 2004.

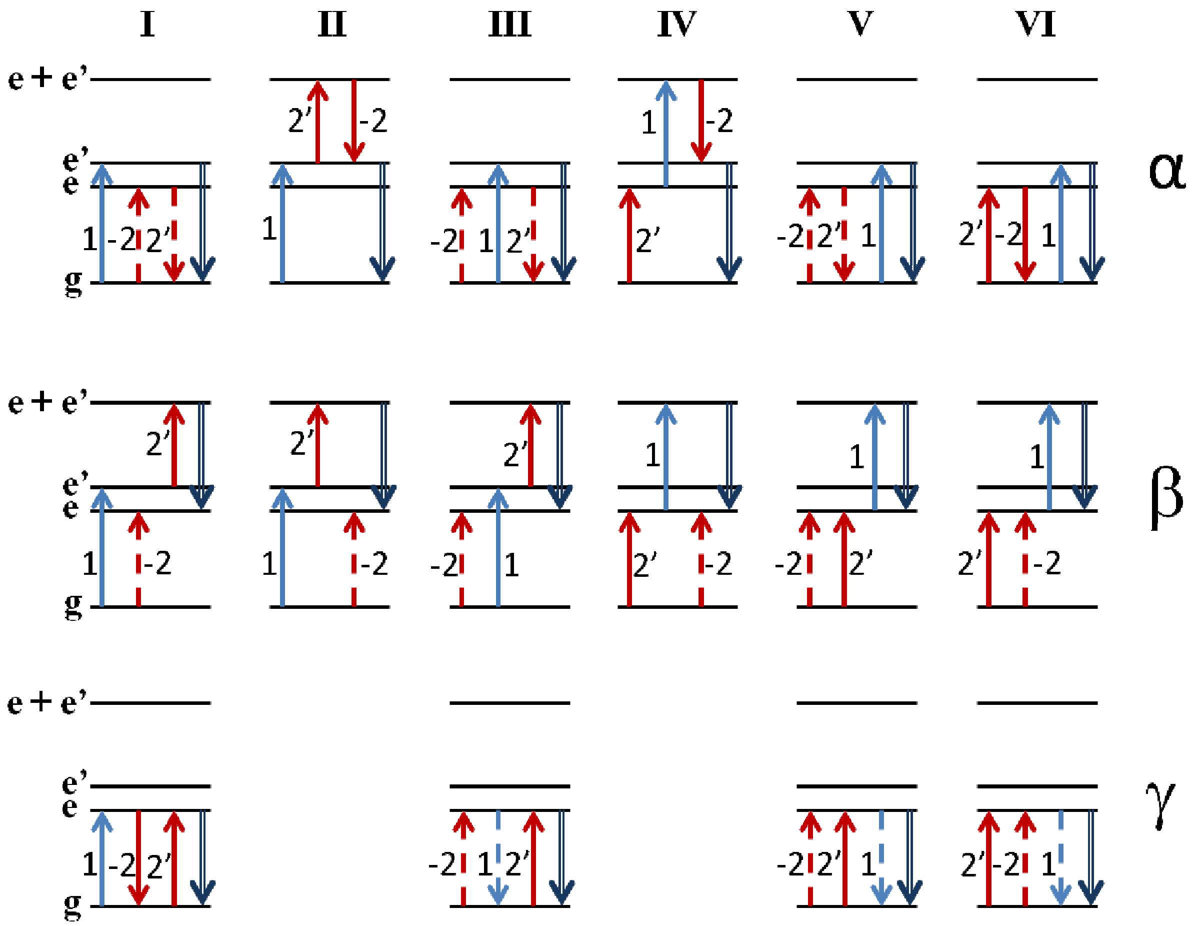

Figure 1—WMEL Diagrams for all six possible three-pulse time orderings, with the first pulse appearing furthest left and time proceeding to the right. Arrows are labeled according to the pulses they represent. Solid arrows correspond to ket-side transitions; dotted arrows represent bra-side transitions. The dark, double arrow is drawn between the ket and bra states of the final coherence, which emits the observed electric field. Alpha pathway emission leaves the system with no more energy than it had initially (they are parametric pathways). Beta pathways leave the system in an excited state (they are non-parametric pathways). Gamma pathways are observed when ω_1-ω_2 is either zero or resonant with a vibrational state (not shown).

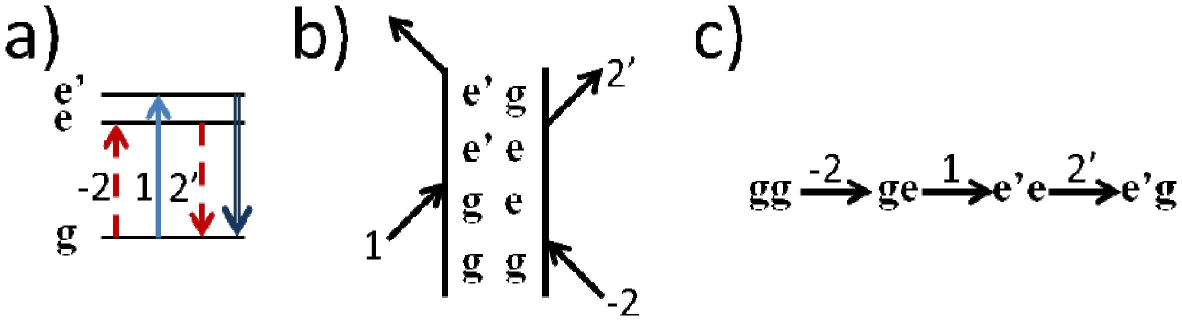

Figure 2—Four-wave mixing processes represented in common depictions. (a) A WMEL diagram, as explained in Figure 1. (b) A Feynman diagram tracing out changes to the ket (left) and bra (right) of the system. Electric field interactions are shown as labeled arrows proceeding in time from bottom to top. The output coherence is shown as the top, unlabeled arrow. (c) A Liouville diagram showing the progression of coherences. Arrows are labeled according to the pulses whose action they represent.

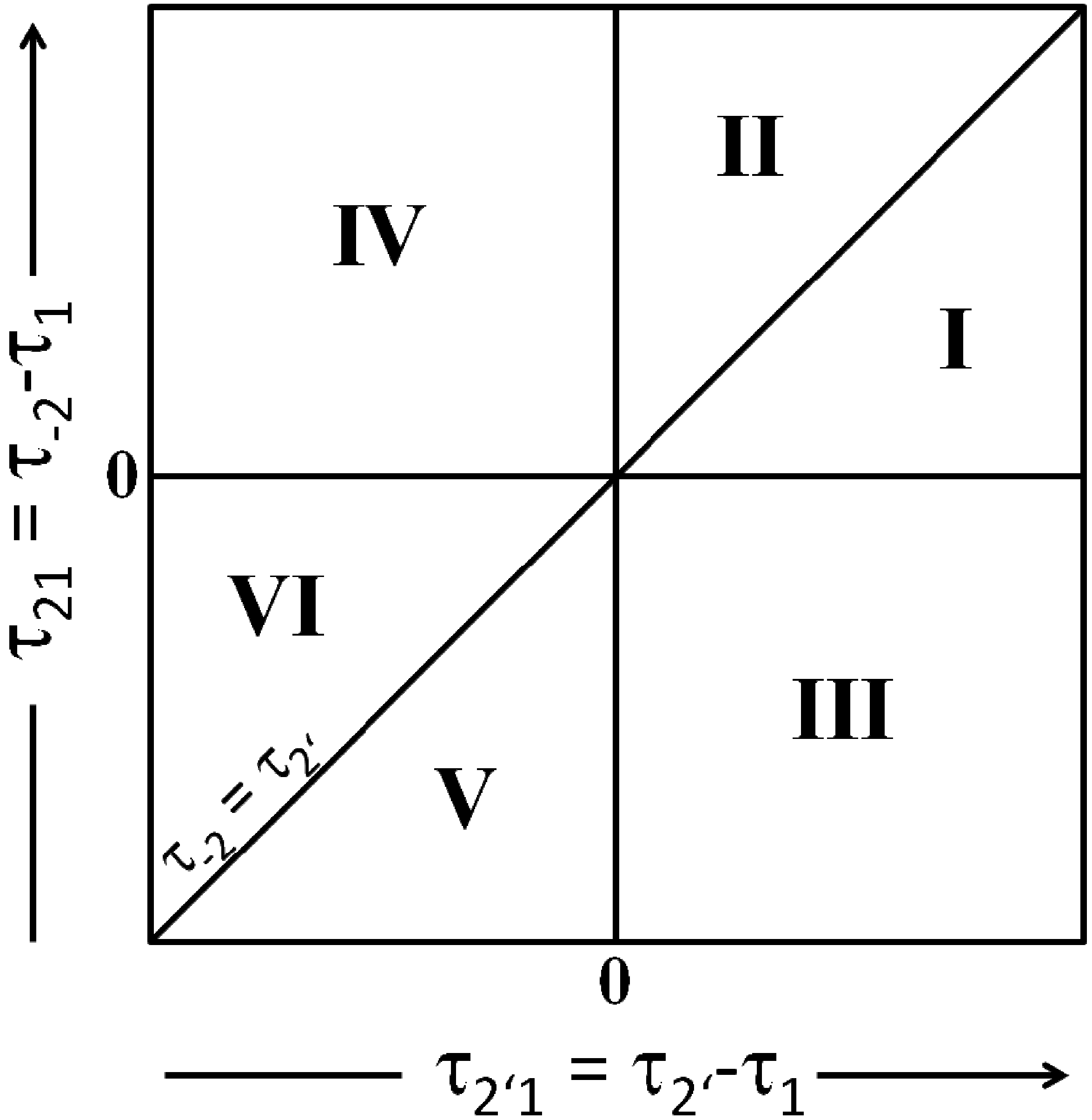

Figure 3—The pathways from Figure 1, as they would appear in a plot varying the relative delays of the three pulses. Positive values along either axis describe a condition in which the corresponding ω_2 pulse arrives after ω_1.

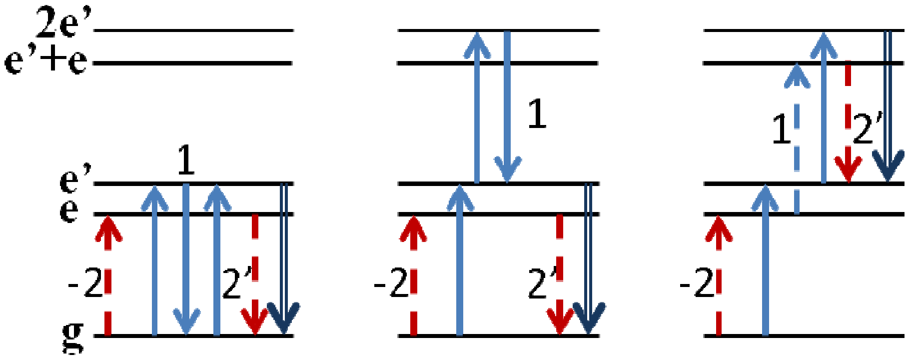

Figure 4—WMEL diagrams showing six-wave mixing variations of pathway IIIα when ω_1 is allowed to interact three times according to the phase matching condition described in the main text. These pathways destructively interfere with pathway III four-wave mixing signal.

Chapter 2: Picosecond Instrumentation

The research group of John Wright has been developing non-linear spectroscopic techniques for several generations of graduate students. The experiments highlighted in this work evolved out of triply vibrationally-enhanced (TriVE) four-wave mixing techniques for studying systems with vibrational transitions in the mid-infrared. [1, 2, 3, 4] While the laser system did require adaptation to access the near-infrared transitions of PbSe quantum dots, much of the instrumentation setup underwent no change. A thorough presentation of laser system components and alignment procedures can be found in the dissertation of Dr. Nathan A. Mathew. A more extensive reporting of the modifications required for PbSe work is included in the dissertation of Dr. Lena Yurs. A comparatively brief overview of each follows.

Both near-IR and mid-IR picosecond pulse generation required simultaneous pumping of picosecond optical parametric amplifiers (OPAs). Production of a suitable pump for these OPAs (Spectra Physics OPA-800c) began with a 650mW beam of 100fs 800nm seed pulses generated in a titanium sapphire Tsunami oscillator pumped by a continuous wave Spectra Physics Millennia V frequency-doubled Nd:YVO4. A Spectra Physics Spitfire titanium sapphire regenerative amplifier, pumped by a Spectra Physics frequency-doubled Nd:YLF Empower-15, stretched, amplified, and recompressed the seed pulse. The regenerative amplifier produced a 1.10mJ beam of 800nm picosecond pulses at a 1 kHz repetition rate, which was then split by a 45/55 800nm beamsplitter and directed into the OPAs.

The OPAs provided independently-tunable picosecond output throughout the infrared. The 800nm pump light was split into three beams. The first and weakest beam generated continuum light by being focused into a small, undoped YAG crystal and undergoing self phase modulation. One of the remaining 800nm beam lines amplified this white light pulse in a beta-barium borate (BBO) crystal. Alteration of the BBO angle relative to the incident beam polarization allowed optimal phase-matching ($\overrightarrow{k_{pump}} = \overrightarrow{k_{signal}} + \overrightarrow{k_{idler}}$) for the process of diverting light from the pump to desired signal and idler beams according to $\omega_p = \omega_s + \omega_i$. A grating selected a desired wavelength (always the wavelength of ω_s for these experiments) and redirected the beam through the BBO, where it overlapped and was amplified according to the same parametric process by the last 800nm beam. The signal and idler beams from this amplification processes were aligned to spatially overlap and were focused into a $AgGaS_2$ crystal rotated to an angle optimized for difference frequency generation (DFG) between the chosen signal and idler. Dichroic filters removed all remnant near-IR light.

The output from one of the OPAs was split by a 65/35 mid-IR beamsplitter before all three beams were directed down the table to the sample. Retroreflectors fixed on delay stages positioned by Nanomover motorized actuators controlled the path length, and relative pulse sequence in time, of the two beams produced by a single OPA (called ω_{-2} and $\omega_{2'}$ in anticipation of their use in the most common experimental phase-matching condition). A silver, 100mm focal length off-axis parabolic mirror focused the three beams into the sample cell. Transmitted beams and light resulting from coherent non-linear processes were collimated in a second off-axis parabolic mirror and directed toward the entrance slit of a monochromator. Irises and other beam-stops provided spatial isolation for the signal beam. The light was then focused onto the entrance slit of a McPherson model 218 monochromator, which provided spectral characterization of the light before it was passed into a liquid nitrogen-cooled Infrared Associates model MCT-10-1.0 HgCdTe detector. Current from the detector was converted to a voltage, passed through a Stanford Research Systems SR250 gated integrator/boxcar averager, and digitized for Labview processing by a National Instruments AT-MIO-16E-1 data acquisition card.

Reproducible alignment and calibration are critical for reliable experiment development. A small fraction of each OPA output was diverted to a pyroelectric detector[5] for power normalization. The voltage from the pyroelectric detectors had a low enough DC-offset to normalize without conversion to energy or power units. With every significant change to the optical table, however, these detectors were calibrated against a Scientech Model 360001 thermopile with known conversion efficiency (see Appendix D: Power Measurement With "The Pig"). A HeNe laser, overlapped in space with each infrared beam, allowed all beams to be aligned according to the desired experimental phase-matching condition. An additional HeNe line passed through the sample cell area in a direction predicted to overlap with four-wave mixing signal of interest. This line was then directed through the corresponding irises and apertures with the intended consequence of successfully guiding the signal light to the monochromator.

With beams overlapped in space at the sample cell position, the intensity of sum-frequency light generated in a $AgGaS_2$ crystal was measured as a function of the delay time between pulses. The dependence was fit to a Gaussian to define the position and width of the temporal overlap of the pulses. The width characterized the temporal profile of the pulses.

Silicon produces efficient four-wave mixing signal from three temporally and spatially overlapped infrared pulses. The last stage of alignment involved generation of non-linear signal from a silicon wafer. The HeNe tracer was used to produce approximate spatial alignment for output light; the signal produced by the silicon wafer was then aligned with more precision through irises and into the monochromator.

2.1. System Adaptations for Near-Infrared Quantum Dot Experiments

Very few changes to the alignment and calibration procedure were required to convert the laser system from the developed mid-IR experimental techniques to use for study of PbSe quantum dots.

BBO-based OPAs pumped by 800nm light efficiently produce light across the near-IR. The signal and idler light emerging from the BBO can be tuned across a wavelength range from 1.1-1.6μm and 1.6-2.7μm, respectively. The signal beam had the same polarization as the difference frequency light for which the table was built, so the adaptation seemed easy—simply remove the DFG crystal and find a way to filter out the idler and any residual 800nm pump light. The 800nm light was removed by an optically-dense cut-on filter. As the idler propagated with a polarization perpendicular to the signal, polarization filters were thought to be sufficient for final isolation of the signal. The parametric processes that amplify the signal and idler in the BBO also provided an array of sum-frequency and second harmonic beams. The second harmonic of the idler beam carries the same polarization as the pump. Further, the wavelength of the doubled-idler in the desired signal frequency ranges is either close to or slightly blue-shifted from that of the signal. These similarities rendered both spectral and polarization-based isolation techniques ineffective. The solution to this dilemma came in the form of an alteration to the OPA alignment procedure—align the seed and the second amplification beam in such a way that the output beams are no longer spatially overlapped. As a fair amount of effort was usually required to attain overlap in the first place, this adaptation was a rare example of a desired modification that was immediately easier to implement than familiar techniques. Use of irises spatially isolated the signal, doubled signal, and some of the divergent 800nm light from all other processes. The cut-on filter became the only optic required for complete isolation of the signal beam.

The seemingly-idyllic solution for converting the OPAs to operation in a new spectral range was tested for robustness. The slight pointing changes induced by tuning the BBO and grating angles for the generation of various wavelengths was found to be small enough to impact neither the passage of signal light through its irises nor the spatial overlap of the three pulses at the sample cell location. The competition between doubled-idler and signal production processes when $\omega_s = \omega_{2i} = 2\omega_i$ did yield a local dip in the power of the signal beam, but careful normalization was usually enough to account for this change. A discussion of the impacts of power fluctuations on multi-photon effects is included in the Experimental Design section.

Laser intensities and fluences used at first were high enough to cause quantum dots to detach from their passivating surface capping ligands and fuse to each other. Figure 1 shows the appearance of this destruction on both the macroscopic and microscopic scales. Removing the 150mm off-axis parabolic mirror increased beam diameters by a factor of about 20 (from ~100μm to 2mm), reducing the peak intensities and pulse fluences by a factor of 400. The unfocused beams produced more scatter than smaller beams of identical intensities because they could not be easily shifted away from cuvette surface defects and deposited films. Attenuation with neutral density filters allowed use of a 250mm lens for a balanced solution to intensity and beam size concerns.

The changes in wavelength range and electric field intensity decreased the sum frequency generation efficiency of the $AgGaS_2$. Attempts to calibrate the delay lines took a few forms. Saturable absorbers such as Q-Switch 5 and a thin germanium wafer were not solutions because the intensities required to produce noticeable saturation with homodyne detection were too high. A 6mm-thick BBO crystal, discarded as damaged by a home-built OPA in the research group of Fleming Crim, provided sum frequency light of high enough intensity to be visible to the naked eye. A silicon diode detector provided the signal response.

A liquid-nitrogen-cooled Teledyne Judson J10D-M204-R01M-30-SP28 Indium Antimonide detector replaced the MCT for all CMDS experiments.

Works Cited

1. Meyer, K. A. *Frequency-Scanned Ultrafast Spectroscopic Techniques Applied to Infrared Four-Wave Mixing Spectroscopy;* PhD Thesis; University of Wisconsin-Madison: Madison, WI, 2004.

2. Rickard, M. A. *Fundamental Studies of Triply Vibrationally Enhanced Four-Wave Mixing Spectroscopy;* PhD Thesis; University of Wisconsin-Madison: Madison, WI, 2008.

3. Kornau, K. M. *Triply Vibrationally Enhanced Four-Wave Mixing Spectroscopy;* PhD Thesis; University of Wisconsin-Madison: Madison, WI, 2009.

4. Mathew, N. A. *Mixed Frequency/Time Domain Coherent Multidimensional Spectroscopy;* PhD Thesis; University of Wisconsin-Madison: Madison, WI, 2010.

5. Hamilton, J. P. *Vibrationally Enhanced Infrared Four Wave Mixing;* PhD Thesis; University of Wisconsin-Madison: Madison, WI, 1994.

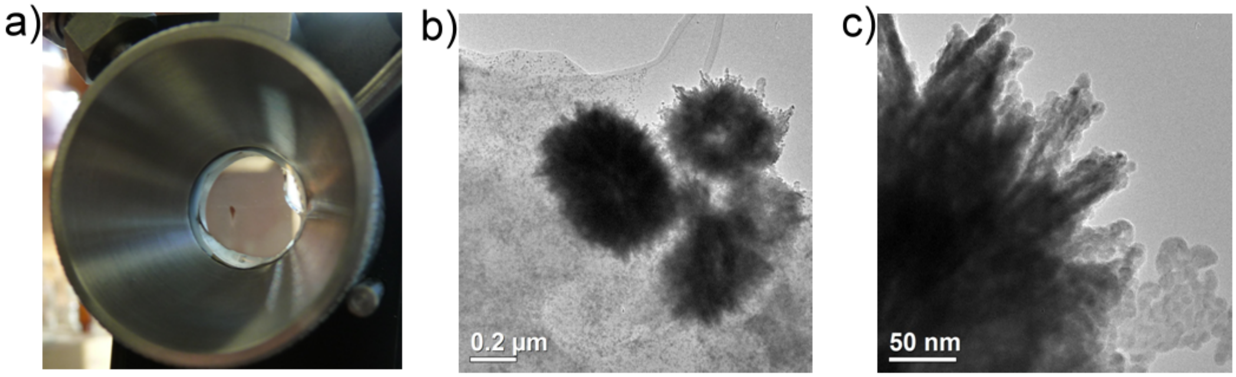

Figure 1—Photo-damaged PbSe quantum dot samples. When incident laser fluences were too high, dots shed ligands and clumped together. (a) The agglomerations fell out of suspension when they grew too large. (b) and (c) TEM images collected by Rachel Selinsky showing the agglomerations.

Chapter 3: Femtosecond Instrumentation

After exploring the capabilities of our experimental techniques using pulses with temporal widths on the order of one picosecond, it became clear that there was much to be gained by developing a similar laser table with shorter pulses. To produce these pulses, the Tsunami was adjusted to output 35fs seed pulses. A 70/30 800nm beamsplitter split the resulting beam with the reflected 70% aligned into the picosecond regenerative amplifier and the transmitted 30% directed toward the new 35fs amplifier (see Figure 1 for the complete table layout). A 20W Nd:YLF Empower beam pumped the new SpectraPhysics Spitfire Pro 4W. Its output was split and pumped a pair of Topas C OPAs, which produced tunable 40fs pulses for the desired experiments. OPA outputs were then split (into a total of three lines—ω_1, ω_{-2}, and $\omega_{2'}$) and directed through a series of optics before being focused into a sample cell. Irises spatially isolated the resulting four-wave mixing output before it was focused into a monochromator. The detected light produced a current in a semiconductor detector, which was subsequently converted to a voltage and passed to a boxcar integrator (Stanford Research Systems) and a shielded connector block (NI-BNC-2110) before being digitized by a data acquisition card for LabView data collection.

3.1. Optical Component Selection

Successful use of the femtosecond pulses required careful component selection and initial setup. To avoid pulse elongation from chirp, the table was designed to use almost exclusively reflective optics. Whenever possible, the surface of these mirrors was chosen to be protected silver. Silver has high reflectivity throughout the visible and near-infrared. The protective oxide coating increases the damage threshold by preventing silver oxidation by the surrounding air in the event of ionization by the high intensity instantaneous electric fields.

The few non-silver optics used deserve specific additional explanation. The output from the OPAs has enough energy to slowly damage even protected silver optics and more than enough to destroy any of the semiconductor nanocrystalline samples of interest. Consequently, each OPA output beam is reflected off the front surface of a thick glass wedge, reducing the beam energy by a factor of 25. The lack of parallelism between the faces of this wedge and the wedge thickness each serve to ensure that the reflection off the back surface of the glass is as spatially separated from the desirable beam as possible. In addition to the power reduction from the wedge, each OPA output was passed through a linearly-variable neutral density filter. These filters allowed experiments and calibration routines to tune pulse energies for each task without changing the optical path length through which the pulses traveled.

The only other non-reflective optic used on the table is a near-IR beamsplitter, which served to generate a pair of pulses from OPA2, labeled -2 and 2’ to anticipate the most commonly used experimental phase-matching condition. Careful spectral calibration of each beam’s energy was important because the splitter varied from 70/30 to 40/60 over the course of the tuning range of the OPA signal beam (λ = 1.1-1.6 mm).

Each beamline passed into a retroreflector mounted on a translation stage with precise position control. Two stages controlled by manual actuators allowed x- and y-axis translation for retroreflector output alignment. A third manual stage provided a large range of imprecise z-axis translation. All delay scans and precise positioning were performed by Newport MFA-CC DC motorized linear stages with a minimum step size of 100nm (corresponding to a change in delay of 1.33fs) and a resolution of 17.5nm (58as). A set of three perpendicular manual translation stages was also used to reproducibly control the sample cell position.

A 1000mm focal length silver spherical mirror focused the three beams into the sample. Parabolic mirrors are a common choice for focusing element because they lack focusing aberrations. The production of these mirrors, however, relies on a machining technique that leaves small, repeated imperfections capable of refracting light with wavelengths as long as some portions of the visible spectrum. A spherical mirror was chosen in the hope of eventually using visible light pulses for experiments. To avoid problems with spherical aberration, alignment procedures intentionally spaced each incoming beam an equal distance from the center of the mirror. The long focal length was chosen to allow higher pulse energies without introducing destructive pulse fluences to the sample. An added advantage to this selection is the improved ease of phase-matching across large tuning ranges made possible by the low relative angles of the incoming beamlines. (See Appendix B—Phase-Matching Near Absorptive Features for further explanation.)

Sample cells used in all femtosecond experiments reported in this document were 1mm-thick IR-quartz cuvettes. These cells offered minimal absorption over the wavelength ranges of interest and short enough path lengths to minimize problems associated with phase-mismatch and the reabsorption of non-linear signal by optically dense samples.

A monochromator was used for all experiments to provide spectral resolution of non-linear signal beams. Because of the wide spectral bandwidth of the excitation beams, and consequently of the signal beam, high spectral resolution would have only decreased the intensity of the light reaching the detector; it would not have provided significant additional information. Consequently, the monochromator chosen was the Horiba Yvon MicroHR, with a focal length of only 140mm. The grating used for these experiments in the near-IR had 150 lines/mm and was blazed for 1μm light. This combination of focal length and grating groove spacing yields a reciprocal linear dispersion of about 48nm/mm. The exit slit was commonly used between 350μm and 500μm, yielding a detected bandwidth of between 18nm and 24nm. These slit settings ensured that the monochromator defined the spectral resolution rather than the excitation pulse bandwidth (typically 35nm-to-50nm-wide). The monochromator model chosen also uses only toroidal focusing mirrors and has two exit apertures—one for an imaging CCD and one with an adjustable exit slit for a single element detector. In time, this device should easily adapt to use in multiplex detection experiments.

Lastly, the detector selected was a liquid-nitrogen-cooled Teledyne Judson J10D-M204-R01M-30-SP28 Indium Antimonide photodiode. This detector has high sensitivity throughout the wavelength ranges of interest in the near-IR and much of the visible spectrum, with a specified sensitivity range of 0.5-2.8μm.

3.2. Initial Arrangement and Calibration

The optical table was initially designed to allow independent alignment of each of three parallel-polarized beamlines. From an arrangement intended to yield approximately equal path lengths (explained below), it was important to ensure that all beam travel occurred either parallel to the table or in periscopes and retroreflectors that would not change the polarization of the electric fields. Linearly polarized light rotates when its pointing is changed in both the direction of its polarization and any perpendicular direction. To verify that no optic introduced vertical deflection of the beam, a fixed-height aperture of fixed height was translated along the optical path. Restrictions accounting for this polarization rotation concern can be relaxed if all beams reflect off the same optics—the polarization may not be vertical or horizontal, but the polarizations should be mutually parallel—and the sample is centrosymmetric.

To enable independent alignment of each line, table design ensured that there were always two adjustable reflective optics available before any beam target—an early optic to adjust position on a later optic whose angle would provide desired directional changes. (See Appendix C—Daily Calibration Routine for examples). Once the alignment procedure had been determined, a collection of irises positioned around the table allowed every adjustable optic to be directed through a unique aperture.

Day-to-day fluctuations in ambient condition can change pointing into and out of the OPAs. It is critically important that beams enter the retroreflectors parallel to the travel direction of the delay stages. If this condition is not met, a change to the z-axis actuators intended to change path length will also change the position of the outgoing beam. To avoid this problem, a pair of irises were positioned such that alignment to these apertures would also direct a beam into the retroreflectors correctly.

Once the basic design was established, the relative path lengths were adjusted so that the pulses would arrive at the sample simultaneously or with known relative delays. A piece of thin, flexible wire used to trace trajectories through the optics provided the first rough path length measurements. Introduction of an extra optical loop, in the form of two additional mirrors, accounted for the majority of the initial path difference. When the relative pathlengths were close, the manual actuators on the retroreflector delay stages provided precise adjustments.

Determination of temporal overlap between any two pulses required use of a 100μm-thick BBO crystal. With the two beams spatially overlapped in the BBO crystal, slow adjustment of the z-axis position of one of the retroreflector delay stages changed the relative pulse timing. When the pulses overlap in time, they produce light at the sum-frequency. Their direction is determined by the sum of the contributing wave vectors. The very first calibrations were performed with high intensity 590nm (orange) beams. When overlapped, they produced ultraviolet light that made the BBO fluoresce and direct a visible violet beam to a white note card positioned behind an absorption filter that removed the bright transmitted orange light.

Isolation of the desired four-wave mixing beam from the transmitted excitation beams became possible once all three beams were aligned to temporal and spatial overlap at the sample. A thin silicon wafer yields a high intensity non-linear signal when the excitation energies are lower than the bandgap (whereas near the bandgap or higher, absorption effects become more significant). The resultant beam had enough energy that it was easy to locate and direct through the monochromator. An aperture positioned to block the transmitted beams isolated the four-wave mixing signal. This isolation allowed mirrors directing the signal beam to the monochromator to be adjusted to optimize the passage of only the desired light.

Because the holders for samples, the silicon wafer, alignment pinholes, and the BBO are different, it was necessary to identify a method for reliably positioning each. The temporal profile of the pulses at various z-axis sample cell positions determined the sample locations. For example, suppose BBO calibration is performed at a particular sample stage z-axis position. Watching silicon output should yield signal maxima and temporal widths as the delays are scanned. These widths and intensities should change as the z-axis position of the silicon wafer is changed because the wafer will be located at positions of varying beam overlap and cross-section. Starting with the pinhole used in daily calibration, it was determined that the BBO should be 0.2in closer to the beam source than the pinhole and that both the silicon wafer and the sample cell should be 0.4in closer. The shallow beam focus used minimized the positioning effects, but slight differences in beam overlap and imperfect beam mode-structure made assurance of consistency important.

The relationship of OPA output power and neutral density filter position to the pulse energy incident upon the sample required calibration. A Spectra Physics 407A detector is the most convenient way to measure OPA output energy, but its sensitivity is not high enough to accurately measure beams with powers as low as those needed for experiments on nanocrystalline samples. The ThorLabs PM100D detector is more sensitive, in general, but the detector head does not respond to light with wavelengths longer than 1μm. “The Pig”, a carefully calibrated thermopile is both sufficiently sensitive and accurate for the pulse characteristics used in these experiments, but it is cumbersome and has a very slow response time. Consequently, The Pig was used to measure the power of each beam line at an array of different wavelengths and neutral density positions. Comparison of these energy measurements to readings taken from the 407A allowed all subsequent energy measurements to be translated from 407A values to real pulse energies, simply by knowing the natural density position and the wavelength.

Comparison of results with existing literature requires some measure of either pulse fluence or intensity at the sample. With pulse energies measured, the only remaining unknown parameter is the beam cross-section area. This value can be determined by placing a razor in the position of the sample cell and translating it across the beam path while measuring the beam power that passes the blade edge. By knowing how far the razor must be moved to block various percentages of the beam power, it is possible to calculate the corresponding beam waist, assuming a TEM_{00} profile. The position versus power plot is an error function (as each slice in position is itself the area of a Gaussian peak), which can then be integrated to find the full width at half maximum. Typical beam diameters were between 450μm and 650μm.

3.3. Later Table Developments

It became clear that further alterations would be necessary as more experiments were performed. Most of these changes simply brought more careful control or more stability, but they are worth noting.

It was understood from the time the femtosecond amplifier was being installed that the system would be extremely sensitive to air currents and temperature fluctuations. The laboratory had recently been equipped with new air conditioning units, and the output of these units had been directed above the ceiling tiles so as to cool the room evenly by way of carefully placed filtered grates. Nevertheless, air currents threatened to cause problems, so an enclosure was constructed around the amplifier, its seed beam, its pump, and part of the area occupied by the OPAs. Few enough stability problems seemed to arise, so the OPAs remained in the open.

Scattered light frequently interfered with experimental scans. To solve this problem, a chopper synchronized to one half of the amplifier repetition rate was added to one of the beamlines (initially ω_1) and the boxcar integrator was configured to perform active baseline subtraction. While the signal-to-noise ratio did improve, some of the data accumulated when the pulses were overlapped in time still had unacceptable fluctuations. The increase in signal intensity as the pulses approach temporal overlap is very sensitive to the exact relative delays, so the relative pulse timing was measured each minute to compare the differences between having the chopper turned on or off for several minutes. The start of the chopper wheel was revealed to induce a substantial change in delay (see Figure 2, particularly from 2:15 to 3:15). All subsequent use of the chopper provided at least an hour for the created air currents to either stabilize or reach steady state. It was also discovered, however, that even with the chopper off there was a small periodic fluctuation to the relative pulse timing.

The only variables changing over the course of the experiments, other than the chopper wheel turning or not, were the ambient conditions. Data that tracked the air conditioner cycles were collected the following day (see Figure 3). The temperature fluctuations at the location of the thermometers used for air conditioner feedback had a period equal to that seen in the changes of relative pulse timing. Completion of the enclosure for the OPAs diminished the magnitude of the fluctuations.

Because most experiments performed in this work force the monochromator to track with ω_1, active baseline subtraction failed to eliminate scattered light from the ω_1 beam that would always be resonant with the light passing through the monochromator. When the chopper was transferred to one of the ω_2 lines, scatter was confined to only those scans or portions of scans when $\omega_2 = \omega_1$ (= ω_m).

Several early concerns regarding alignment surrounded the choice of focusing optic. While the reasons for choosing a long focal-length spherical mirror have already been described, a change to the table alignment was required for optimal use of this mirror. When the three excitation beams were directed into the mirror while parallel to each other, their position of overlap fell earlier than the location of each individual beam waist minimum. This difference is caused by spherical aberration. The separation from one end of a beam to another is small, so the shortening of the focal length is minimal. The separation between beams is comparatively large, so the distance to the point of overlap is significantly diminished. Introduction of a scheme to align the beams in such a way that they were diverging from each other as they reached the focusing optic extended the distance to overlap until it better matched the focal length of each individual beam. This alignment added further benefits: the incidence angles of the three beams at the sample were lower and the beam cross-sections were smaller at the point of overlap. These two effects further relaxed any intensity decreases due to phase-mismatch, improved the temporal resolution of experiments by decreasing the relative profiles of the pulses, and enabled use of the pulses where their phase front curvature was minimized.

The insertion of a 6mm-thick BK7 window in the beam path between the amplifier and OPA2 was a late addition to the table, designed to improve the temporal profile of the pulses produced by the OPAs. The line pumping OPA1 passes through a 4mm-thick beamsplitter at a 45-degree angle relative to incidence. That beamsplitter, then, introduced about 5.6mm of BK7 path—thick enough to effect the sensitive calibration of the OPA. The amplifier compressor was adjusted daily to yield the highest OPA1 output power, but the difference in chirp between the OPAs meant that OPA2 was then being pumped by sub-optimal pulses. The additional window was added to match the chirp produced prior to OPA1. The optic has 800nm broad-band anti-reflection coating on both surfaces.

The element that focused light onto the monochromator entrance slit was one of the few non-reflective optics on the table. For many early experiments, the element chosen was a simple plano-convex BK7 lens. As all concerns for temporal profiles are limited to the form of the pulses at the sample, a mirror was not deemed necessary. It was observed that beams reaching the lens to the left or right of its center required realignment when their wavelength was changed from one end of a tuning curve to the other. Initially, this was feared to be due to changes in OPA output pointing, but a beam hitting the top of the lens did not seem to experience this need for realignment. Because of the typical position of the signal beam on the lens (almost directly below the center of the lens), then, there was little problem with initial experiments. The problem still required attention, as it was determined that the magnitude of deflection due to chromatic aberration by such a lens was significant enough to send incoming beams up to 100μm toward or away from the intersection of optical axis with the plane of the monochromator entrance slit. This deviation presented little problem in situation where beams were deflected up or down. In the cases of beams deflected to the left or right, the change was significant enough to shift the spot into or out of the monochromator entrance slit, which was usually held at 200μm wide. The purchase of a near-IR achromatic doublet eliminated this problem.

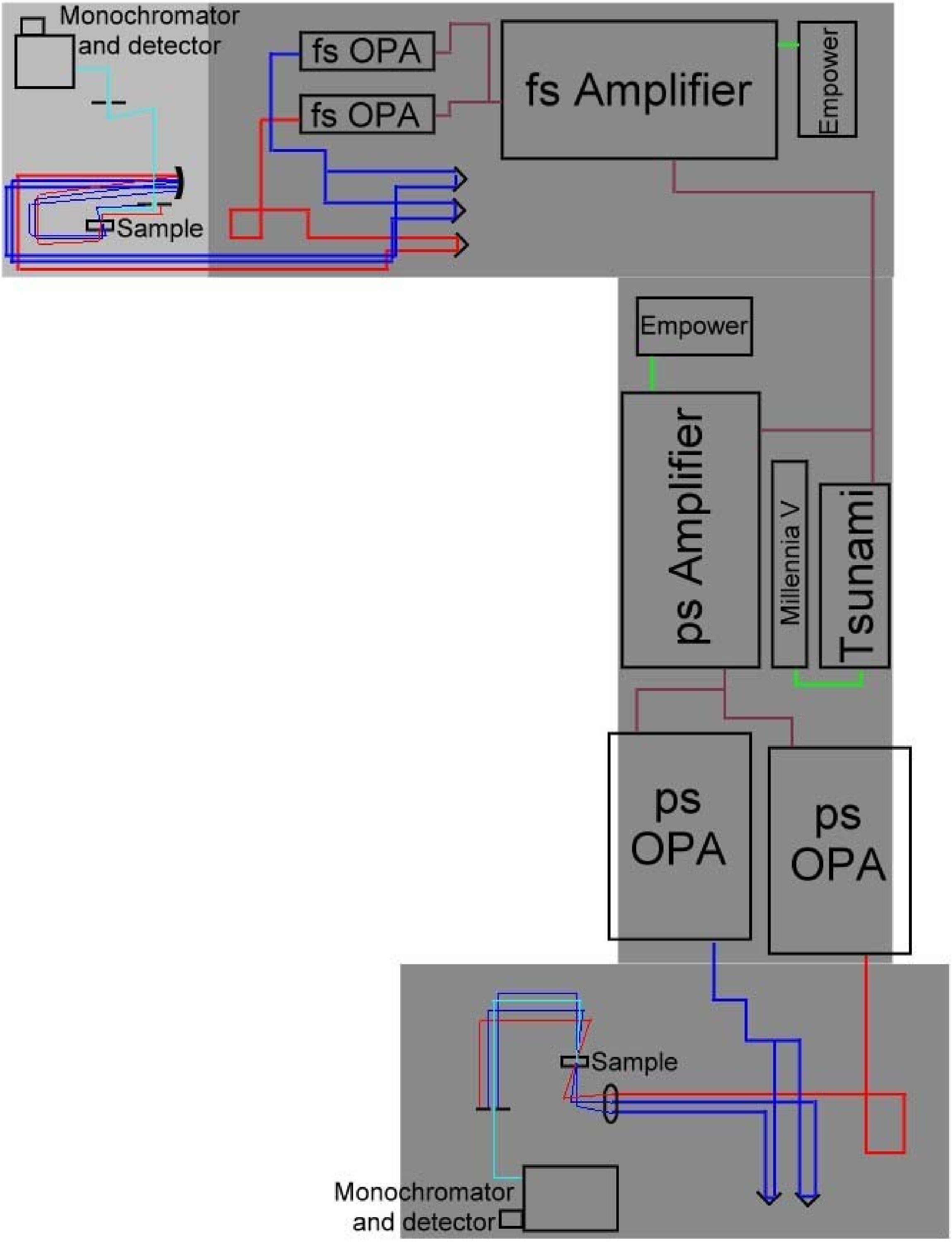

Figure 1— Laser table after addition of femtosecond laser system. For either table, the red beam traces the path of w1, the blue beam traces the path of w2 and w2', and the light blue path shows the desired four-wave mixing output. Purple lines show 800nm light from either the seed or a regenerative amplifier. Green lines show doubled Nd:YLF or ND:YAG pump light.

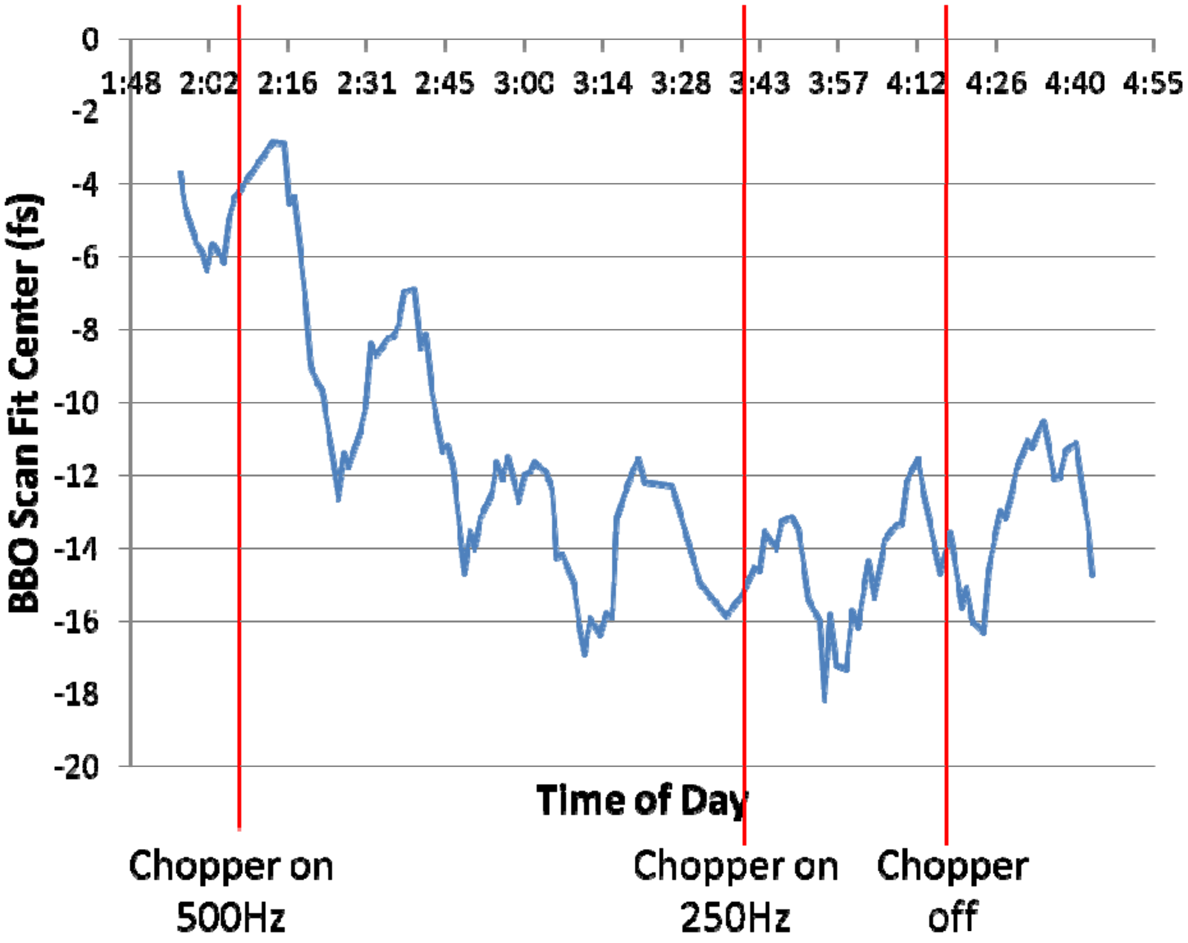

Figure 2—Zero Delay Value Drift and Fluctuation. Shown above is the retroreflector position (converted to femtoseconds away from the initial calibration of the day) yielding maximum pulse overlap at the sample cell as this value changed over the course of the afternoon. Vertical red lines indicate times when chopper wheel settings were changed. Notice both the drift in delay after turning the chopper on and undulations with 25-minute period.

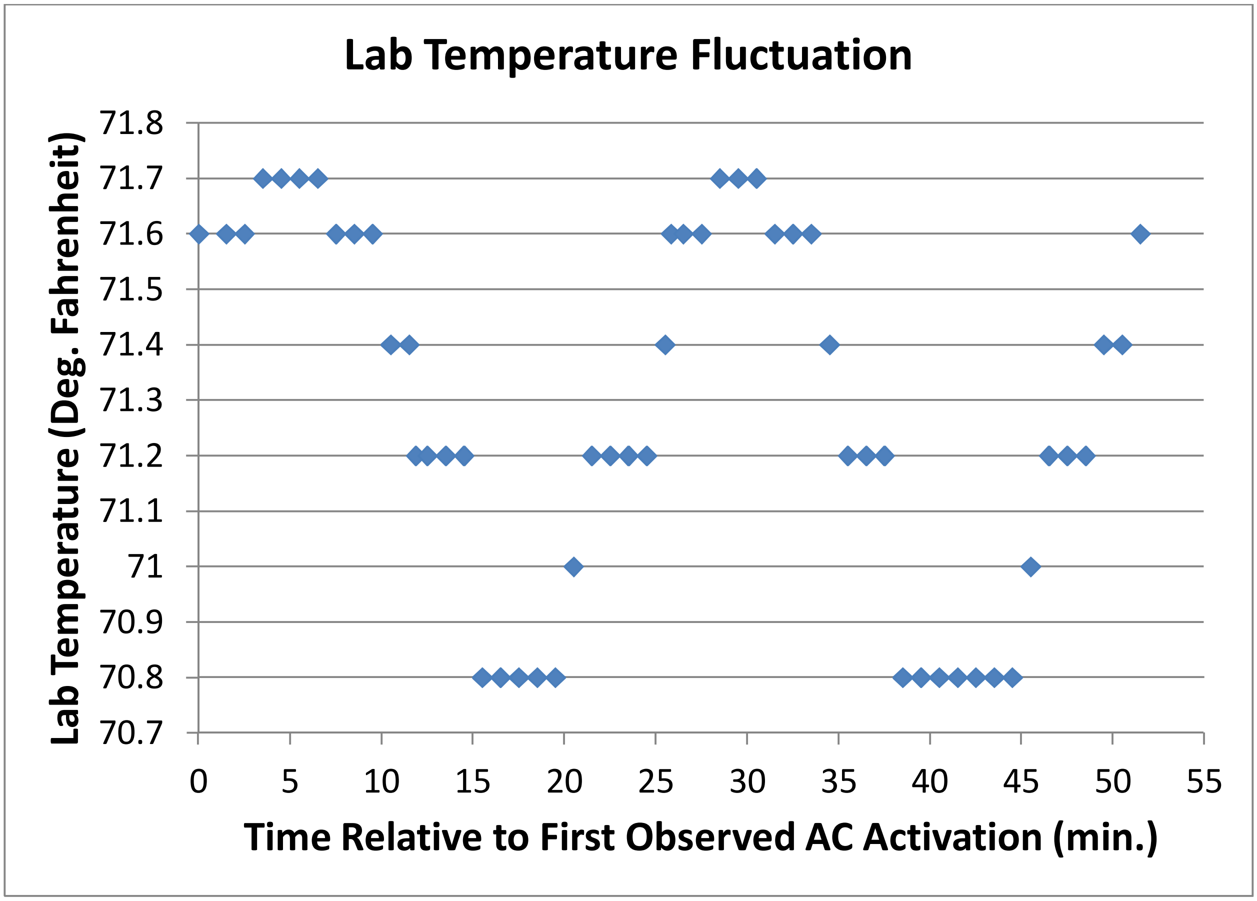

Figure 3—Lab Temperature Fluctuation. The data plotted show the temperature measured by digital thermometers located above the Tsunami. Notice the 25-minute period of the oscillation.

Chapter 4: Experimental Design

The power of MR-CMDS lies in its flexibility. For every experiment, there are easily-adjusted experimental parameters chosen and a combination of variables scanned. Pulse fluences, phase-matching condition, beam polarization, and pulse duration are a few of the parameters chosen before the start of any given experiment. Scans then vary some subset of the two excitation frequencies (ω_1, ω_2), the monochromator frequency (ω_m), and the temporal spacing between the pulses (τ_{21}, $\tau_{2'1}$) while measuring the intensity of light produced, isolated, and passed through the monochromator. Experiments varying excitation frequencies reveal energetic structure and state couplings; experiments varying time delays explore lifetimes and dynamics. Thoughtful selection of dimensions for one-dimensional and two-dimensional slices in this five-dimension variable space provides detailed characterization of the properties hard-to-study samples.

4.1. Sample Preparation

The experiments discussed in this work focus on colloidal PbSe quantum dots. MR-CMDS techniques were developed on systems with vibrational transitions of interest. Technique descriptions, then, will make use of experiments performed on (1) rhodium dicarbonyl acetylacetonate (RDC) dissolved in hexane and (2) octane diluted by CCl_4. The significance and detailed analysis of these experiments is reported elsewhere.[1, 2, 3, 4, 5, 6, 7] Sample cells used for vibrational system studies featured a pair of 2mm-thick calcium fluoride windows separated by Teflon spacers according to the optical density needed for each experiment. Path lengths were usually chosen to be between 100 and 250μm.

Rachel Selinsky synthesized the quantum dot samples used in most picosecond PbSe experiments. Yanghai Yu synthesized the third batch studied with the picosecond laser system. Dan Kohler prepared all samples studied on the femtosecond laser system. Each used a colloidal synthesis technique developed and described by Guyot-Sionnest.[8] Absorption scans provided the first characterization of each sample. The wavelengths of the 1S and 1P exciton absorption peaks determine the range over which the OPAs must be tuned. The 1S absorption location provided a measure of the nanoparticle diameter,[9, 10, 11] as well. Calculation of particle dimensions allowed better comparison between this work and results from around the field. Transmission electron microscopy (TEM) characterization verified dimension calculations, but also revealed the presence of particle agglomeration, deformity, and polydispersity. Agglomeration was the chief result of exposure to too much laser energy. Deformity, polydispersity, and the alignment of dots into wires indicated flaws in synthesis or its component reactants.

The first attempted experiments with PbSe made use of the same sample cells as those in mid-IR studies. Sapphire windows improved the transparency of the cell in the near-IR. Initial explorations revealed two significant problems in the sample handling—sample absorbances that were too low for strong four-wave mixing signal and laser intensities leading to the destruction of samples, as described further with discussion of other picosecond instrumentation adaptations.

If excitation lasers are aligned such that phase-mismatch in a sample is minimized, then four-wave mixing signal strength will increase monotonically with sample absorbance until reabsorption processes become significant.[12, 13] As the substance under study fixes the absorptive cross-section of interest, path length and concentration became the varied parameters when absorption values were found to be too low. PbSe quantum dot samples have low saturation concentrations when suspended in the long chain organic acids used as capping ligands [14] for surface passivation. It was not possible to increase the sample path length enough to achieve the desired absorbance with oleic acid as the solvent. Other stronger solvents, carbon tetrachloride and chloroform, in particular, were capable of providing much higher concentrations. The use of oils as capping ligands caused the sample to diffuse through the grease used to seal the sample cells, which in turn gave these stronger solvents access to the glue used to fix the sample cell windows to the rest of the cell. The solvents then dissolved this glue. The slow leaks that formed exposed the samples to ambient atmospheric conditions, greatly increasing their rate of oxidation. Further, even these higher concentrations required path lengths on the order of 1mm. Consequently, experiments came to use quartz cuvettes with 1mm widths. To avoid oxidation, these cuvettes were filled under an inert atmosphere in a glove box, capped with a Teflon stopper, and further sealed with Parafilm.

4.2. Experimental Parameters

Every line of MR-CMDS experiments required that certain parameters be set before alignment and calibration.

The phase-matching condition used in all experiments included here was fixed. Earlier work [1, 7] used an alternative phase-matching condition in order to emphasize certain energy-transfer processes. This work used the condition $\overrightarrow{k_{out}} = \overrightarrow{k_1} - \overrightarrow{k_{-2}} + \overrightarrow{k_{2'}}$, where $\overrightarrow{k_{-2}}$ and $\overrightarrow{k_{2'}}$ correspond to the pair of beams produced by a single OPA output. By choosing a pathway with both a positive and a negative interaction at ω_2, it is possible to use that pair to create populations that can be probed by an independently-tuned ω_1. Experiments with intermediate populations allow MR-CMDS results to be directly compared to work that uses the comparatively-common pump-probe and transient grating techniques.

Though not an option for the first year of the PbSe quantum dot studies, pulse duration must be chosen to match the coherence lifetime of sample of interest. In order to retain the full flexibility of a mixed time/frequency domain technique, pulse widths must be able to resolve quantum states in frequency space and observe coherent dynamics in the time domain. Experiments performed with picosecond pulses offered the right balance for vibrational mode investigations, but were largely equivalent to a frequency-domain approach for PbSe quantum dot exciton state studies. Though a lot of information can be extracted from frequency-domain studies, attention shifted to femtosecond experiments as soon as the system had been constructed.

It can be advantageous to adjust the relative polarizations of the excitation pulses. When one pulse is rotated from being vertically polarized to horizontally polarized, the resulting four-wave mixing signal is also rotated.[15] A polarization filter then eliminated scatter from two of the three excitation beams. Polarization rotation can also selectively excite modes with well-defined relative angles or be used to create polarization gratings[16, 17] and the angular momentum dynamics they access, but was not used with that intention for any explorations reported here.

The most frequently-adjusted parameter for MR-CMDS experiments was pulse fluence. An increase in fluence opened a category of experiments with RDC and $W(CO)_6$ that explored the 2- and 1-dimensional vibrational potential wells of each up to seven quanta in vibrational modes.[5, 18, 19]

The first PbSe experiments sought to control laser powers in order to avoid damaging the samples. Original plans made use of pulse intensities that matched those used in similar existing studies. **20** When TEM results showed that the samples were still deteriorating due to QD agglomeration, it became clear that fluence was a better measure of sample damage. The targeted intensities originated from experiments using 100fs pulses. When pulse *fluence* values were adjusted to match those in other work, sample longevity improved greatly.

The high native energy output of the femtosecond OPAs (250-300μJ/pulse) required dramatic attenuation before being useful for the study of PbSe quantum dots. The high maximum available energy, and hence capability to damage samples or unintentionally generate multiexciton states, made it imperative that pulse energies be carefully characterized. Those pulse energies, combined with measured beam cross-sections at the sample, were converted to a calculation of the number of photons absorbed per quantum dot per pulse. Studies by Moreels,[9] provided a calibration curve relating quantum dot size to integrated molar absorptivity. For consistency, the center of the 1S exciton absorption feature was used to identify the quantum dot diameter for each sample according the relationship determined by Moreels:

$$E_{1S} = 0.278 + \frac{1}{0.016d^2 + 0.209d + 0.45}$$

where E_{1S} is the energy of the 1S exciton in electron-volts and d is the diameter of the quantum dot in nanometers. This calculated diameter was then shown to relate to the integrated absorptivity (in meV*cm^{-1}/μM) by

$$\int \varepsilon dv = 3.1d^{0.9}$$

Assuming it can be described by a Gaussian profile, the peak molar absorptivity, and hence the absorptive cross-section, can be calculated from this integrated value:

$$\varepsilon = \frac{\int \varepsilon dv}{s\sqrt{2\pi}} = \sigma \mathrm{N_A} * 10^9$$

where s is the standard deviation of the Gaussian distribution across which the absorptivity is integrated, σ is the absorptive cross-section in cm^2, and $\mathrm{N_A}$ is Avogadro's number. The standard deviation was determined by fitting the linear absorption scan profile to a Gaussian distribution function, as $s_\varepsilon = s_A$ because $A = \varepsilon lC$ and neither the path length l nor the concentration C depend on incident light frequency.

The product of the calculated absorptive cross-section and the measured pulse fluence (adjusted from J/cm^2 to photons/cm^2) gave a measure of the expected number of photons absorbed by each quantum dot. In order to satisfy the established phase-matching condition, any higher order effects require an odd number of interactions with each pulse. At low fluence, processes interacting only once with each pulse dominate, but it is important to calculate the significance of higher-order effect contributions at the pulse fluences used during each experiment. The ratio between Poisson probability density for three-photon events and for single-photon events provides a measure of this significance. Unless otherwise noted, experiments on the femtosecond system used pulse energies chosen to keep this ratio below 1:10 for each beam. (See Appendix E: Fluence Calculations for an example calculation using values for fs Batch 8 in the Mathcad worksheet developed for this work.)

4.3. Technique Development and Overview

MR-CMDS projects typically proceed through a common set of initial experiments, motivated by a combination of understanding gained in previous work and system-specific hypotheses. The picture formed by these initial investigations informs the subsequent experiments that flesh out the unique properties of the sample of interest. Prior to even the simplest of non-linear experiments, an OPA tuning range is set according to results gained from linear absorption profiles. This overview of common techniques displays some data collected in studies of RDC and octane. Figures 1 and 2 show the FT-IR profiles of these two samples to provide context for the discussion.

Two-dimensional scan collection times can vary between an hour and 30 hours. It is both wise and common, then, to choose the bounds of these long scans only after exploration with brief one-dimensional slices in the ω_1, ω_2, ω_m, τ_{21}, $\tau_{2'1}$ five-dimension space.

Scans that change a single set of frequency variables while holding pulse timing and all other frequencies constant can provide information about the coupling between a single mode and all others. For example, Figure 3 shows a scan in which ω_1 and ω_m are scanned together. In this experiment, the ω_2 frequency was fixed to be resonant with the methylene asymmetric stretch. The delays were chosen to allow ω_{-2} and $\omega_{2'}$ to create a population in that mode and then allow ω_1 to interact with the existing population. As ω_1 became resonant with modes that are coupled to the established population, the intensity of the four-wave mixing signal increased dramatically.

Studies performed on RDC revealed an interaction with solvent molecules that allowed coherent energy transfer from one vibrational mode to another.[6, 7] Coherence transfer is revealed by free induction decay signal at frequencies shifted away from the modes that are accessed by simple laser-driven transitions. The spectral resolution granted by use of a monochromator permits distinction between the signals produced by each type of process. Figure 4 shows an example of signal observed at different frequencies when ω_1 is resonant with the symmetric carbonyl stretch and ω_2 is resonant with the antisymmetric stretch. The strongest signal still appeared at the frequency predicted by usual processes, but the appearance of light at 2015cm^{-1} indicated significant coherent energy transfer.

Energy transfer dynamics also appear as the relative timing of the excitation pulses is varied. In some cases, the desired information is simply the lifetime of a particular state. A population can be prepared by tuning ω_{-2} and $\omega_{2'}$ to be resonant with a state and overlapping them in time. A profile of the population lifetime can then be acquired by scanning the delay between these pulses and ω_1 and recording the subsequent change in intensity. In some cases, ω_1 will only be resonant with a state coupled to the population if the state prepared by ω_{-2} and $\omega_{2'}$ first relaxes to another state. Figure 5 shows a pair of profiles corresponding to changes in signal created by changing the delay between population creation and probing. By convention, negative values for τ_{21} and $\tau_{2'1}$ indicate that the corresponding ω_2 pulse arrives that many picoseconds prior to ω_1. In one case (shown by the red trace), the state accessed by ω_1 was directly coupled to the state prepared by ω_2. In the other case (black trace), the signal only grew in a few picoseconds after the creation of a population by ω_2—a signature of population relaxation. Both traces reveal excited state lifetimes, but each also has decay components resulting from different relaxation pathways. By observation of grow-in times and fits to the exponential decay profiles, both qualitative (population-relaxation-assisted vs. direct transition) and quantitative (population and coherence lifetimes) information can be acquired by single delay scans.

As soon as preliminary scans reveal basic information about the five-dimensional experimental space, two-dimensional scans can be chosen to provide more complete pictures of the sample properties and provide extensive constraints leading to more significant simulations and fits.

Experiments collected while varying excitation laser frequencies provide detailed structural information. Figure 6 shows an example of this type of experiment, performed in RDC, in which ω_{-2} and $\omega_{2'}$ are timed to allow the formation of a population before the arrival of ω_1. Peaks along the diagonal appeared in the same locations as peaks in the FT-IR scan. Peaks slightly red-shifted in ω_1 space from the diagonal correspond to overtones. Four-wave mixing signal is only generated at off-diagonal frequency pairs when the modes accessed by ω_1 and ω_2 are coupled. The signal appearing to the red of cross-peak fundamental transitions revealed the properties of combination bands. This type of scan can provide different information when different pulse time orderings are chosen[21] or when higher pulse energies are used.[5] Figure 7 shows an example of a scan with parameters roughly matching those used in Figure 6, but in which all laser intensities were increased to allow each pulse to interact with the sample multiple times. The higher number of interactions allowed the first two pulses to create populations in not only the first excited vibrational state, but in higher overtones as well, creating a progression of red-shifted peaks each corresponding to new modes in the two-dimensional potential well.

Variation of pulse timing at fixed excitation frequencies produces a picture allowing simultaneous measurement of all resonant population and coherence lifetimes. Figure 8 shows such a scan with $\omega_1 = \omega_m$ set equal to one RDC stretching mode and ω_2 set equal to the other (the lower-right cross-peak in Figure 6). The slow decay of intensity along the diagonal where both τ_{21} and $\tau_{2'1}$ values are negative showed the slow relaxation of the vibrational population. The comparatively swift losses away from that diagonal correspond to coherence dephasing rates (see Theory chapter for details). The absence of signal in most of the top half of the plot resulted from pulse time orderings that would have required different excitation frequencies in order to be resonant.

As changes in experimental parameters allow acquisition of different information from frequency scans, so such changes can be helpful for delay scans. Figure 9 is a delay scan that mimics Figure 8 in all settings except the position of the monochromator. When the monochromator is set to pass light with a frequency equal to that of ω_2 (seen as the lower-intensity peak in Figure 4), the only light reaching the detector is that produced by coherence transfer events. The beating pattern shown in this scan is a signature of coherence transfer, and the period of the beats is determined by the energy difference between the initial and final modes involved in the transfer.

The last common scan type used in this work mixes dynamical and energetic information, usually by fixing one excitation frequency and scanning population lifetimes corresponding to variations in the other excitation. Figure 10 shows a Wigner plot of octane in which ω_2 was fixed and was tuned to resonance with the methylene asymmetric stretching mode. The vertical axis shows the frequencies of modes coupled to the population created by the first pair of pulses (as in Figure 3). The horizontal axis reveals how that coupling changed based on the length of the population waiting time (as in Figure 5). In this system, the only mode coupled to the directly excited state was itself (when $\omega_1 = \omega_2 = 2927\text{cm}^{-1}$); all other modes only came to be coupled to the population after some relaxation time was allowed to pass. The behavior shown by this plot revealed that a mode other than the methylene asymmetric stretch must be preferentially excited at 2927cm^{-1}. The methylene symmetric stretch ($\omega_1 = \omega_m = 2854\text{cm}^{-1}$) is mechanically coupled to the asymmetric stretch, so its peak should have shown the same grow-in behavior as the $\omega_1 = \omega_m = 2927\text{cm}^{-1}$ cut. The simultaneous comparison of dynamics possible in plots like that shown in Figure 10 make this type of scan an appealing choice when single delay scans present apparently-inconsistent information.

Works Cited

1. Mathew, N. A. *Mixed Frequency/Time Domain Coherent Multidimensional Spectroscopy;* PhD Thesis; University of Wisconsin-Madison: Madison, WI, 2010.

2. Rickard, M. A. *Fundamental Studies of Triply Vibrationally Enhanced Four-Wave Mixing Spectroscopy;* PhD Thesis; University of Wisconsin-Madison: Madison, WI, 2008.

3. Kornau, K. M. *Triply Vibrationally Enhanced Four-Wave Mixing Spectroscopy;* PhD Thesis; University of Wisconsin-Madison: Madison, WI, 2009.

4. Mathew, N. A.; Rickard, M. A.; Kornau, K. M.; Pakoulev, A. V.; Block, S. B.; Yurs, L. A.; Wright, J. C. Coherent Multidimensional Vibrational Spectroscopy of Representative N-Alkanes. *Journal of Physical Chemistry A* **2009,** *113* (36), 9792-9803.

5. Mathew, N. A.; Block, S. B.; Yurs, L. A.; Kornau, K. M.; Pakoulev, A. V.; Wright, J. C. Multiply Enhanced Odd-Order Wave-Mixing Spectroscopy. *Journal of Physical Chemistry A* **2009,** *113* (48), 13562-13569.

6. Rickard, M. A.; Pakoulev, A. V.; Kornau, K.; Mathew, N. A.; Wright, J. C. Interferometric Coherence Transfer Modulations in Triply Vibrationally Enhanced Four-Wave Mixing. *Journal of Physcal Chemistry A* **2006,** *110* (40), 11384-11387.

7. Rickard, M. A.; Pakoulev, A. V.; Mathew, N. A.; Kornau, K. M.; Wright, J. C. Frequency- and Time-Resolved Coherence Transfer Spectroscopy. *Journal of Physical Chemistry A*

2007, *111* (7), 1163-1166.

8. Wehrenberg, B. L.; Wang, C.; Guyot-Sionnest, P. Interband and Intraband Optical Studies of PbSe Colloidal Quantum Dots. *Journal of Physical Chemistry B* **2002,** *106* (41), 10634-10640.

9. Moreels, I.; Lambert, K.; De Muynck, D.; Vanhaecke, F.; Poelman, D.; Martins, J. C.; Allan, G.; Hens, Z. Composition and Size-Dependent Extinction Coefficient of Colloidal PbSe Quantum Dots. *Chemistry of Materials* **2007,** *19* (25), 6101-6106.

10. Ellingson, R. J.; Beard, M. C.; Johnson, J. C.; Yu, P.; Micic, O. I.; Nozik, A. J.; Shabaev, A.; Efros, A. Highly Efficient Multiple Exciton Generation in Colloidal PbSe and PbS Quantum Dots. *Nano Letters* **2005,** *5* (5), 865-871.

11. Schaller, R. D.; Pietryga, J. M.; Goupalov, S. V.; Petruska, M. A.; Ivanov, S. A.; Klimov, V. I. Breaking the Phonon Bottleneck in Semiconductor Nanocrystals via Multiphonon Emission Induced by Intrinsic Nonadiabatic Interactions. *Physical Review Letters* **2005,** *95,* 196401-1961-4.

12. Carlson, R. J.; Wright, J. C. Absorption and Coherent Interference Effects in Multiply Resonant Four-Wave Mixing Spectroscopy. *Applied Spectroscopy* **1989,** *43* (7), 1195-1208.

13. Kornau, K. M.; Rickard, M. A.; Mathew, N. A.; Pakoulev, A. V.; Wright, J. C. Multiresonant Coherent Multidimensional Vibrational Spectroscopy of Aromatic Systems: Pyridine, a Model System. *Journal of Physical Chemistry A* **2011,** *115* (16), 4054-4062.

14. Yurs, L. A. *Multiresonant Coherent Multidimensional Spectroscopy of Quantum-Confined Nanomaterials;* PhD Thesis; University of Wisconsin-Madison: Madison, WI, 2011.

15. Hochstrasser, R. M. Two-Dimensional IR-Spectroscopy: Polarization Anisotropy Effects. *Chemical Physics* **2001,** *266,* 273-284.

16. Cameron, A. R.; Riblet, P.; Miller, A. Spin Gratings and the Measurement of Electron Drift Mobility in Multiple Quantum Well Semiconductors. *Physical Review Letters* **1996,** *76* (25), 4793-4796.

17. Kim, J.; Wong, C. Y.; Scholes, G. D. Exciton Fine Structure and Spin Relaxation in Semiconductor Colloidal Quantum Dots. *Accounts of Chemical Research* **2009,** *42* (8), 1037-1046.

18. Mathew, N. A.; Yurs, L. A.; Block, S. B.; Pakoulev, A. V.; Kornau, K. M.; Wright, J. C. Multiple Quantum Coherence Spectroscopy. *Journal of Physical Chemistry A* **2009,** *113* (33), 9261-9265.

19. Mathew, N. A.; Yurs, L. A.; Block, S. B.; Pakoulev, A. V.; Kornau, K. M.; Sibert, E. L.; Wright, J. C. Fully and Partially Coherent Pathways in Multiply Enhanced Odd-Order Wave-Mixing Spectroscopy. *Journal of Physical Chemistry A* **2010,** *114* (2), 817-832.

20. Harbold, J. M.; Du, H.; Krauss, T. D.; Cho, K.-S.; Murray, C. B. Time-Resolved Intraband Relaxation of Strongly Confined Electrons and Holes in Colloidal PbSe Nanocrystals. *Physical Review B* **2005,** *72* (19), 195312(6).

21. Meyer, K. A.; Thompson, D. E.; Wright, J. C. Frequency and Time-Resolved Triply Vibrationally Enhanced Four-Wave Mixing Spectroscopy. *Journal of Physical Chemistry A* **2004,** *108* (52), 11485-11493.

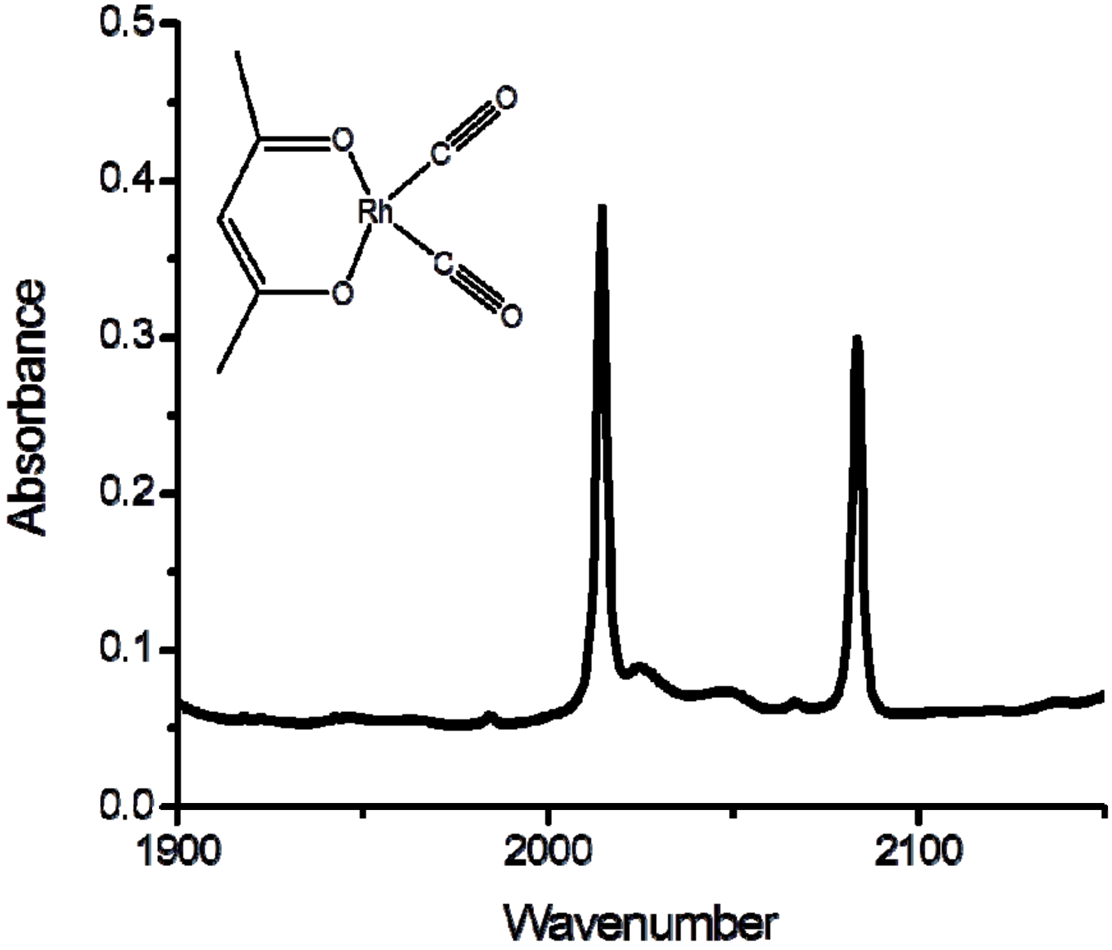

Figure 1—Absorption Spectrum of RDC dissolved in hexane in the spectral neighborhood of the symmetric (2084cm^{-1}) and anti-symmetric (2015cm^{-1}) carbonyl stretching modes. Inset is a representation of the structure of RDC.

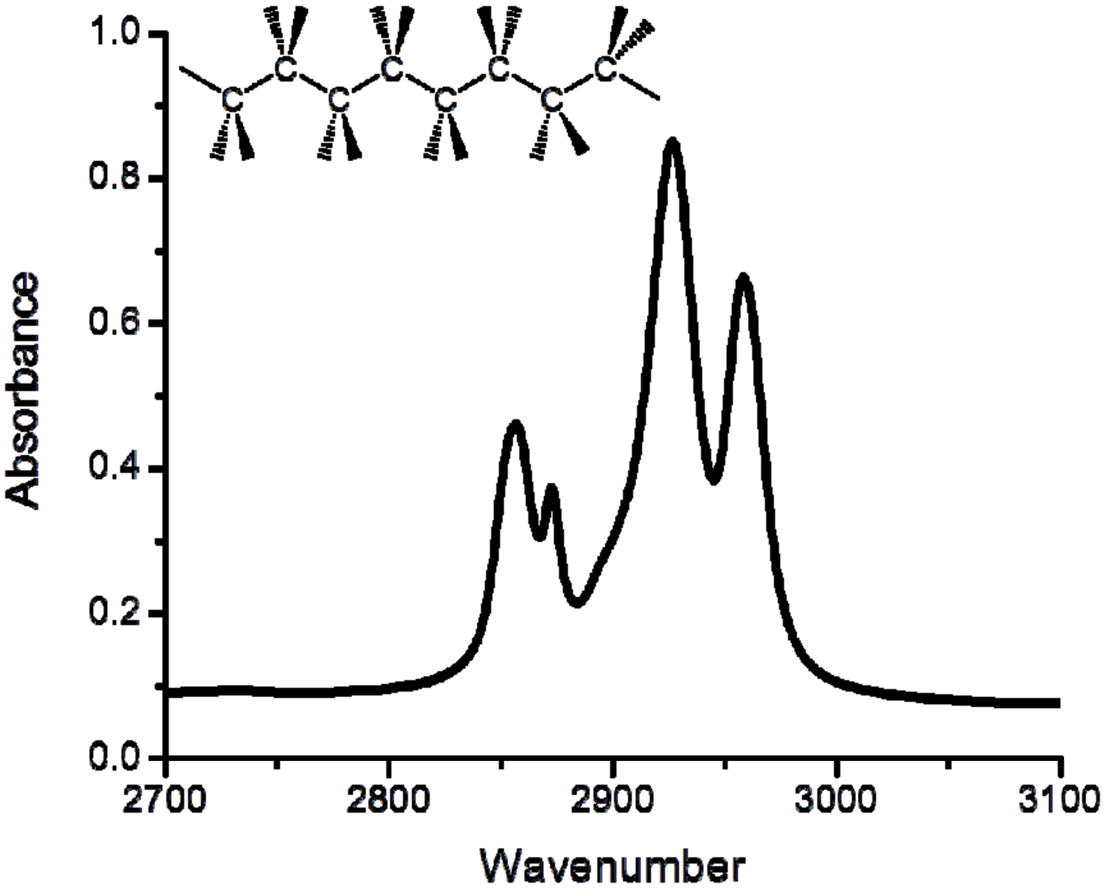

Figure 2— Absorption Spectrum of octane diluted by carbon tetrachloride in the spectral neighborhood of methyl (2956cm^{-1} and 2870cm^{-1}) and methylene (2927cm^{-1} and 2854cm^{-1}) asymmetric (2956cm^{-1} and 2927cm^{-1}) and symmetric (2870cm^{-1} and 2854cm^{-1}) stretching modes. Inset is a representation of the structure of octane.

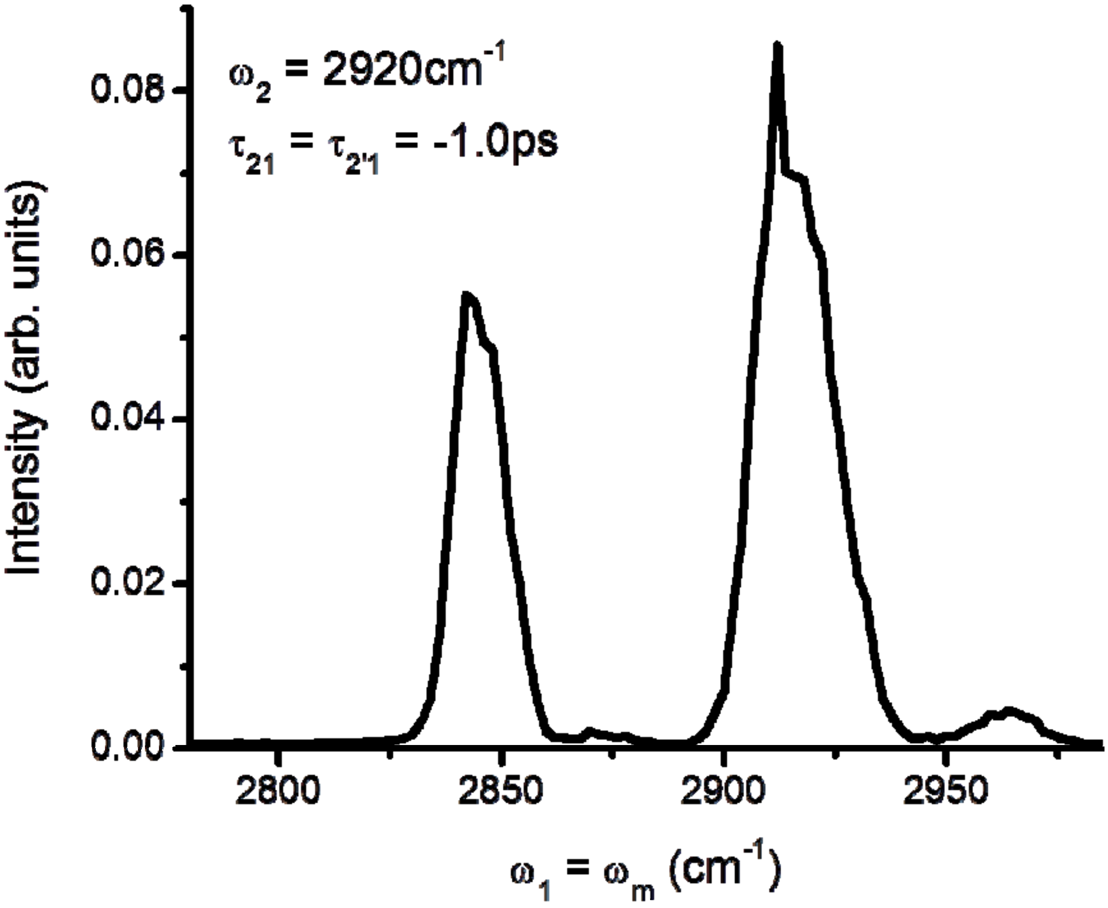

Figure 3—A frequency scan of octane. As labeled, ω_2 is held at a resonance with the methylene asymmetric stretch mode and the delays are fixed such that ω_1 arrives 1ps after ω_2 and $\omega_{2'}$. As ω_1 becomes resonant with modes that are coupled to the existing population, non-linear signal intensity increases.

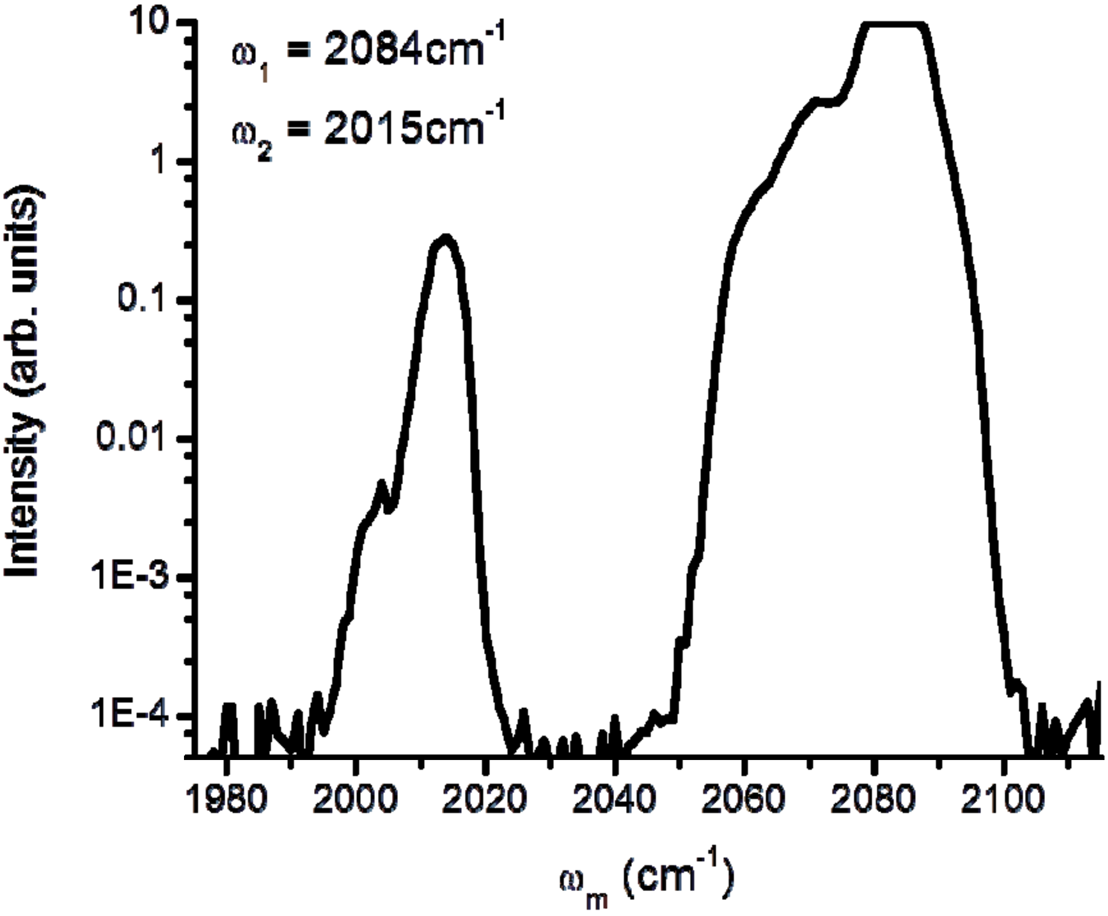

Figure 4—Monochromator scan revealing coherence transfer in RDC. All pulses were overlapped in time. Processes involving no energy transfer produce light at $\omega_m = \omega_1 =$ 2084cm^{-1}. Only coherences interacting with the solvent, while retaining their phase, produce light at the antisymmetric stretch frequency 2015cm^{-1}.

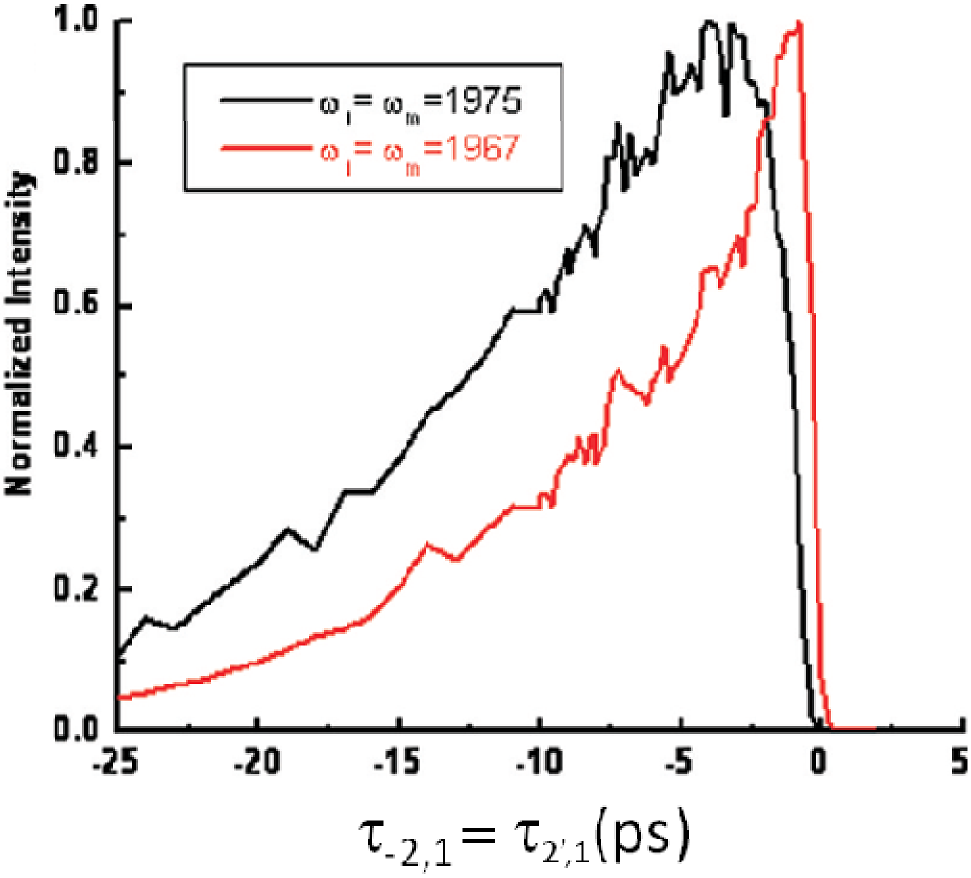

Figure 5—RDC Population lifetime scans collected by overlapping ω_{-2} and $\omega_{2'}$ in time and varying the delay before the arrival of ω_1. For these scans, ω_2 was set equal to 2080cm^{-1} and the pulse intensity was increased so as to create various overtone states. ω_1 was made resonant with a state either directly coupled to this overtone (red trace) or coupled to a state only populated by the relaxation of the prepared overtone (black trace).

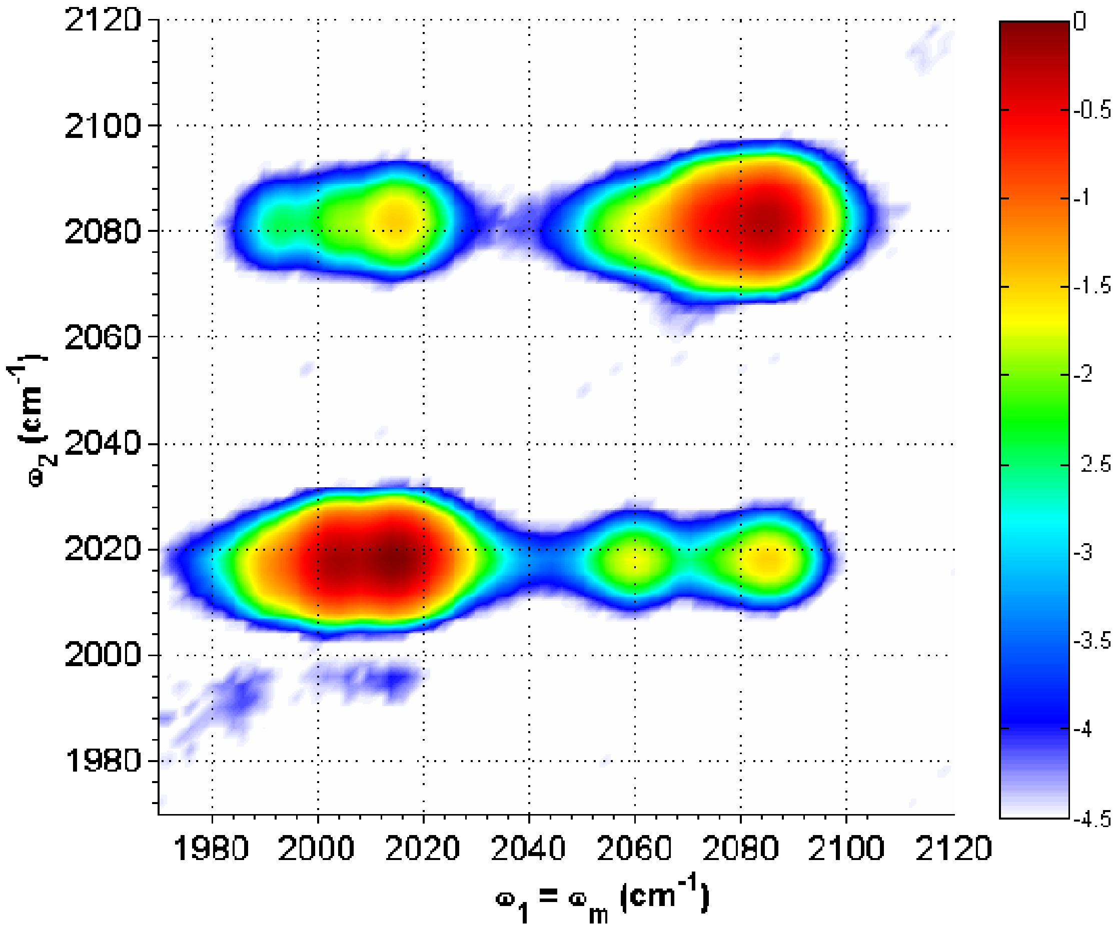

Figure 6—2D Frequency Scan of RDC, normalized and shown on a logarithmic intensity scale. τ_{-21} = -5.0ps and $\tau_{2'1}$ = -3.5ps, so a population is formed before ω_1 arrives. Peaks along the diagonal correspond to modes seen in 1D absorption scans. Peaks slightly red-shifted from each diagonal peak correspond to overtones. Off-diagonal peaks appear only when their respective modes are coupled. Peaks shifted to the red of the each fundamental correspond to combination band transitions.

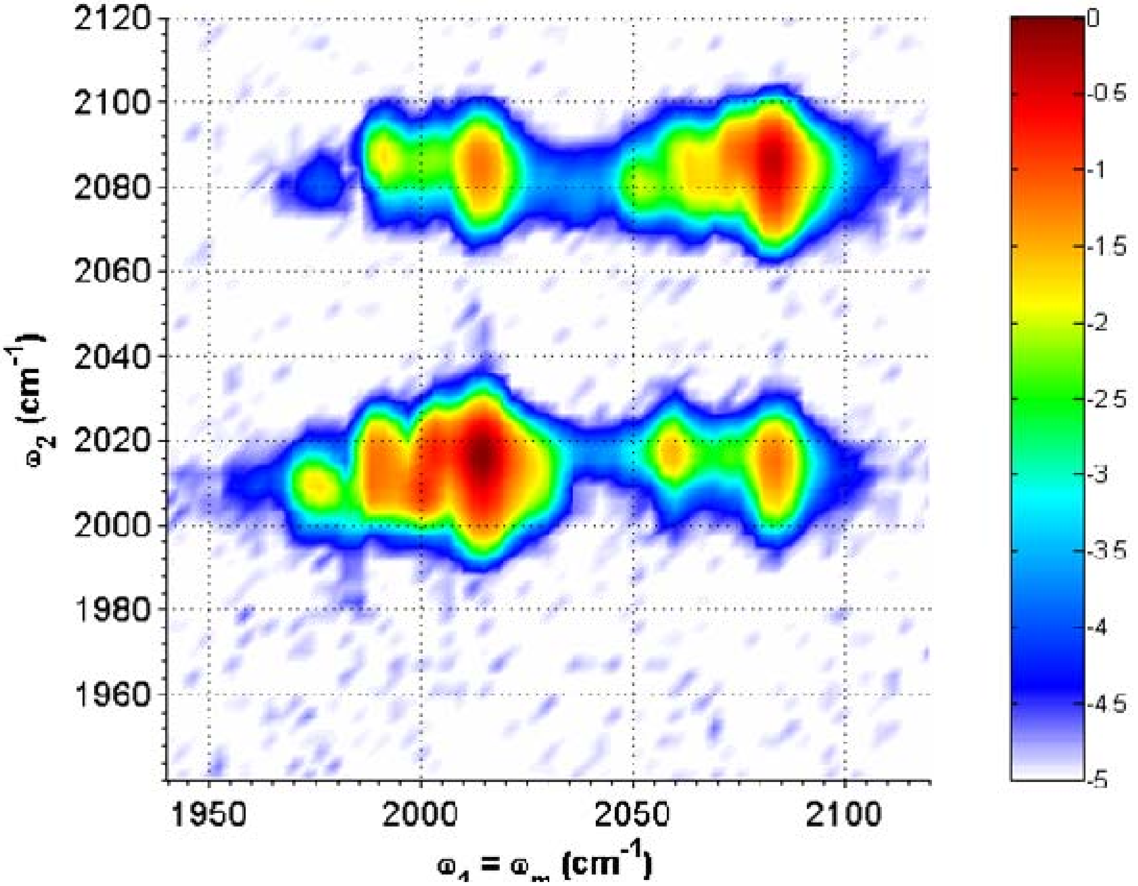

Figure 7—2D frequency scan of RDC with high excitation pulse intensities, normalized. This scan reveals what happens to a scan like the one seen in Figure 6 when pulses are intense enough to interact with the sample multiple times—peaks corresponding to overtones and combination bands higher and higher up the potential well appear, red-shifted according to the increasing well anharmonicity.

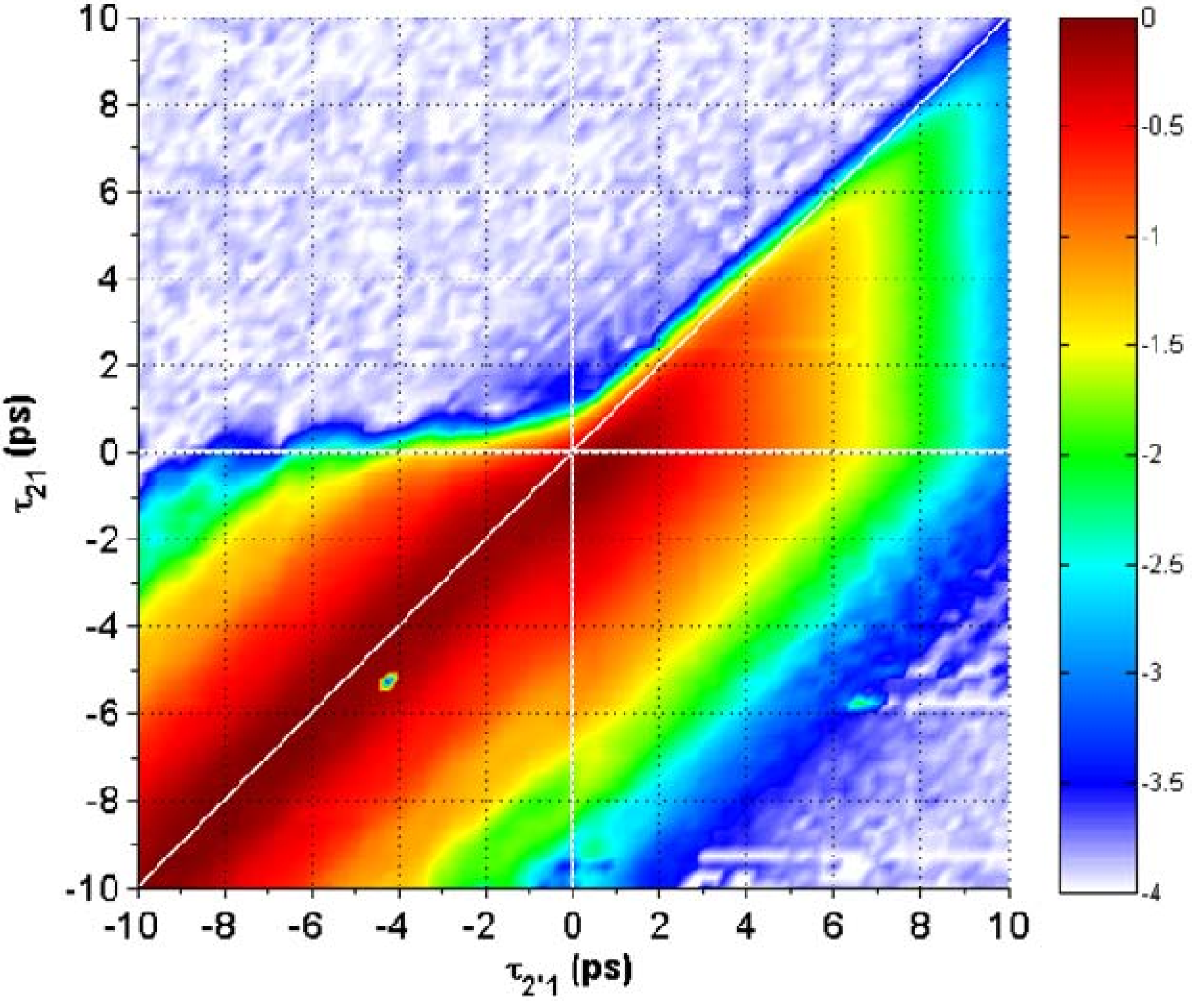

Figure 8—RDC 2D delay scan, normalized and shown in logarithmic scale. $\omega_1 = \omega_m = 2084cm^{-1}$, $\omega_2 = 2015cm^{-1}$. The signal plotted along the lower-left diagonal corresponds to a population lifetime. Decays similar to the one shown along the positive x-axis measure coherence dephasing rates. No signal appears in the upper left quadrant and half of the upper right quadrant because those time orderings require transitions to states with which the excitation pulses are not resonant.

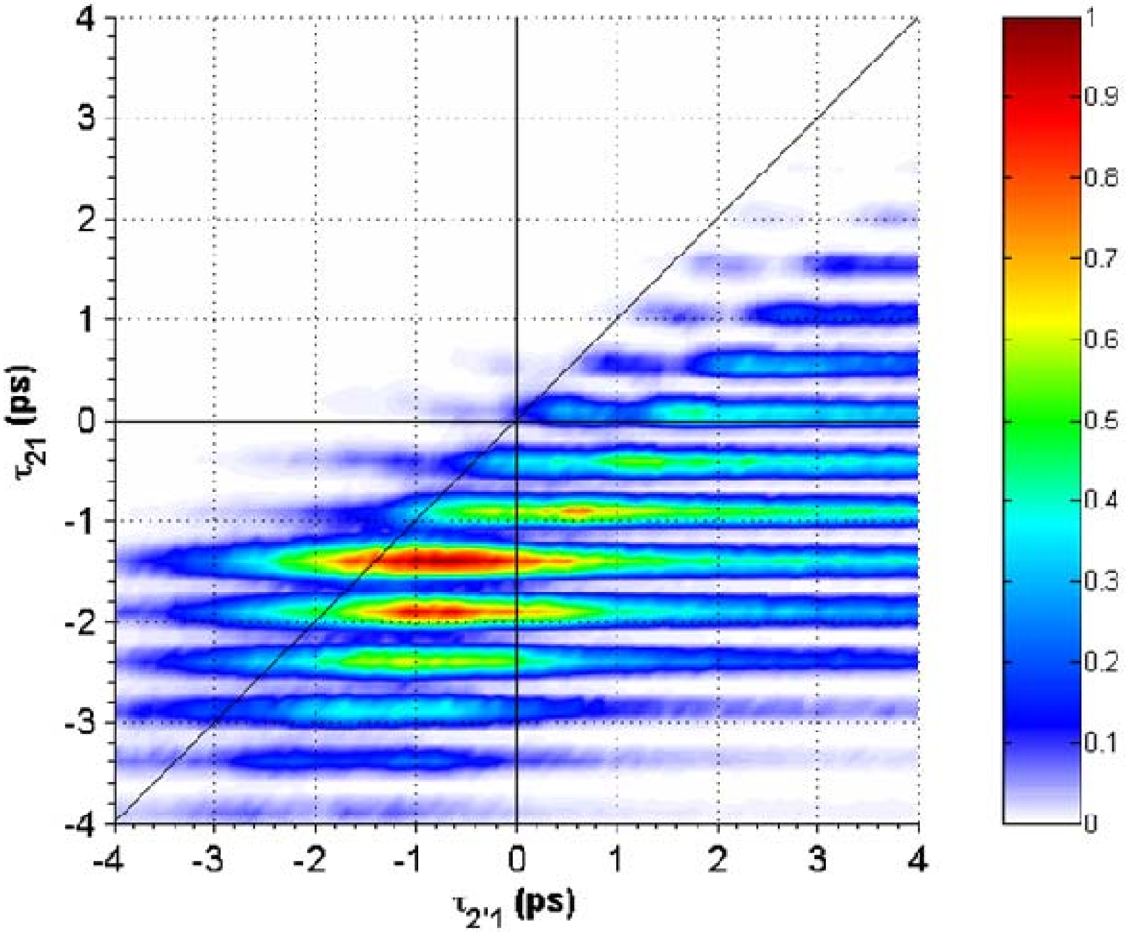

Figure 9— RDC 2D delay scan with quantum beating, normalized. $\omega_1 = 2084\text{cm}^{-1}$, $\omega_2 = \omega_m = 2015\text{cm}^{-1}$. The monochromator isolates signal produced by oscillators experiencing coherence transfer events. The beat frequency corresponds to the energy difference between the initial and final states in the transfer.

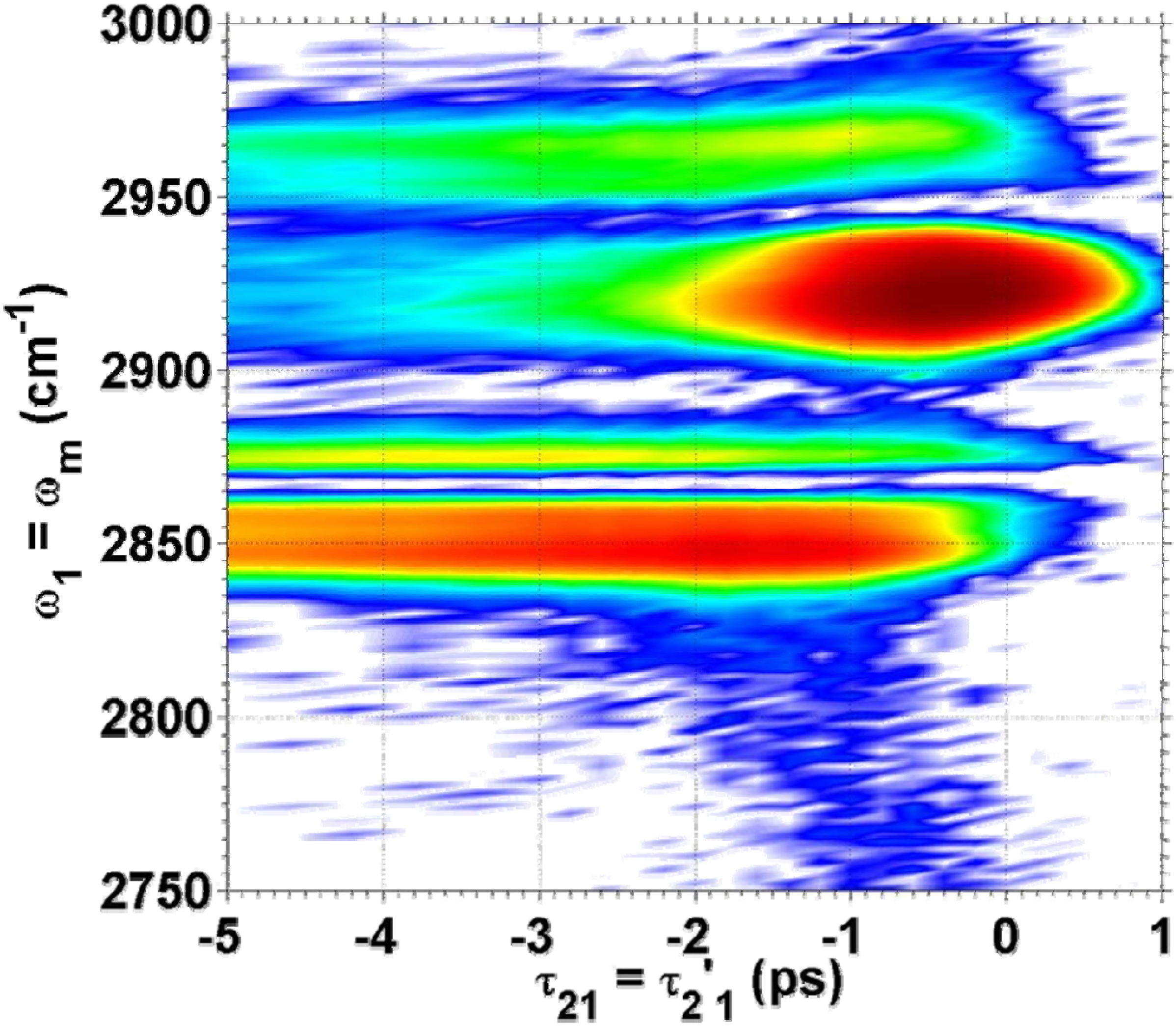

Figure 10—Octane Wigner plot, normalized. ω_2 = 2927cm^{-1}. Notice that the $\omega_1 = \omega_2$ peak grows in with the excitation pulse profile, but the other peaks only grow in after the initial population has already been allowed to decay. The state directly excited is then shown to not be coupled to other neighboring transitions, but relaxes quickly to a longer-lived state that is coupled to the others.

Chapter 5: Review of Picosecond Experimental Capabilities

Though it became clear that full use of MR-CMDS techniques to study quantum-confined semiconductor systems would require femtosecond laser pulse durations, it was also important to ensure that the capabilities of picosecond pulse experiments were understood. Most results are discussed elsewhere,[1,2,3] but a brief overview is included here for comparison with later developments. Unless otherwise stated, the data discussed here were collected on a sample with an absorption spectrum shown in Figure 1.

Laser pulses on the order of 1 picosecond in duration cannot directly observe PbSe coherent dynamics, but they can access structural information and study incoherent dynamics. Delay scans such as the pair shown in Figure 2 demonstrate the dynamics directly observable with picosecond pulses. The width of the features matches the convolution of the two Gaussian pulses used to establish the population. The quality of fit between the data and simulations does not have a local maximum as coherence lifetimes are changed; only an upper limit to the coherence lifetime can be determined from this type of experiment. **1** Traces along the $\tau_{21} = \tau_{2'1}$ diagonal can be fit to reveal population lifetimes which are typically on the order of tens-to-hundreds of picoseconds.

Being unable to directly measure coherence lifetimes limits MR-CMDS to being a frequency domain approach when only picosecond pulses are available. This limit still allows direct study of quantum dot energetic structure. Figure 3 shows a pair of two-dimensional frequency scans scaled and positioned to show relative shape and frequency location. OPA tuning ranges were unable to stretch across both regions simultaneously, so the picture had to be assembled in parts. These experiments revealed that MR-CMDS could extract the 1P exciton peak from the rising PbSe band edge background. Peaks only appear away from the diagonal when modes are coupled. In this case, the 1P exciton is coupled to the 1S exciton created by ω_2 and $\omega_{2'}$, but the rising background is not, so it yields no signal. The 1P exciton peak is also visible when all excitation lasers are resonant with it (see Figure 4), but the intensity is much lower owing to the smaller 1P transition dipole (as is immediately apparent from the linear absorption plot) and its short lifetime. Figure 5 shows a population lifetime scan with all lasers tuned to the 1P exciton transition. The fit shows a fast decay lifetime of 1.8ps treats the slower decay component as a constant. The fast decay matches the range of expected lifetimes for the 1P-to-1S relaxation,[4, 5, 6] and the slow decay that is obscured by fluctuations then shows the 1S exciton lifetime. The high relative-amplitude fluctuations are explained in the following section. Tuning ω_1 to the 1S exciton frequency should have provided higher four-wave mixing signal, but sample degradation created increasingly severe scattered light interference before the tuning range could be appropriately adjusted.

The continuous wave limit becomes a very effective approximation for simulating spectral scans varying excitation frequencies. Spectra collected at various relative pulse timings clarified the observed features and improved frequency domain simulations used to extract PbSe characteristic parameters. Experiments performed when all pulses were overlapped in time included contributions from multiple population pathways—those probing populations created by ω_1/ω_{-2} and those created by $\omega_{2'}/\omega_{-2}$. Figure 6 shows a pair of scans—one with (a) and one without (b) contribution from pulse time-orderings allowing ω_1/ω_{-2} populations. Simulation fits (6c and 6d) allowed extraction of coherence lifetimes that could not be directly measured from delay scans. The lifetime measured was 46fs—comfortably within the upper limit established by the direct time domain experiments.[1]

5.1. Crossed-Polarization Studies

Colloidal quantum dot suspensions tend to scatter incident laser beams. When samples have aged or are poorly passivated, the component quantum dots can acquire surface defects[3, 7, 8,] that can cause agglomeration or assembly into nanobead chains (see Figure 7), which scatter near-IR light very effectively. Contaminated reagents resulted in one sample (absorption scans of which is shown in Figure 8) that was particularly poorly passivated, leading to ultrafast surface charge trapping[3] and problematic scatter intensities. The scattered light acted as a heterodyning field, that modulated the detected signal as relative pulse delays changed.[1, 2] A trace along the border between pathways V and VI measures the excited state population as a function of time and should have provided a smooth decay profile even in the presence of the described heterodyning scatter, as the relative delay between ω_{-2} and $\omega_{2'}$ was not changing over the course of the experiment. The relative delay of the picosecond pulse envelopes is largely insensitive to the small changes in beam overlap and pointing with delay stage position, but the relative phase is considerably more sensitive. These subtle changes resulted in erratic interference patterns, shown in Figure 9, that made fitting the scan profile to a simple exponential decay meaningless. It was possible to measure the population lifetimes by setting ω_1 equal to ω_{-2} so they created an excited state probed by $\omega_{2'}$ (see Figure 10), but this technique did not prevent the erratic interference from manifesting in scans showing signal changes due to alterations in other variables.

One attempt to improve the isolation of the four-wave mixing signal from scattered light was a line of experiments with crossed excitation field polarizations. Rotation of one beam from vertical to horizontal polarization rotates the polarization of the output field to horizontal.[9] Placing a polarizer before the monochromator then eliminates all scatter from the vertically polarized beam lines. As long as the ω_1 beamline was vertical, the scatter it produced, which also served as the heterodyning field, would be eliminated by the polarizer.

Figures 11 and 12 show two-dimensional delay scans with all beams vertically polarized and with $\omega_{2'}$ horizontally polarized and the signal filtered by a polarizer. The most obvious difference is that the population created by ω_{-2} and $\omega_{2'}$ (usually visible along the pathway V/VI diagonal, where $\tau_{2'1} = \tau_{21} < 0$) seems to have disappeared except for a slight preferential weighting for $\tau_{21} < 0$ near $\tau_{2'1} = 0$. The signal along the positive $\tau_{2'1}$ –axis (the border between pathways I/III) probes the population created by ω_{-2} and ω_1, seems unchanged. One-dimensional scans collected along this axis with a variety of excitation frequencies are shown in Figure 13. The character of the decay shown by this experimental configuration is identical to the pathway I/III decays with all beams parallel polarized (as in Figure 10).

The character of frequency scans in a crossed-polarization scheme confirms that processes from time orderings other than pathway I/III do not contribute substantial signal, even when all pulses are overlapped in time. Figure 14 shows a scan of this batch of quantum dots when all beams were vertically polarized and $\tau_{21} = \tau_{2'1} = -2$ps. Though interference with scattered light distorted the spectrum from a shape that looks roughly like an oval positioned along the diagonal (characteristic of samples with significant inhomogeneous broadening), the scan still provided information about the energetic structure of the quantum dots. When the polarization of $\omega_{2'}$ was rotated, there was no signal at $\tau_{21} = \tau_{2'1}$ = -2ps (shown in Figure 12). When all pulses were overlapped in time, the frequency scan had lost all the characteristics seen in corresponding parallel polarization studies and instead exhibited signal only along the diagonal where $\omega_1 = \omega_2$, as shown in Figure 15. Studies on other quantum dot samples reveal that this characteristics matches that when $\tau_{2'1}$ is positive and τ_{21} = 0ps (pathway I/III). Figure 16a shows a representative scan of PbSe dots when all pulses are overlapped in time (as in Figure 15), but all pulses are vertically polarized. Figure 16b shows a scan in pathway I/III, which is qualitatively identical to the scan produced with one horizontally polarized beam. Comparison of Figures 15 and 16 reveals that the only four-wave mixing signal in the cross-polarized experiment resulted from processes where ω_1 and ω_{-2} form a population.

Cross-polarized transient grating (CPTG) experiments have been used to study quantum wells [10] and CdSe quantum dot [11] fine structure relaxation. Transient grating experiments with parallel-polarized light create a spatial population grating from the first two excitation beams, then scatter a probe beam from the grating at varying delay times. The intensity of the diffracted probe light diminishes as the fringes lose their visibility with population decay. When two linearly- and perpendicularly-polarized excitation beams cross, they create a spatial polarization grating instead of an intensity grating. This polarization grating oscillates in space between orientations of diagonally-polarized light and circularly-polarized light. Light with different circular polarizations can cause transitions with different changes in angular momentum (+1 or -1). In semiconductors, exciton fine structure is usually inaccessible to common spectroscopic methods because peak widths are large enough to obscure the comparatively small splittings. As the fine structure states do have distinct angular momenta, circularly polarized light can selectively excite transitions to certain states. The polarization grating, then, creates a spin-state (or angular moment state, more generally) grating. As various fine structure states relax, the fringes of this grating become less visible and the non-linear signal intensity decreases.

Attempts to use CPTG techniques on PbSe have proven to be more difficult.[12] The electronic fine structure states are close enough that phonon-mediated relaxation at room temperature occurs through multiple pathways at timescales below 100fs. Dynamics on that timescale are not accessible to picosecond experiments, such as those reported here. The angular momentum fringes created by picosecond cross-polarized pulses lose their visibility fast enough that the process yields no observable signal. The population grating formed by the vertically-polarized ω_1 and ω_{-2} decays at its usual slow rate in time ordering I/III; the only penalty to using a perpendicularly-polarized probe is a uniform decrease in four-wave mixing signal intensity by a factor of one third.[9]

Use of cross-polarized beams is not a helpful adaptation for removal of scattered light in picosecond quantum dot CMDS experiments. Though the interference of scattered light *is* mostly removed in this polarization regime, it only yields signal in a time-ordering that also shows decreased interference with scattered light when all beams are parallel-polarized. The fine structure properties accessible to CPTG experiments are of interest to a technique that can study both structure and dynamics, but sub-100fs pulses would be required to observe the behavior in PbSe, and cryogenic temperatures would still be very helpful for accessing some of the relaxation rates.[12]

Works Cited

1. Yurs, L. A.; Block, S. B.; Pakoulev, A. V.; Selinsky, R. S.; Jin, S.; Wright, J. C. Multiresonant Coherent Multidimensional Electronic Spectroscopy of Colloidal PbSe Quantum Dots. *Journal of Physical Chemistry C* **2011,** *115* (46), 22833-22844.

2. Yurs, L. A. *Multiresonant Coherent Multidimensional Spectroscopy of Quantum-Confined Nanomaterials;* PhD Thesis; University of Wisconsin-Madison: Madison, WI, 2011.

3. Yurs, L. A.; Block, S. B.; Pakoulev, A. V.; Selinsky, R. S.; Jin, S.; Wright, J. C. Spectral Isolation and Measurement of Surface-Trapped State Multidimensional Nonlinear Susceptibility in Colloidal Quantum Dots. *Journal of Physical Chemistry C* **2012,** *116* (9), 5546-5553.

4. Wehrenberg, B. L.; Wang, C.; Guyot-Sionnest, P. Interband and Intraband Optical Studies of PbSe Colloidal Quantum Dots. *Journal of Physical Chemistry B* **2002,** *106* (41), 10634-10640.

5. Harbold, J. M.; Du, H.; Krauss, T. D.; Cho, K.-S.; Murray, C. B. Time-Resolved Intraband Relaxation of Strongly Confined Electrons and Holes in Colloidal PbSe Nanocrystals. *Physical Review B* **2005,** *72* (19), 195312(6).

6. Schaller, R. D.; Pietryga, J. M.; Goupalov, S. V.; Petruska, M. A.; Ivanov, S. A.; Klimov, V. I. Breaking the Phonon Bottleneck in Semiconductor Nanocrystals via Multiphonon Emission Induced by Intrinsic Nonadiabatic Interactions. *Physical Review Letters* **2005,** *95,* 196401-1961-4.

7. Tyagi, P.; Cooney, R. R.; Sewall, S. L.; Sagar, D. M.; Saari, J. I.; Kambhampati, P. Controlling Piezoelectric Response in Semiconductor Quantum Dots via Impulsive Charge Localization. *Nano Letters* **2010,** *10,* 3062-3067.

8. Tyagi, P.; Kambhampati, P. False Multiple Exciton Recombination and Multiple Exciton Generation Signals in Semiconductor Quantum Dots Arise From Surface Charge Trapping. *Journal of Chemical Physics* **2011,** *134* (9), 094706-091-10.

9. Hochstrasser, R. M. Two-Dimensional IR-Spectroscopy: Polarization Anisotropy Effects. *Chemical Physics* **2001,** *266,* 273-284.

10. Cameron, A. R.; Riblet, P.; Miller, A. Spin Gratings and the Measurement of Electron Drift Mobility in Multiple Quantum Well Semiconductors. *Physical Review Letters* **1996,** *76* (25),

4793-4796.

11. Kim, J.; Wong, C. Y.; Scholes, G. D. Exciton Fine Structure and Spin Relaxation in Semiconductor Colloidal Quantum Dots. *Accounts of Chemical Research* **2009,** *42* (8), 1037-1046.

12. Johnson, J. C.; Gerth, K. A.; Song, Q.; Murphy, J. E.; Scholes, G. D.; Nozik, A. J. Ultrafast Exciton Fine Structure Relaxation Dynamics in Lead Chalcogenide Nanocrystals. *Nano Letters* **2008,** *8* (5), 1374-1381.

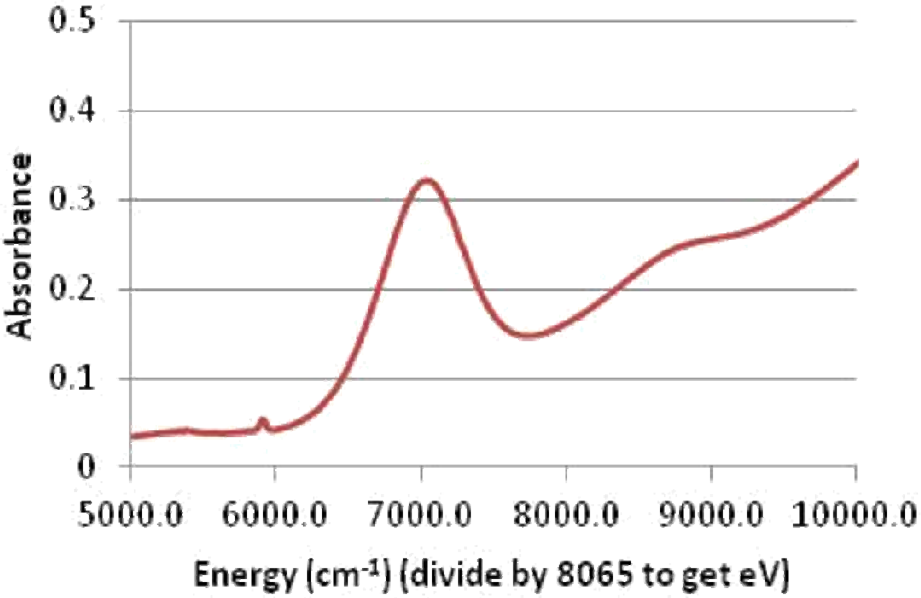

Figure 1—Linear absorption spectrum of PbSe quantum dots used in picosecond experiments. The 1S exciton peak is centered at 7000cm^{-1} and the 1P exciton peak is centered around 8700cm^{-1}.

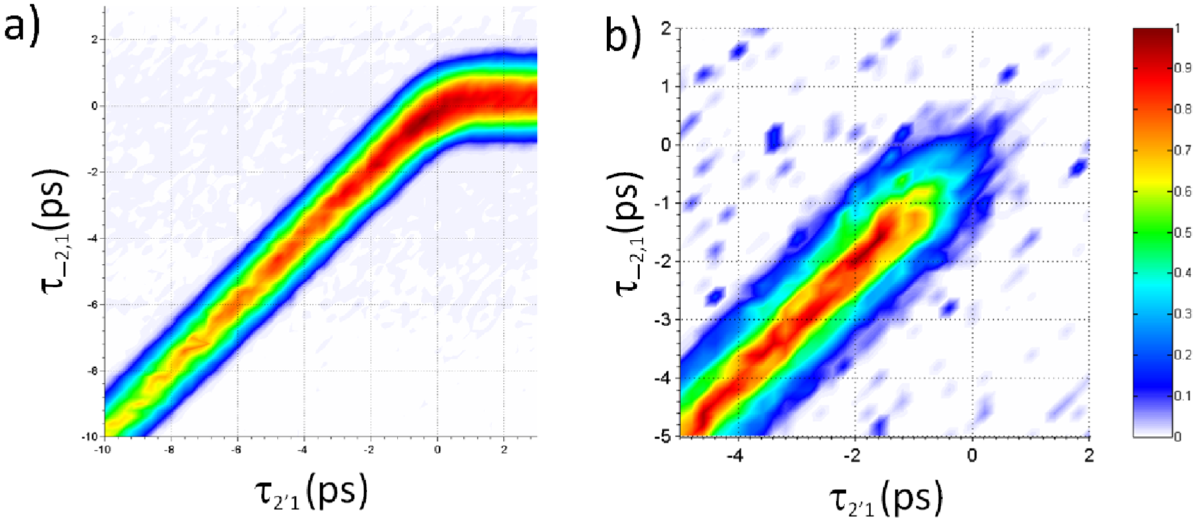

Figure 2— Two-dimensional delay scans collected on the picosecond system. (a) $\omega_1 = \omega_2 = \omega_m = \omega_{1S}$, so $\tau_{21} = 0$ and $\tau_{2'1} > 0$ traces the dynamics of a population state, just as $\tau_{21} = \tau_{2'1} < 0$ does. (b) $\omega_1 = \omega_m = \omega_{1P}$ and $\omega_2 = \omega_{1S}$, so now $\tau_{21} = 0$, $\tau_{2'1} > 0$ traces the lifetime of a zero quantum coherence between the 1S and 1P exciton states.

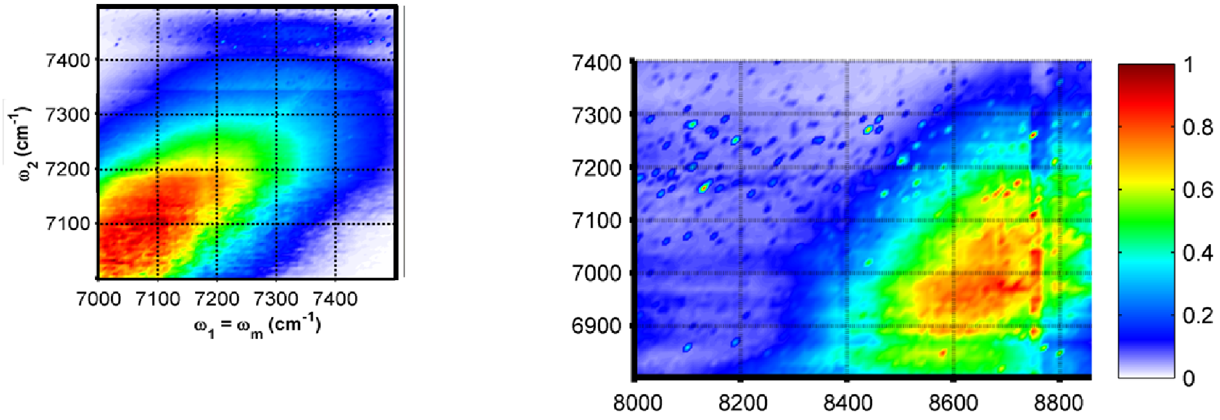

Figure 3—A pair of two-dimensional frequency scans positioned and scaled to show relative size and location. $\tau_{21} = \tau_{2'1} = -2.0$ps. Each scan was normalized independently, so relative intensity cannot be determined from this figure. In each scan, ω_2 and $\omega_{2'}$ are resonant with the 1S exciton transition. The absence of appreciable four-wave mixing signal at lower ω_1 frequencies in the scan on the right reveals that the 1P exciton is directly coupled to the 1S exciton, but the non-quantum-confined excitons with frequencies between the 1S and 1P transition are not.

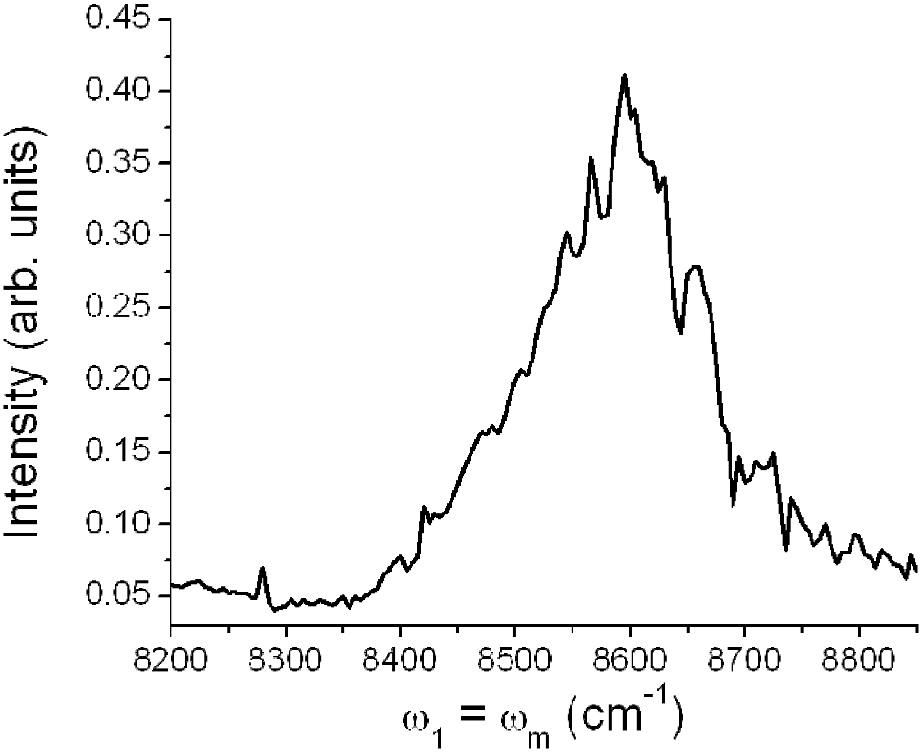

Figure 4—Frequency scan with $\omega_2 = \omega_{1P} = 8600\text{cm}^{-1}$. $\tau_{21} = \tau_{2'1} = -2.0\text{ps}$. The range over which ω_1 varied shows the presence of a 1P exciton diagonal feature. Creation of a 1P population allowed the incoherent dynamics of the state to be studied (Figure 5).

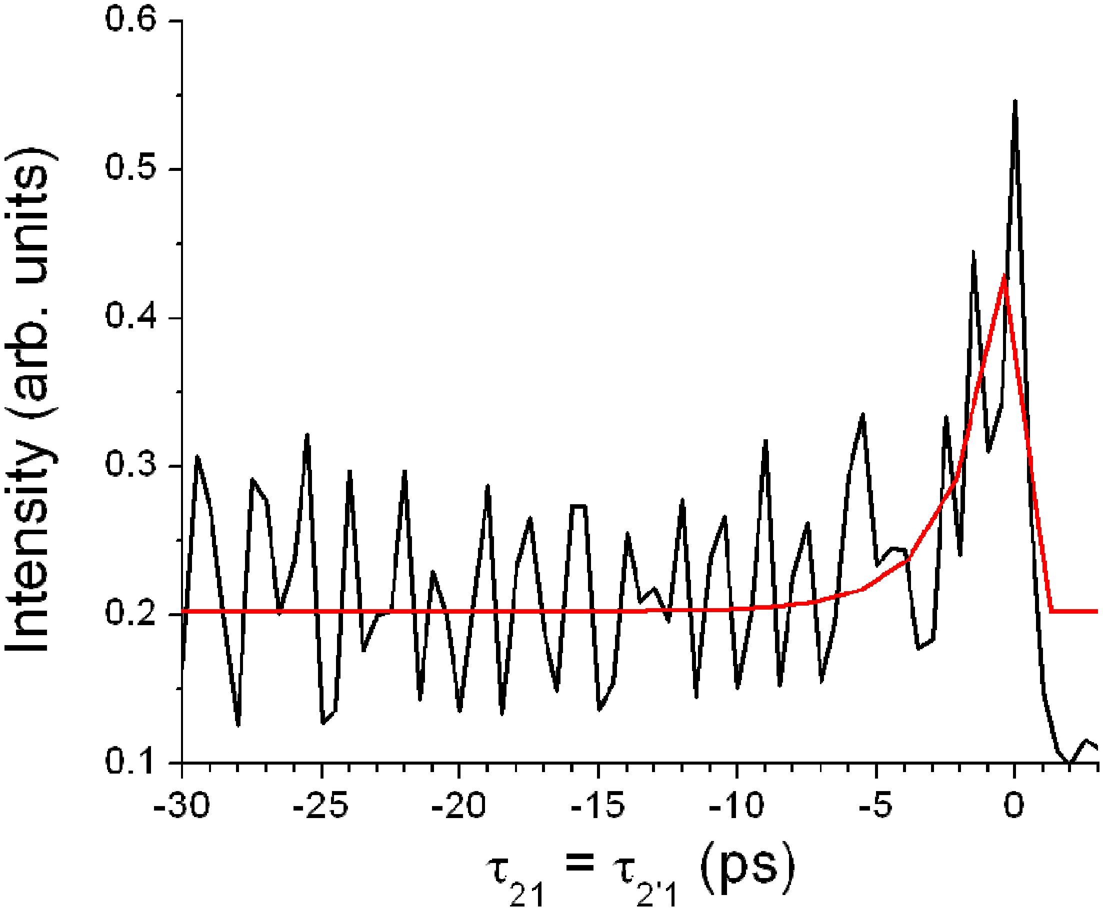

Figure 5—1P exciton population lifetime. Here $\omega_1 = \omega_2 = \omega_m = \omega_{1P} = 8600\text{cm}^{-1}$. The red trace shows a fits to the product of a Gaussian distribution centered near zero and an exponential decay. The decay lifetime is 1.8ps, corresponding to the relaxation from 1P to 1S. The long-time signal above the baseline, which is shown at positive values for τ, corresponds to the 1S exciton lifetime, but is treated as a constant because any decay is obscured by the high amplitude modulations (explained in the text).

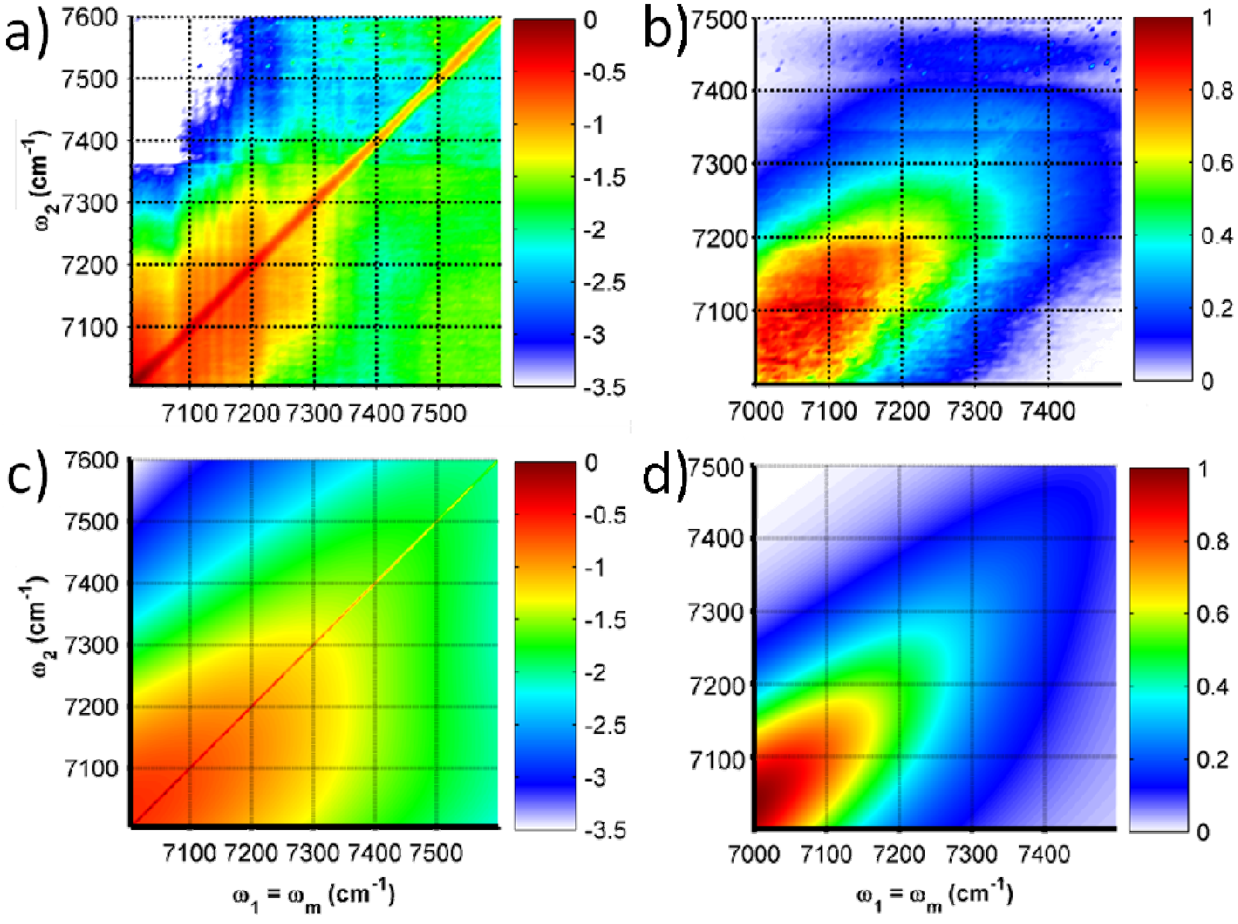

Figure 6— Two-dimensional frequency scans and simulations at different time delays. (a) $\tau_{21} = \tau_{2'1}$ = 0ps, so contributions from all pulse sequences are visible. Notably, the sharp feature along the diagonal results from populations created by ω_1 and ω_2 (see pathway I/III figures in Appendix A—Frequency Domain Simulations). The color bar shows the logarithmic scale used to represent the intensity values in the plot. (b) $\tau_{21} = \tau_{2'1}$ = -2.0ps, so only populations created by $\omega_{2'}$ and ω_2 (see pathway V/VI figures in Appendix A) provide significant contributions. The scale here is linear. (c) and (d) The corresponding frequency domain simulation results.

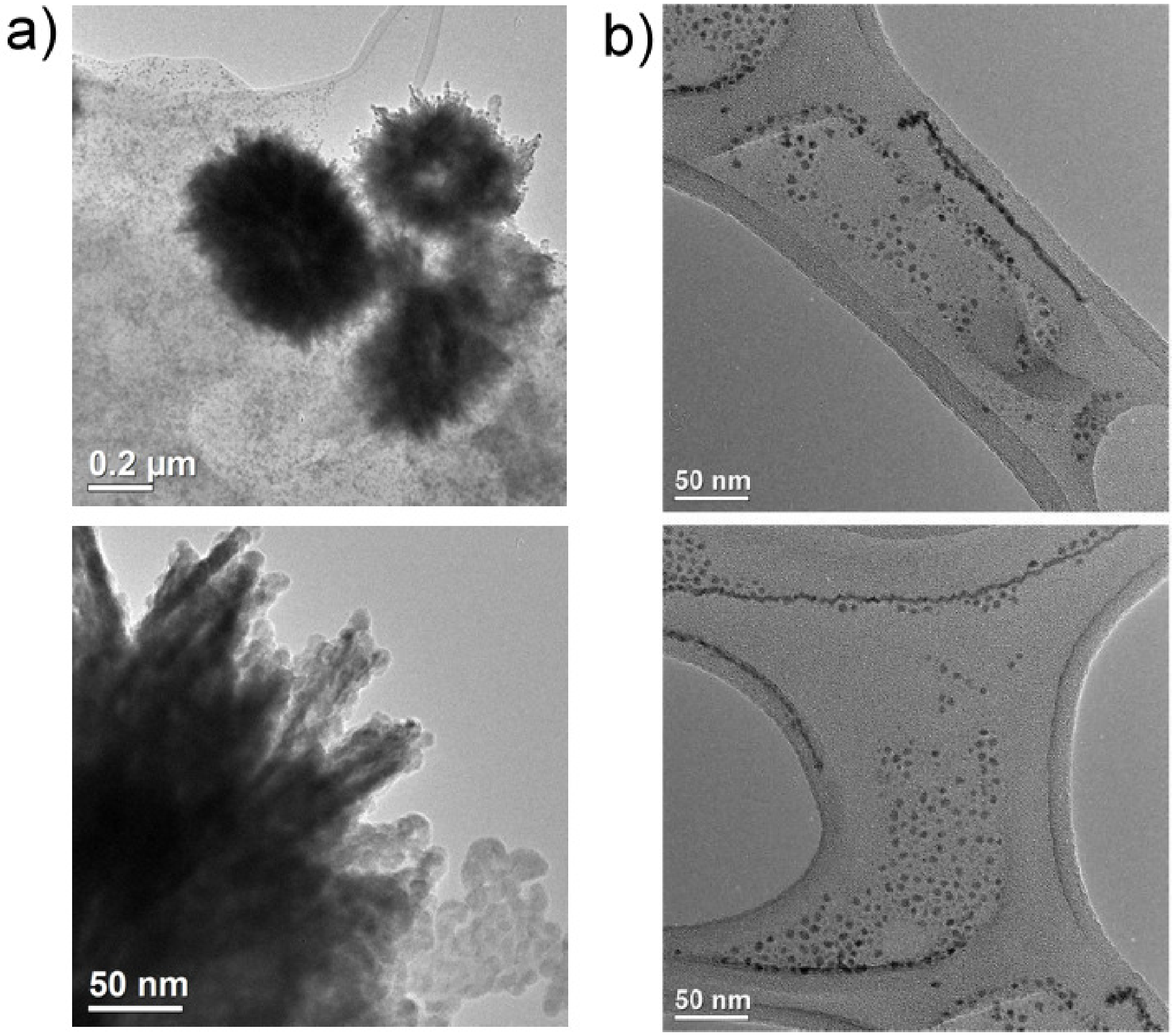

Figure 7—TEM images of nanoparticles that efficiently scatter laser light. (a) TEM of agglomerations caused by heating. (b) Chains formed by the aligned fusion of quantum dots, enabled by imperfect surface passivation.

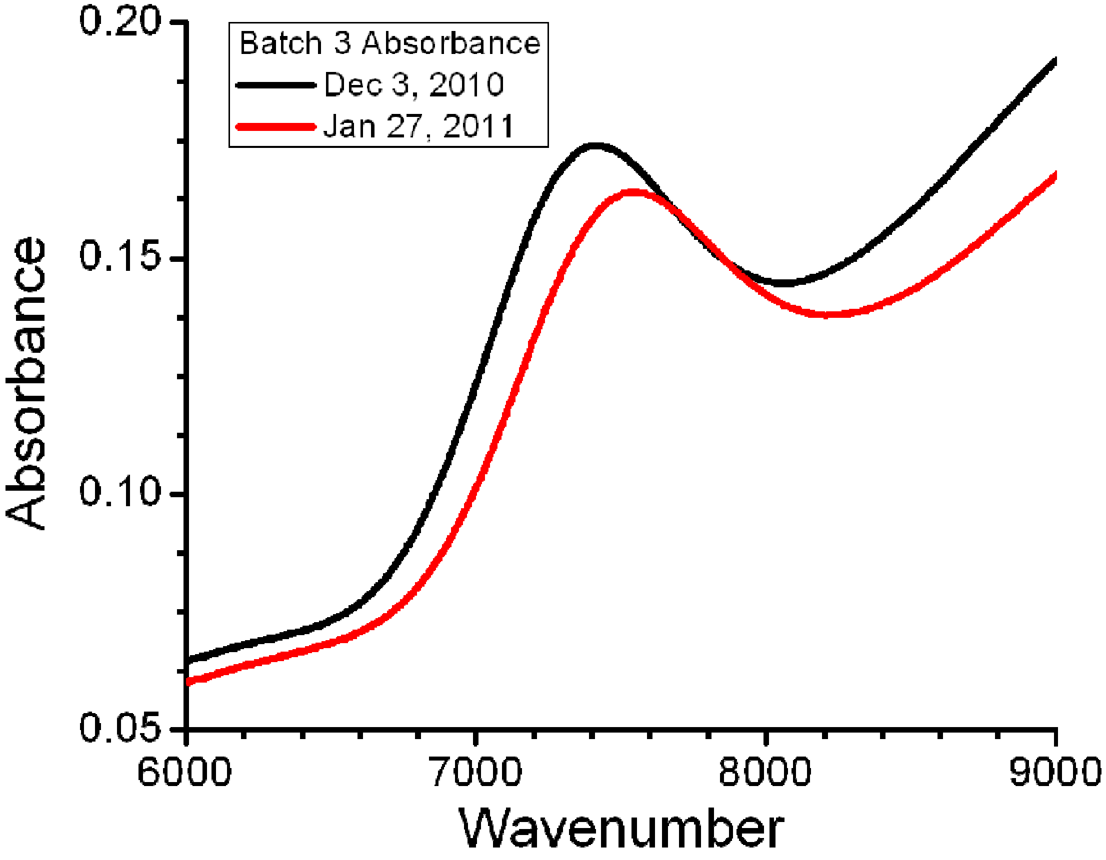

Figure 8— Absorbance profiles for the 1S exciton peak of picosecond batch 3. The blue shift of this peak over the course of two months suggests the possibility of significant structural alteration.

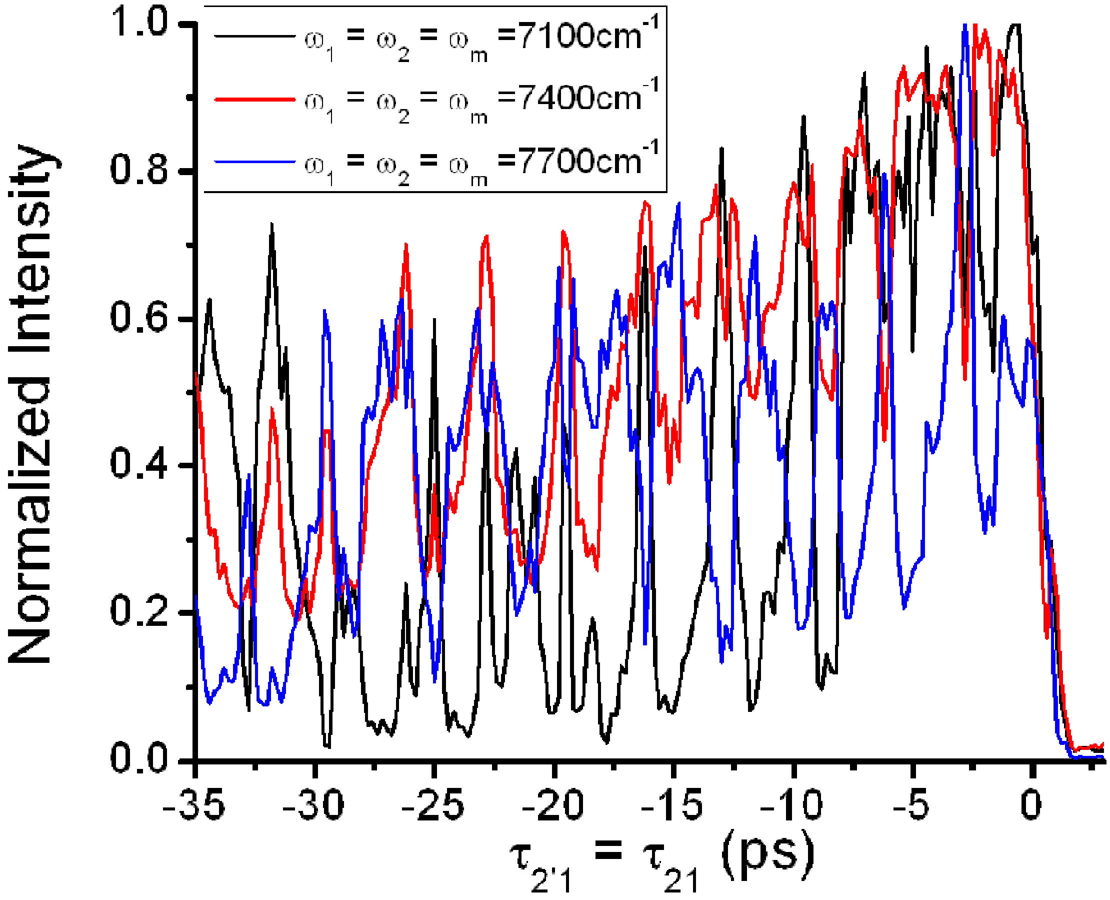

Figure 9—Population decay profiles with erratic heterodyne interference. Scans collected at the center, to the blue, and to the red of the 1S exciton absorption feature are shown.

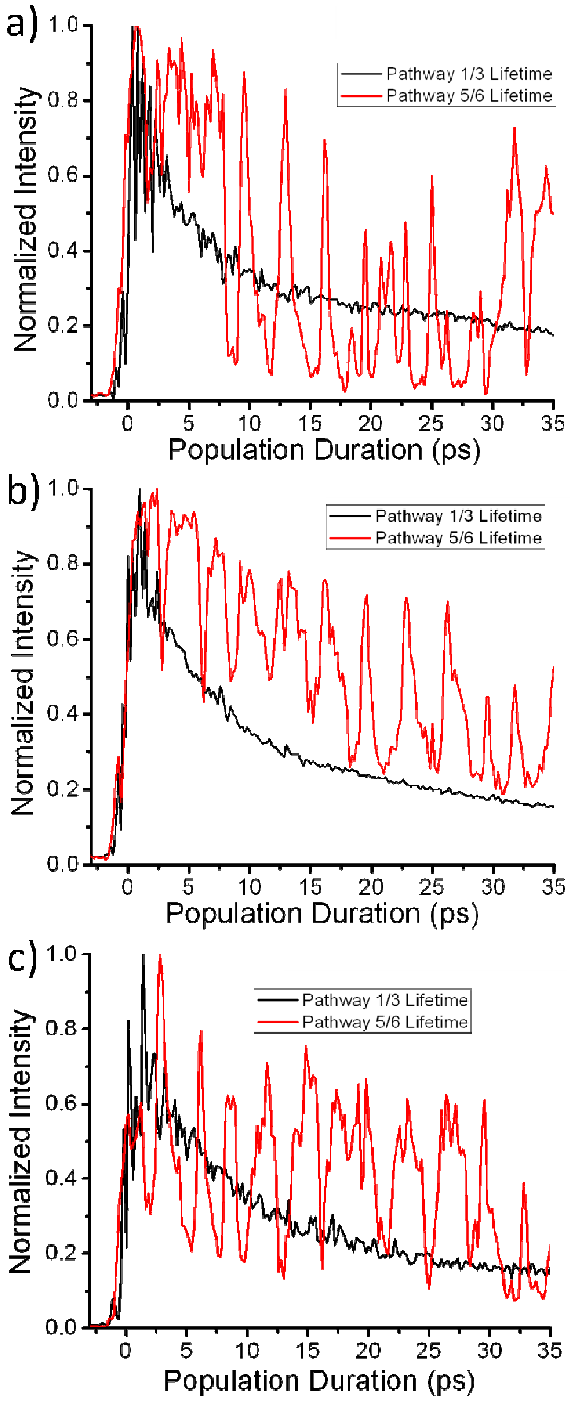

Figure 10—Scans comparing population lifetime traces as measured by time-ordered pathway V/VI scans (red) and pathway I/III scans (black). $\omega_1 = \omega_{-2} = \omega_{2'}$ = (a) 7100cm^{-1}, (b) 7400cm^{-1}, (c) 7700cm^{-1}.

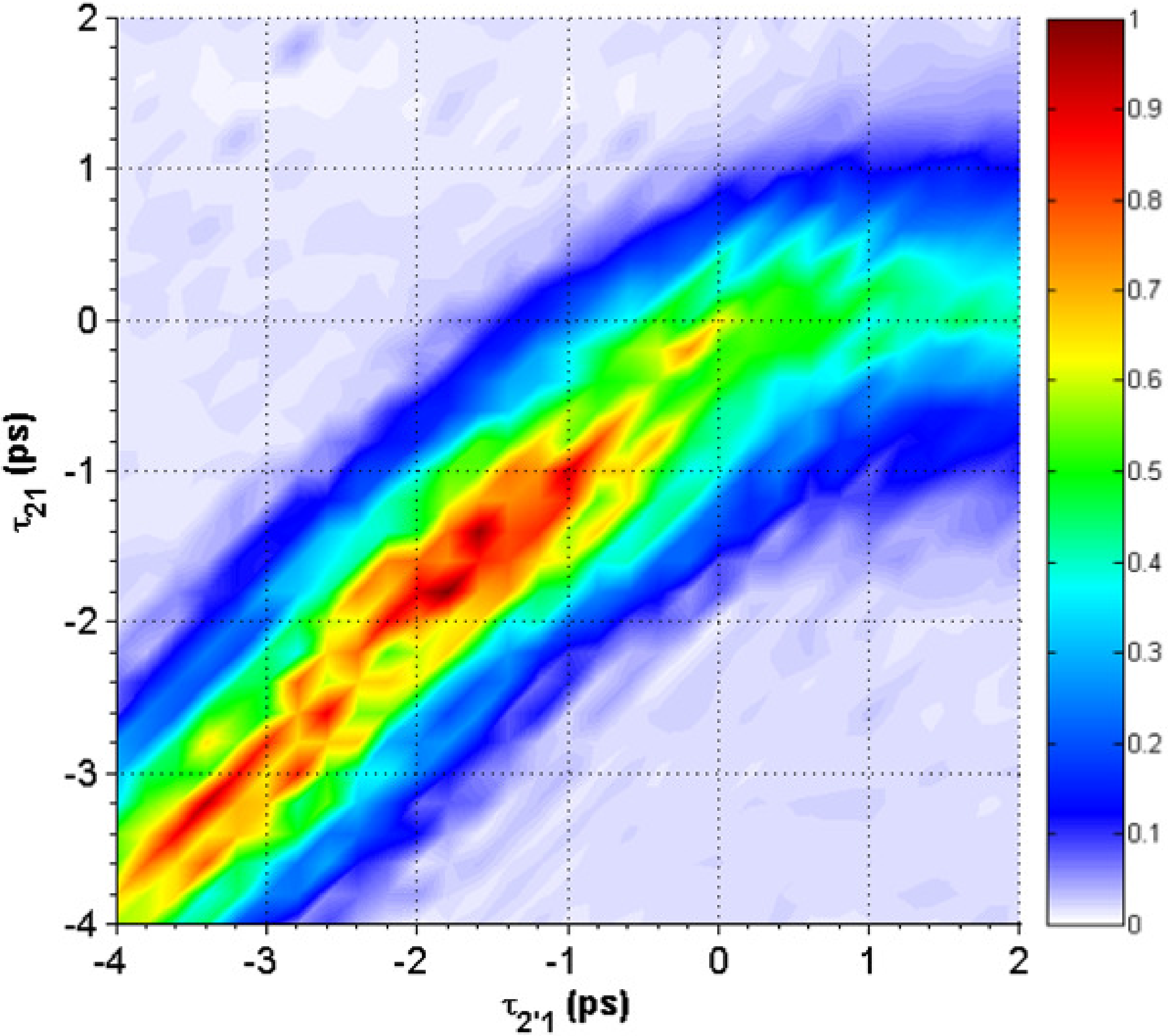

Figure 11—2D delay scan with all excitation beams vertically polarized. $\omega_1 = \omega_2 = \omega_{2'} = 7400cm^{-1}$. Notice the erratic interference patterns along the negative $\tau_{21} = \tau_{2'1}$ diagonal. Signal along the positive $\tau_{2'1}$ axis is weaker, but decays at the excited state relaxation rate, as shown by pathway I/III plots in Figure 8.

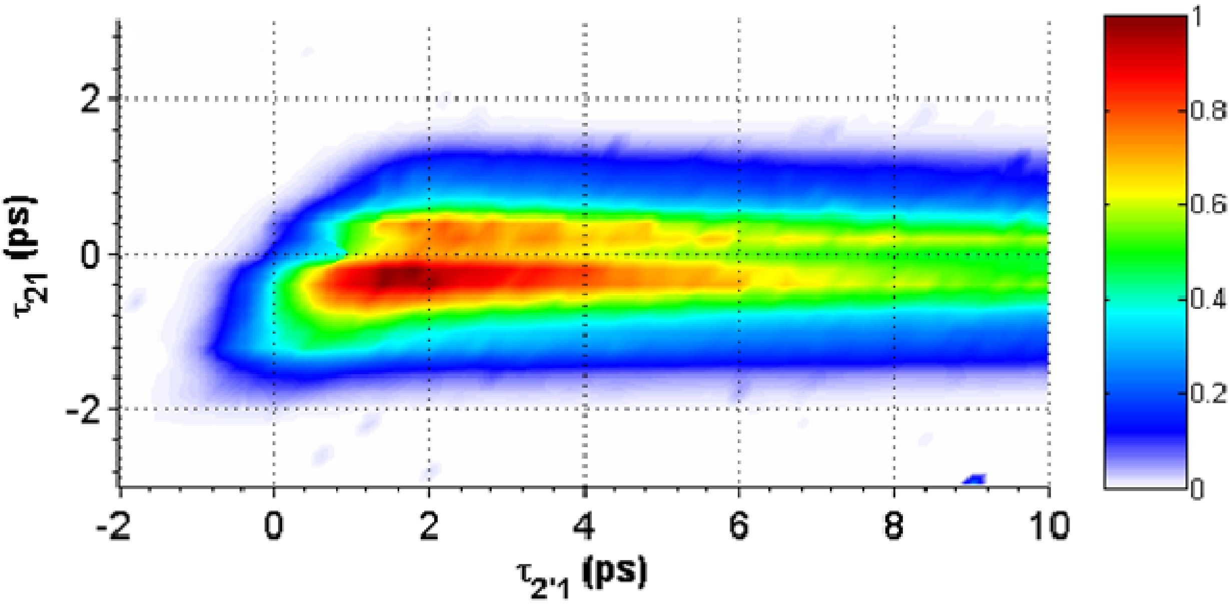

Figure 12—2D delay scan with $\omega_{2'}$ horizontally polarized. Again $\omega_1 = \omega_{-2} = \omega_{2'} = 7400\text{cm}^{-1}$. Notice the lack of signal along the pathway V/VI diagonal, showing vanishingly short lifetime in the angular momentum grating formed by ω_{-2} and $\omega_{2'}$. The splitting between the two peaks is the result of interference between four-wave mixing signal (the phase of which is determined by the relative timing of the two pulses that create the population grating) and scattered light from $\omega_{2'}$, made possible only because the monochromator does not spectrally discriminate against this scatter.[1] A 7400cm^{-1} modulation, sampled at the step size used in this experiment (200fs), results in a beating pattern with 67fs period.

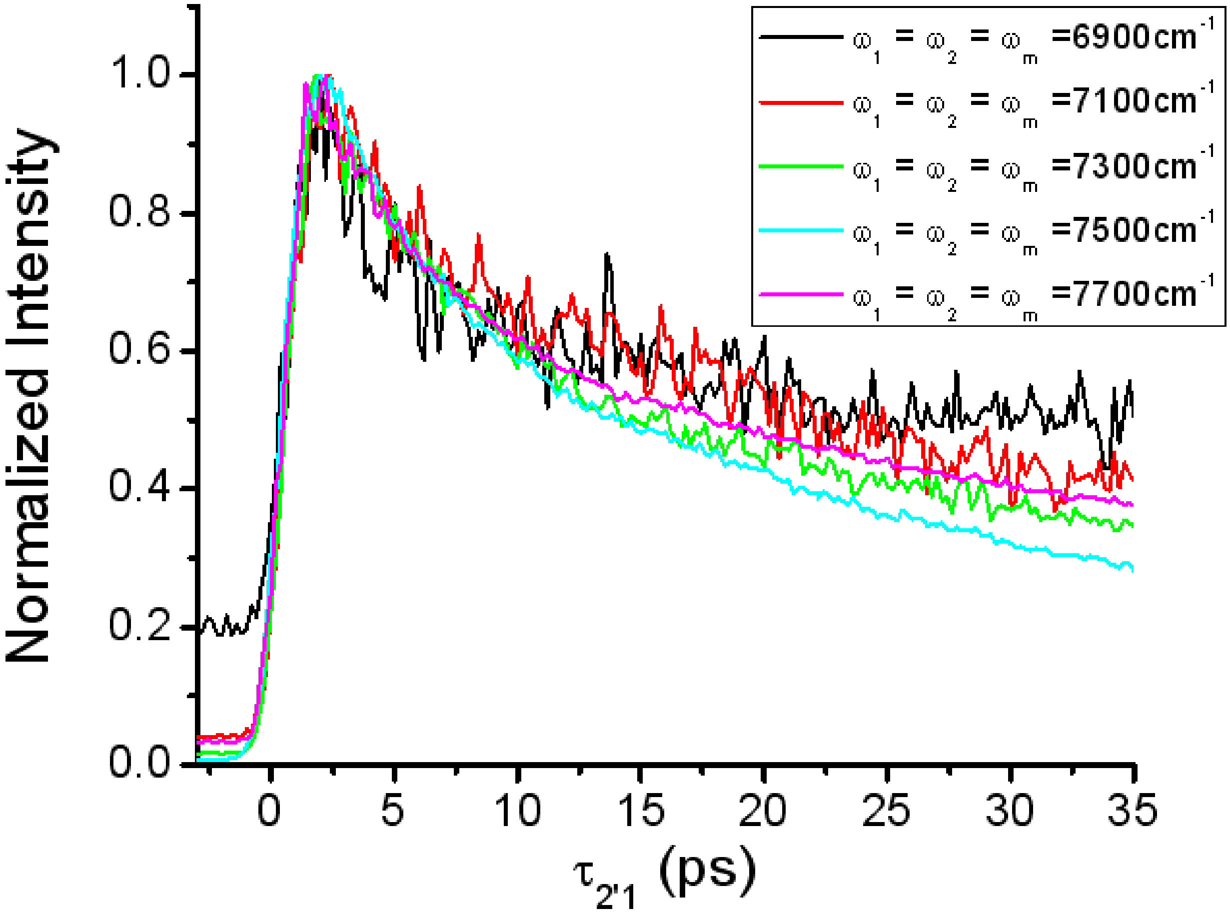

Figure 13—Population lifetimes studied with a crossed-polarization scheme. In these scans, τ_{21} is held at zero, while the delay between the population created by ω_2 and ω_1 is varied. The probe of the population grating, $\omega_{2'}$, has a polarization perpendicular to the other two fields. The rotation of the probe polarization does not allow it to observe any dynamics other than those visible in similar scans with parallel polarization (see Figure 9).

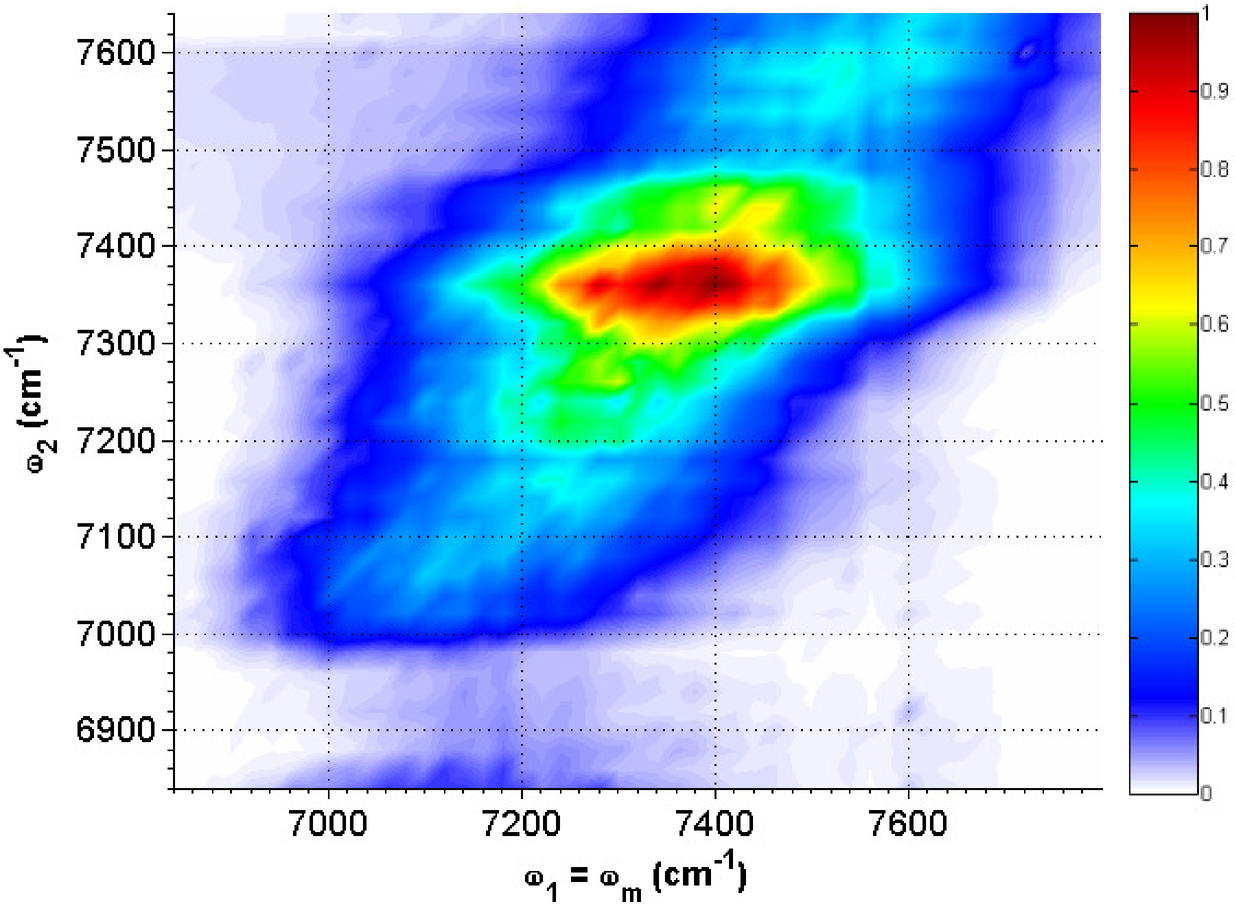

Figure 14—Two-dimensional frequency scan of PbSe quantum dots with all beams vertically polarized. $\tau_{21} = \tau_{2'1} = -2.0$ps. Peak elongation along the diagonal is a common feature of CMDS studies on systems with inhomogeneously broadened peaks. The anti-diagonal width corresponds to the homogeneous line width. Notice that there are some minor abrupt cut-off (as around $\omega_2 = 7000$cm^{-1}) and distortion (the ridge at $\omega_2 = 7360$cm^{-1}) artifacts associated with varying interference of heterodyning scatter.

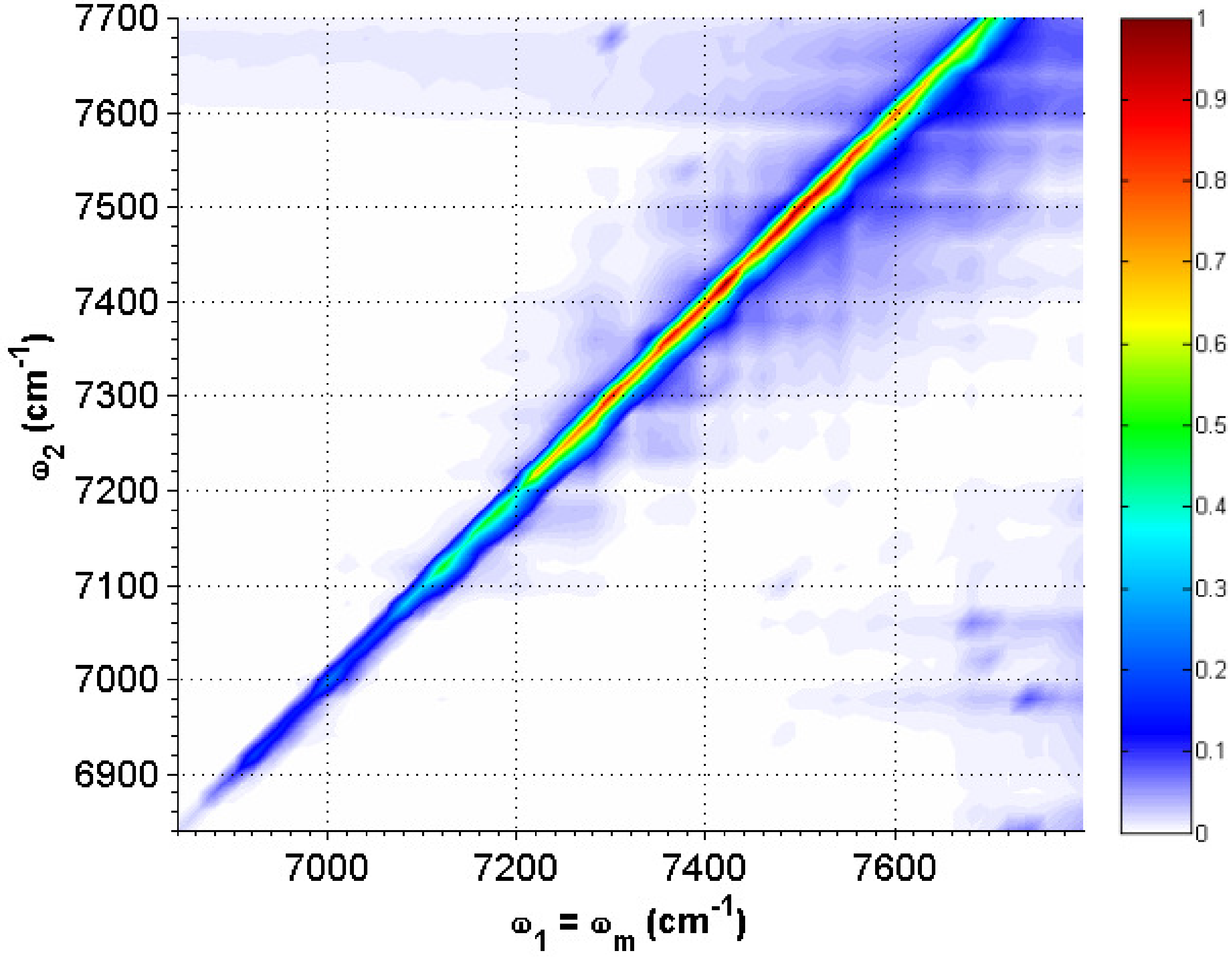

Figure 15—Two-dimensional frequency scan of PbSe quantum dots with $\omega_{2'}$ horizontally polarized. $\tau_{21} = \tau_{2'1} = 0$ps. The intensity of light along the diagonal varies as the excitation lasers scan across the 1S exciton peak (see Figure 7), but little other information can be gained.

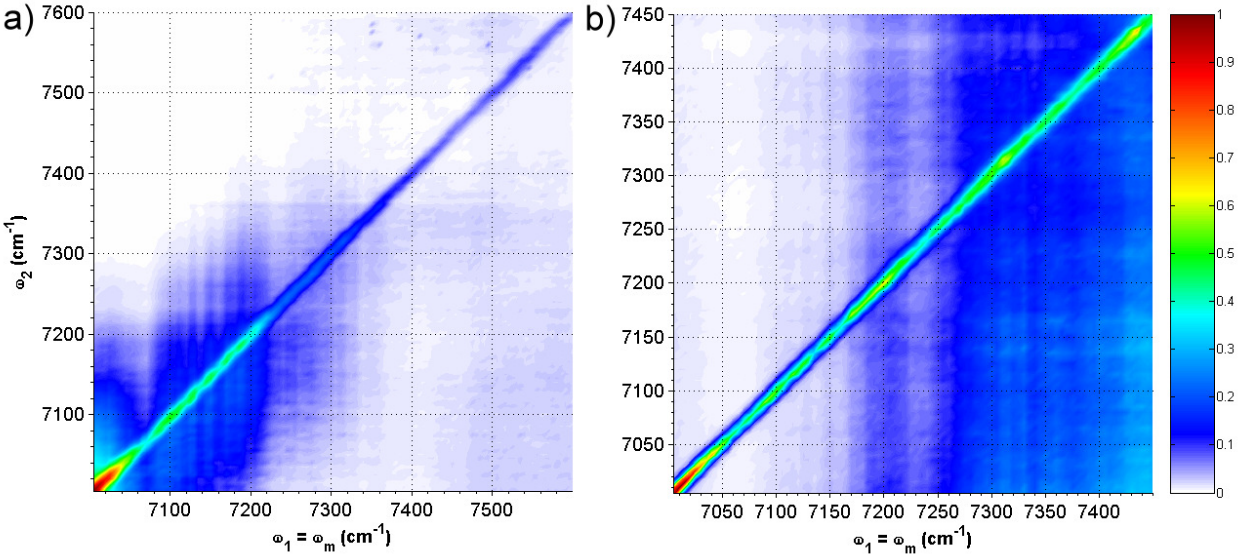

Figure 16—Frequency scans of PbSe quantum dots featuring contributions from (a) all pulse time orderings and (b) only the time ordering allowing the creation of a population with ω_2 and ω_1. The center of the 1S exciton absorption feature is 7000cm^{-1} for this sample, so only the blue half of the peak appears in these scans. (a) $\tau_{21} = \tau_{2'1} = 0$ps, so signal from pathways involving a population created by ω_2 and $\omega_{2'}$ appears to the sides of the sharp peak along the diagonal. (b) $\tau_{21} = 0$ps and $\tau_{2'1} = 3.0$ps. The rising background on the high ω_1 half of plot (b) (and to a lesser extent also in plot (a)) is scattered light, which becomes more visible as its frequency shifts away from regions of high absorption in the sample, such as the 1S exciton feature.

Chapter 6: Femtosecond Experimental Results and Discussion

A report and discussion of femtosecond system PbSe quantum dot experimental progress follows. Spectra from three syntheses are used to demonstrate capabilities, limitations, and technique development. Linear absorption scans for these three samples are shown in Figure 1 and are numbered according to the records of Dan Kohler, who synthesized the batches.

6.1. Early Results and Exploration

Although the fundamental principles of electronic multiresonant CMDS are identical to vibrational multiresonant CMDS, there are many subtle experimental differences that arise from the femtosecond implementation. This section adopts an historical description so future readers can learn from the issues that motivated the development of this femtosecond MR-CMDS system.

The earliest experimental goal on the new laser table was simply the spatial and spectral isolation of four-wave mixing signal. In order to find this signal and provide early characterization, high laser fluences were used. The earliest experiments showed the highest intensity when the pulses were overlapped in time, with a fast decay that lasted no longer than the pulse duration. Figure 2 shows a two-dimensional delay scan with all laser frequencies tuned to the center of the 1S exciton transition. Example cross-sections along the $\tau_{2'1} = \tau_{21}$ diagonal from multiple days are shown in Figure 3. Rough pulse fluence measurements led to the assumption that experiments were performed in energy regimes matching those of similar experiments performed on the picosecond table. Picosecond experiments did not show the dramatic spike at zero delay observed here. The higher peak laser intensity (at matching fluence) likely created short-lived multiexciton states by multiphoton processes,[1, 2] but the absence of fluence calibration data makes it impossible to assess with certainty.

Use of lower excitation fluences became possible as daily alignment procedures improved. A study designed to reveal the effects of varying excitation intensity helps identify the nature of the sharp peak in the earliest experiments. Figure 4 shows three population lifetime scans performed in sequence at varying ω_2 and $\omega_{2'}$ energies (the pulses creating the population state). Only qualitative information is available to describe the fluences, but some observations are important. The relative intensity of the spike at zero time delay is considerably more sensitive to excitation fluence than the long lifetime decay component. The comparative invariance of the long-lived feature suggests that the transition was saturated until the fluences dropped down to those used in the experiment shown by the black trace. Reduction of fluence from “high” to “medium” may simply have reduced the number of excitons involved with the multiexciton state, thereby decreasing the emission stimulated by the last pulse. Another important observation from this experiment is the shift of the sharp feature to longer delays as the pulse intensity decreases. One potential explanation for the peak near zero delay is that it results from high non-resonant signal from the solvent and higher energy PbSe exciton states, which are only visible when the pulses are overlapped in time. If the long delay component is constant over this time scale because it corresponds to a single exciton in each dot, then the relative intensity of the non-resonant signal could change as it continues to scale as a product of the excitation intensities. However, if the sharp feature results only from intense non-resonant background, then its position in time should not have shifted as its relative intensity decreased.

The "medium power" trace then starts to reveal a slower multiexcitonic recombination rate than the "high power" trace.[2]

Alternatively, the different relaxation rates observed between "high" and "medium" intensities could correspond to different rates of relaxation to surface trap states. Previous work has shown that variation of excitation fluence can have unexpected consequences for transient absorption decay profiles.[3] A two-dimensional delay scan taken at "low" intensity (see Figure 5) reveals a slow increase in output intensity as the population is allowed to relax. It also shows that the condition for maximum intensity occurs when $\tau_{2'1} > \tau_{21}$. This shift is expected for an inhomogeneously broadened transition because the stimulated photon echo from the rephasing pathway creates a larger output signal. This explanation is not definitive, however, because there was a problem in the delay calibration resulting from a failure to effectively include the required delay stage motor backlash correction. Since the scans shown in Figure 4 were taken with $\tau_{2'1} = \tau_{21}$, the signal intensity is low and the data have a lower signal-to-noise ratio. In addition, later calculations and general practices at the time of these experiments suggest that the fluences far exceeded the usual saturation intensities. (See Appendix E—Fluence Calculations.) Observations of sample damage support the possibility of an increasing number of surface defects, so it is likely that both effects contributed to the combination of behaviors observed in the data.

The power dependence studies shown in Figure 4 revealed the shape of population lifetime scans collected with low pulse fluences. Further studies adjusted excitation fluences so that this character could be observed until more careful calibration curves could be constructed and pulse fluences chosen with greater precision. (See Appendix E—Fluence Calculations.)

The four weeks of exploratory experiments with high fluence beams were enough to significantly damage the sample. Incomplete sample cell sealing may also have caused a slow leak of ambient atmosphere into the sample, accelerating oxidation, but the deterioration of the sample, revealed in Figure 6 by the dramatic blue-shift in the quantum-confined exciton peaks, is also characteristic of extreme photo-treatment.[4] The extent of the sample damage led to an abandonment of further investigation with this sample, so comparison with previous surface defect studies with the picosecond system[5] is not possible.

6.2. Artifacts of the System

As control software problems were eliminated and sample exposure limits were better identified, some observed data abnormalities could be identified. Some of these instrumentation artifacts could be corrected and eliminated and some required developing different strategies. The most disruptive artifacts arose from changes in ambient temperature, multiple reflections, and delay stage pitch and yaw.

As described in the Femtosecond Table Instrumentation section, under normal experimental conditions, the air conditioner units cycled on and off with a period of between 25 and 28 minutes. The temperature modulations created by this cycling resulted in small beam deflections and relative delay changes. Figure 7 shows the manifestation of these effects clearly. The scan was collected as a sequence of vertical slices, each requiring a little less than seven minutes. The $\tau_{2'1}$ increment was 20fs, so the 80fs undulations correspond very closely to the pattern of air conditioner cycling. These undulations appear in two ways—as an increase in observed scattered light (particularly visible on the logarithmic scale shown in Figure 7b) and a slight shift in the delay value corresponding to actual temporal overlap of the pulses. The delay shift is most visible along the $\tau_{2'1}$ axis (where signal depends on the temporal overlap of ω_{-2} and ω_1), and does not appear significant along the negative $\tau_{2'1} = \tau_{21}$ diagonal. This observation reveals that the relative timing of ω_{-2} and $\omega_{2'}$ is not sensitive to the temperature changes, but the relative timing between at least ω_{-2} and ω_1 is. This sensitivity suggests that the temperature fluctuation influences the behavior of the OPAs, rather than changing individual optics further down the table. The variations in scattered light intensity are likely due to small changes in beam direction, leading to varying overlap of beams with small PbSe deposits on the interior surface of the sample cell.

The effects of temperature-induced delay fluctuation usually are not undetected in experiments varying only excitation pulse frequencies. If $\tau_{2'1} = \tau_{21} = -200$fs for one slice and -210fs for another, the four-wave mixing signal intensity fluctuation in is negligibly more than simple point-to-point noise (consider those regions for Figures 3, 4, 5, and 7 as examples). However, if the pulses are overlapped in time for a frequency scan, then small fluctuations in relative delay can induce significant changes in observed intensity, as shown in the fast rising edges in Figure 3, Figure 4 (even in the low power experiment), and other delay scans. Figure 8 shows a scan collected over the course of about eight hours for which the pulses were overlapped in time. The undulations that are clearly visible are the result of subtle repositionings on the steep population grow-in slope.

Shortly after realizing that the cause of these modulations was ambient temperature fluctuation, an additional enclosure for the OPAs was added to the table. The additional barrier between laboratory air and the sensitive optics in the OPAs eliminated the relative delay fluctuations, as can be seen by their absence in later delay scans. Any remaining changes in pointing have not produced observable effects because a chopper has enabled active baseline subtraction, and hence elimination of all scatter other than that of a single ω_2 beamline, and sample handling has reduced degradation, also reducing the prevalence of sample cell surface deposits.

The signal along the negative $\tau_{2'1}$ axis in Figure 7 is another experimental feature that does not directly reveal to PbSe quantum dot properties. Figure 9 shows a similar faint feature along the positive $\tau_{2'1} = \tau_{21}$ diagonal. In each case signal appears in line with a long-lived population state. Explorations revealed that this signal does not decrease as it is traced away from the delay origin, but rather increases slowly until it spikes, then disappears entirely about 8ps away from zero delay. Tests with a silicon wafer, which has a very short population lifetime, showed no long decay, but still revealed a small echo of the peak at $\tau_{2'1} = \tau_{21} = 0$, again about 8ps away (as shown in Figure 10). This peak has about 4% of the intensity of the main feature.

The best explanation for this weak feature is that a faint reflection of each beam passes out of the OPAs, delayed by 8ps. The weak delayed pulse can still probe a population, so if two pulses are sent in with longer delay relative to the beam line producing the echo (longer $\tau_{12'}$ and $\tau_{2,2'}$, and hence also longer $-\tau_{2'1}$, when waiting for the arrival of $\omega_{2'}$; longer $\tau_{2'1}$ and τ_{21}, when waiting for the arrival of ω_1), they overlap with the delayed pulse. In the absence of a more intense feature, this weak signal is visible against the background. The presence of the feature in scans with the silicon wafer reveals that it has nothing to do with PbSe, nor with the sample cell. The only optical surfaces on the table capable of multiple collinear reflections are those of the neutral density filters and the beam-splitter. However, these filters are 2mm thick, so the delay between a transmitted pulse and a pulse that reflects off each surface should be closer to 20ps (approximating the index of refraction as 1.5). The beam-splitter would only induce a delay for ω_{-2}, and the faint signal is observed for faint echoes of ω_1 and $\omega_{2'}$. Elimination of optical table elements leaves OPA components as the remaining possible reflection sources. The 4% relative intensity suggests an element that does not produce the echo after a pair of simple air/glass interface reflections. Though the particular element still has not been identified, its source in the OPA makes it difficult to remove the reflection. The comparative rarity of seeing the faint population decay signal with an ω_1 echo suggests that it may be easy to unintentionally align the system such that the echo and the main pulse travel in slightly different directions. Reflections off the back surfaces of the bandpass filters attached to the outputs of the OPAs meet all of the observed requirements, but their source has not been confirmed.

The last significant instrumentation artifact to be discovered and identified is a periodic shift in beam pointing resulting from delay stage irregularities. Appearance of the artifact in only long delay scans caused it to go unobserved for the first several months of experiments. The shift in pointing leads to a decrease in observed signal intensity because of a combined loss of beam overlap and relative delay consistency. Figure 11 shows a pair of population lifetime scans of Femtosecond Batch 4, collected two days apart. The modulations not only persist from one day to the next, but also exist and retain their phase, even for long relative delay times. Tests of this behavior showed that the frequency (see Figure 12) and phase (see Figure 13) of the undulation are dependent on neither OPA frequencies—absolute, relative to each other, or relative to the 1S exciton feature—nor delay step size (eliminating scatter interference theories). The small shifts in time delay that the software creates to compensate the changes caused by different OPA frequencies (seen in Appendix C—Daily Calibration Routine) are too small to appear in scans observing this phenomenon. Small phase shifts from one week to the next can be observed, as shown by the vertical dashed lines in Figure 13 (March 13) and Figure 14 (March 21), but the period remains the same. Ruling out OPA involvement left only delay stage behavior to explain the observed modulations.

The screws on the delay stages have one full rotation for every ~500μm of travel. Every 500μm of travel changes the beam path length by 1mm, which corresponds to a delay change of 3.3ps. As the screw rotates, the stage resting on it experiences small changes in pitch and yaw depending on the phase of the screw rotation. The stages were acquired with the goal of having optimal short-distance control and reproducibility, but the motor required to achieve those exacting standards suffers from angle changes over longer travel ranges. Figures 11a and 12 show a second repeated modulation (visible as a shoulder or a smaller peak to the right of each modulation peak) with the same frequency once the delay times are long enough for the four-wave mixing signal to have diminished substantially. The appearance of two peaks suggests that, over the course of translating the two stages, there are two phase ranges over which the beams are directed to more complete spatial overlap at the sample cell position.

As only minor realignment is required from day to day, the absolute position of the motorized delay stages that corresponds to ($\tau_{21} = \tau_{2'1} = 0$) changes minimally. If a full alignment is required after a couple days, then the positions of the two motorized delay stages will have to be adjusted to the new alignment. This adjustment tends to result in the delay stage screws, and hence the 3ps modulation pattern, being at a different phase at zero delay. The small phase differences visible between scans separated by multiple days result from changing the position of the ω_1 beamline non-motorized stage. The two motorized stages are adjusted to for temporal overlap with ω_1, so manual adjustment of ω_1 also determines the screw phase range used over the course of experiments near zero delay. Intentional selection of that range allowed most scans to avoid the sharp decrease in signal that comes from the screw phases that cause poorest overlap.

These ~3ps modulations are very difficult to eliminate without additional hardware, but there are alignments for the retroreflectors that minimize the modulation. No procedure has been developed to intentionally produce these optimal alignments, but the optimization has been observed several times. The scans in Figures 11-14 show representative modulations. For experiments requiring only short delay ranges, the position of the ω_1 retroreflector stage was adjusted so that the sharp decline at the edge of every 3ps modulation did not occur in the featured scan range. Experiments performed prior to this identification may contain dips over the course of scans that are the result of this delay stage behavior. Future experiments will incorporate a coupled nanosecond delay stage designed to cover long-range delay scans, in part to eliminate this phenomenon.

6.3. Fast Dynamics Around Zero Delay

The PbSe quantum dot dynamics seen in Figures 2, 3, 4, and 7 exhibit several effects that arise from a combination of multiexcitonic effects, shifts due to inhomogeneous broadening, non-resonant signal from the solvent and higher energy PbSe excited electronic states, and interference effects from different excitation pulse time orderings. Simulations based on Domcke's approach [6] that directly integrate the Schrodinger equation elucidate the effects. The simulations include the excitonic four-wave mixing dynamics, but have not yet incorporated higher order processes and purely driven processes. These calculations provide the qualitative interpretations of data that assess the femtosecond system capabilities. Table 1 shows the parameters used in the simulations—each chosen to be indicative of common experimental conditions or previously-determined PbSe quantum dot characteristics.[7]

Figure 15 reveals the effects of inhomogeneous broadening. In Figure 15a, no broadening effects are added. A slight dip at zero delay results from the interference of polarizations created by fully coherent processes with short lifetimes. Figure 15b shows the result of a simulation adaptation created by Blaise Thompson in which the signal from a Gaussian distribution of quantum dot 1S exciton peaks is allowed to interfere. The result of this interference is a preferential weighting of rephasing pathways that appear to cause a shift to lower τ_{21} values. This shift also moves the apparent origin away from temporal overlap, so some of the fully coherent processes weaken, so their interfering contribution diminishes. Figure 16 shows the effects of inhomogeneous-broadening-induced shifts on population lifetime cross-sections. Scans collected along the $\tau_{21} = \tau_{2'1}$ diagonal (the boundary between time-orderings 5 and 6) show similar behavior with and without broadening contributions, but the signal intensity diminishes unless the slice is collected along the shifted ridge. Scans tracing along the $\tau_{21} = 0$ axis (or parallel) show only a slightly early grow-in because of the absence of fully coherent process interference.

Non-resonant transitions from higher energy states in both the solvent and analyte can contribute non-linear polarization signal even when all excitation lasers are significantly detuned from their central transition frequencies because the associated dipole moments are strong and the oscillator concentration tends to be high. Fast dephasing rates, combined with the large shift from resonance, ensure that this signal exists only while all three excitation pulses are overlapped in time. Further, because the excitation frequencies are so far from those resonances, only the real part of their polarization (which depends on the inverse of the detuning instead of the imaginary part's dependence on the square of the inverse of the detuning) tends to be significant, and that tends to be effectively constant over frequency ranges in the infrared. The energy of the non-quantum-confined excited electronic states of PbSe is low enough to contribute a small imaginary component.[7] Figure 17 shows the contributions of (a) no constant background, (b) constructively interfering background, and (c) destructively interfering background to simulations of a typical two-dimensional delay scan. Figure 18 shows cross-sections of these scans revealing the corresponding common population lifetime scan behavior. The interference can cause the appearance of faster population grow-in by counteracting the destructive interference of the fully coherent process contributions or it can induce the creation of an apparent shoulder in the population formation.

Because the non-resonant signal is constant, it is the sign of the real part of the polarization created by resonant transitions that determines whether the background signal will interfere constructively or destructively. Frequency domain simulations can provide insight into this behavior by showing the sign of the real part of $\chi_{1S}^{(3)}$ at different excitation frequencies (see Figure 19, and for further explanation and examples see Appendix A—Frequency Domain Simulations). The center of this resonant feature is intense and minimally influenced by the background, but its tails and other portions of the scan range are influenced more noticeably. Figure 19 shows that the resonant feature is not symmetric about the $\omega_1 = \omega_2$ diagonal. This asymmetry means that moving away from the diagonal may reveal different relative background signal intensity when blue-shifting one excitation than when red shifting it. Figures 24 and 25, discussed in greater detail later, illustrate this effect by showing qualitatively different behavior when ω_1 is 300cm^{-1} to the blue of the center of the 1S exciton feature and when it is about 300cm^{-1} to red.

As the relative contributions of the resonant and non-resonant signal change, the qualitative character of delay profiles can also change dramatically. Figures 20 and 21 show two-dimensional delay scan and population lifetime scan behaviors for different contribution ratios. As the relative resonant signal contribution decreases, the appearance of the background signal grows from a dip to a shoulder to a peak and finally to the most prominent feature.

Because of the short lifetime of solvent and high energy PbSe transition signals, any particularly intense fast dynamics signatures that last longer than the duration of the excitation pulses are attributed to multiphoton effects. Careful monitoring of pulse fluences limited, but did not eliminate the appearance of these features.

Understanding the behavior of non-resonant background, inhomogeneous broadening, and multiphoton effects allows meaningful qualitative interpretation of the short-delay behavior. For example, two population lifetime traces of Femtosecond Batch 3 PbSe quantum dots are shown in Figure 22. The black trace was generated when all three pulses were resonant with the strong 1S exciton transition. The blue trace was generated when ω_{-2} and $\omega_{2'}$ were resonant with the weaker 1P exciton transition. The relative intensities of the longer-delay tails are 6:1, suggesting the possibility of significant qualitative behavior changes. The dip after the peak at zero delay confirmed the presence of the anticipated non-resonant background interference. The presence of an intense fast decay component in the 1S exciton profile, which nevertheless lasts somewhat longer than the excitation pulse duration, suggests contributions from multiexciton relaxation.

Figure 23 shows a collection of population lifetime scans collected at different excitation frequencies from Femtosecond Batch 8. As the lasers become increasingly detuned from the 1S exciton transition, the non-resonant feature becomes more apparent. Though the noise from scattered light makes it difficult to assess with confidence, the various patterns of negligible interference ($\omega_1 = \omega_2 = \omega_m = \omega_{1S} = 6800\text{cm}^{-1}$), small shoulder ($\omega_1 = \omega_2 = \omega_m = 6900\text{cm}^{-1}$; shoulder at -40fs when compared to the same delay at 6800cm^{-1}), and peak followed by a dip ($\omega_1 = \omega_2 = \omega_m = 6950\text{cm}^{-1}$; peak at -40fs, dip at -80fs) may all be present in such a scan. The delayed grow-in of the resonant feature matches the behavior predicted by simulations, as shown in Figures 18 and 21. Figure 24 shows a similar scan on Femtosecond Batch 4, but only ω_2 is varied from lifetime scan to lifetime scan. ω_1 is held on the blue edge of the 1S exciton feature (where Figure 19 suggests that the detuning will result in even more significant loss of resonant intensity). The qualitative character of the scan is striking—horizontal cross sections of this scan show the same interference pattern as seen in Figure 20d and Figure 22. The slow-rising resonant signal is brightest when ω_2 can be tuned to a frequency that compromises between interacting with the highest number of dots in the sample distribution (at the center of the 1S exciton feature near 6900cm^{-1}) and interacting with the dots most efficiently probed by ω_1 (at 7200cm^{-1}). The non-resonant signal is likely dependent on ω_2 only because when $\omega_1 = \omega_2$, the simultaneous interaction with ω_1 and ω_{-2} allows the creation of a ground state population, similar to the interactions in gamma pathways. Figure 25 shows an experiment similar to Figure 24, but ω_1 is shifted to the red of the center of the 1S exciton distribution of Femtosecond Batch 4. The red shift in ω_1 for the resonant feature (shown in Figure 19) helps interpret the absence of a non-resonant feature in this scan. The intense resonant signal overwhelms contributions from the non-resonant states. ω_2 shows the same compromise behavior between ω_1 and ω_{1S} here as in Figure 24.

6.4. General Femtosecond System Experimental Capabilities

While dynamics observable at very short time delays are complicated, most of the capabilities of the femtosecond laser system have now been adapted to successfully use the techniques first developed on vibrational systems with long coherence lifetimes.

Incoherent dynamics were observable on the picosecond system and, while elementary, the ability to measure these dynamics is important for future CMDS work. Figure 26 shows a typical 1S exciton population decay profile for Femtosecond Batch 8 PbSe quantum dots. The biexponential fit reveals two contributions—a primary contribution with an 11ps lifetime and a secondary contribution with a 70ps lifetime. Although longer delay times are needed to better define the longer lifetime, it is consistent with that observed by others for PbSe quantum dots. The shorter lifetime has also been observed, but has not been unidentified.[5, 7]

Incoherent intraband transfer dynamics can be observed and measured with femtosecond instrumentation. Figure 27 shows a population lifetime scan for which ω_2 was tuned to resonance with the 1P exciton transition and ω_1 probed the 1S exciton transition. The increase in intensity over two picoseconds corresponds to relaxation between the 1P and 1S exciton states. Figure 27b shows a single exponential fir with a lifetime of 1.4ps. This lifetime agrees well with the range of reported values.[8, 9, 10] Here again the weak resonant signal allows non-resonant background contributions to be relatively significant at zero delay.

The primary capabilities of MR-CMDS that were inaccessible to picosecond quantum dot studies pertain to coherence lifetimes and fully coherent processes. Figure 28a shows a two-dimensional delay scan of Femtosecond Batch 8 quantum dots collected at low pulse fluence with all lasers tuned to the center of the 1S exciton transition. At first glance, the scan appears qualitatively identical to those collected under similar conditions with the picosecond system. The fit shown in Figure 28b uses excitation pulse profiles measured on the day the scan was collected. It is strongly dependent on the coherence dephasing rate. Unlike simulations of picosecond data, the fit error is at a clear minimum when the single exciton coherence lifetime (Γ_{eg}) is 45fs and the biexciton double-quantum coherence lifetime ($\Gamma_{2e,g}$) is 17fs. Addition of a small amount of destructively interfering non-resonant background at zero delay improves the fit further. Table 1 shows the particular parameters used for the fit. The population lifetime value (~1.1ps) used for the fit is artificially low. Figure 29 compares the cross-sections along the $\tau_{21} = \tau_{2'1}$ axis and suggests that the noise in the data obscures what is probably a slow decay. The scan in Figure 26a directly traces the decay of the same spectral feature (collected earlier that same day) over a longer range. The fit population lifetime decay rate minimizes the error between the simulation and the data, but does not reflect this slower trend.

The coherence lifetimes from Figure 28 are reproducible under different excitation frequency conditions, as well. Figure 30 shows the data and fit for a two-dimensional delay scan of Femtosecond Batch 8 quantum dots. Here ω_1 is shifted from ω_2 and the center of the 1S exciton distribution by 200cm^{-1}, dramatically decreasing the efficiency for creating 1S populations with ω_1 and ω_{-2} when $\tau_{2'1} > 0$. While the intensity difference between the diagonal and $\tau_{2'1} > 0$ parts of Figure 30 do not match, the qualitative agreement is consistent. Further, the coherence lifetimes used in the fit for Figure 28a also describe the data in Figure 30.

The femtosecond system increased the temporal resolution, but degraded the spectral resolution of experiments. The decreased spectral resolution, however, did not eliminate direct exploration of energetic structure. For example, Figure 31 shows a frequency domain spectrum of Femtosecond Batch 4 quantum dots and a corresponding simulation used to fit the data. Fit parameters are summarized in Table 2. The spectrum was collected at delays where ω_2 and $\omega_{2'}$ created a population ($\tau_{21} = \tau_{2'1} = -40\text{fs}$) and ω_1 probed that population. The central frequency of the 1S exciton transition corresponds very closely to the center of the linear absorption profile and the lifetimes match those of delay scans. The fit quality was improved by small contributions from pathways 1 and 3 and from non-resonant background. Both contributions are expected from the proximity to zero delay relative to the pulse duration.

Two-dimensional frequency scans at longer population lifetime settings did frequently produce one feature that is currently without explanation—a small dip in intensity at a single ω_1 value in the middle of the exciton peak. Figure 32 shows four scans, collected at different delays, on different days, from different batches that show this partial node. The behavior does not always appear at the same frequency, but does always divide the 1S exciton peak (data pertaining to the 1P peak is not available). The dip corresponds to neither OPA output powers, nor frequency accuracy, nor the appearance of a biexciton feature. It does seem to only appear after a significant delay from establishing the 1S state population. The dip is also only observed when the spectral feature is not elongated along the $\omega_1 = \omega_2$ diagonal, but broadened into a round feature whose width in ω_2 space does not match the expected inhomogeneous line width.

A cross-peak between the 1S and 1P exciton is also accessible. Figure 33 shows a frequency scan of Femtosecond Batch 3 quantum dots for which the lasers are tuned across the

1P exciton and a portion of the 1S exciton. For this scan, $\tau_{21} = \tau_{2'1} = -600$fs, so features can result from population relaxation events. The dominance of the feature that is shown to grow in over time in Figure 27 suggests that the off-diagonal feature is the result of a relaxation from the 1P exciton to a state with either a 1S electron or 1S hole. Figure 22 shows that 1S exciton features are present, but the tuning range available on the day this two-dimensional scan was collected could not access it.

One advantage of MR-CMDS is the ability to gain clearer understanding of energetic structure by isolating particular pulse sequences that distinguish between different coherent pathways. Scans described so far focus on either experiments with all pulses overlapped in time or ω_{-2} and $\omega_{2'}$ overlapped in time. The narrow diagonal feature resulting from frequency scans where ω_{-2} and ω_1 are similar can be seen in Figure 34 (from Femtosecond Batch 4). The character of this feature results from the domination of processes where ω_{-2} and ω_1 create a population. Scans of this kind show extreme line-narrowing near $\omega_1 = \omega_2$ because their intensity depends inversely on ω_2-ω_1-$i\Gamma_{ee}$, and Γ_{ee} is very small. Use of continuous wave lasers can resolve this long lifetime contribution, but pulsed lasers are broad enough that the spectra resulting from this process reveal only the convolution of the Gaussian distributions of ω_1 and ω_2.

Pulse sequences that access only fully coherent processes can isolate coherence transfer signal and direct coupling between states by eliminating population relaxation, though the signal they produce is typically far weaker. Because of the relative strengths of fully- and partially-coherent processes, excitation pulses must be short enough that their tails do not efficiently access the brighter partially-coherent pathways, but close enough to overlapping in time to be within the lifetimes of the coherences accessed. While complete temporal resolution of different pulse sequences does not yield a measurable signal when pulse durations and coherence lifetimes are approximately equal, the regime does allow for the relative emphasis of one time ordering over another. Figure 35 shows a two-dimensional frequency scan collected from Femtosecond Batch 8. For this experiment, $\omega_{2'}$ and ω_1 are overlapped in time, creating a double-quantum coherence (1S+1S,g coherence) that is later probed by ω_{-2} according to patterns shown in Chapter 1: Theory Overview for time-ordered pathways II and IV. The high population of acoustic phonon modes at room temperature increases the dephasing rate, so the fully-coherent process cannot be completely isolated and contributions from partially-coherent processes are still important. Simulations with and without contributions from fully-coherent processes (see Figures 35b and c), however, reveal that preferential emphasis of these weaker processes is possible even at room temperature. The intended introduction of cryogenic cooling will extend coherence lifetimes by depopulating phonon modes. Longer coherence lifetimes will allow resolution of each distinct pulse sequence. Further, while the separation is not complete in the room temperature experiments reported here, the ability to selectively emphasize a weak fully-coherent process is a strong indication that the aspects of MR-CMDS techniques lost in picosecond experiments have been restored with the use of femtosecond laser pulses.

Works Cited

1. Ellingson, R. J.; Beard, M. C.; Johnson, J. C.; Yu, P.; Micic, O. I.; Nozik, A. J.; Shabaev, A.; Efros, A. Highly Efficient Multiple Exciton Generation in Colloidal PbSe and PbS Quantum

Dots. *Nano Letters* **2005,** *5* (5), 865-871.

2. Klimov, V. I. Mechanisms for Photogeneration and Recombination of Multiexcitons in Semiconductor Nanocrystals: Implications for Lasing and Solar Energy Conversion. *Journal of Physical Chemistry B* **2006,** *110* (34), 16827-16845.
3. Tyagi, P.; Kambhampati, P. False Multiple Exciton Recombination and Multiple Exciton Generation Signals in Semiconductor Quantum Dots Arise From Surface Charge Trapping. *Journal of Chemical Physics* **2011,** *134* (9), 094706-091-10.
4. Dai, Q.; Wang, Y.; Zhang, Y.; Li, X.; Li, R.; Zou, B.; Seo, J.; Wang, Y.; Liu, M.; Yu, W. W. Stability Study of PbSe Semiconductor Nanocrystals Over Concentration, Size, Atmosphere, and Light Exposure. *Langmuir* **2009,** *25* (20), 12320-12324.
5. Yurs, L. A.; Block, S. B.; Pakoulev, A. V.; Selinsky, R. S.; Jin, S.; Wright, J. C. Spectral Isolation and Measurement of Surface-Trapped State Multidimensional Nonlinear Susceptibility in Colloidal Quantum Dots. *Journal of Physical Chemistry C* **2012,** *116* (9), 5546-5553.
6. Gelin, M. F.; Pisliakov, A. V.; Egorova, D.; Domcke, W. A Simple Model for the Calculation of Nonlinear Optical Response Functions and Femtosecond Time-Resolved Spectra. *Journal of Chemical Physics* **2003,** *118* (12), 5287-5301.
7. Yurs, L. A.; Block, S. B.; Pakoulev, A. V.; Selinsky, R. S.; Jin, S.; Wright, J. C. Multiresonant Coherent Multidimensional Electronic Spectroscopy of Colloidal PbSe Quantum Dots. *Journal of Physical Chemistry C* **2011,** *115* (46), 22833-22844.
8. Wehrenberg, B. L.; Wang, C.; Guyot-Sionnest, P. Interband and Intraband Optical Studies of

PbSe Colloidal Quantum Dots. *Journal of Physical Chemistry B* **2002,** *106* (41), 10634-10640.

9. Harbold, J. M.; Du, H.; Krauss, T. D.; Cho, K.-S.; Murray, C. B. Time-Resolved Intraband Relaxation of Strongly Confined Electrons and Holes in Colloidal PbSe Nanocrystals. *Physical Review B* **2005,** *72* (19), 195312(6).
10. Schaller, R. D.; Pietryga, J. M.; Goupalov, S. V.; Petruska, M. A.; Ivanov, S. A.; Klimov, V. I. Breaking the Phonon Bottleneck in Semiconductor Nanocrystals via Multiphonon Emission Induced by Intrinsic Nonadiabatic Interactions. *Physical Review Letters* **2005,** *95,* 196401-1961-4.
11. Schaller, R. D.; Sykora, M.; Pietryga, J. M.; Klimov, V. I. Seven Excitons at a Cost of One: Redefining the Limits for Conversion Efficiency of Photons into Charge Carriers. *Nano Letters* **2006,** *6* (3), 424-429.

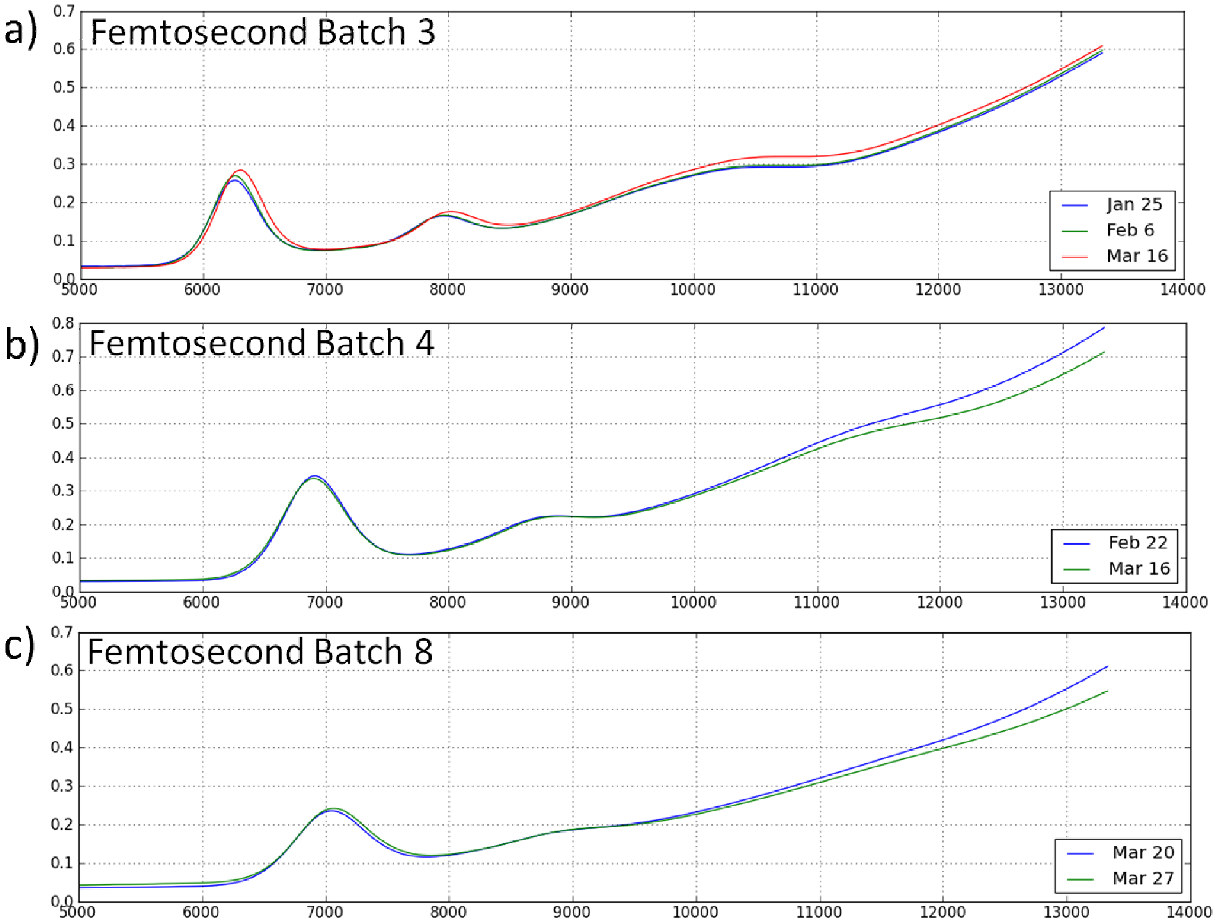

Figure 1—Linear absorption plots of the three primary samples used for this work. Samples are labeled according to the numbering records of Dan Kohler. Discussion of results refers to these samples according to these numbers. Absorption profiles were recorded for each batch on different dates to provide an indication of sample degradation rates. Images used with permission from Dan Kohler.

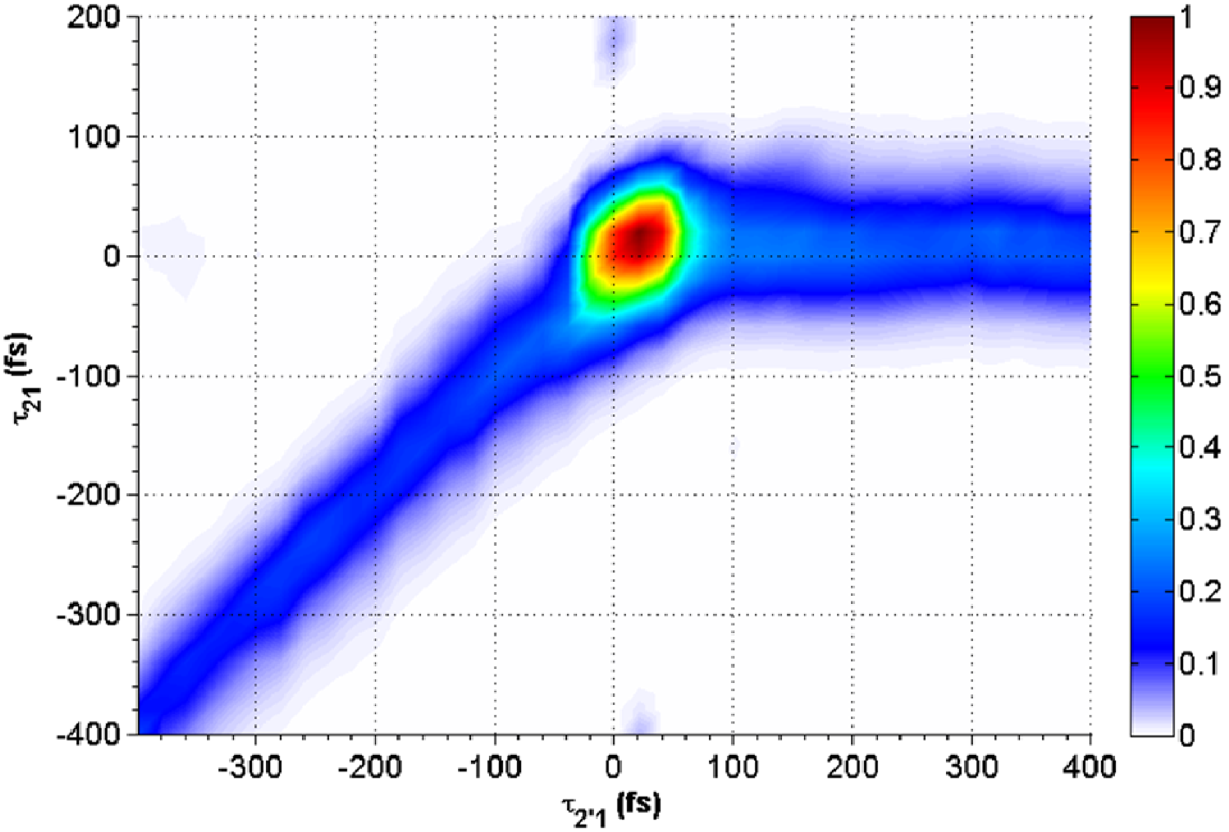

Figure 2—Early delay scan results. Here $\omega_1 = \omega_2 = \omega_m = 6620\text{cm}^{-1} = \omega_{1S}$. Long population lifetimes are visible for $\tau_{2'1} = \tau_{21} < 0$ and $\tau_{2'1} > 0$, $\tau_{21} = 0$, but appear faint and narrow compared to the sharp peak when all pulses are overlapped in time.

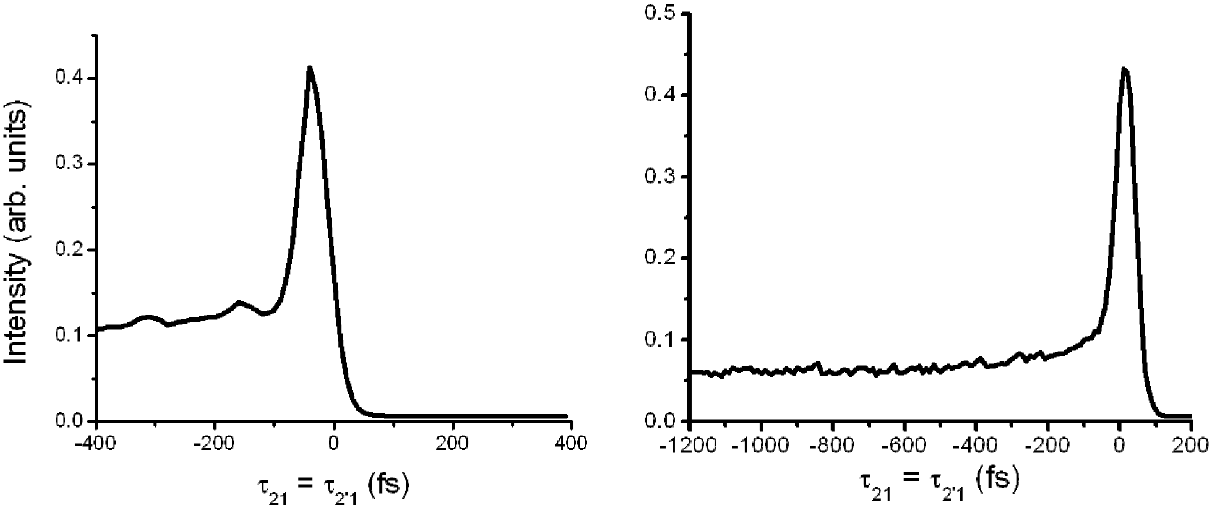

Figure 3—Population lifetime slices. $\omega_1 = \omega_2 = \omega_m = 6620 \pm 50\text{cm}^{-1} = \omega_{1S}$. Notice that the sharp peaks have slightly different positions from the calibrations on different days and that the relative size of the sharp peak and the long lifetime signal differ, likely according to undocumented precise neutral density filter position and OPA output power.

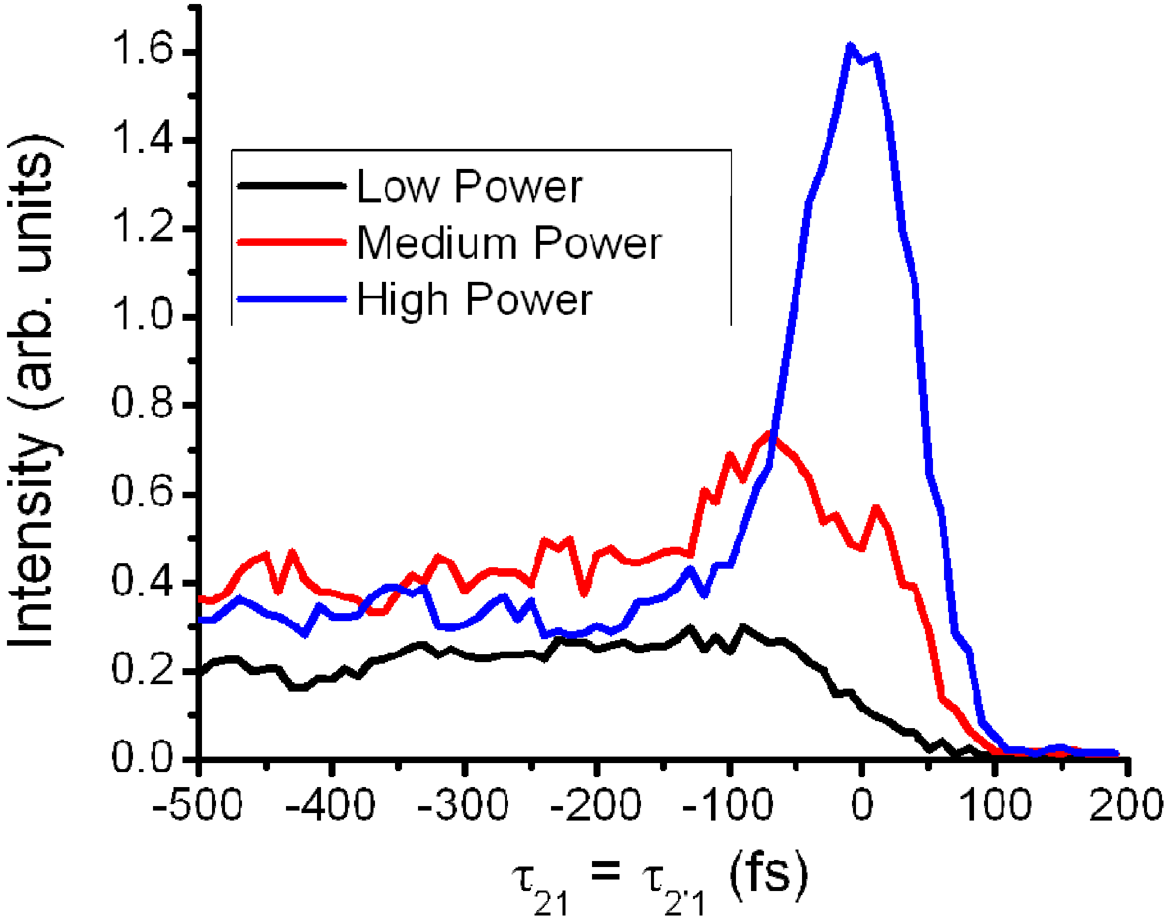

Figure 4-- Power dependence of population lifetime scans. $\omega_1 = \omega_2 = \omega_m = 6900\mathrm{cm}^{-1}$. These excitation frequencies are equal to the central frequency of the 1S exciton transition according to its drift over time. Only qualitative information regarding excitation intensity is available.

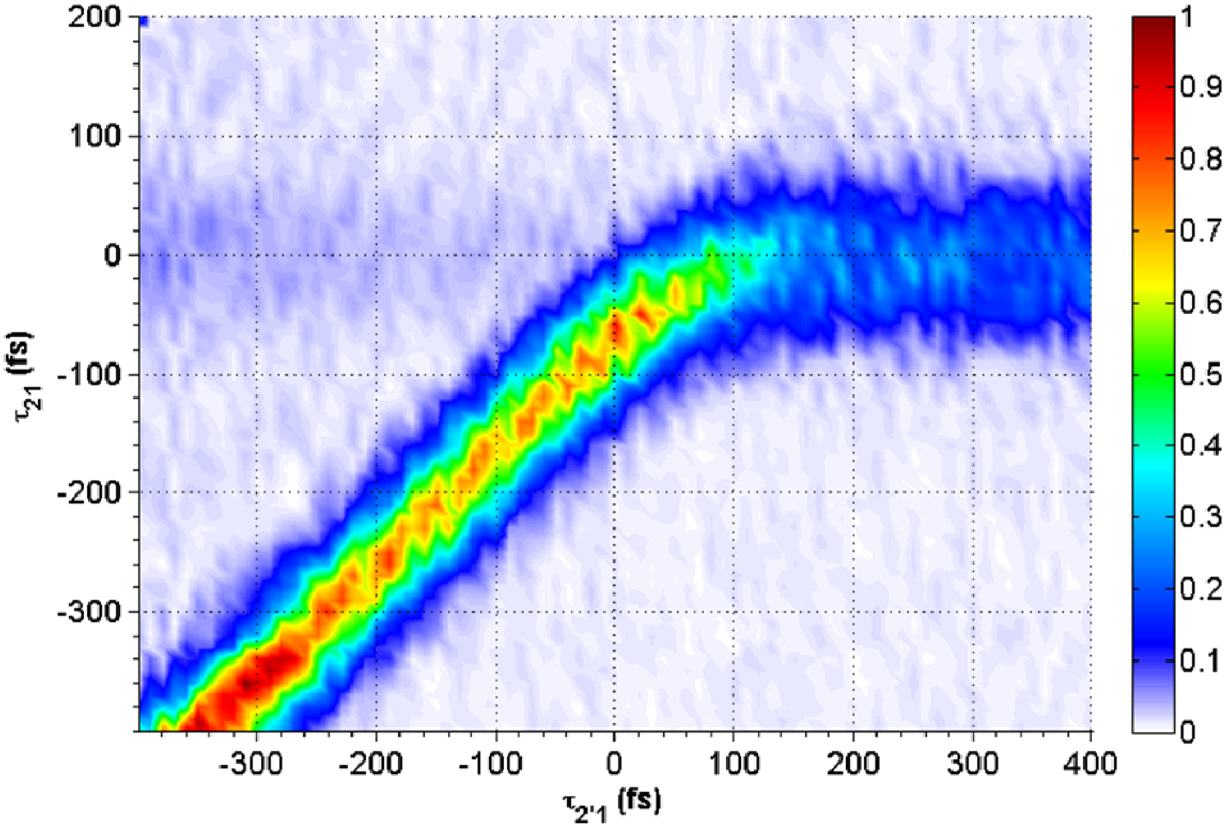

Figure 5—Delay scan at "low" intensities taken after the scans shown in Figure 3. Again $\omega_1 = \omega_2 = \omega_m = 6900\text{cm}^{-1}$. The significant shift of signal away from the $\tau_{2'1} = \tau_{21}$ diagonal is due to a calibration error briefly discussed in the text. The low signal along the $\tau_{2'1} > 0$, $\tau_{21} = 0$ axis is the result of low ω_1 intensity, and the creation of a proportionally small excited state population in the sample. The apparent increase in intensity at longer population lifetimes may be due to relaxation to a surface trap state.

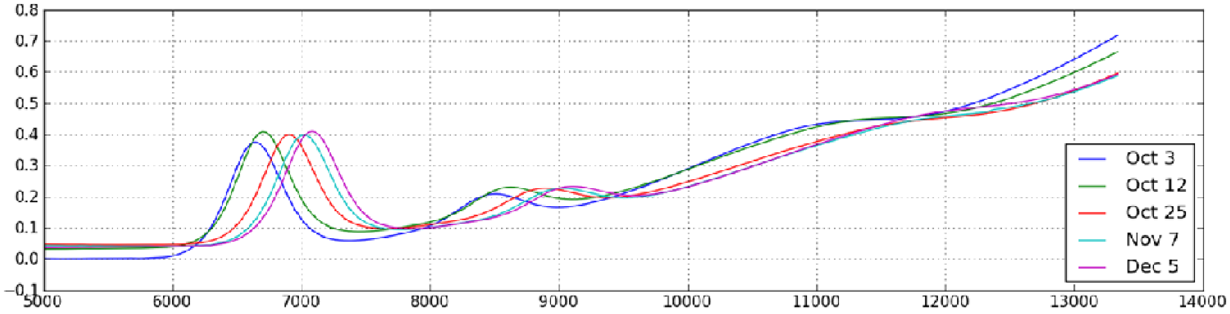

Figure 6—Femtosecond Batch 1 quantum dot absorption profiles over time. The horizontal axis is in units of wavenumbers and the vertical axis is the sample absorbance. Though experiments on this batch of quantum dots ended in early November (2011), the sample was still occasionally used for alignment, and was otherwise allowed to continue aging. The blue shift is evidence of oxidation of selenium and subsequent loss of PbSe dot volume from collisions. Image used with permission from Dan Kohler.

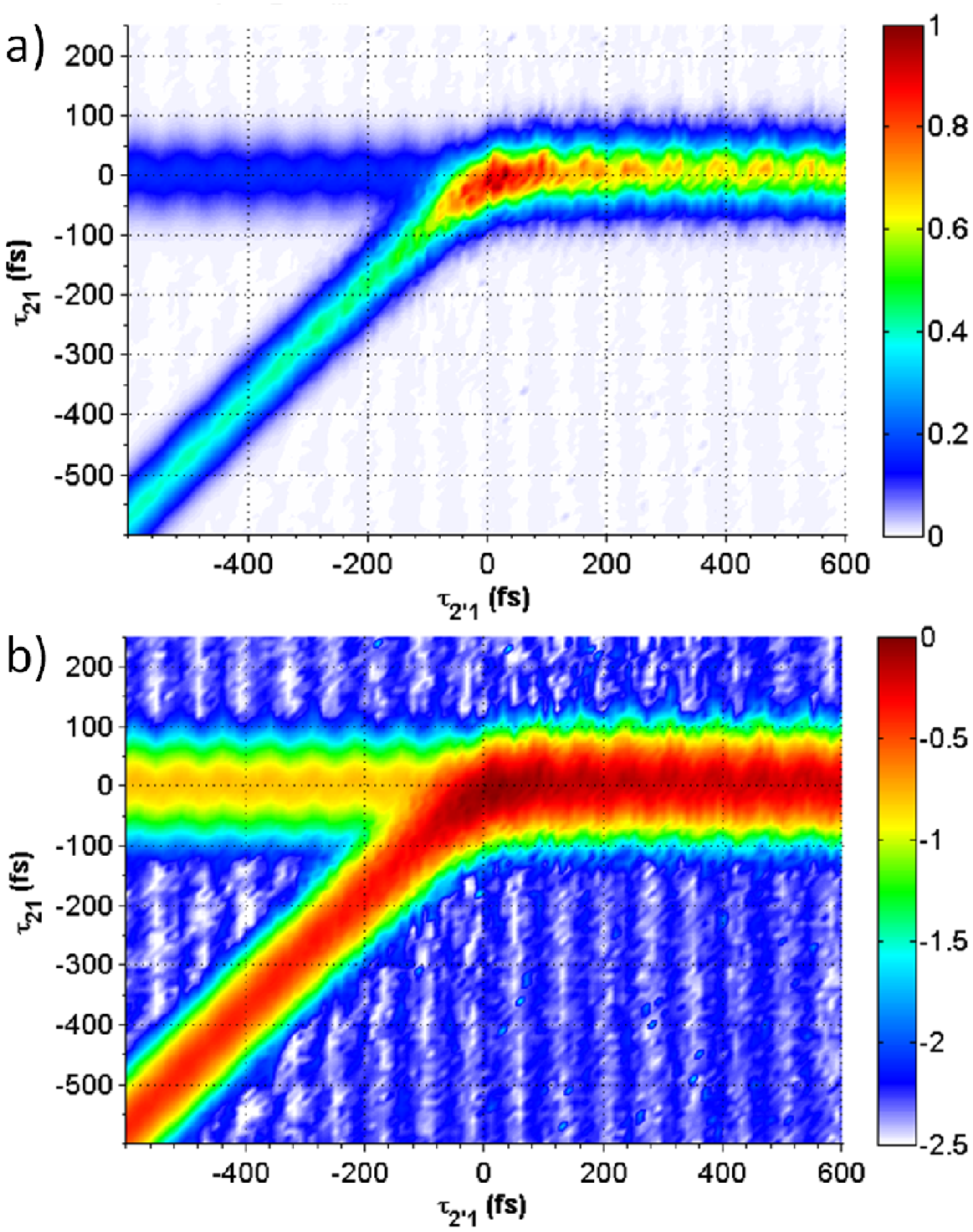

Figure 7— Two-dimensional delay scans of PbSe quantum dot Femtosecond Batch 3. Here excitation frequencies are tuned as close to the center of the 1S exciton transition frequency as tuning curves allowed: $\omega_1 = \omega_2 = \omega_m = 6350\text{cm}^{-1}$. Plots show the impacts of 28-minute air-conditioner cycles, resulting in changes in relative ω_1 and ω_2 timing and scattered light intensity. (a) Intensity shown on a linear scale. (b) The same scan shown on a logarithmic intensity scale. Scans were collected as a sequence of vertical (fixed $\tau_{2'1}$) slices.

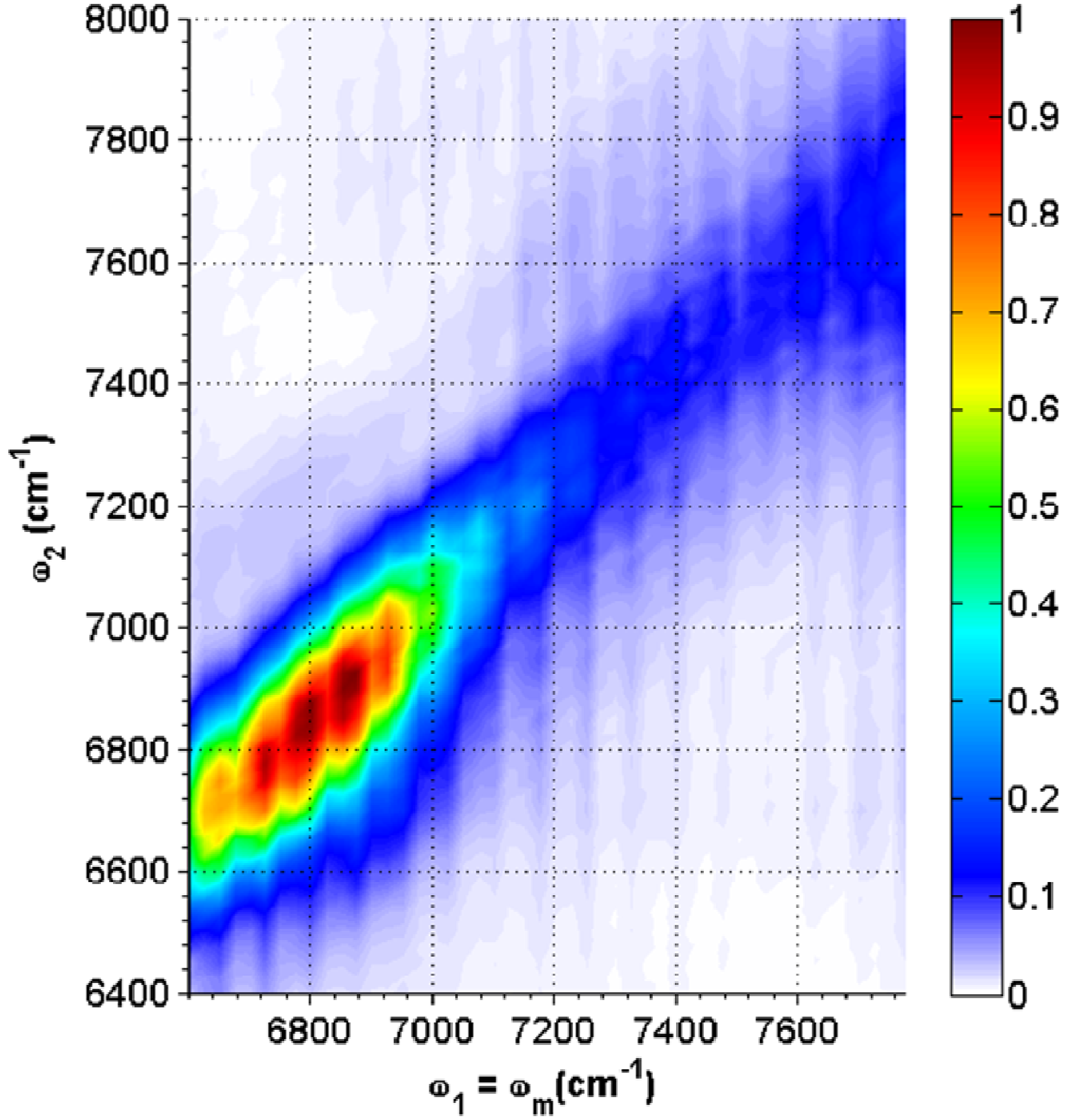

Figure 8—Two-dimensional frequency scan of PbSe quantum dot Femtosecond Batch 4. Here $\tau_{2'1} = \tau_{21} = 0$, but small temperature fluctuations cause those delay values to vary. As the delay varies, the amount of time allowed for populations to be formed changes; the sensitivity of the intensity to this grow in time is revealed by the modulations. The scan was collected as a sequence of vertical (fixed ω_1, ω_m) slices.

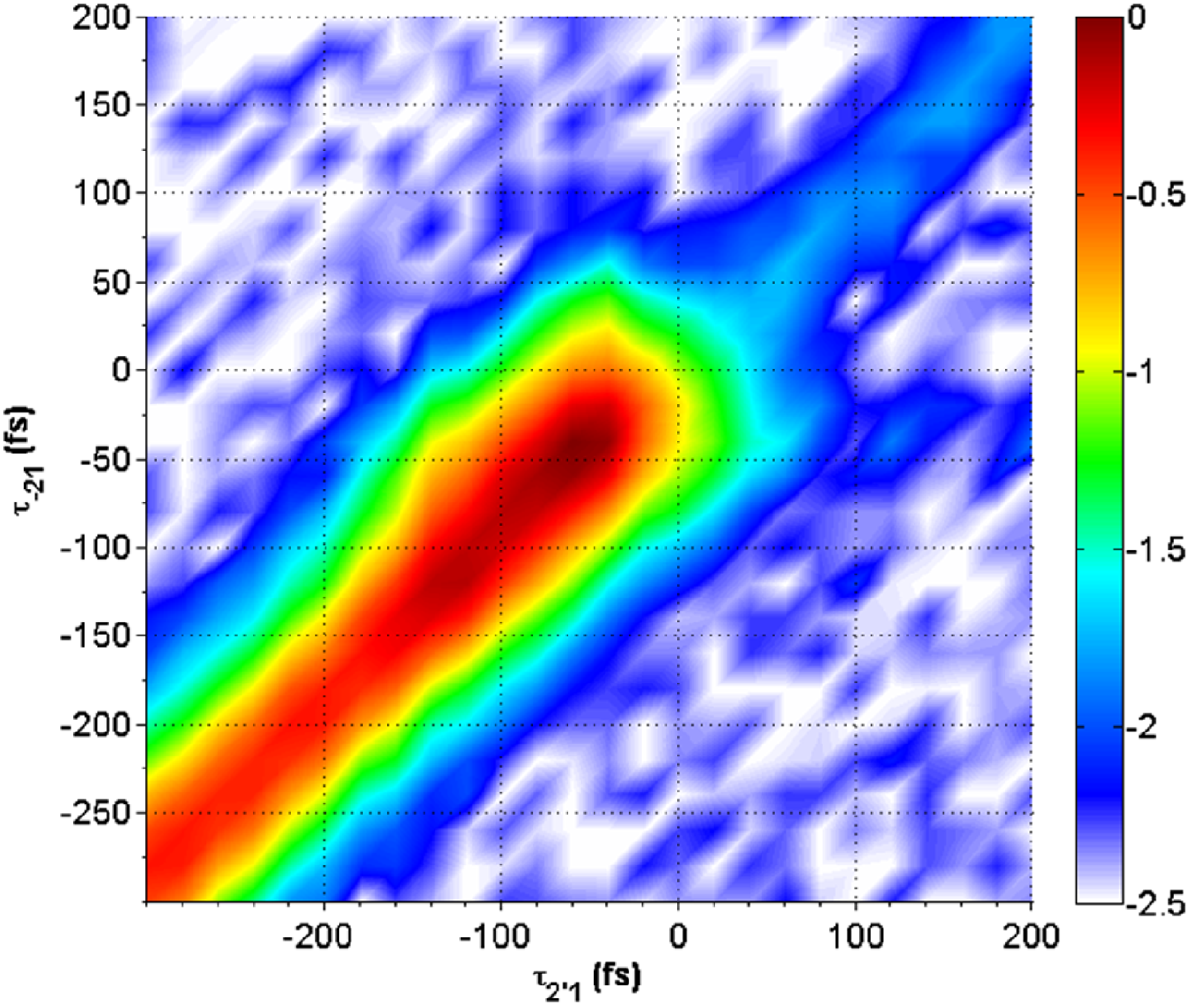

Figure 9—A two-dimensional delay scan of Femtosecond Batch 4 PbSe quantum dots. The scale shown is logarithmic to emphasize the weak signal at positive $\tau_{2'1}$ and τ_{21}. Here $\omega_1 = \omega_m = 7400\text{cm}^{-1}$ and $\omega_2 = 6600\text{cm}^{-1}$. Using the two excitation frequencies to interact with opposite tails of the 1S exciton peak strongly suppresses contributions from processes requiring ω_1 and ω_{-2} to create a population (strongest when $\tau_{2'1} > 0$ and $\tau_{21} = 0$). Further overall signal decreases increased the visibility of the signal resulting from the ω_1 echo.

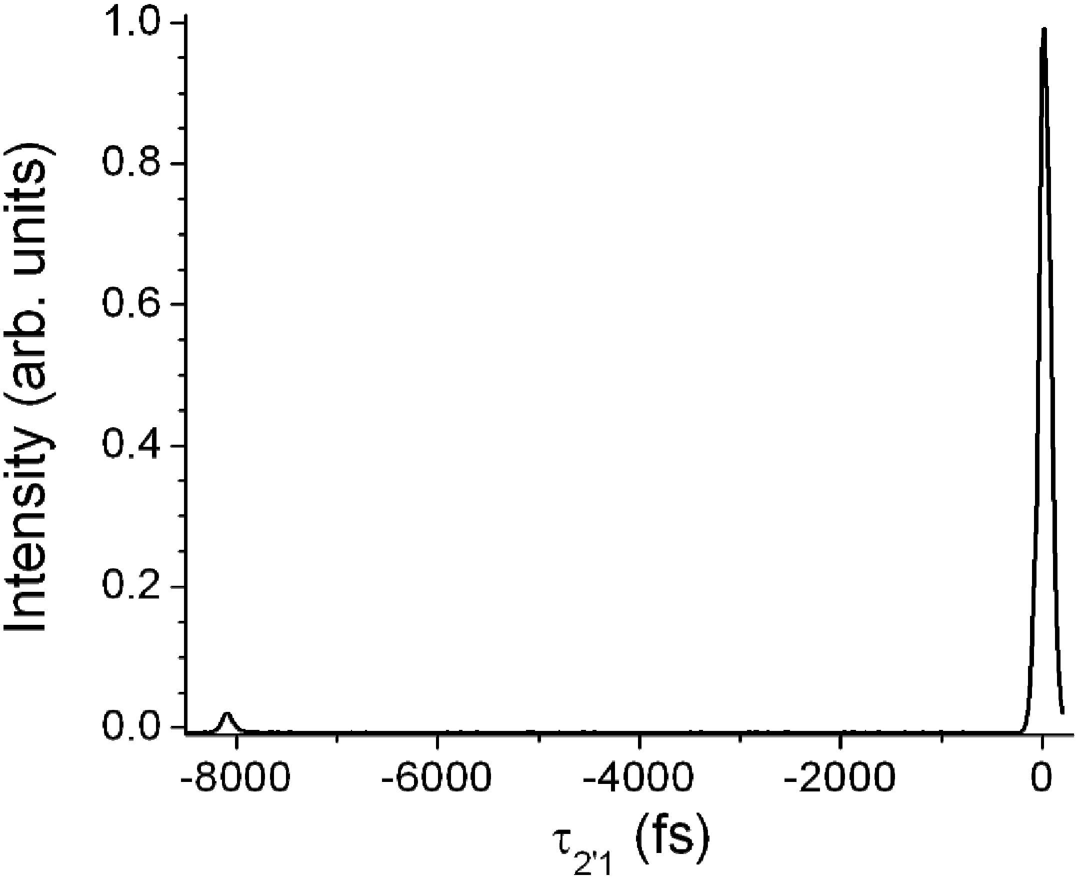

Figure 10—One-dimensional delay scan of a thin silicon wafer. Here $\omega_1 = \omega_2 = \omega_m = 7690\text{cm}^{-1}$ and $\tau_{21} = 0$. Temporal overlap of all pulses is shown at $\tau_{2'1} = 0$ and the signal due to the faint reflection of $\omega_{2'}$ is visible near $\tau_{2'1} = -8\text{ps}$. The small negative offset is due to the integrator box power supply, but the relative heights of the two peaks are still visibly about 1:20.

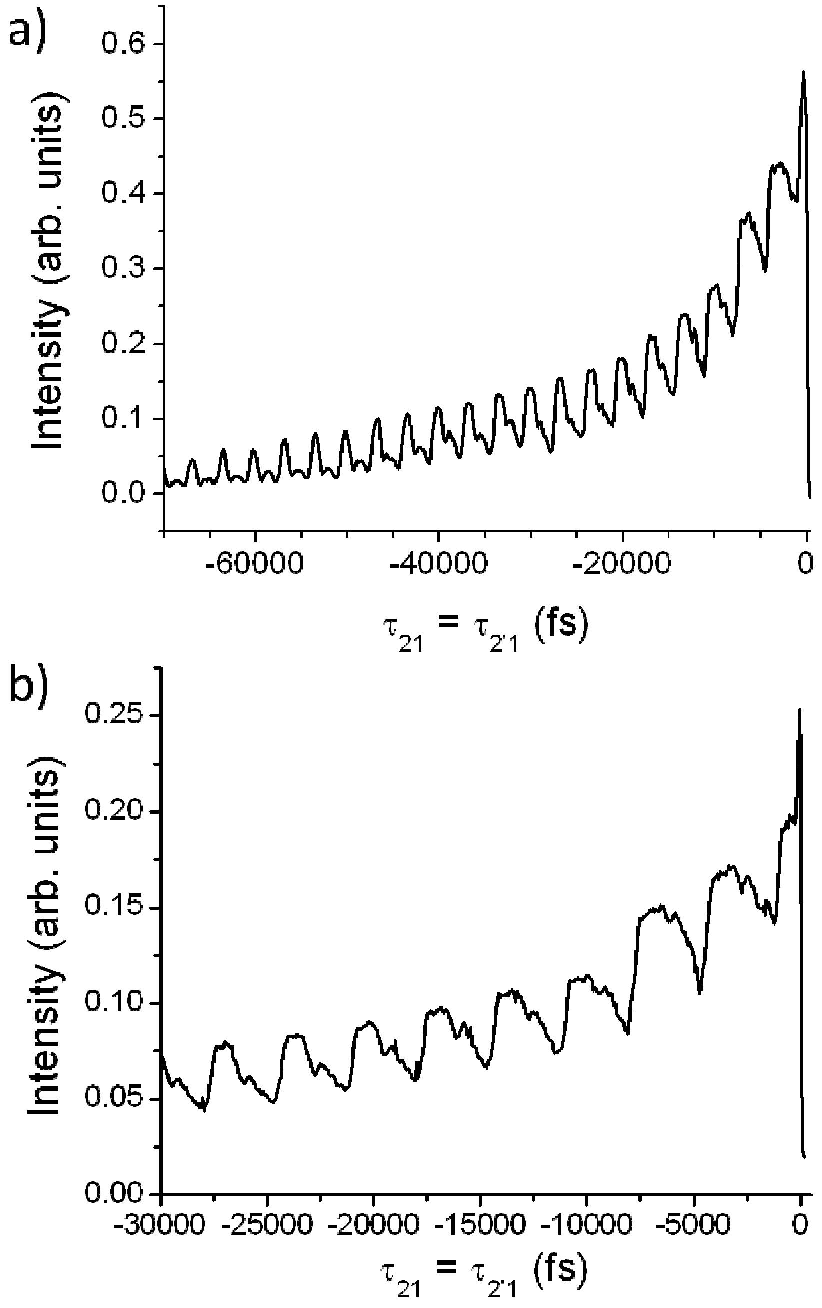

Figure 11—Population lifetime scans on Femtosecond Batch 4 revealing ~3.2ps periodic undulations. (a) $\omega_1 = \omega_2 = \omega_m = 6850\mathrm{cm}^{-1}$. This scan was collected on March 14, 2012. (b) $\omega_1 = \omega_2 = \omega_m = 6900\mathrm{cm}^{-1}$. This scan was collected on March 16, 2012. Both scans show the same artifact. Daily alignment procedures did not seem to disrupt the pattern.

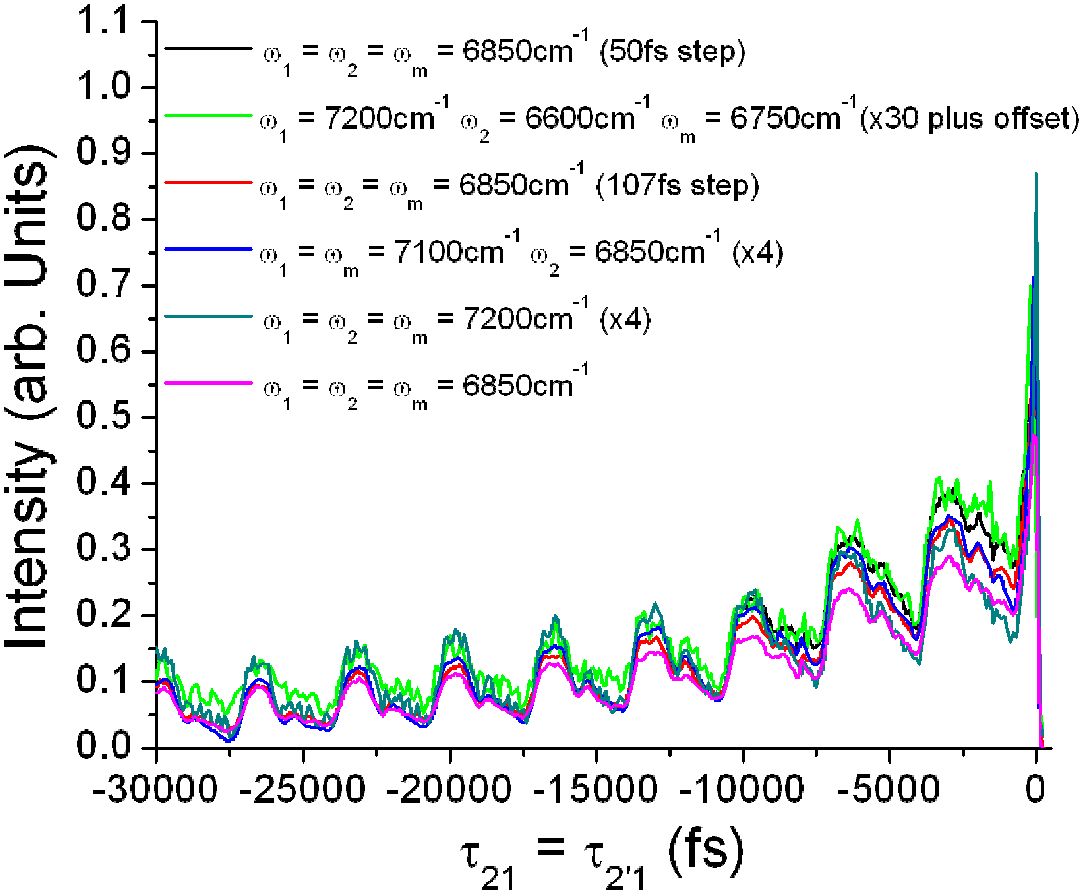

Figure 12—Population lifetime scans taken of Femtosecond Batch 4 on March 13, 2012. The modulation frequency shows no dependence on excitation frequency or step size. Vertical offset and scaling were introduced as labeled to demonstrate the invariability to scan parameter alterations.

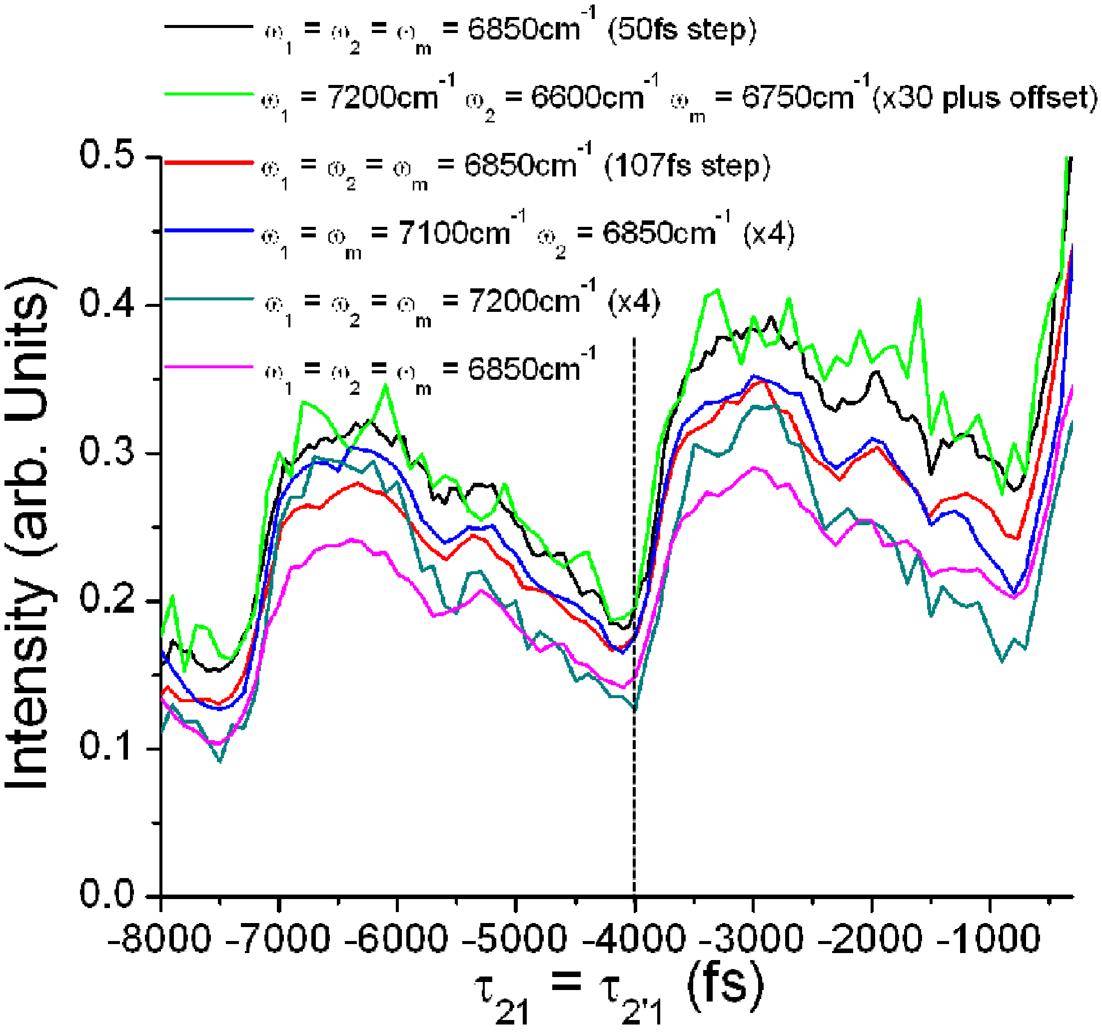

Figure 13—A subsection of the scan shown in Figure 12. Here the modulation phase shows no dependence on excitation frequency or step size. The vertical dashed line at $\tau_{2'1} = \tau_{21} = -4000$fs serves to show the phase of the modulation at that delay for comparison with the phase shown in Figure 14.

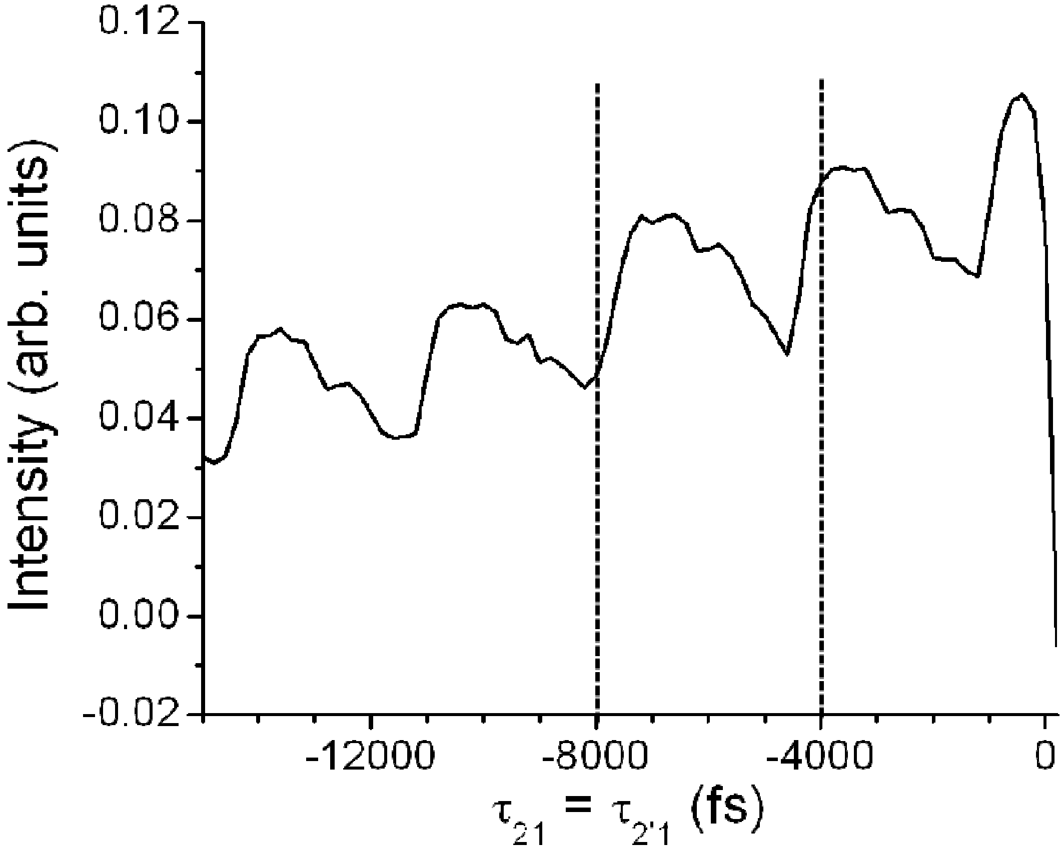

Figure 14— Population lifetime scans on Femtosecond Batch 4 taken on March 21, 2012. Here $\omega_1 = \omega_2 = \omega_m = 6900\text{cm}^{-1}$. Vertical dashed lines are included for ease of comparison with the modulation phase at the same delay values in Figure 13. The shift of ~600fs can be produced by an ω_1 retroreflector actuator position change of 90μm—well within the range that could be estimated from full realignment from one week to the next.

Parameter	Figure 15-18, 19-21	Figure 28b Values
$\Gamma_{eg} = \Gamma_{2e,e}$	.02 fs^{-1}	.022 fs^{-1}
$\Gamma_{ee} = \Gamma_{gg}$	.0003 fs^{-1}	.0009 fs^{-1}
$\Gamma_{2e,g}$	.052 fs^{-1}	.057 fs^{-1}
$2\omega_{eg} - \omega_{2e,g}$ (Coulombic coupling)	120 cm^{-1}	120 cm^{-1}
$\mu_{2e,e}/\mu_{eg}$	1.4	1.4
$\sigma_{\text{excitation pulse}}$	21 fs	ω_1, ω_{-2}: 21fs; $\omega_{2'}$: 25fs

Table 1— Table showing delay simulation parameters used for qualitative comparison of various effects (middle column). Values were chosen to match common PbSe quantum dot characteristics and femtosecond system instrumentation parameters. (Right column) Parameter values used for the best fit of data shown in Figure 28a.

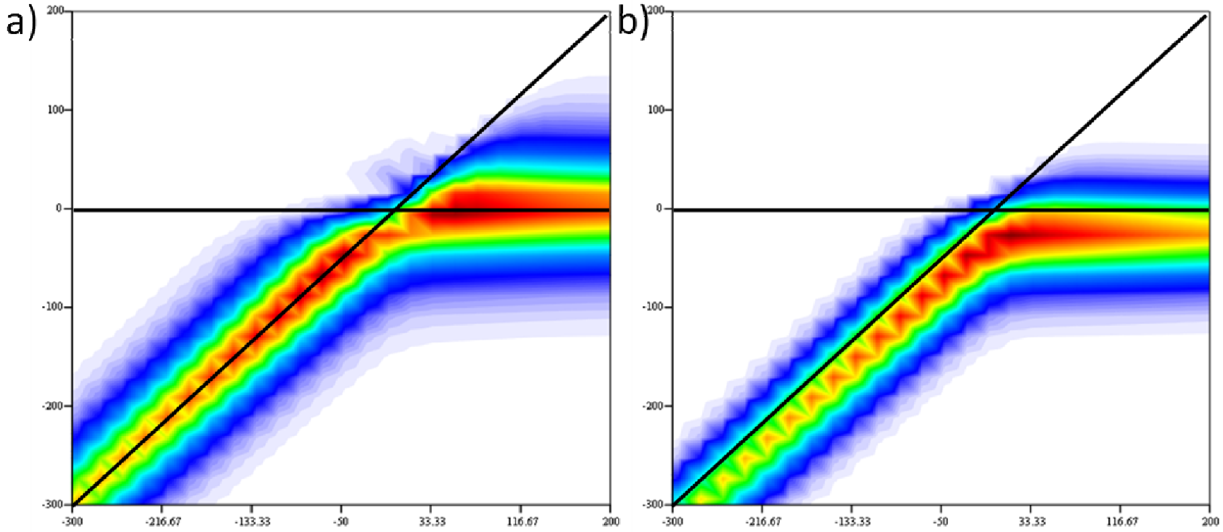

Figure 15—Two-dimensional delay scan simulations demonstrating the effects of inhomogeneous broadening. Axes represent the time delay ranges commonly used in experiments (200fs to -300fs). Delays corresponding to pulse overlap in time are shown by the added black lines for $\omega_{-2}/\omega_{2'}$ (diagonal) and ω_{-2}/ω_1 (horizontal). (a) No inhomogeneous broadening. Near zero delay (the intersection point of the two black lines), the intensity dips due to interference between multiple fully-coherent processes. (b) Inhomogeneous broadening simulated by a Gaussian distribution of quantum dot transition energies (σ = 600cm^{-1}) has been added. The shift away from the lines indicating perfect pulse overlap reveals preference for rephasing pathways. The dip near zero delay has disappeared because of the shift away from the pulse time-orderings that produce the fully coherent processes.

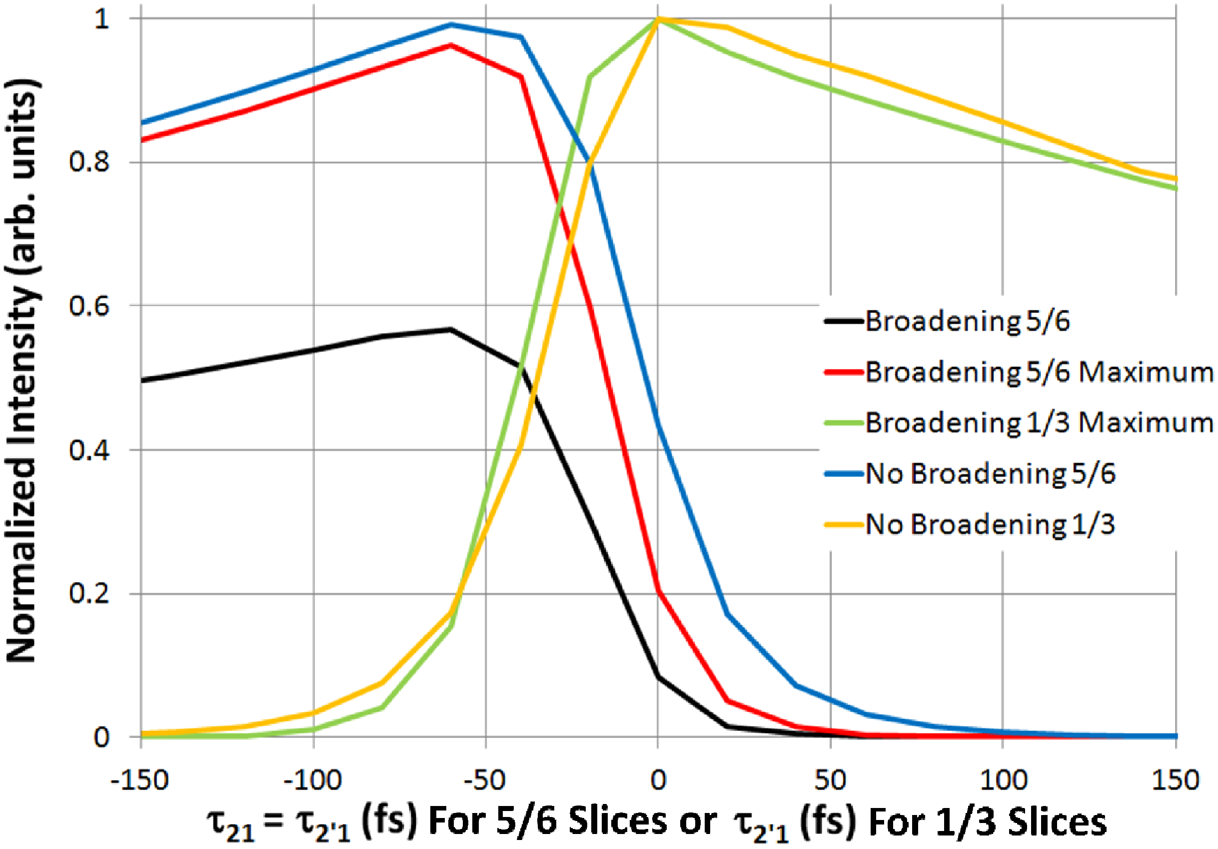

Figure 16—Cross-sections of the scans in Figure 15 showing population behavior. Traces compare population behavior observed in the presence of inhomogeneous broadening shifts (black, red, and green) and in their absence (blue and orange). The labels used correspond to the pulse time orderings described in the Theory section. Traces also show the possible intensity difference between a population lifetime scan taken with $\tau_{21} = \tau_{2'1}$ (black) and taken along the peak maximum, offset from the diagonal (red). The grow-in times for pathway 5/6 scans are not significantly dependent on the presence or absence of broadening.

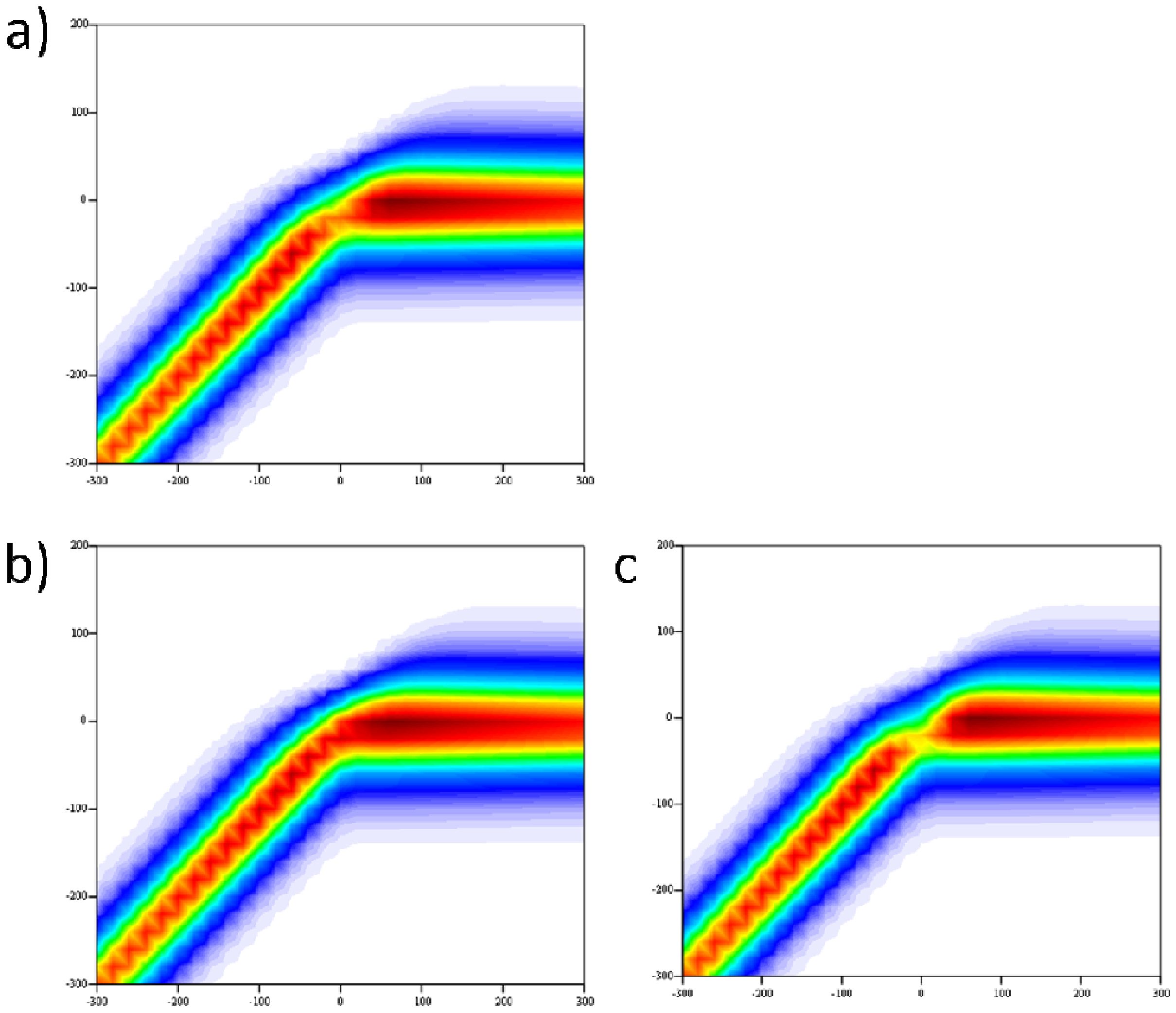

Figure 17—Two-dimensional delay scans comparing (a) the absence of non-resonant background signal with (b) constructive non-resonant contributions and (c) destructive non-resonant contributions. Axes represent the time delay ranges commonly used in experiments (200fs to -300fs).

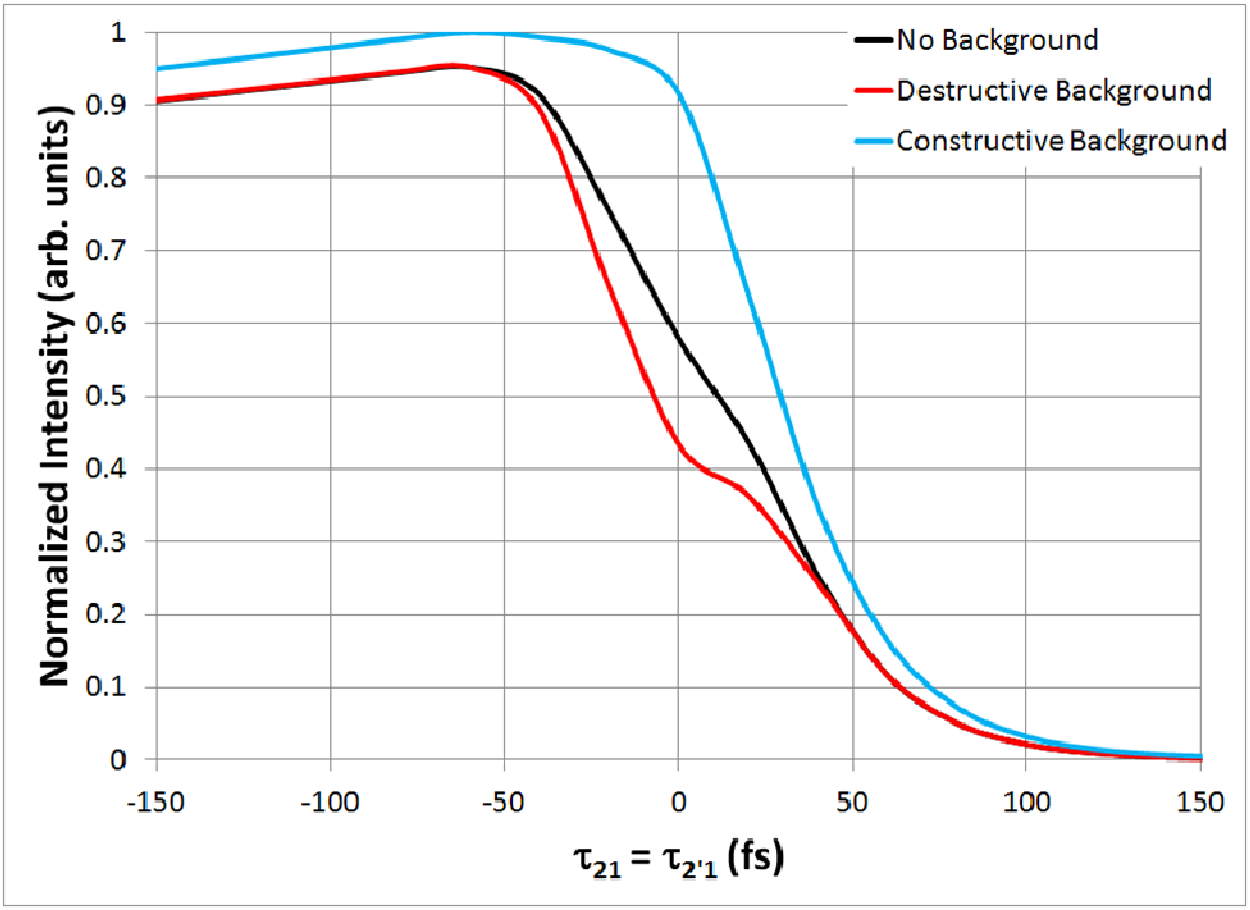

Figure 18—Population lifetime profiles highlighting the effects of non-resonant four-wave mixing interference. Vanishingly short state lifetimes for highly-detuned solvent and non-confined PbSe electronic state transitions isolate contributions to delays that overlap all three pulses in time. Constructive interference can give the appearance of reducing the population grow-in time. Destructive interference suppresses early population-time signal, potentially producing a shoulder in the rising slope.

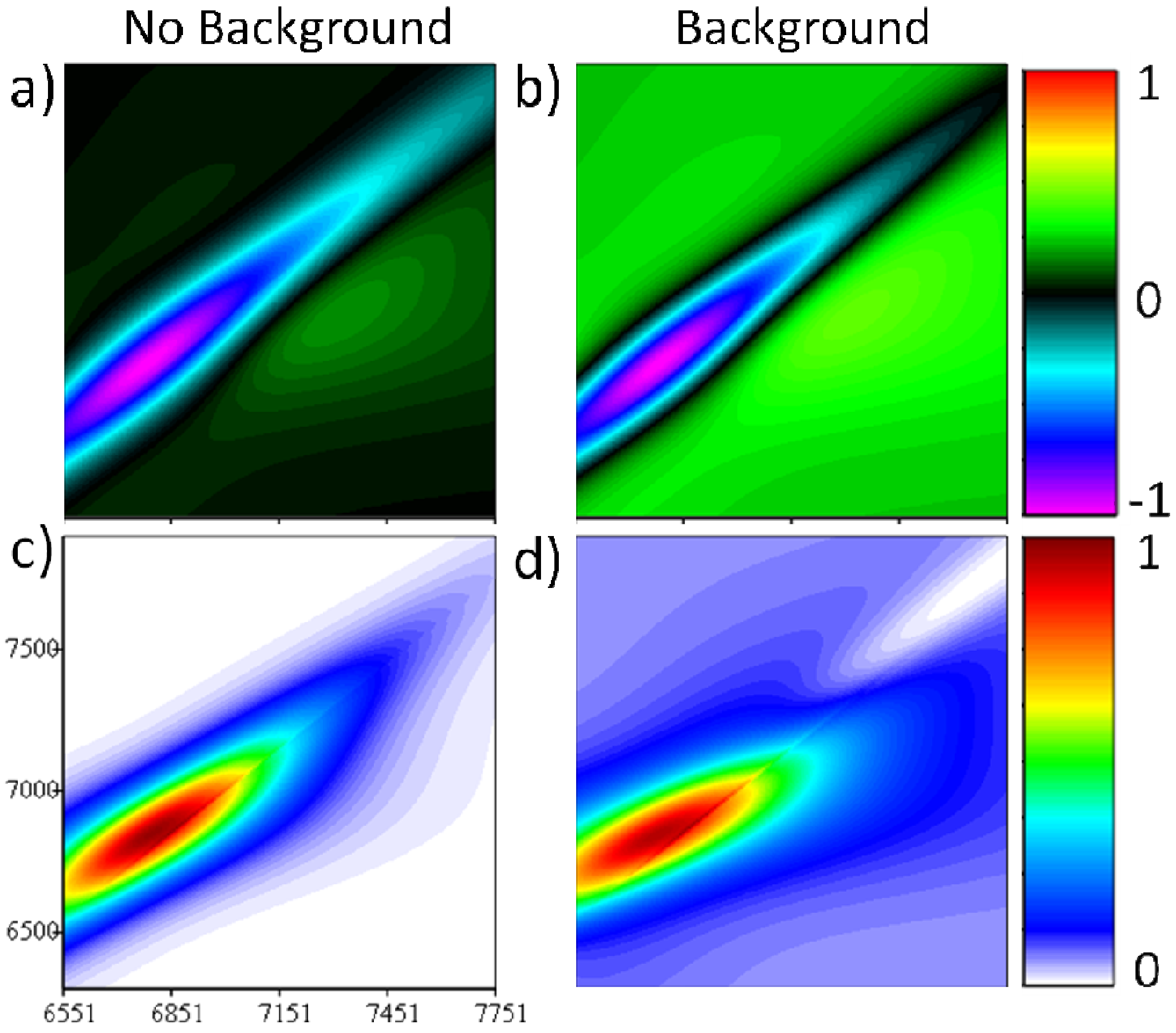

Figure 19—Two-dimensional frequency plots simulating a 1S exciton peak created when all pulses are overlapped in time. (a) and (b) show the real portion of the sample polarization with and without the addition of non-resonant signal contributions. (c) and (d) show the manifestation of these contributions on experiments that can only observe electric field intensities. Signal produced near-resonance with the 1S transition experiences destructive interference with the constant background; some signal shifted away from the 1S feature experienced constructive interference.

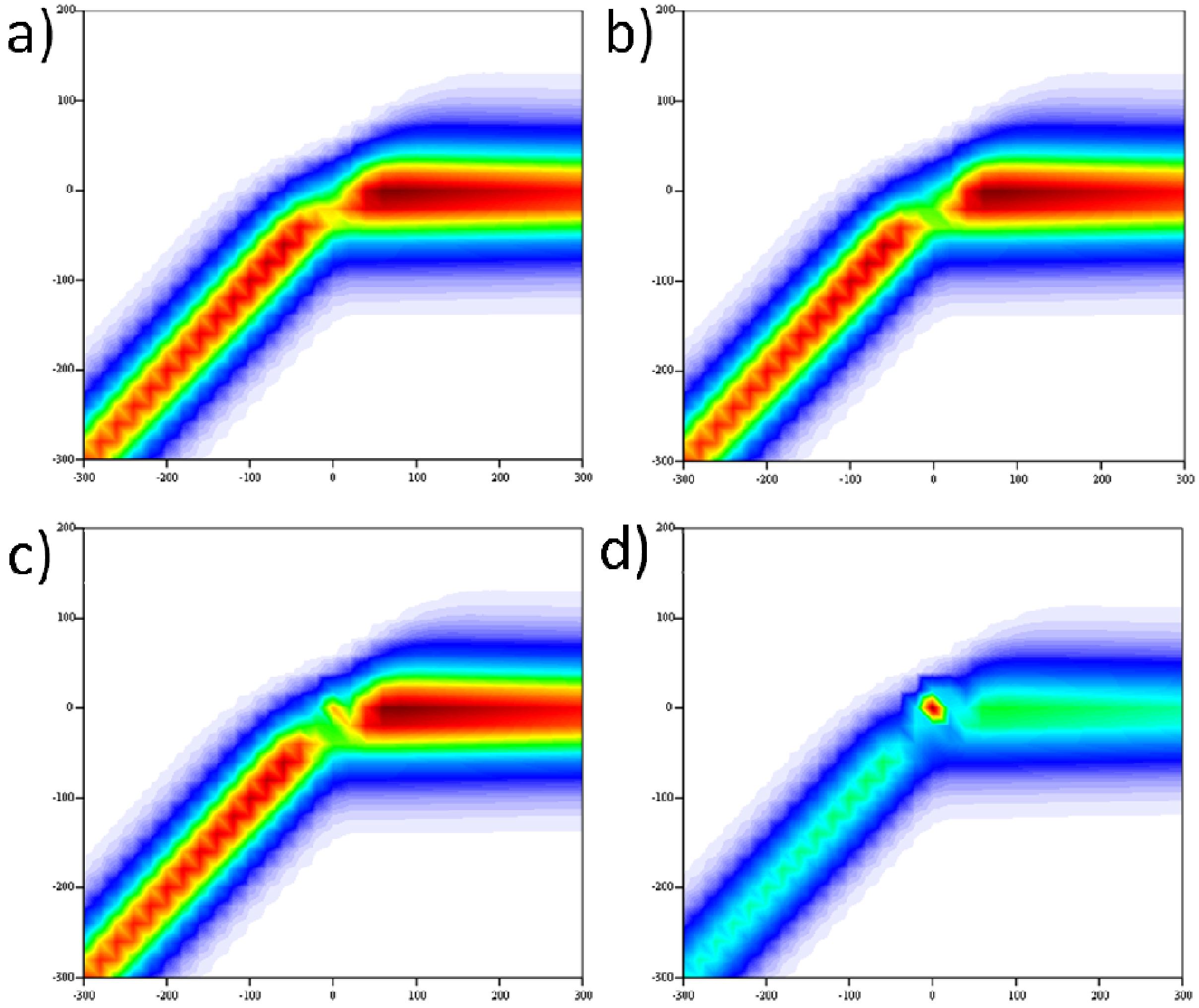

Figure 20— Two-dimensional delay scans comparing relative influence of non-resonant signal contributions. (a) The magnitude of the non-resonant signal matches that in Figure 17c. The relative intensity of the resonant signal is then decreased by a factor of (b) 4, (c) 8, and (d) 16. Over the range of a frequency-domain experiment, the resonant signal intensities can change by these factors or more. Axes again represent the time delay ranges commonly used in experiments (200fs to -300fs).

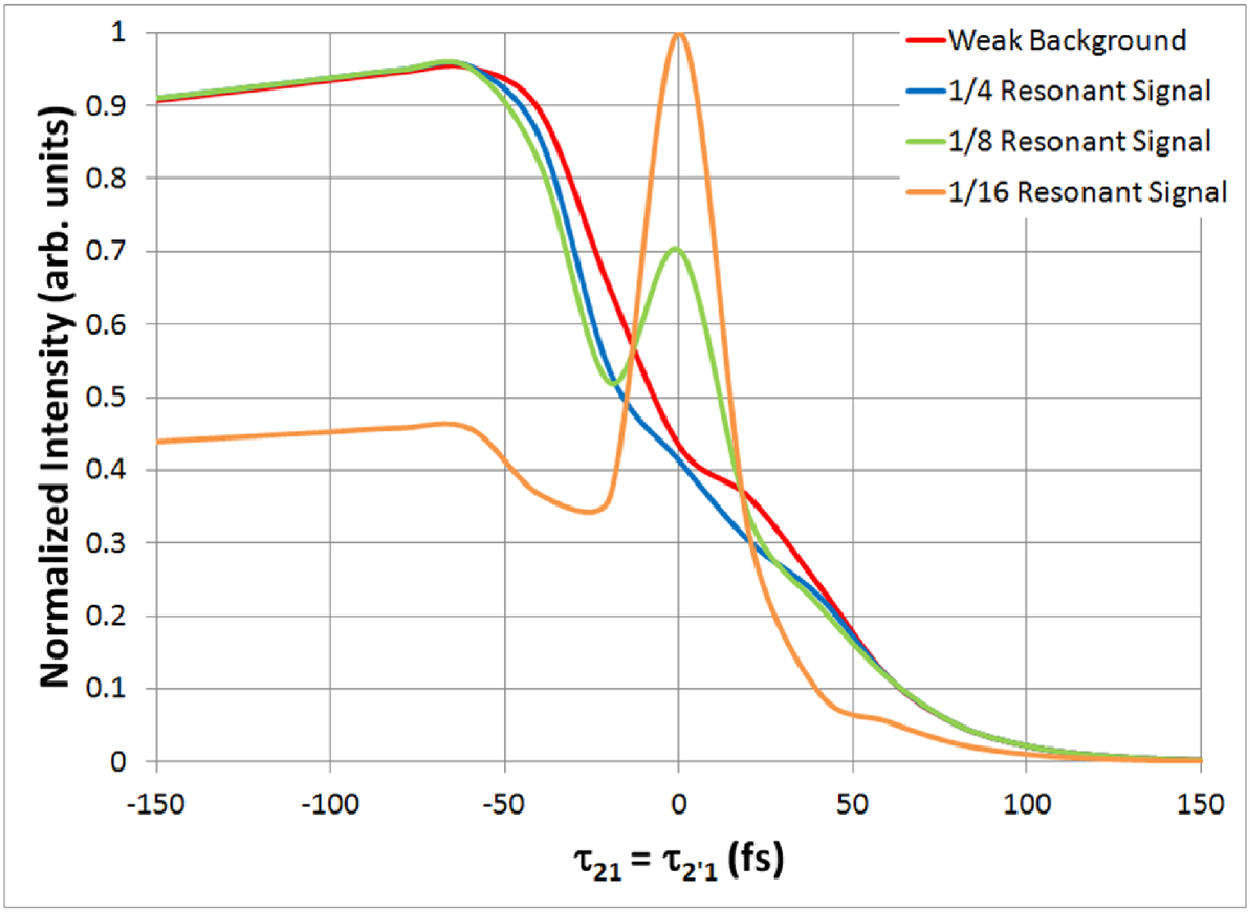

Figure 21— Population lifetime profiles revealing the qualitative effects of varying relative non-resonant/resonant four-wave mixing intensities, as shown in Figure 20. Notice that the rising slope can have a shoulder (red), two shoulders as the non-resonant contribution becomes more significant (blue), or a distinct peak (green). At very low resonant signal intensities, the delay profile can appear to decay quickly and grow back in.

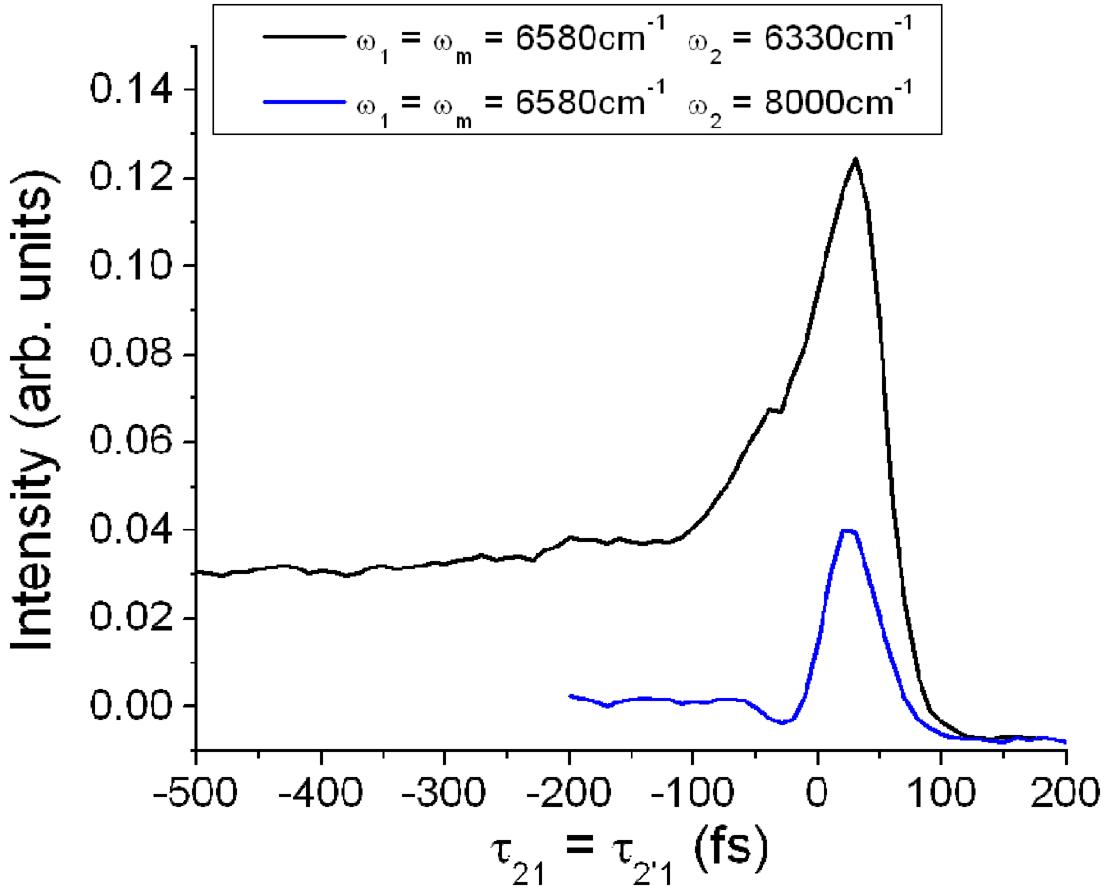

Figure 22—A pair of population decay profiles for PbSe quantum dot Femtosecond Batch 3. $\omega_{2'}$ and ω_{-2} pulse energies were below the fluences required for significant multiexciton generation at both frequencies (at 6330cm^{-1} energies were 200nJ and 500nJ, respectively; at 8000cm^{-1} they were 400nJ and 250nJ). ω_1 pulse fluence was high enough for the average number of photons absorbed by each quantum dot to be 1.5 (pulse energy ~1000nJ), suggesting the possibility of some multiphoton absorption processes. Here the delay calibration procedures were not yet optimized, so the location of the zero delay peak is shifted.

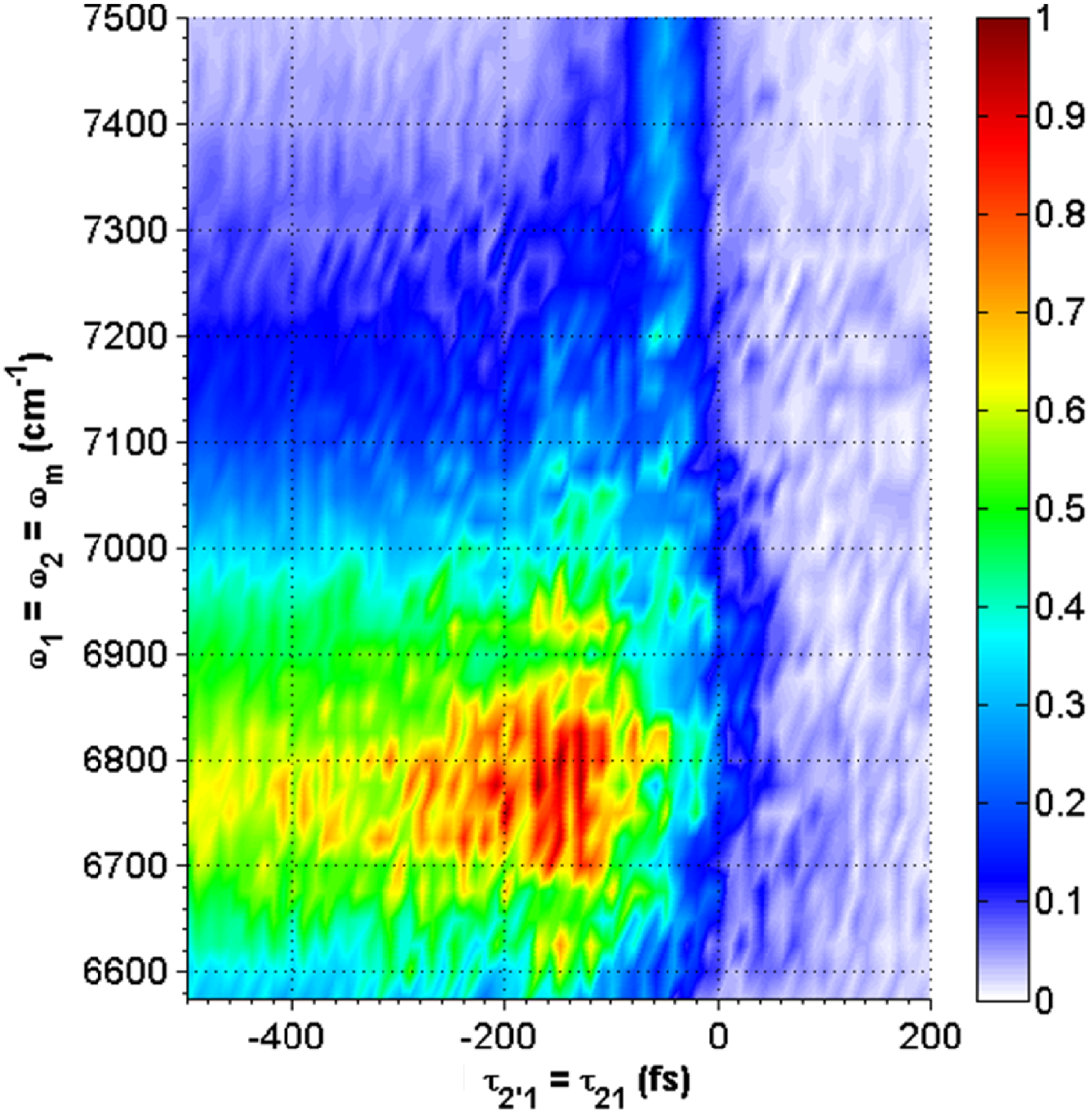

Figure 23—Population lifetime profiles near the 1S exciton transition of PbSe quantum dot Femtosecond Batch 8. The weak signal high $\omega_1 = \omega_2 = \omega_m$ and $\tau_{21} = \tau_{2'1}$ = -40fs results from non-resonant contributions that stand out against the background when there is no appreciable resonant signal. The 40fs shift results from an unknown delay miscalibration.

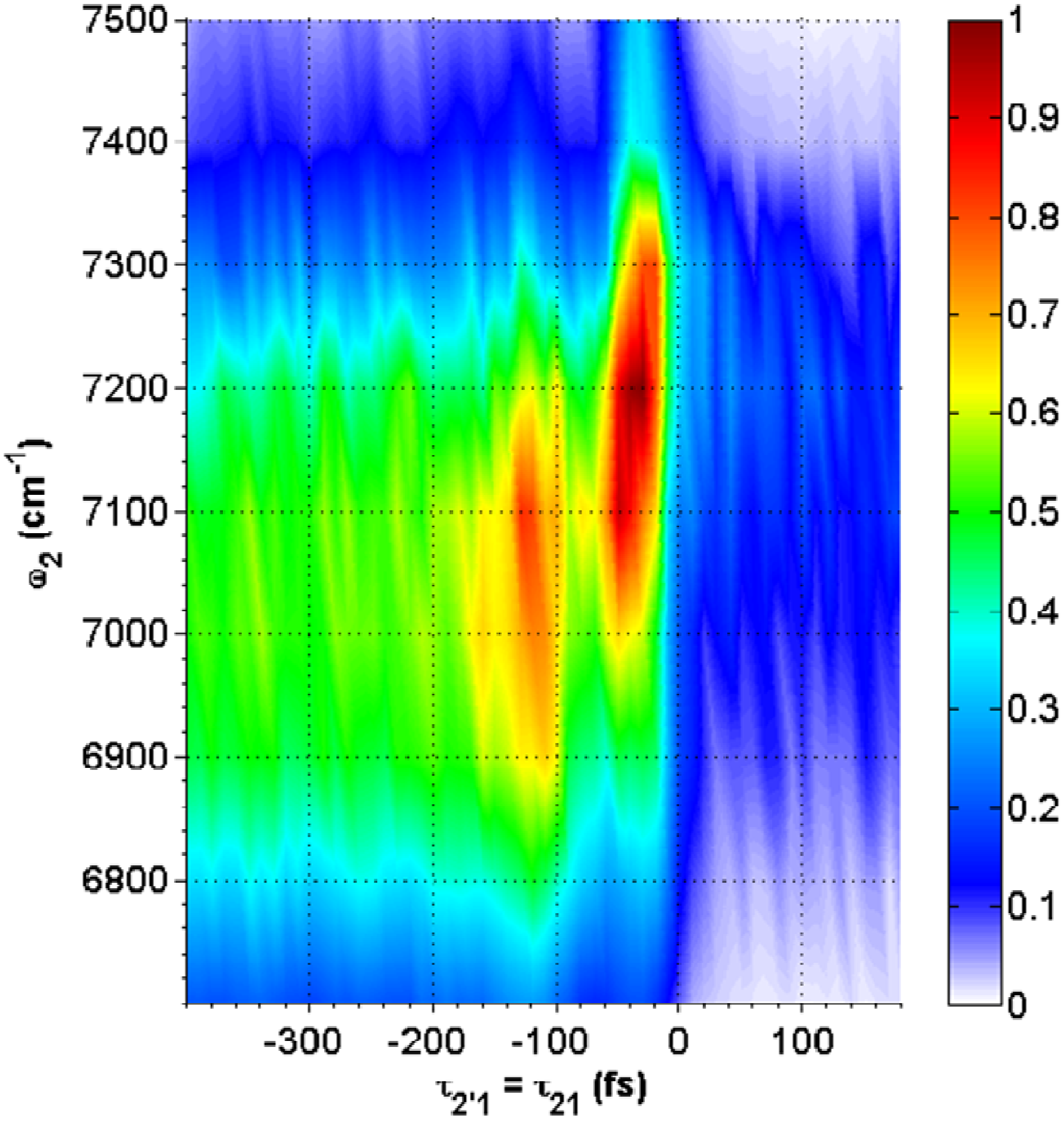

Figure 24— Population lifetime profiles to the blue of the 1S exciton transition of PbSe quantum dot Femtosecond Batch 4. Here $\omega_1 = \omega_m = 7200\text{cm}^{-1}$, more than 300cm^{-1} higher than the center of the 1S exciton transition. ω_2 values provide optimal signal at longer delays when compromising between interacting with a high number of dots (as revealed by the Gaussian distribution of the 1S exciton transition) and with the dots more efficiently accessed by ω_1. Sharp non-resonant signal is visible at short delays. Positive delay times show scattered light when $\omega_2 = \omega_m$.

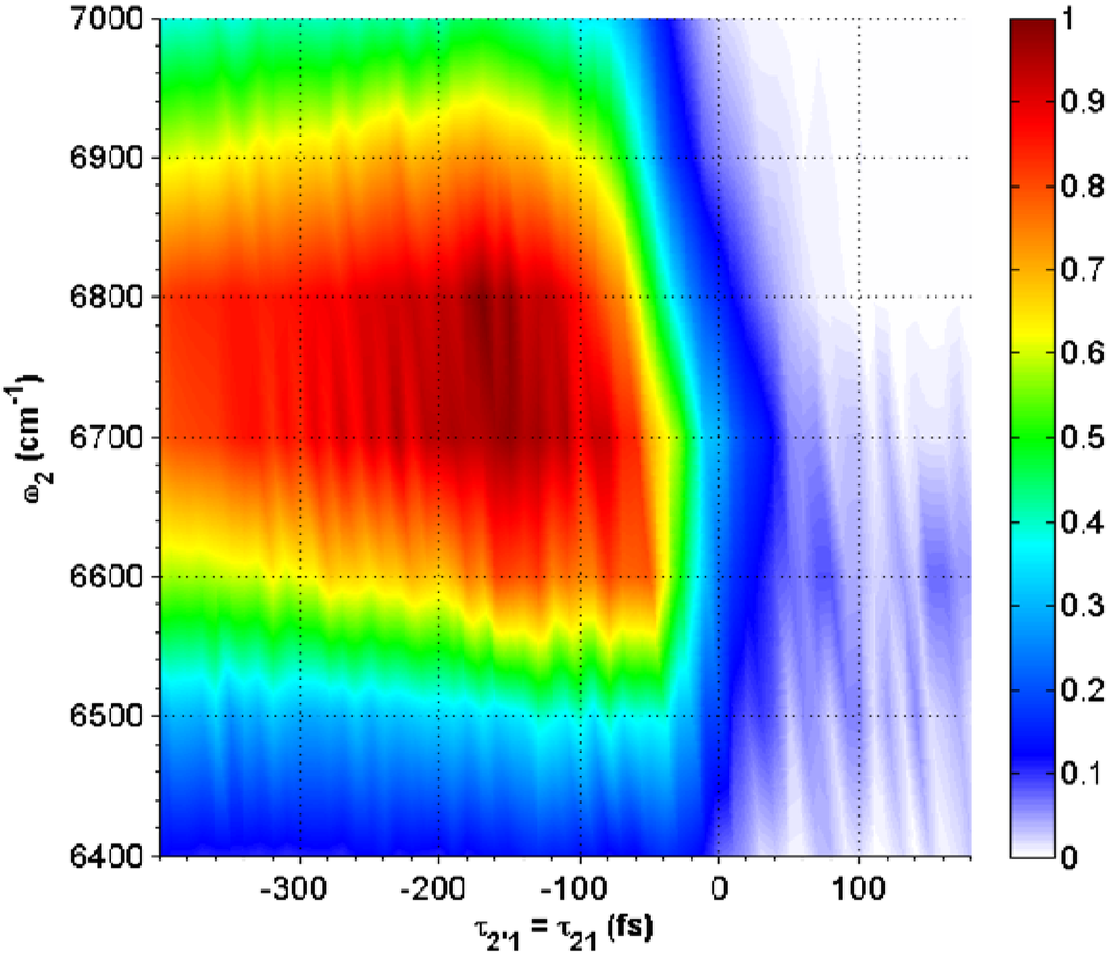

Figure 25— Population lifetime profiles to the red of the 1S exciton transition of PbSe quantum dot Femtosecond Batch 4. Here $\omega_1 = \omega_m = 6600\text{cm}^{-1}$, almost 300cm^{-1} lower than the center of the 1S exciton transition. Again, ω_2 values provide optimal signal at longer delays when compromising between interacting with a high number of dots and with the dots more efficiently accessed by ω_1. Here no significant sharp non-resonant signal is visible at short delays, as predicted by the high resonant signal found when ω_1 is shifted to the red of ω_2 near a resonant feature (see Figure 19). Again, positive delay times show scattered light when $\omega_2 = \omega_m$.

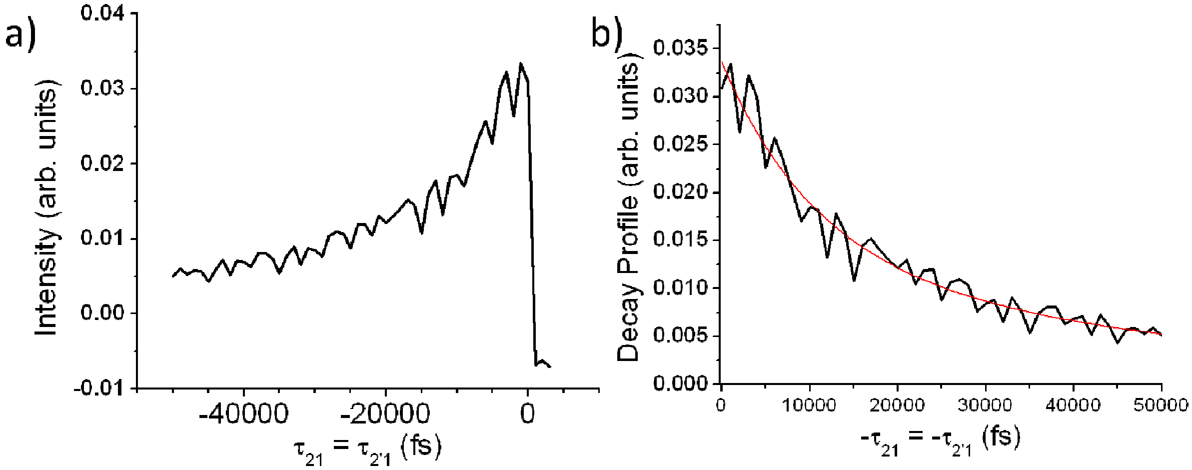

Figure 26— A population decay profile for PbSe quantum dot Femtosecond Batch 8 (a) and the fit to that decay profile (b). Here $\omega_1 = \omega_2 = \omega_m = 6900\text{cm}^{-1}$ and pulse fluences were chosen minimize multiphoton effects. The alignment was such that the ~3ps modulation artifact was not significant. The biexponential decay fit has a primary contribution with a lifetime of 11ps and a lesser contribution with a lifetime of 70ps (though slight adjustments of contribution magnitudes allow this second lifetime to be much longer without significant loss of fit quality).

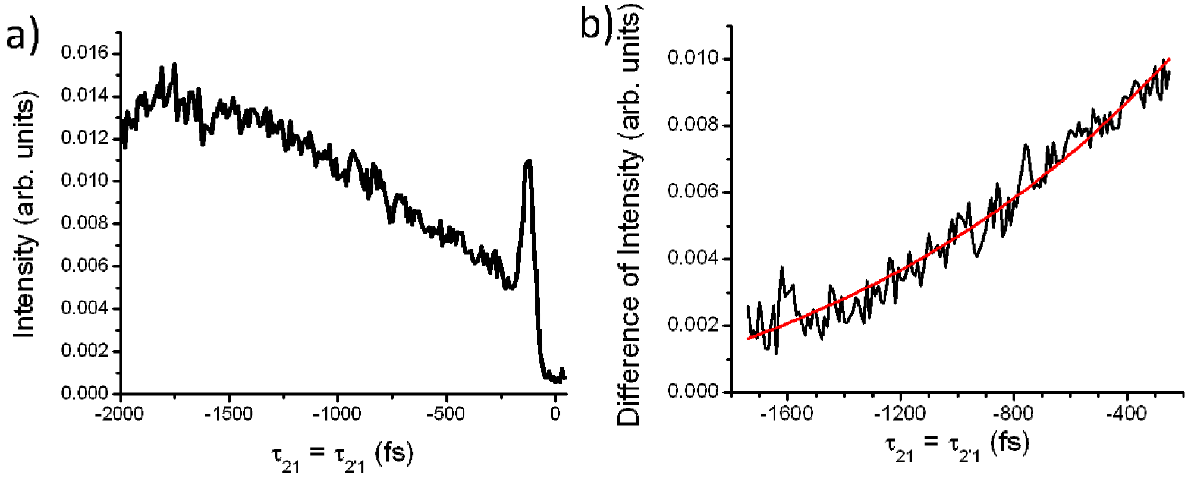

Figure 27— A population transfer profile for PbSe quantum dot Femtosecond Batch 3 (a) and the fit to that profile (b). Here $\omega_1 = \omega_m = 6450\text{cm}^{-1}$ (near resonance with the 1S exciton transition) and $\omega_2 = 7840\text{cm}^{-1}$ (on resonance with the 1P exciton transition). The sharp peak at early time delays corresponds to the appearance of non-resonant contributions, made visible by the weakness of the resonant feature at these excitation frequencies. The grow-in (isolated and fit to a single exponential in (b)) corresponds to the relaxation of the 1P exciton electron and/or hole to the 1S state and has a lifetime of 1.4ps. The intensity decrease at $\tau_{21} = \tau_{2'1} = -1800$fs is likely due to the 3ps cycle of pitch/yaw on the delay stages. The exponential fit excludes these data points.

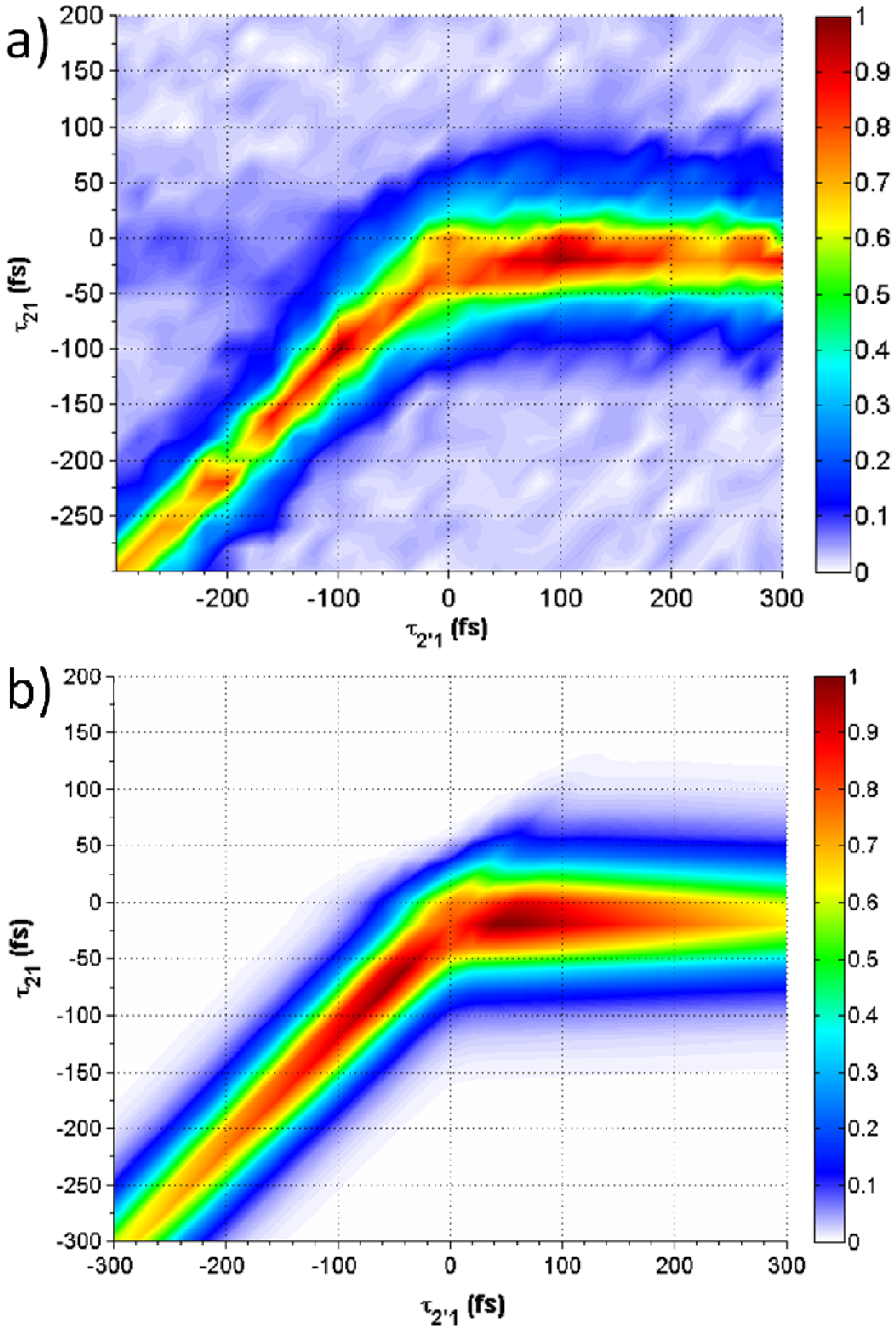

Figure 28— Two-dimensional delay scan (a) and simulation fit (b) of PbSe quantum dot Femtosecond Batch 8. Here excitation frequencies are tuned to the center of the 1S exciton transition frequency: $\omega_1 = \omega_2 = \omega_m = 6950\text{cm}^{-1}$. The fit quality is sensitive to the impact of contributions from coherence lifetimes, population lifetime, and non-resonant background. Fit parameters are included in Table 1. The shift to negative τ_{21} values in the data is due to inhomogeneous broadening; the corresponding shift in the simulation is artificial. For simplicity, inhomogeneous broadening was not included in this simulation. The weak signal along the negative $\tau_{2'1}$ axis results from a double reflection artifact; no attempt is made to reproduce it in the fit.

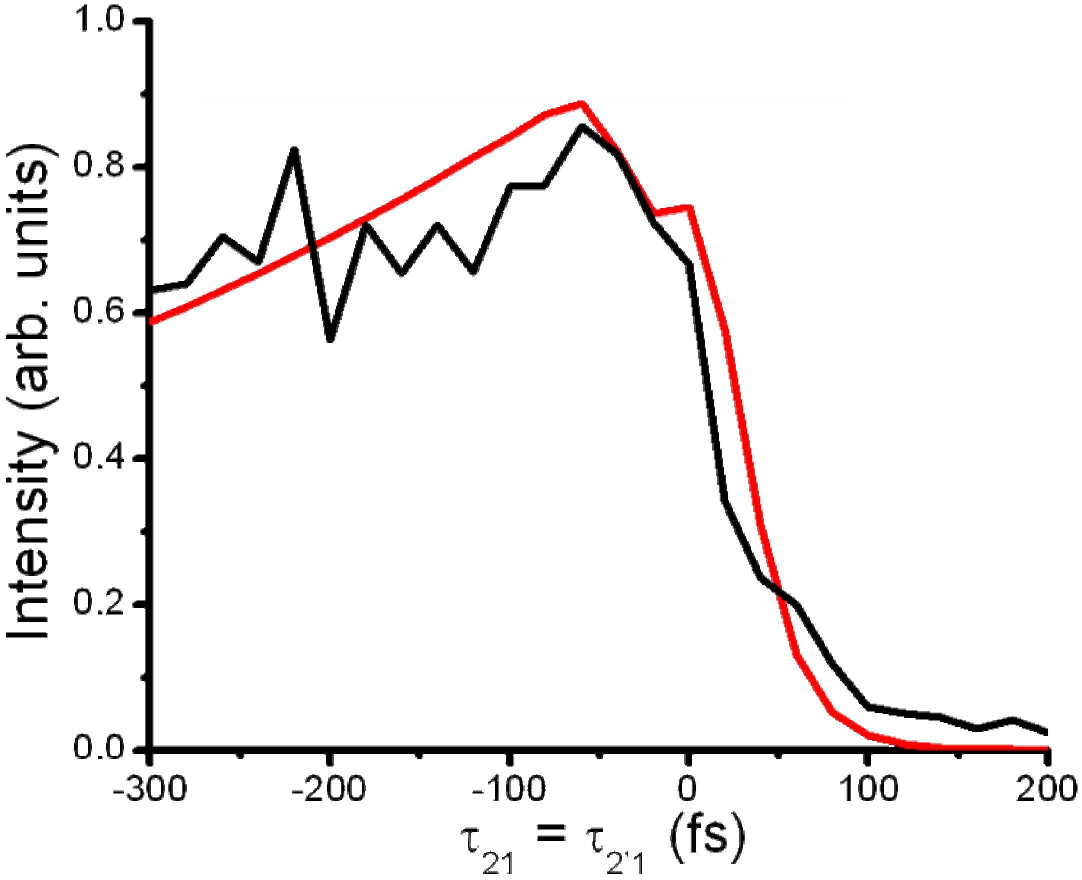

Figure 29—Comparison of $\tau_{21} = \tau_{2'1}$ cross-sections from Figure 28 data (black) and simulation (red).

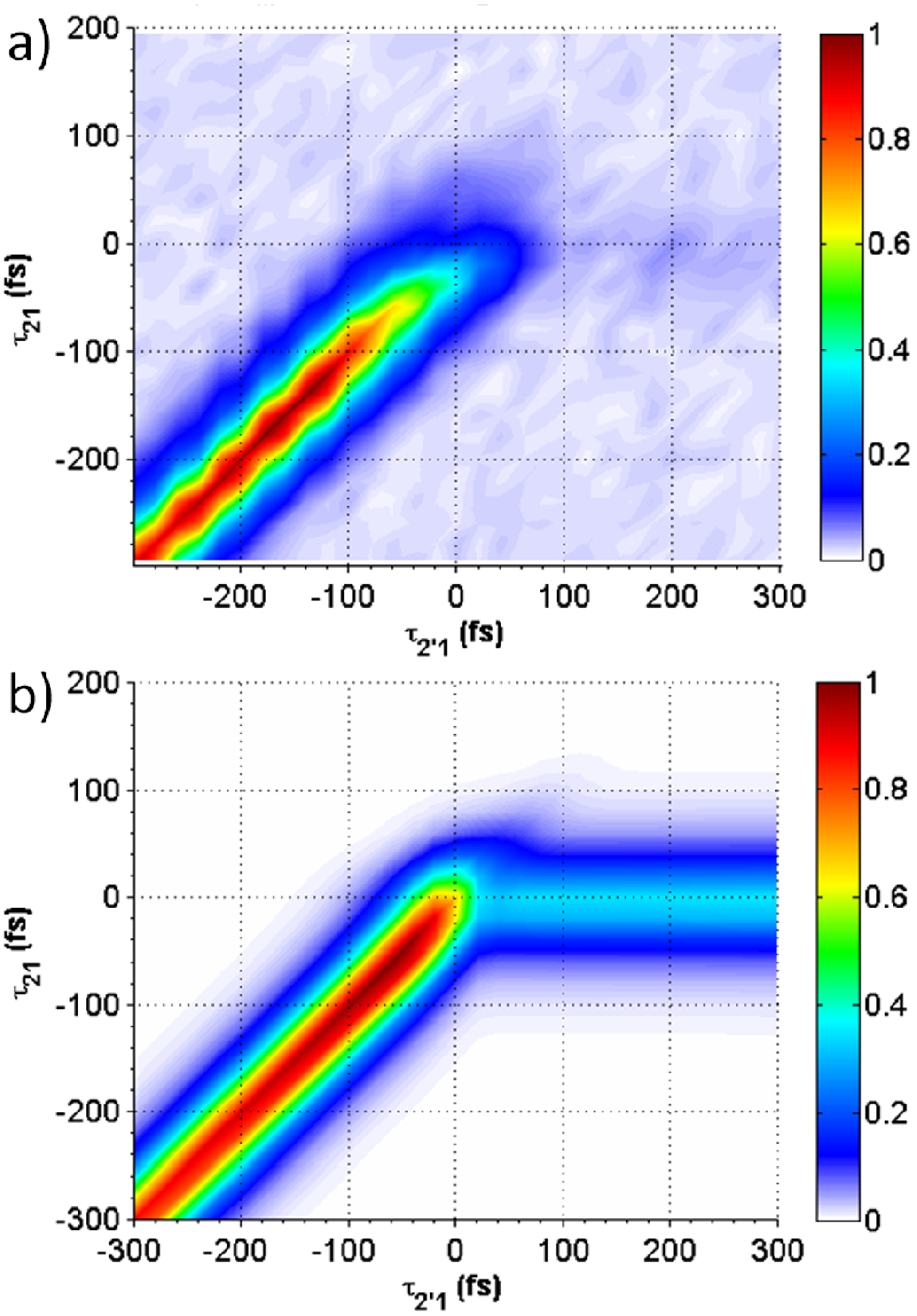

Figure 30— Two-dimensional delay scan (a) and simulation fit (b) of PbSe quantum dot Femtosecond Batch 8. Here excitation frequencies are tuned near to the center of the 1S exciton transition frequency: $\omega_2 = 6900\text{cm}^{-1}$ and $\omega_1 = \omega_m = 6700\text{cm}^{-1}$. The relative detuning suppresses signal along the positive $\tau_{2'1}$ axis, as seen in the simulated fit. Coherence lifetime values are equal to those used to fit data in Figure 28.

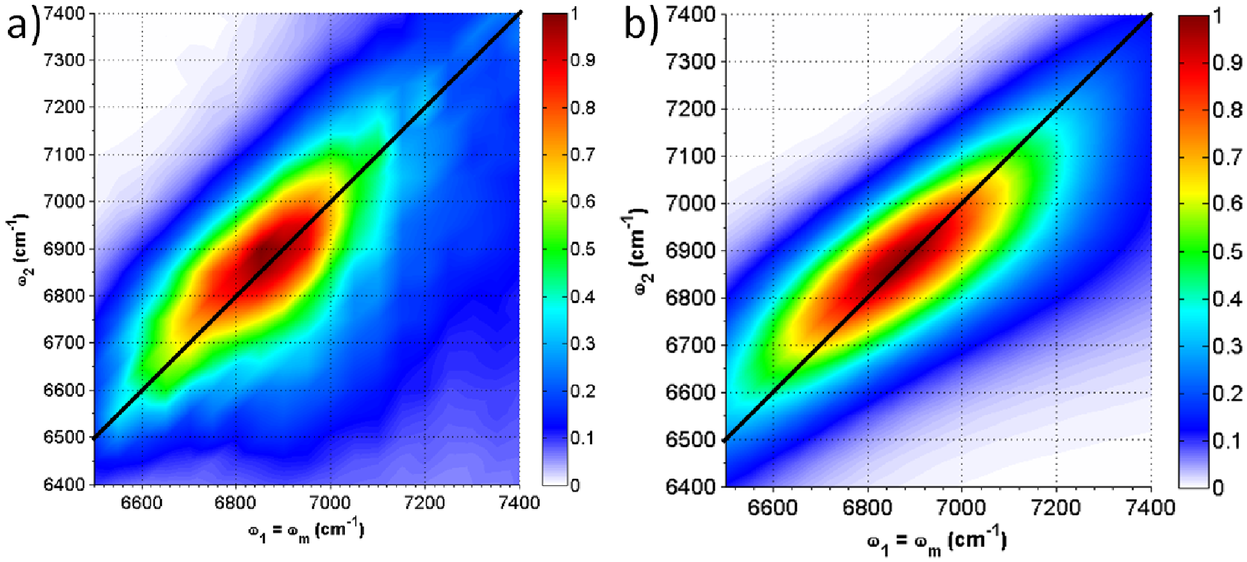

Figure 31—Two-dimensional frequency scan of Femtosecond Batch 4 (a) and its corresponding frequency-domain simulation (b). Here $\tau_{21} = \tau_{2'1} = -40$fs, so some contributions from other time-orderings and from non-resonant background signal can be expected. Small additions of each improved the quality of the simulation fit. Simulation parameters are shown in Table 2. Black lines trace out the $\omega_1 = \omega_2$ diagonals.

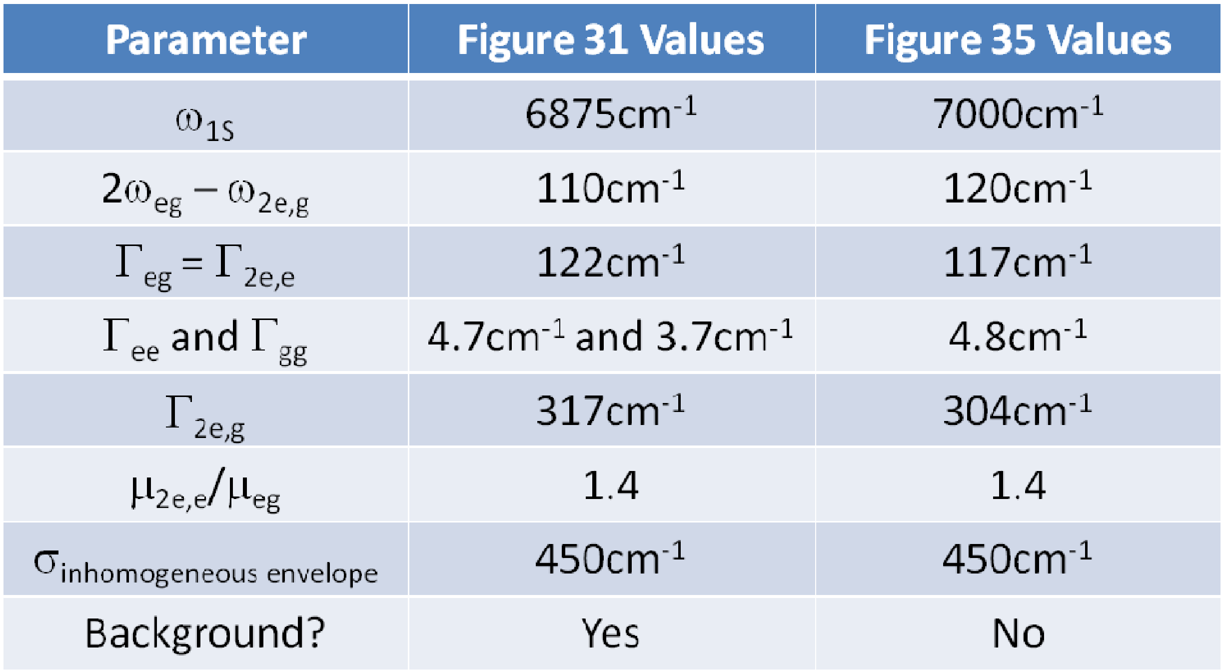

Parameter	Figure 31 Values	Figure 35 Values
ω_{1S}	6875cm^{-1}	7000cm^{-1}
$2\omega_{eg} - \omega_{2e,g}$	110cm^{-1}	120cm^{-1}
$\Gamma_{eg} = \Gamma_{2e,e}$	122cm^{-1}	117cm^{-1}
Γ_{ee} and Γ_{gg}	4.7cm^{-1} and 3.7cm^{-1}	4.8cm^{-1}
$\Gamma_{2e,g}$	317cm^{-1}	304cm^{-1}
$\mu_{2e,e}/\mu_{eg}$	1.4	1.4
$\sigma_{\text{inhomogeneous envelope}}$	450cm^{-1}	450cm^{-1}
Background?	Yes	No

Table 2—Frequency-domain simulation parameters for scans shown in Figures 31 and 35. Coherence dephasing rates were varied slightly around those measured in delay scans. Coulombic coupling and 1S exciton transition frequency values were also adjusted to optimize the fits.

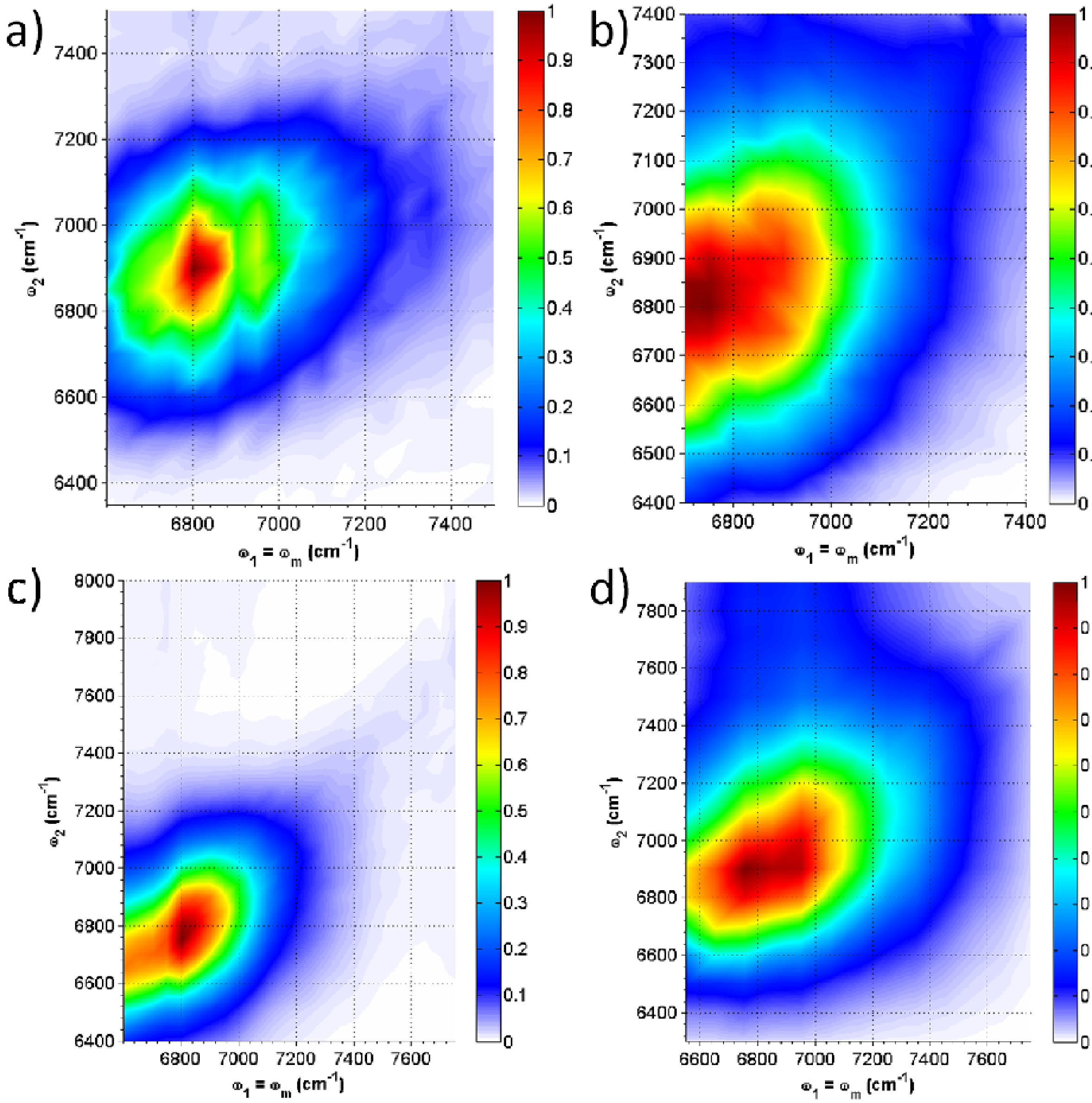

Figure 32—Two-dimensional frequency scans showing division of the 1S exciton feature in a variety of conditions. (a)-(c) Experiments measured 1S exciton structure of Femtosecond Batch 4 quantum dots; (d) measured that of Femtosecond Batch 8. A variety of experiment dates and population times are represented: (a) March 15, 2012 4.5ps, (b) March 2, 2012 1.0ps, (c) March 9, 2012 100fs, and (d) April 11, 2012 50fs. The feature seems to broaden and lose some diagonal character as the population lifetime grows longer. The relative intensity of the left part of the peak increases with population lifetime as well. OPA power and alignment quality do not seem to correlate with the observed feature. The proximity to any part of the phase of 3ps delay stage modulations is unknown.

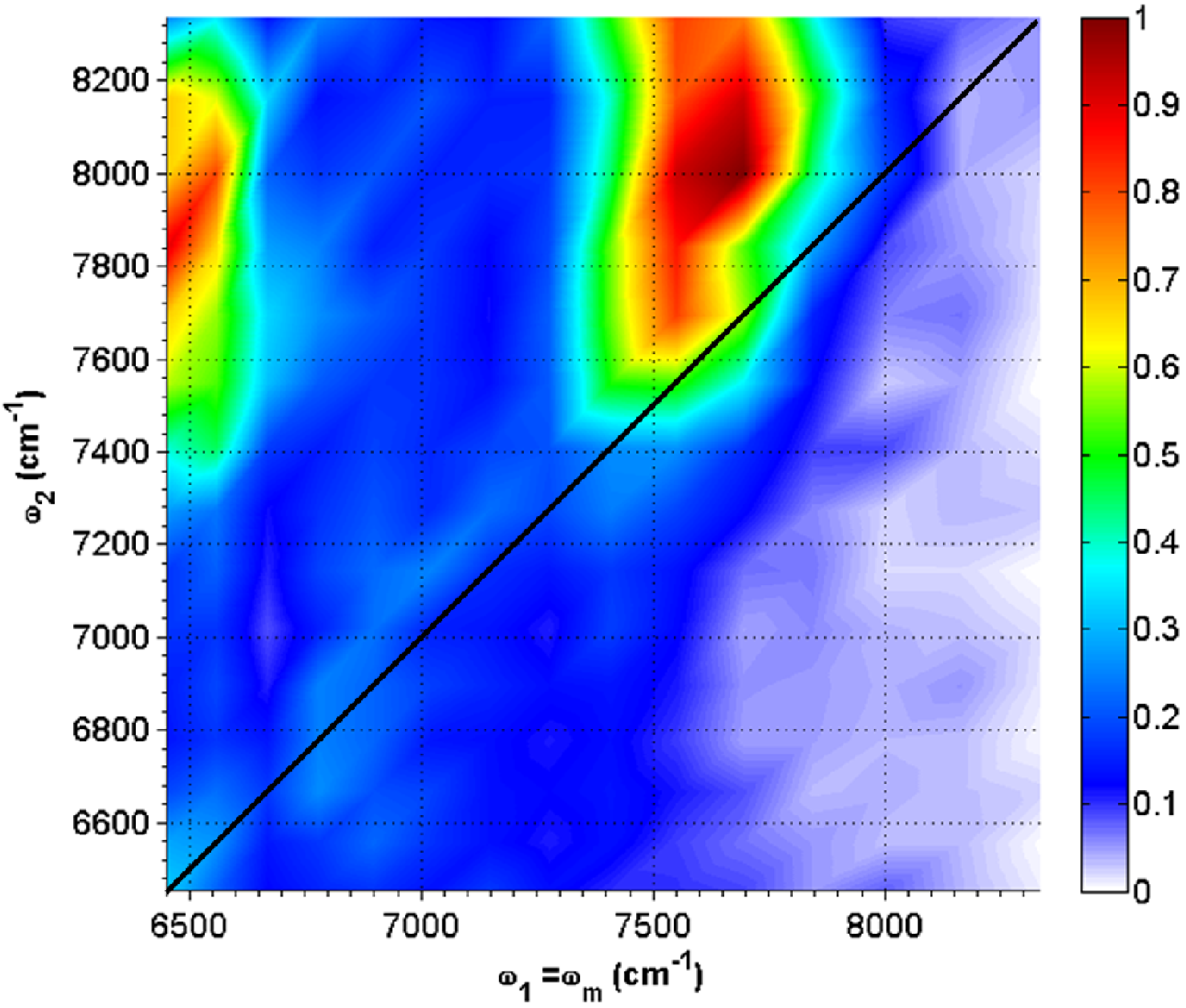

Figure 33—Two-dimensional frequency scan of Femtosecond Batch 3 quantum dots at a population lifetime of -600fs. Resonance with the 1P exciton transition increases the intensity of associated features. The 1S exciton diagonal feature is present and real (see Figure 22), but not accessed in the scan range shown. Though frequency-domain simulations do predict that resonant features will be shifted off the diagonal (shown by a black line), the magnitude of the shift for the 1P exciton diagonal feature is larger than expected.

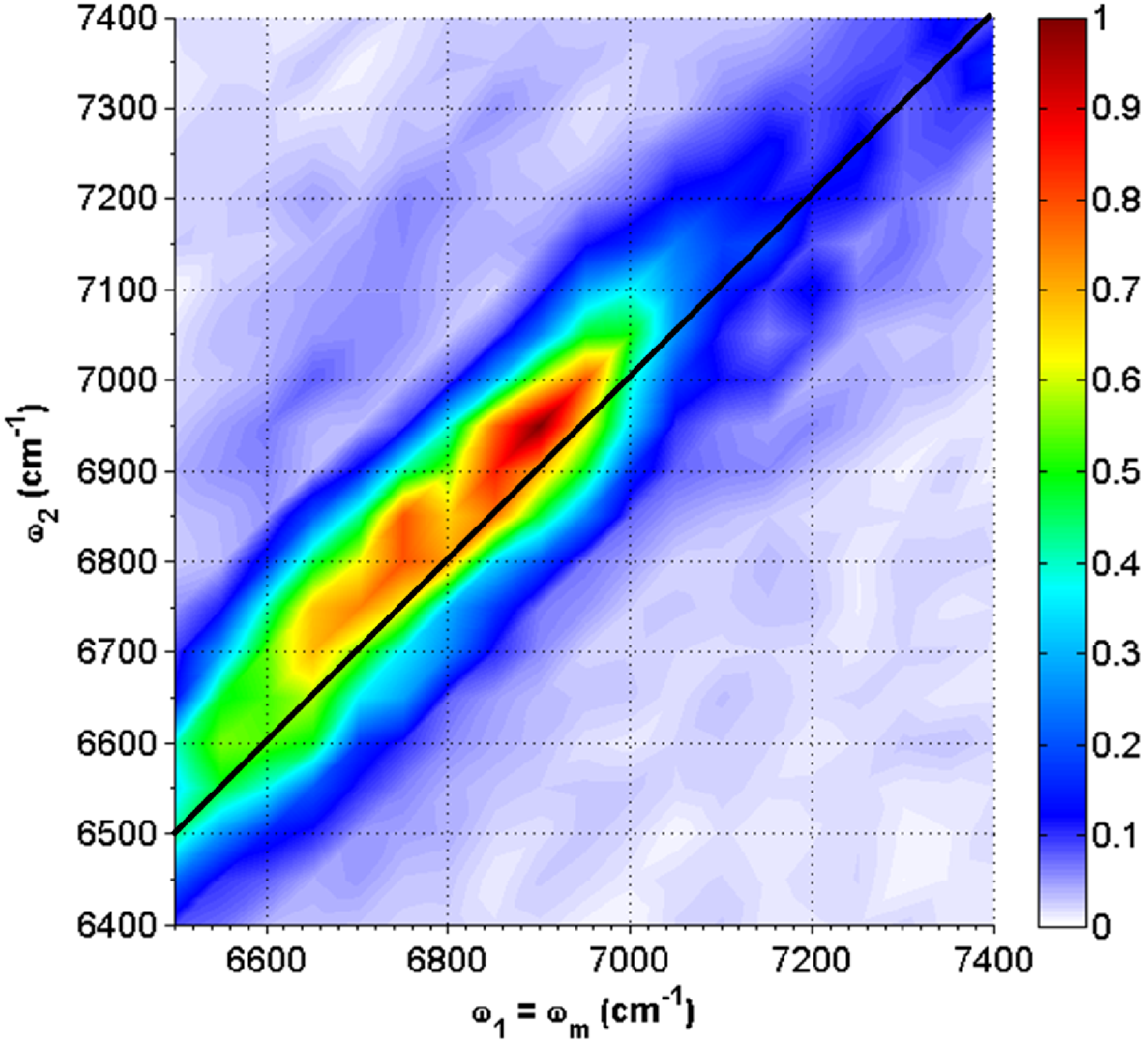

Figure 34— Two-dimensional frequency scan of Femtosecond Batch 4 with $\tau_{21} = 0$ and $\tau_{2'1} = 100$fs. The diagonal character is characteristic of scans with this pulse sequencing because the strongest four-wave mixing signal results from processes in which ω_1 and $\omega_{2'}$ create a population. The cause of the shift to the left of the diagonal is unknown, but its magnitude is not appreciably larger than calibration fluctuations observed over the course of a day.

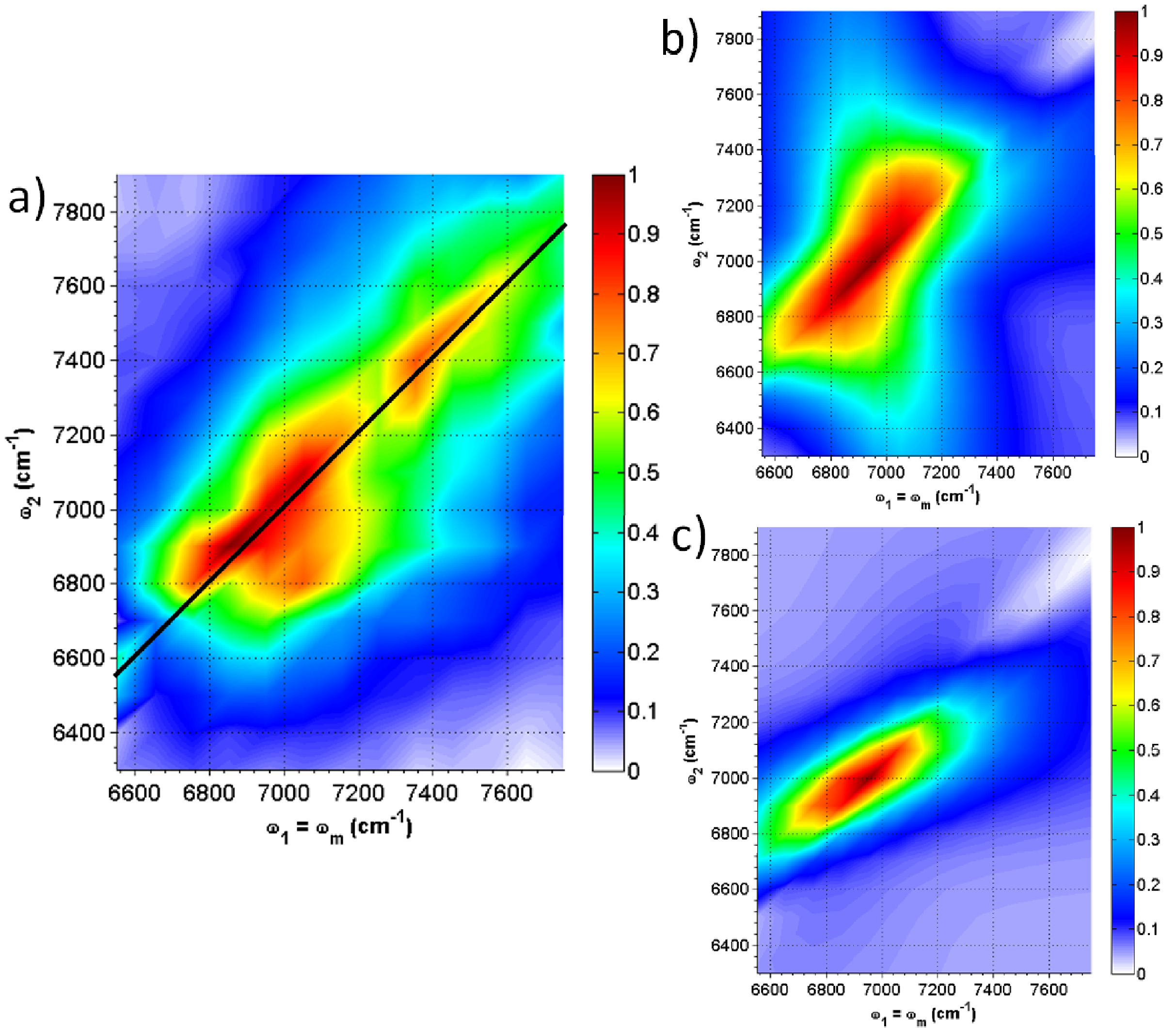

Figure 35—(a) A two-dimensional frequency scan of Femtosecond Batch 8 quantum dots with $\tau_{21} = 75$fs and $\tau_{2'1} = 0$. (b) The best fit simulation of the 1S exciton peak scan shown in (a) featuring contributions from fully-coherent and partially-coherent processes and some non-resonant background. (c) The same frequency domain simulation as shown in (b), but with all double quantum coherence contributions (those that pertain distinctly to $\tau_{21} > 0$fs and $\tau_{2'1} = 0$) removed. The visible superiority of (b) to (c) reveals that fully coherent processes not observable with long excitation pulses are once again accessible.

Chapter 7: Outlook and Future Directions

The purpose of assembling a laser system with sub-50fs pulses was to adapt multiresonant coherent multidimensional spectroscopy methodologies developed on vibrational systems for use in the study of quantum-confined semiconductor systems. Preliminary work performed with picosecond laser pulses provided important sample handling procedures, identified key experimental parameters, and produced frequency-domain data. The inability to directly observe coherence lifetimes in explorations with picosecond pulses revealed a few critical limitations. Without the ability to selectively study fully coherent phenomena, many of the questions pertaining to both fundamental quantum dot characteristics and the behavior of more-complicated nanostructures are unanswerable. Preliminary experiments and developments with the femtosecond system suggest that the flexibility of MR-CMDS techniques is restored and available to contribute toward probing quantum-confined nanomaterials and guiding heterostructure synthesis for such applications as solar energy and solar fuel generation.

Studies performed with picosecond pulses provided an important picture of PbSe quantum structure and incoherent dynamics; the femtosecond system has now been shown to have those capabilities. Earlier work demonstrated the coupling between the 1S and the 1P exciton states and measured the relaxation from the 1P to the band-edge. Additionally, the long 1S exciton population lifetime was directly measured and compared to results from the broader scientific community. Fits to frequency-domain data provided coherence lifetimes and Coulombic coupling energies between two 1S excitons. Femtosecond system experiments provided a similar measure of intraband relaxation and also showed the capability for use in tracing long population decay. Though excitation pulses were spectrally broad, spectra exploring basic excitonic structure revealed that none of the capabilities available to the picosecond system were lost in the transition.

Experiments using sub-50fs pulses improved upon the groundwork of the picosecond explorations by offering access to fully-coherent behavior. Delay scans directly measured coherence lifetimes. Frequency scans showed selective weighting of spectral features from specific coherence sequences.

Utilization of improved time resolution successfully improved upon initial experiments and sacrificed few, if any, previously enjoyed capabilities.

7.1. Future Directions

Early experiments with the new laser system have not yet explored some of the loose ends left by the set of picosecond experiments. Future research can move in two directions—improvement of the existing technique and/or expansion to more complicated systems of study.

When first establishing the femtosecond system, pulse fluences damaged the quantum dot sample under study. The damaged dots may display some of the surface trapping observed by the picosecond system, but may also observe the relaxation directly in the time domain. Intentional phototreatment of quantum dot samples may provide an opportunity to gain a greater understanding of that surface state and its associated dynamics. Various surface passivation studies, akin to those performed by the Kambhampati group, may be beneficial as the project expands to characterization of interfaces and charge transfer.

Research featuring the 1P exciton state is currently indicative of the technique capabilities, but is still incomplete. More extensive experiments studying the evolution of the hot exciton state may provide a comparison with hot electron transfer in later work.

Furthermore, higher energy quantum-confined exciton states currently are not thoroughly characterized. Current instrumentation capabilities will allow larger tuning ranges, but some logistical barriers must be overcome. Once those obstacles are removed, a more complete picture of quantum dot excitonic structure should be available. Those scans will likely have to be performed in pieces, then stitched together, as the phase mismatch resulting from larger tuning ranges will certainly create anomalous spectral features.

Polarization rotation did not prove to be fruitful for the intended studies with the picosecond system. The fast fine structure relaxation that eliminates the angular momentum grating created by two cross-polarized beams could not be observed by the picosecond pulses. Though some measurement of these states and their dynamics has already been performed, there may be merit in establishing further understanding of their behavior. Those same states may be of interest in charge transfer studies, as the coupling between the fine structure of the quantum dots and the charge acceptor may be relevant.

The most broadly advantageous adaptation of the femtosecond system experiments is almost certainly the incorporation of cryogenic sample cooling. The coherence lifetimes are currently long enough to be measured by the pulses, but decreasing the coherence dephasing rate will allow improved isolation of fully coherent pathways, help resolve multiexcitonic energetic structure, and increase the odds of observing coherent energy transfer in complicated nanostructure systems.

Indeed, the capabilities are now either in place or close at hand for studying those semiconductor structures that may prove to be invaluable contributions to solar energy and fuel technologies. The structures themselves are fast becoming available, and multiresonant coherent multidimensional spectroscopy is primed to provide the simultaneous structural and dynamical characterization required to inform and guide further synthetic strategies and developments.

Appendix A: Frequency Domain Simulations

The spectroscopy techniques developed for the experiments discussed in this work aim to use the advantages of both frequency- and time-domain approaches to isolate structural and dynamical properties of challenging systems. An experiment in which excitation frequencies are scanned against each other while measuring output intensity provides information pertaining to the analyte energetic structure, but complicated interferences from different four-wave mixing processes can make it difficult to interpret spectra intuitively. MR-CMDS chooses pulse sequences and timings to emphasize or isolate one set of processes from the others.

Previous work has calculated the spectral signatures of each time-ordered pathway, but has done so for experiments with large scan ranges relative to transition and inhomogeneous line widths.[1] This appendix shows example calculated spectra using parameters and scan windows that better match PbSe quantum dot studies focusing on the 1S exciton and 1S+1S biexciton states. Table 1 summarizes the parameters used. The equations used to generate these images are taken from the Theory section and its description of the incorporation of inhomogeneous broadening (see Theory equations (32)-(34) for an example). Pulse sequences are discussed according to their pathway labels shown in Theory Figure 1. To better inform the interference patterns expected for scans only measuring non-linear signal intensity, pictures provided here show the real and imaginary portions of the emitted electric field in addition to the magnitude. Pathway pairs I/III and V/VI are shown only as combinations because experiments selecting either pair typically overlap the pulses in time in order to create a long-lived population state with minimal losses due to coherence dephasing.

Figures 1-3 show electric field contributions from the alpha, beta, and gamma pathways associated with each pulse time sequence. Spectra for pathway I/III are very narrow because when $\omega_1 = \omega_2$ their excitations can create a long-lived population state when they are resonant with a transition. The efficiency of creating this state is dependent on the amplitude of the convolution of the two excitation pulses. Theory equations (17) and (19) inform this behavior, as their denominators depend on $(\omega - \omega_2)$ and Γ_{gg} or Γ_{ee}. With long population lifetimes (small decay rates), the sensitivity to the difference between excitation frequencies becomes all the more severe. Because the simulations are performed in the continuous-wave limit, their frequency profiles are delta functions. In real experiments, pulse widths broaden the diagonal feature, but the strong diagonal character is still evident. Though pathways V and VI can also create populations, pulses from the same OPA create them, so $\omega - \omega_2$ always equals zero and there is no additional diagonal line severity.

The discussion of destructive interference between alpha/gamma and beta pathways in the Theory section can be seen clearly in contrasting Figures 1/3 and 2. In the absence of Coulombic coupling, the resulting spectral line shape merely changes amplitude with the introduction of non-parametric pathways. If the coupling is significantly larger than the homogeneous line widths, as is often the case in studies of vibrational modes, these beta pathways can be resolved as separate peaks. As shown in Figure 4, when the line width is larger than the coupling, the signal from non-parametric processes appear to distort or shift the spectrum. As a consequence, Coulombic coupling in PbSe quantum dots can be extracted from frequency domain data, but it can be difficult to do so by cursory inspection.

Figure 5a shows a frequency scan when all processes are allowed to contribute. When all transitions are resonant, the decay rates are all that remain to determine polarization magnitudes (see Theory equations (16)-(19)). As a consequence, the contributions of pathways with slow decay rates are more significant, as shown by the dominant character of pathways accessing long-lived populations (I/III and V/VI) in the overall spectrum.

Figure 5b introduces non-resonant background to the combined PbSe 1S exciton signal. Most of the non-resonant contribution to spectra results from the high ultraviolet electronic transition $\chi^{(3)}$ of the CCl_4 solvent used in colloidal PbSe experiments. The electronic transitions of the PbSe are closer to the wavelength range under study, but also contribute less because of the low quantum dot concentration relative to the solvent. The real part of the non-resonant signal depends on the inverse of the detuning, whereas the imaginary part depends on the inverse of the detuning squared. The large detuning from the CCl_4 transitions then dictates that their contribution is mostly real, and the modest detuning of the PbSe suggests that a little imaginary contribution may still be present. For each contribution, however, the magnitude of these frequency dependences changes very little across the frequency range featured in this work. As a consequence of this reasoning, the simulation shown in Figure 5b treats the non-resonant signal as a constant with only a small imaginary component, as used in similar interference studies.[2] Because of the sign information lost in the intensity spectrum, it is not intuitively clear how the addition of a constant background will distort and interfere with a spectrum, so careful calculation is important. The high energy states accessed by the excitation beams are so far detuned that the state lifetimes are effectively zero, so the interference is only significantly present when all three pulses are overlapped in time.

Works Cited

1. Meyer, K. A.; Thompson, D. E.; Wright, J. C. Frequency and Time-Resolved Triply Vibrationally Enhanced Four-Wave Mixing Spectroscopy. *Journal of Physical Chemistry A* **2004,** *108* (52), 11485-11493.
2. Yurs, L. A.; Block, S. B.; Pakoulev, A. V.; Selinsky, R. S.; Jin, S.; Wright, J. C. Spectral Isolation and Measurement of Surface-Trapped State Multidimensional Nonlinear Susceptibility in Colloidal Quantum Dots. *Journal of Physical Chemistry C* **2012,** *116* (9), 5546-5553.
3. Yurs, L. A.; Block, S. B.; Pakoulev, A. V.; Selinsky, R. S.; Jin, S.; Wright, J. C. Multiresonant Coherent Multidimensional Electronic Spectroscopy of Colloidal PbSe Quantum Dots. *Journal of Physical Chemistry C* **2011,** *115* (46), 22833-22844.

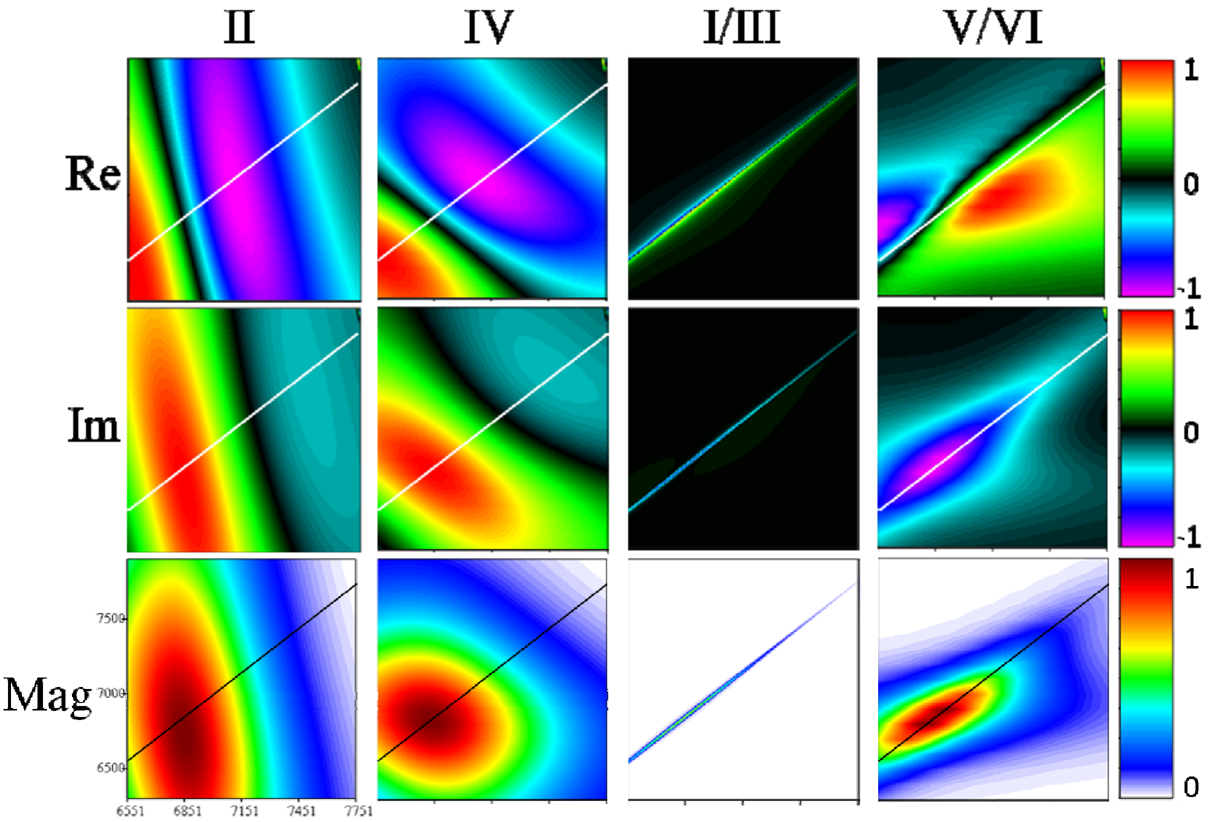

Figure 1—The real contribution, imaginary contribution, and magnitude of the polarization created by the alpha processes of time orderings labeled above each column. The range of each spectrum was chosen to represent a common tuning range for experiments reported in this work—6550cm^{-1}< ω_1< 7750cm^{-1} and 6350cm^{-1}< ω_2< 7850cm^{-1}. The thin lines through each picture other than those for pathway I/III (which are themselves little more than a thin line along this diagonal) show where $\omega_1 = \omega_2$; the spot marks the center frequency of the 1S exciton peak.

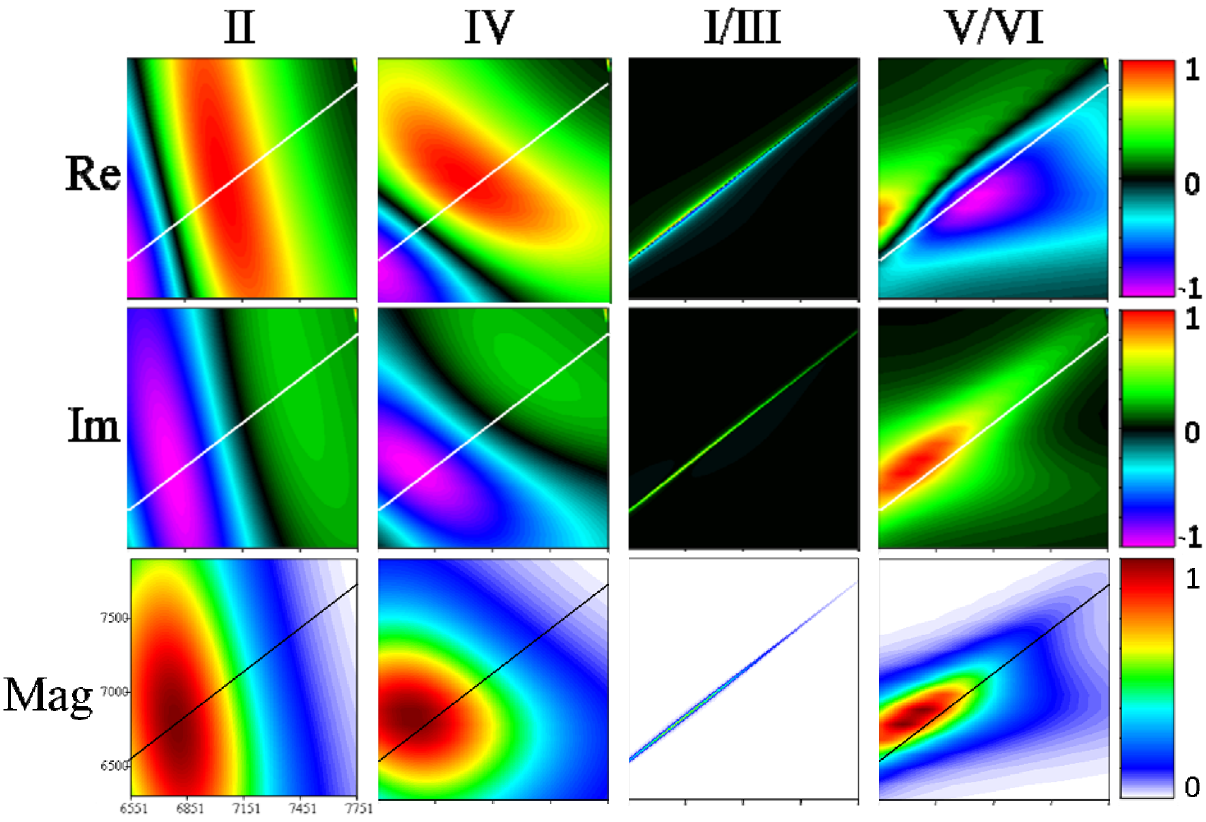

Figure 2— The real contribution, imaginary contribution, and magnitude of the polarization created by the beta processes of time orderings labeled above each column. The thin lines through each picture show where $\omega_1 = \omega_2$; the spot marks the center frequency of the 1S exciton peak.

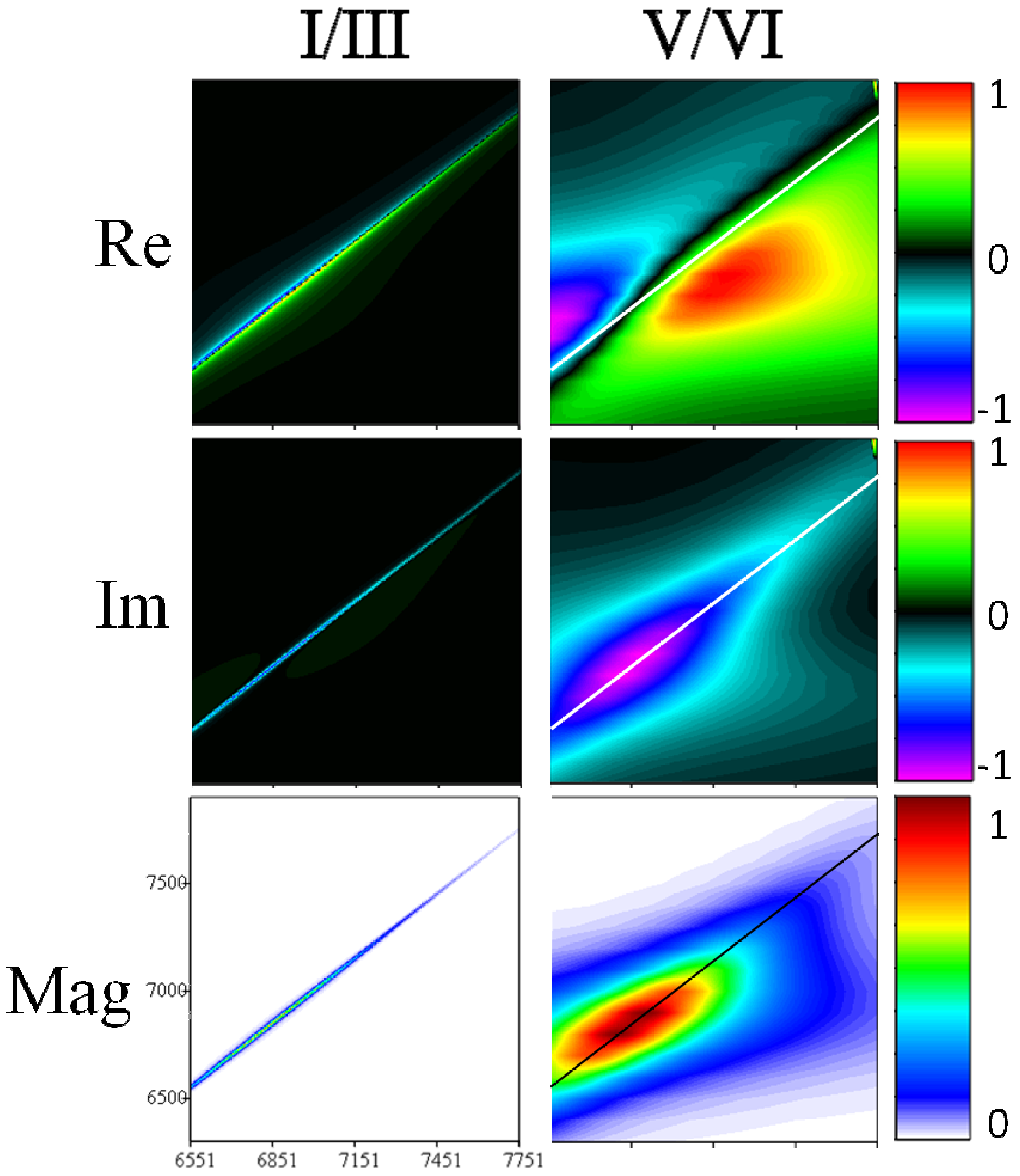

Figure 3— The real contribution, imaginary contribution, and magnitude of the polarization created by the gamma processes of time orderings labeled above each column. The thin lines through the pathway V/VI spectra show where $\omega_1 = \omega_2$; the spot marks the center frequency of the 1S exciton peak.

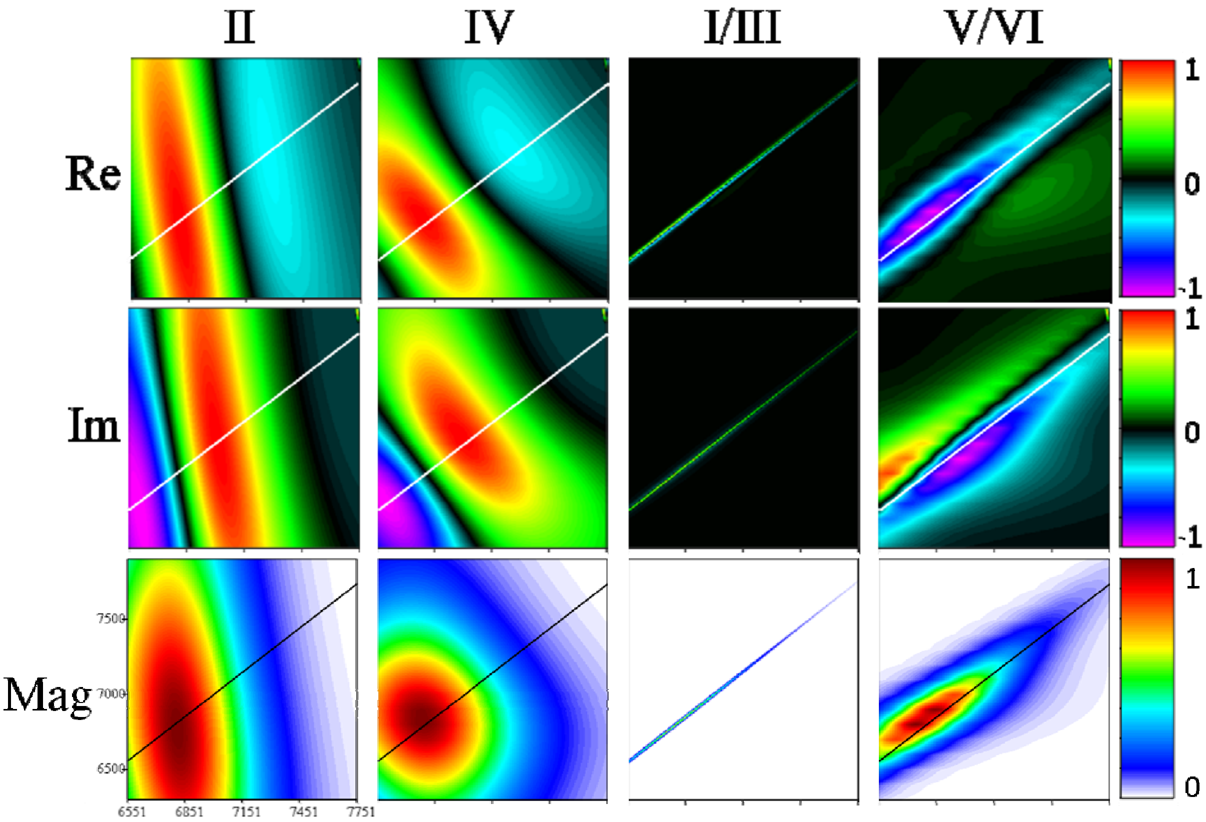

Figure 4— The real contribution, imaginary contribution, and magnitude of the polarization created by the sum of alpha, beta, and gamma processes of time orderings labeled above each column. The thin lines through each picture show where $\omega_1 = \omega_2$; the spot marks the center frequency of the 1S exciton peak.

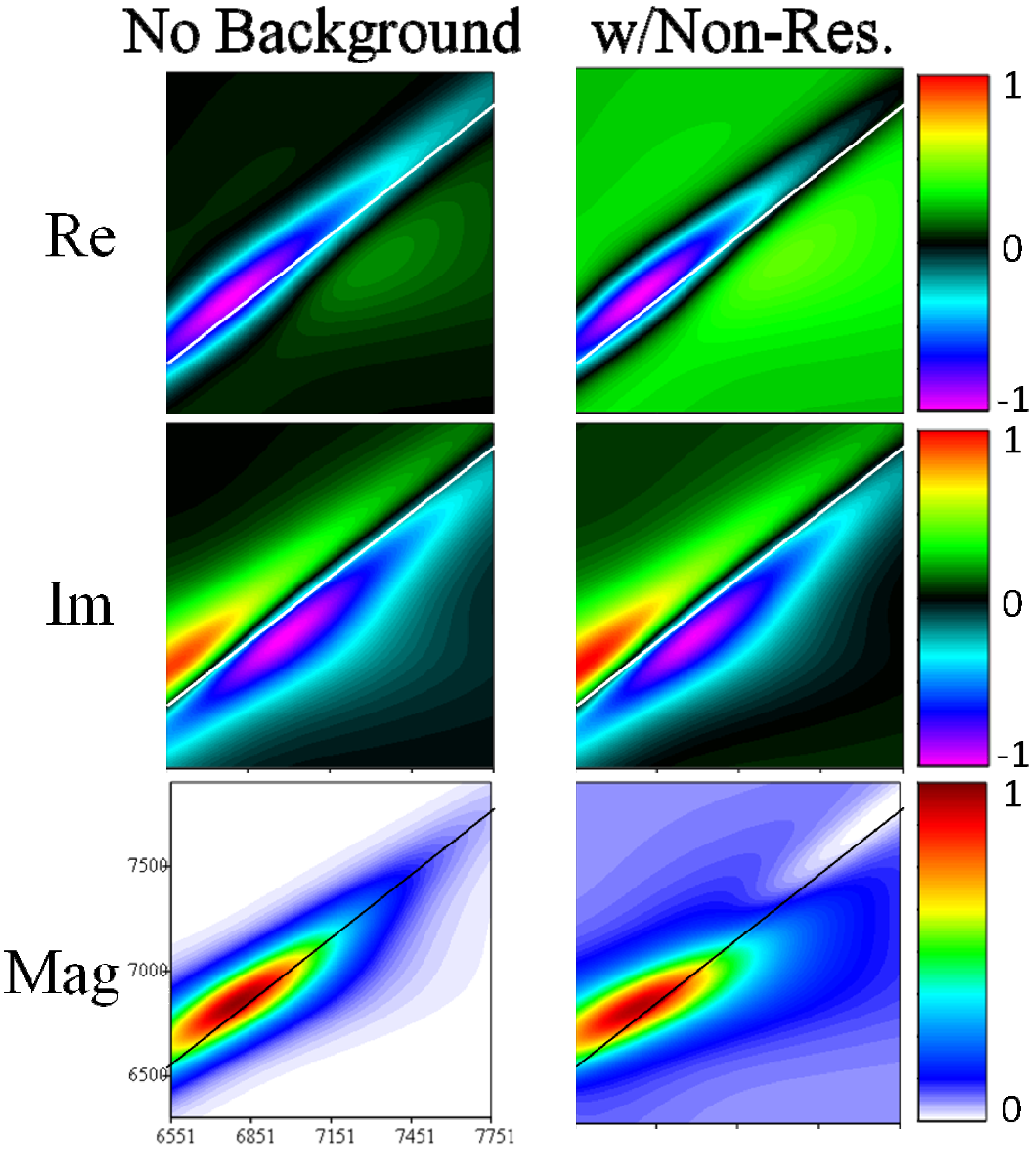

Figure 5— (a) The real contribution, imaginary contribution, and magnitude of the polarization measured when all pathways contribute. (b) The same spectra, but with a constant background added to simulate non-resonant background contribution. The thin lines through each picture show where $\omega_1 = \omega_2$; the spot marks the center frequency of the 1S exciton peak.

ω_{eg}	6850 cm^{-1}
Coulombic coupling ($2\omega_{eg}$ - $\omega_{2e,g}$)	120 cm^{-1}
$\mu_{2e,e}/\mu_{eg}$	1.4
$\Gamma_{eg} = \Gamma_{2e,e}$	117 cm^{-1}
$\Gamma_{ee} = \Gamma_{gg}$	4.8 cm^{-1}
$\Gamma_{2e,g}$	304 cm^{-1}
σ	500 cm^{-1}

Table 1—Fitting parameters used in displayed plots. Decay lifetimes used match those measured in PbSe time-domain spectra. The 1S exciton frequency was chosen to match that of two batches featured in this work. The ratio of transition dipole moments was taken from PbSe CMDS literature.[3] The inhomogeneous lifetime parameter was chosen to match common PbSe batch dispersity.

Appendix B: Phase Matching Near Absorptive Features

When working with samples that absorb strongly, it is important to consider the influence of perturbations to the index of refraction in the spectral vicinity of analyte resonances. Such changes in the refractive index can diminish the intensity of four-wave mixing output by inducing or increasing a phase mismatch. To calculate the magnitude of this impact, a rigorous investigation is required.

The experiments performed for this project make use of the following phase matching expression, where $\overrightarrow{k_{out}}$ is the wave vector of the electric field launched by the non-linear polarization created by $\overrightarrow{k_1}$, $\overrightarrow{k_2}$, and $\overrightarrow{k_{2'}}$. The phase-matching condition is met when $\Delta\vec{k} = 0$.

$$\Delta\vec{k} = \overrightarrow{k_1} - \overrightarrow{k_2} + \overrightarrow{k_{2'}} - \overrightarrow{k_{out}}$$

Initial alignment for the experiments of any given day involves optimizing the incident beam pointing to achieve phase-matching. This alignment is performed with $\omega_1 = \omega_2$, leading the angles between each beam and the optical axis to be close to equal. As various experiments are conducted, the difference between ω_1 and ω_2 changes. Without realigning the system between data points, it is impossible to entirely avoid phase mismatch. The intensity of the output field diminishes with mismatch and path length, l, according to $sinc^2(|\Delta\vec{k}|l/2)$. It becomes important, then, to choose experimental parameters that minimize this mismatch in the frequency range of any set of experiments.

To calculate the magnitude of the phase mismatch, $\Delta\vec{k}$, consider the following definition, $\overrightarrow{k_4} \equiv \overrightarrow{k_1} - \overrightarrow{k_2} + \overrightarrow{k_2'}$ so that $\Delta\vec{k} = \overrightarrow{k_{out}} - \overrightarrow{k_4}$. Using column vectors to characterize the x-, y-, and z-axis components of the vectors, with the z-axis defining the optical axis,

$$\overrightarrow{k_4} = \begin{pmatrix} -|\overrightarrow{k_1}|sin(\varphi) \\ 0 \\ |\overrightarrow{k_1}|cos(\varphi) \end{pmatrix} - \begin{pmatrix} 0 \\ |\overrightarrow{k_2}|sin(\varphi) \\ |\overrightarrow{k_2}|cos(\varphi) \end{pmatrix} + \begin{pmatrix} |\overrightarrow{k_2}|sin(\varphi) \\ 0 \\ |\overrightarrow{k_2}|cos(\varphi) \end{pmatrix} = \begin{pmatrix} sin(\varphi)(|\overrightarrow{k_2}| - |\overrightarrow{k_1}|) \\ -|\overrightarrow{k_2}|sin(\varphi) \\ |\overrightarrow{k_1}|cos(\varphi) \end{pmatrix}$$

where φ is the angle between each vector and the optical axis and the vector representations of each incident beam correspond to the orientation chosen during lab alignment. Calculating intensity losses from phase mismatch requires determination of the magnitude of $\Delta\vec{k}$. According to the law of cosines,

$$|\Delta\vec{k}| = |\overrightarrow{k_{out}} - \overrightarrow{k_4}| = \sqrt{|\overrightarrow{k_{out}}|^2 + |\overrightarrow{k_4}|^2 - 2|\overrightarrow{k_{out}}||\overrightarrow{k_4}|\cos(\gamma)}$$

Here γ is simply the relative angle between $\overrightarrow{k_{out}}$ and $\overrightarrow{k_4}$. As all vector magnitudes are non-negative, it is apparent upon inspection that the highest intensity light, which corresponding to a $\overrightarrow{k_{out}}$ direction with minimized $|\Delta\vec{k}|$, occurs when $\gamma = 0$. Then

$$|\Delta\vec{k}| = |\overrightarrow{k_{out}} - \overrightarrow{k_4}| = \sqrt{|\overrightarrow{k_{out}}|^2 + |\overrightarrow{k_4}|^2 - 2|\overrightarrow{k_{out}}||\overrightarrow{k_4}|} = |\overrightarrow{k_{out}}| - |\overrightarrow{k_4}|$$

This value can, in turn, be calculated directly by recalling that we use a monochromator to isolate output light with frequency equal to ω_1, as that output frequency is expected for all processes in which electric field energy is conserved between the incident fields and the excited oscillator. Hence $|\overrightarrow{k_{out}}| = |\overrightarrow{k_1}|$. The magnitude of $\overrightarrow{k_4}$ can be calculated from its vector representation above:

$$|\overrightarrow{k_4}| = \sqrt{sin^2(\varphi)\left(|\overrightarrow{k_2}|^2 - 2|\overrightarrow{k_1}||\overrightarrow{k_2}| + |\overrightarrow{k_1}|^2\right) + |\overrightarrow{k_2}|^2 sin^2(\varphi) + |\overrightarrow{k_1}|^2 \cos^2(\varphi)} =$$

$$= \sqrt{2|\overrightarrow{k_2}|sin^2(\varphi)(|\overrightarrow{k_2}| - |\overrightarrow{k_1}|) + |\overrightarrow{k_1}|^2}$$

Notice that, when $|\overrightarrow{k_1}| = |\overrightarrow{k_2}|$, $|\overrightarrow{k_4}| = |\overrightarrow{k_1}|$ and $|\Delta\vec{k}| = 0$. In all other cases, it is important to calculate $|\overrightarrow{k_1}|$ and $|\overrightarrow{k_2}|$.

As $|\vec{k}| = 2\pi n \upsilon$ and the frequency, υ, is already well known for each beam from calibration, only refractive index requires further attention. Of particular interest over the frequency ranges of these experiments is the rapidly-varying change in index of refraction in the spectral vicinity of a resonance, as opposed to the slow variation due to the high energy electronic resonances of the solvent. Because both absorption coefficient (α) and index of refraction are characteristics of the linear susceptibility ($\chi^{(1)}$), one can be calculated from the other by use of the Kramers-Kronig transformation. In the case of a pure substance—a decent approximation for case of an effectively constant solvent index of refraction—the change in index of refraction due to a resonance is

$$\Delta n = \frac{\delta c \alpha}{2\omega\Gamma} = \frac{\delta c A}{2 l \omega\Gamma} \ln(10)$$

where δ is the difference between the transition frequency and the frequency of the observation, c is the speed of light, A is the linear absorbance of the sample, l is the pathlength of the sample, ω is the frequency of observation, and Γ is the dephasing rate of a coherence between the state of interest and the ground state.

Using the above equations for index of refraction and phase mismatch, it is then possible to use a linear absorbance spectrum, in concert with lifetimes measured in four-wave mixing experiments and common beam alignment angles, to calculate the loss of output intensity due to imperfect phase-matching. An example of the magnitude of this effect using $\varphi = .02$ (an upper limit for the value used for the line of experiments discussed here), an ω_2 frequency resonant with the transition, and the absorption profile of PbSe quantum dot sample “fs Batch 8” (included as a dashed line) is shown in Figure 1. Earlier experimental designs made use of faster focusing optics, increasing the angle by a factor of two or more. For comparison, Figure 2 shows the intensity loss incurred by phase mismatch when the angle is increased to $\varphi = .05$.

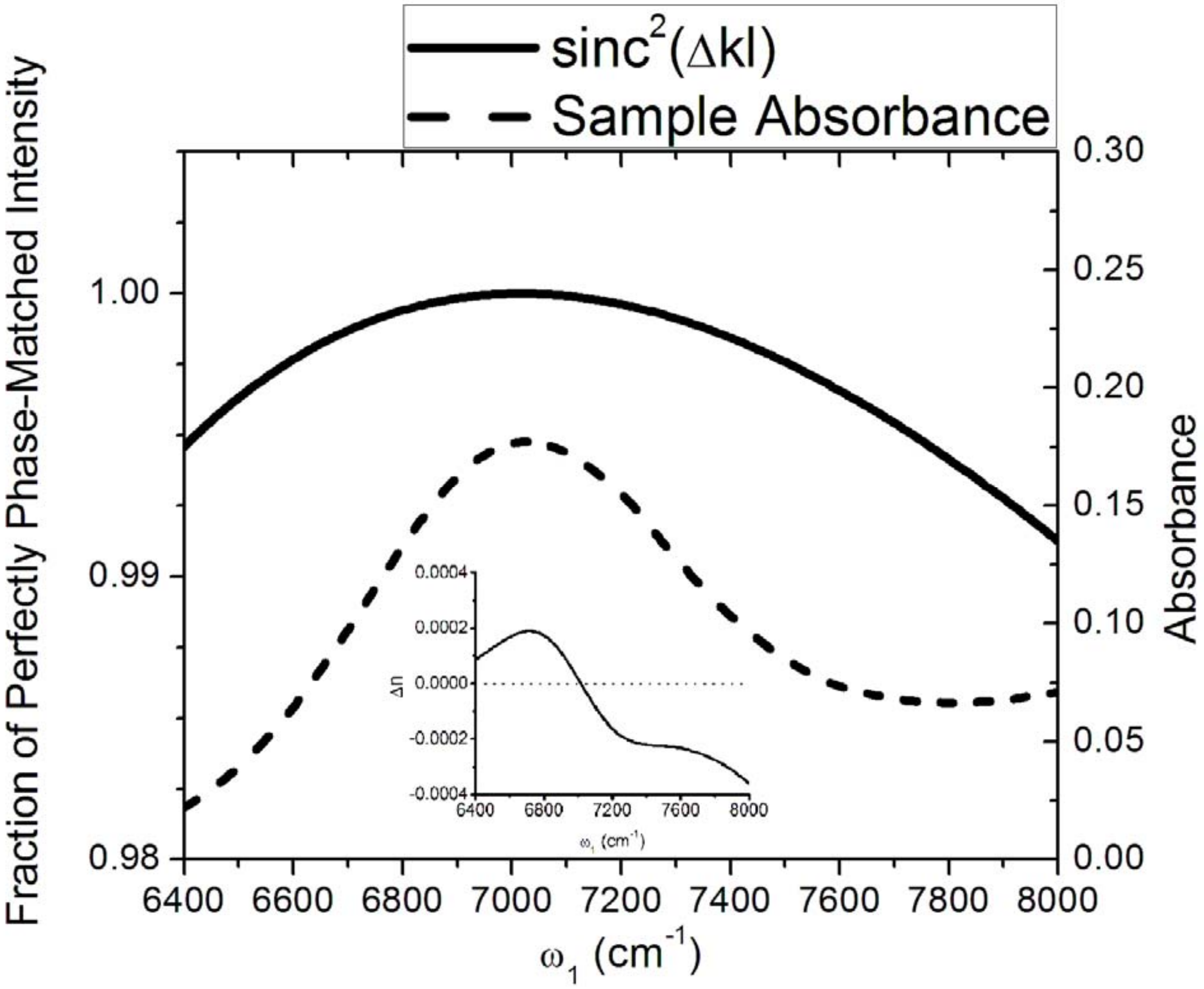

Figure 1—Index of refraction impacts on four-wave mixing intensity. With ω_2 tuned to resonance at 7017cm^{-1}, the solid curve shows the fraction of the intensity that could have been seen if phase matching angles had been optimized at that pair of frequencies. The dashed line shows the absorbance of the sample (1mm path length) over the frequency range of interest. (Inset) The perturbation to the index of refraction owing to the exciton resonance.

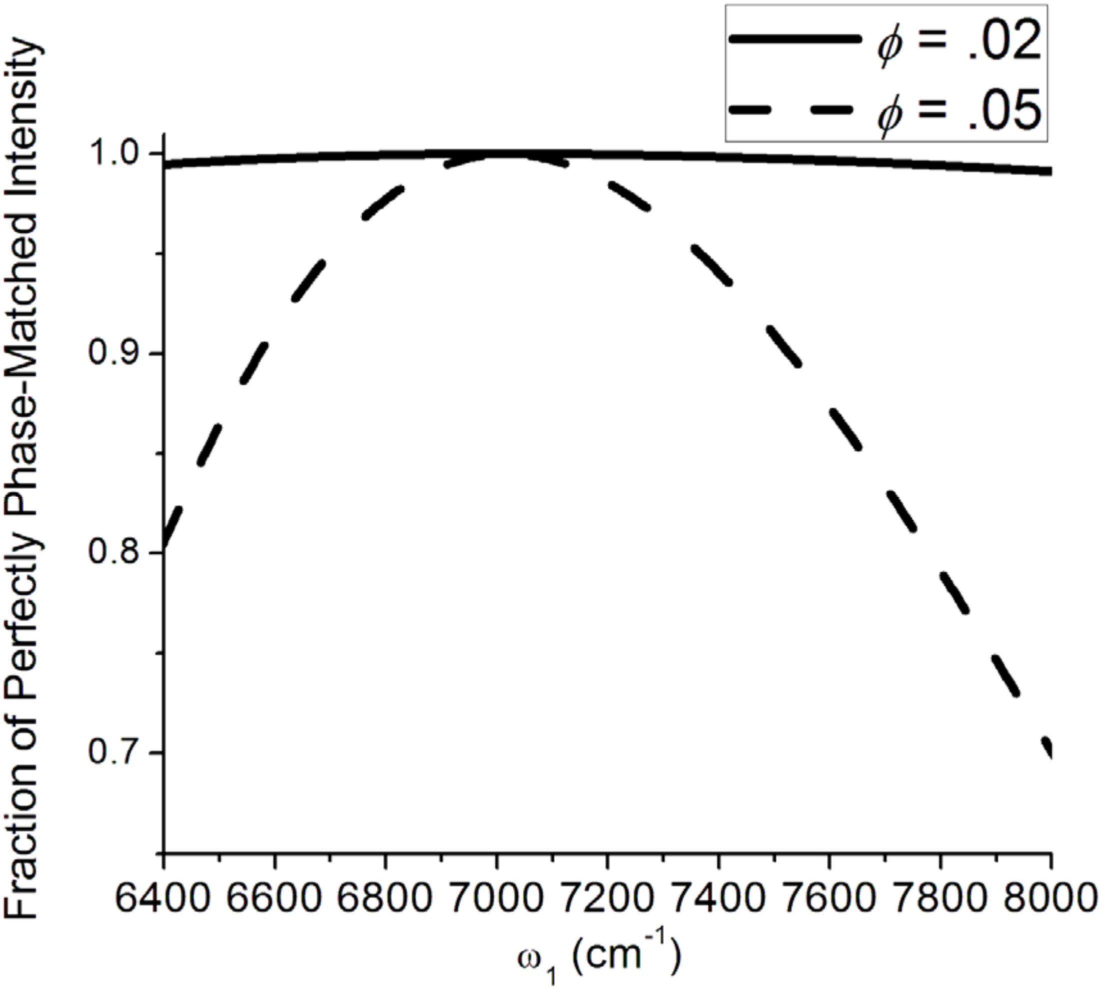

Figure 2—Index of refraction impacts on four-wave mixing intensity as the angle is changed. The solid line shows the fluctuation in output intensity as laser frequencies vary when using the low angle alignment featured in this line of experiments. The dashed line shows the same fluctuations when the angles between the input beams and the optical axis are increased, as corresponds to one of the shallower focuses of the alternative alignment schemes considered.

Appendix C: Daily Calibration Routine

The femtosecond laser system is particularly sensitive to ambient laboratory temperature drift and air currents. As the environment can and does fluctuate, careful daily (and sometimes twice daily) calibration is important for confidence in experimental results. The following instructions should allow a reproduction of the routine that was used as the standard procedure. All optical component designations correspond to labeling shown in Figures A-C (at the end of this appendix).

With a well-aligned Spitfire Pro 4W regenerative amplifier, use the Spitfire operation software to turn on the Empower and turn its current up to the most recent operating setting. If not already activated, turn on Pockels cells channels 1, 2, and 3 by opening the Channels Step window from the View menu (see Figure 1) and pressing the buttons to the right of each channel's name (they will be green and illuminated when the cells are turned on, as shown in Figure 2). At the time of the writing of this document, the timings were set at 107.00ns, 126.00ns, and 238.00ns for the three channels, respectively. The Spitfire requires a solid 30 minutes to stabilize. This waiting time is well-spent filling any detector dewars, turning on any choppers that will be used during the day, and starting COLORS, the femtosecond system operation LabVIEW program developed by Schuyler Kain. Once the amplifier has warmed up, measure the output power with a 407A Spectra Physics power meter in the beamline going to OPA2 (between BS1 and M1). The power measured should be 1.80±0.02W. If the output power is too low, small changes in seed routing mirrors can sometimes restore the loss. If the measured power is still too low, the Empower current may have to be increased. Increasing the current, however, is only a temporary fix and can greatly affect OPA tuning curves. Eventually, a realignment of the Spitfire will be required to restore output power at lower pump current.

Light from the optimized Spitfire is used to pump a pair of matching optical parametric amplifiers (TOPAS C). Internal alignment changes are seldom required, and the details of those alterations are not included in this document. Please refer to the manual or documentation from Schuyler Kain for details. Daily operation and optimization requires the OPA actuators to be set to positions known to produce efficient pulse generation. For studies performed in the near-infrared, 1300nm was commonly used as the daily reference point for much of the alignment process. For consistency, begin optimization with OPA1. Position the 407A behind Wi2. Adjust the pointing into OPA1 using M5 to maximize output power. From that local power maximum, adjust the pulse compression setting from the main window of the Spitfire software to further increase the OPA output power. This pair of actions should be repeated iteratively until there is no further improvement. Practically, the changes brought about by these actions are usually small enough to see no improvement from iterations beyond the first. Optimization of OPA2 is performed in a similar manner, but the 407A should (obviously) be positioned behind Wi3 and only the input pointing (using M3) should be adjusted. A BK7 window, Wi1, has been placed in the beam path before OPA2 in order to closely reproduce the chirp in the beamline sent to OPA1 produced by being transmitted through BS1. Because of this compensation, optimal compression for one OPA has been shown to be optimal for the other once tuning curves are established with any particular set of optics.

The next calibration step seeks to test and correct the OPA tuning curves. This process begins by closing OPA2. If the system was used in the past week, there should be no need to fully realign the table. If the beam is passing through the optical path of the table (easily determined by adjusting ND1 or ND2 to pass all light and checking for obstructions with a white note card), the tuning process will only require adjustment of M27 to pass the beam through the entrance slit of the monochromator. Monitor the detector voltage in LabVIEW to ascertain when the light is passing through the entrance slit. Adjust ND1 to ensure that voltage reported by Labview, multiplied by the integrator box scale setting (usually 1 or 0.5), does not exceed the maximum of the linear detection range of 0-2V of the currently-employed InSb detector. When adjusting this filter, be sure that you can see the back reflection of the beam on the black metal shield on the edge of the table. Rotate the filter to the point where the back-reflected spot hits the shield, but if rotated any more would be clipping the M12 mirror mount. If monochromator slits must be closed in order to achieve the desired voltage, close the exit slit. The entrance slit is usually set to 100μm for this step. If it is closed further, deflections caused by chromatic aberration from L1 may prevent light from other wavelengths from entering the monochromator. If L1 is achromatic, close both entrance and exit slits until the voltage levels return to the desired range.

From the COLORS main window (see Figure D, at the end of this appendix), in the ColorTune window accessed from the TUNE button, choose the "Test" tab, as circled in Figure 3. For the first investigation, leave the "Use tune points" box checked and run the module. The file produced provides spectral pulse profile Gaussian fit information for each tuning curve point. If the test results reveal that the tuning curve points all have nice Gaussian profiles (fit values all above 0.97), wavelength correction is sufficient. Simply substitute the value of the fit center for the corresponding wavelength entry in the tuning curve file. Once this substitution is complete, save the adjusted tuning curve file and close the TUNING window. Reload the OPA by going to the Advanced Controls window (ADV button) for the OPAs (Figure 4), and the ADV menu for that window (Figure 5). Reload OPA1, verifying that tuning curve file pathways still display. Close the most advanced window, then press the CAL ALL button in the first Advanced Controls window to reset the locations of the OPA actuators, making sure that the desired OPA is being calibrated, as indicated by the "OPA1…" or "OPA2…" in the upper left corner of this window. With the new tuning curve file now loaded, return to the TuneTest module, now running through the tuning curve in even intervals (instead of only at the tuning points), usually of 25nm. Check the TuneTest fit file to verify that the interpolated wavelength values are accurate.

If the TuneTest results reveal that the tuning curve has many points that have a poor fit to a Gaussian profile (less than 0.90 should certainly receive attention; more than half of the points below a fit quality of 0.95 should also draw some attention), an additional optimization step may be required. A poor Gaussian fit, particularly when accompanied by common amplitudes, is often an indication of wings in the pulse profile. The appearance of the plotted data points relative to the curve fit should confirm or deny this possibility. Many times, the presence of wings is an indicator of poor internal timing in the OPA. The addition of an offset to the D2 column of the tuning curve file may help correct this problem. With the beam directed into the monochromator and neutral density levels set as one would choose for a TuneTest, open the OPA advanced control window. Apply changes to the D2 actuator position to optimize the voltage reading from the detector connected to the output of the monochromator. Note the difference between the angles (as opposed to the microstep values) of the initial and final D2 positions. Enter this value into the tuning curve file and run a TuneTest to see if the wings have disappeared or the fits improved.

Repeat this tuning procedure with OPA2. It is advisable to block delay 1 for this process. The beamline coming from delay 2 is deflected vertically by chromatic aberration, so a more uniform pulse energy profile can be expected. With either of these two OPA2 beamlines, however, the spectral dependence of the beamsplitter (BS2) will lead to significant variation in power from one end of the tuning curve to the other. When adjusting ND2, send the back reflection through aperture A1. The reflected beam is already angled slightly upward, so there is little risk of sending the beam back into the OPA.

To avoid the appearance of beam power related artifacts in scans, it is important to ensure that there are no major variations in power as an OPA scans across its tuning range. To avoid the appearance of peaks and dips in data that are due solely to OPA intensity at specific wavelengths, run power smoothness tests for each OPA before attempting any experiments. These tests are run after the accuracy of the tuning curves have been tested and confirmed. Simply watch the voltage from the 407A as the OPA in study is scanned from one end of the tuning curve to the other. To avoid cross talk in BNC connector block (NI-BNC-2110), close one of the shutters for the monochromator before doing this scan. If the resultant scan shows any strong local dips or peaks (see Figure 6 for an example), then some optimization will be required. It is common for beam intensity to diminish significantly at the edges of a tuning range, for example as the BBO’s signal beam draws close to the degeneracy point; such power precipices may be difficult to correct.

The COLORS software includes a powerful tuning curve optimization routine called the SmartTune module. This module will iteratively optimize actuators in the OPAs at a single wavelength or for each point in the tuning curve. To make the most efficient use of this capability, it is important to perform some preliminary investigations. As in the procedure for determining a D2 offset, direct the beam into the monochromator and apply appropriate neutral density levels, then open the OPA advanced control window. Apply changes to each of the actuator positions in turn while watching the voltage reading from the detector connected to the output of the monochromator. C1 and D1 control the crystal angle and delay pertaining to the generation of the pre-amplified signal and idler beams. D1 ensures that the seed and pump are overlapped in time at the crystal; C1 is changes to ensure correct phase-matching for desired signal and idler outputs. C2 and D2 control the phase-matching and temporal overlap of the pre-amplified signal and the power-amplification pump. If changes of 50 microsteps in any of the four actuators yield an increase of detected light, make a note of it. Access the smart module via its tab in the TUNING window, as circled in Figure 7. Select the actuators in need of change in the order they are best optimized (usually D2 first, then either C2 or D1; C1 should rarely be changed) and two or three iterations. A color tolerance of 1% is preferable if you're trying to optimize the power of tuning curve points that already output light very near to their stated wavelength. After the module has been run to completion, the position of the OPA should reflect the best position discovered. Substitute those angle values for the corresponding values in the tuning curve file and rerun the power smoothness test. Variations of 10-15% or less from point to point are acceptable.

General table alignment follows OPA calibration. If major changes to the table were made since the last alignment, it may be necessary to repeat the procedure used when the table was first arranged (see Femtosecond Table Instrumentation in the Instrumentation chapter). To generate reproducible experimental conditions, it should only be necessary to vary alignment into retroreflectors, pointing into the focusing mirror, and overlap at the sample cell position.

Alignment into the retroreflectors is both important and simple. If the beams are not parallel to the translation axis of the delay stages, then any movement of the stages will result in pointing changes. A series of irises have been positioned such that, if aligned to, the desired angles can be achieved. Use W1 to align to A1 and M6 to align to A2. Verify that the corresponding beamline also passes through the center of A3. Similarly, adjust W2 to direct the beam through A4 and M14 to direct through A5. The OPAs emit light intensely at the calibrated wavelength and weakly at various other sum frequencies and harmonics. Near-IR experiments commonly use 1300nm for this alignment step. At this setting, a small red dot at about 650nm (the doubled signal light) is spatially aligned with the desired 1300nm light (an IR viewer and the power meter verify this claim). Align the red spot, not the white/blue/green blur.

A mounted metal plate with graph paper is used to reproduce beam pointing into the spherical focusing mirror, FM1. The graph paper has dots drawn on to indicate the desired position of the beams. At the first mask position (MP1), use the actuators on the retroreflector stages to align to the inner perimeter of dots. Loosen the knobs that are used to hold the stages firmly in place before adjusting the corresponding actuators. Move the mask to its second location (MP2) and use M8, M10, and M16 to overlap the beams with the outer ring of dots. Iterate between these two steps until each beam is overlapped with its dot at both MP1 and MP2. Tighten the translation stage knobs again; slight vibrations can dramatically change temporal overlap if those stages are not fixed in place. The motorized delay controls work on different stages that are significantly more stable.

When the pulses differ in frequency by hundreds of wavenumbers, the change in index of refraction in quartz (as found in the sample cell windows) will induce a shift in the relative delay up to 15fs. In order to eventually account for this shift, insert into the beam paths, just after

M22, a piece of quartz with thickness about 1mm. This insertion may cause slight pointing changes, so it is important to perform all spatial alignments with this quartz in place.

The preceding procedure brings the beams close to spatial overlap at the sample cell position. To further improve the overlap, place a pinhole (50 or 100μm should be small enough) in the sample cell position. Note the z-axis position of the translation stage, as its position in future alignment and calibration steps will be chosen relative to this point. It has been common to choose “5.00” (as in 500/1000 of an inch) as the position for the pinhole. Adjust the x- and y-axis positions of the sample cell stage to allow as much intensity from the three beams as possible. Then, using either a power meter or visual inspection, again adjust mirrors M8, M10, and M16 until all three beams pass through the pinhole as efficiently as possible. Final overlap optimization will be performed in the next step.

Once the beams are overlapped in space, it is possible to calibrate their overlap in time. Place the BBO in the sample stage perpendicular to the z-axis and move the z-axis position 0.200 inches closer to the laser source. If an actuator reading of “5.00” was used for the pinhole, move the stage to the “7.00” position. Adjust the neutral density filters ND1 and ND2 to let most light pass. The signal-to-noise ratio improves dramatically when working with pulses of energy 8-10mJ instead of the hundreds of nanojoules used in careful PbSe nanocrystal experiments. Performing the initial calibration with OPAs set to 1300nm should make most of the nonlinear processes of interest visible to the naked eye. Place a note card or white beam stop far enough from the crystal to see the three transmitted (and spatially-overlapped frequency-doubled) beams separated from each other; immediately before mirror M25 is a good location. Double check to ensure that the beams are passing through BBO material, as there are cracks in the crystal (from overheating when initial delay calibration was being performed) and gaps where the crystal no longer is. Though the rotation of the crystal should be adjusted to minimize scatter and optimize sum frequency light, if no non-linear light is visible, a starting angle reading of 40 degrees has worked for vertically polarized light in the past. If the delays were calibrated the day before, sum frequency peaks located between any pair of the transmitted beam spots may already be visible. If no such delay dependent spots are visible, note the position of the z-axis actuator controlling the w1 beamline retroreflector (RR3), loosen its tightening screw, and use it to translate that delay stage slowly. Perfectly spatially-aligned beams will overlap in time for less than 10μm of delay stage translation, so it can be easy to miss. As soon as some sum frequency light has been seen for both ω1/ω2 combinations, tighten the delay stage and use the main window of COLORS to provide the delay adjustments needed to easily see light from each combination of beams.

In order to obtain a reliable calibration of the relative pulse delays and characterize their temporal profiles, it is important to fit the intensity of each sum frequency peak as it changes with delay. It is complicated to coordinate monochromator settings for each delay scan in an upcoming alignment step, so use the ThorLabs PM100D detector for this process instead of the InSb. Remove the BNC cable connected to the “Last Sample” output or “Averaged Output” on the boxcar integrator, shown in Figure 8 and connect it to the output from the ThorLabs detector control box. Make sure that the settings of the ThorLabs detector are set to 675nm sensitivity (or even further to the red) with a scale maximized at 1.10μW. If the OD1 neutral density filter had been attached to the detector head, remove it. The detector will power down after a while if the AC power adapter is not plugged in. Because of the possibility of drifting “ground” between different power outlets, be sure to have the BNC cabling in electric contact with some other device, or a high DC voltage may be the only reading to appear from the ThorLabs detector in the COLORS software. Pulse delays are very sensitive to air currents in lab, so if experiments will be making use of a chopper, make sure that it has been on for at least 30 minutes so that the ambient conditions are in a steady state. Position the detector directly in front of aperture A7 with a small iris immediately after mirror M26. Adjust the height and lateral location of each of these objects to select and isolate each sum frequency beam, in turn. Begin by isolating the beam located between ω_1 and $\omega_{2'}$, controlled by D1 (and placing a card in front of A3 to block the ω_{-2} beamline).

Before scanning the delays, it is important to establish reasonably stable lighting conditions. This can be done by turning the lights off and standing very still to avoid casting a shadow on the detector, or by covering part of the table with black felt to prevent ambient light from hitting the detector. Once lighting conditions are stabilized, open the PulseScan module in COLORS and select D1 as the scanning variable. Start the scan about 200fs higher than the best estimate for the delay of overlap (which may be 0fs, if you were already close to calibrated), and end it 200fs lower. 20fs steps should be sufficient for this stage of the procedure. When the scan has completed, there should be a Gaussian fit profile overlaying the data points and a value for the full width at half max, as shown in Figure 9. Click on the ZERO button at the bottom of the screen to set the center of this distribution as the location of zero delay. This act should also move the delay to that position. Watching the signal strength on the main window, adjust the pointing of M16 until the SFG light is maximized. This procedure should verify that the spatial overlap is optimal. As this pointing change may induce slight timing adjustment, it will be necessary to reset the zero position, but this will be accomplished after accounting for the pulse timing variations due to spectral tuning.

Calibration of D2 and verification of pulse widths will follow, but if scans are to be performed at any laser frequencies other than those used to calibrate delays, it will be necessary to run the ZeroTune module. This process accounts for changes in delay caused by varying crystal angles in the OPAs and the changes in quartz refractive index mentioned earlier—which together can introduce an error of the same order as the laser pulsewidth. While aligned to calibrate D1, open the module and select OPA1 corrections. This routine will measure the delay at different laser wavelengths and use that information to adjust the physical location of "zero" any time the wavelength is moved. Verify that the settings match the desired delay and wavelength range, then run the module. When it is complete, the main COLORS window should indicate that the correction array has been created. Run the module again, but do so for OPA2 D1, instead.

Reposition the iris and the detector to measure the SFG beam created by ω_1 and ω_{-2} (D2). Repeat the procedure above to find a rough zero, optimize overlap (now using mirror M10), and measure the delay corrections needed by OPA2 D2.

With all of the spectral correction arrays created and loaded into COLORS, set the OPAs back to 1300nm and set the zero points for D1 and D2. Lastly, position the detector between the beamlines for $\omega_{2'}$ and ω_{-2} and use the pulse module to plot sum frequency intensity as a function of relative delay with one of the delays set at 0fs. This scan should confirm the calibration and serve as an autocorrelation plot for purposes of divining pulse temporal width.

The last stage of alignment couples the desired four-wave mixing output into the monochromator. Reconnect the BNC cable from the ThorLabs detector to the boxcar ("Last Sample" when no chopper is used, "Averaged Output" when using active background subtraction). Verify that the Polarity Control AVERAGED OUTPUT switch on the back of the boxcar averager is set to "toggle" for active baseline subtraction experiments. Close A7 until it blocks all three laser lines, but passes any light that might be four-wave mixing light. Silicon produces strong four-wave mixing signal from wavelengths in the near-infrared out to several microns. Place the silicon plate in the sample cell position and move the stage to a z-axis position of "9". At D1 = D2 = 0fs and $\omega_1 = \omega_{-2} = \omega_1$, there will be plenty of light. Increase the neutral density until each beam has no more than the energy desired for subsequent experiments. Adjust the pointing of M27 until the signal is optimally pointed into the monochromator and verify that it is signal by testing its dependence on each beamline. Next close A7 until the aperture is as small as it can be without constant pressure. Change the height and horizontal position of this aperture until the most light passes through, then open it back up to as much as 1cm in diameter. In similar fashion, but using the positioning screws whenever possible, optimize the position of A6. Leave A6 no more than 2 or 3mm open. These two apertures do much to limit the amount of scatter reaching the detector from transmitted beams.

Finally, place the sample cell into its mount and remove the piece of quartz between M22 and the sample cell. The z-axis position should be adequately close to that used for the silicon wafer. For PbSe quantum dot samples, a monochromator front slit width of 200μm and a back slit width of 350μm have been found to be suitable for minimizing scatter and retaining sufficient spectral resolution. If the scatter-to-signal ratio is still high, adjust the horizontal and vertical position of the sample cell to move away from any regions that might have scratches or laser-induced salt deposits. All the rest is in the experimental design.

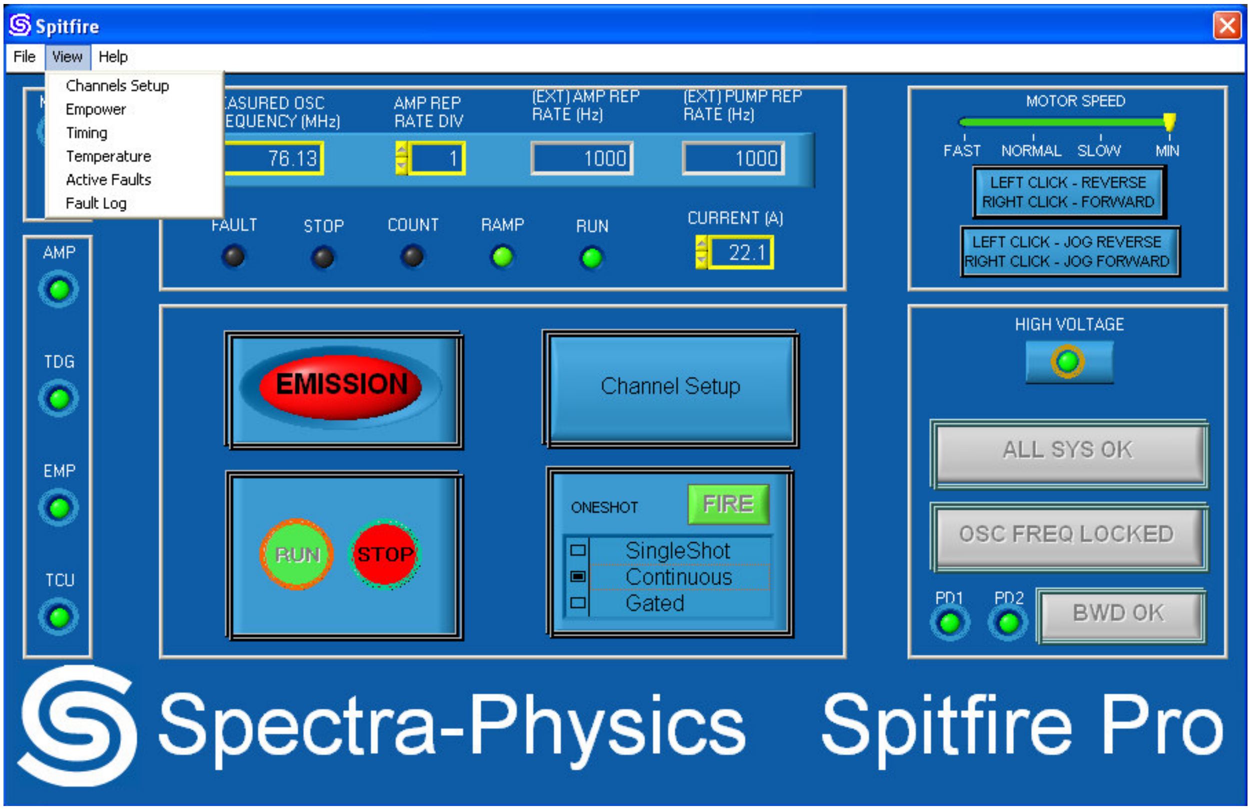

ASURED OSC EQUENCY (MHz): 76.13

AMP REP RATE DIV: 1

(EXT) AMP REP RATE (Hz): 1000

(EXT) PUMP REP RATE (Hz): 1000

CURRENT (A): 22.1

☐ SingleShot
▣ Continuous
☐ Gated

Figure 1— Spitfire Main window. Notice the Empower current set at 22.1A. Notice the oscillator frequency at 76.13MHz. Notice the indicator lights on the left revealing that the amplifier, the Timing Delay Generator, the Empower, and the Temperature Control Unit are all powered. Notice from the grayed-out "Run" button and the illuminated red "Emission" indicator that the Empower is on. Notice that the two photodiode indicator lights (labeled PD1 and PD2) are illuminated, indicating that the seed is mode-locked and at least close to correctly aligned. In cases where the seed alignment is poor, the observed oscillator frequency will fluctuate and the grayed-out "OSC FREQ LOCKED" button will be yellow and the cavity will be sealed-off. Correct alignment and press the yellow button to reset the error and enable amplifier activity. In cases where the seed alignment is poor or has lost mode-locking, the bandwidth detector (BWD) will close the cavity and the grayed-out "BWD OK" will be yellow. Reestablish mode-locking, ensure that the two photodiode indicators are illuminated, and press the yellow button to reset the error. Lastly, notice in the top right corner the controls for the compressor mirror delay. These controls are not optimal, but are functional. The button will not appear to be depressed when using the right-click action, but the delay is still moving. Do not use the "jog" buttons during regular alignment; the movement speed is too high. After amplifier realignment, large adjustment may be needed. Slide the MOTOR SPEED setting from MIN to SLOW or NORMAL by left-clicking and dragging the yellow pin to the desired setting, then quickly left-clicking on the new setting again to confirm that the move was intentional.

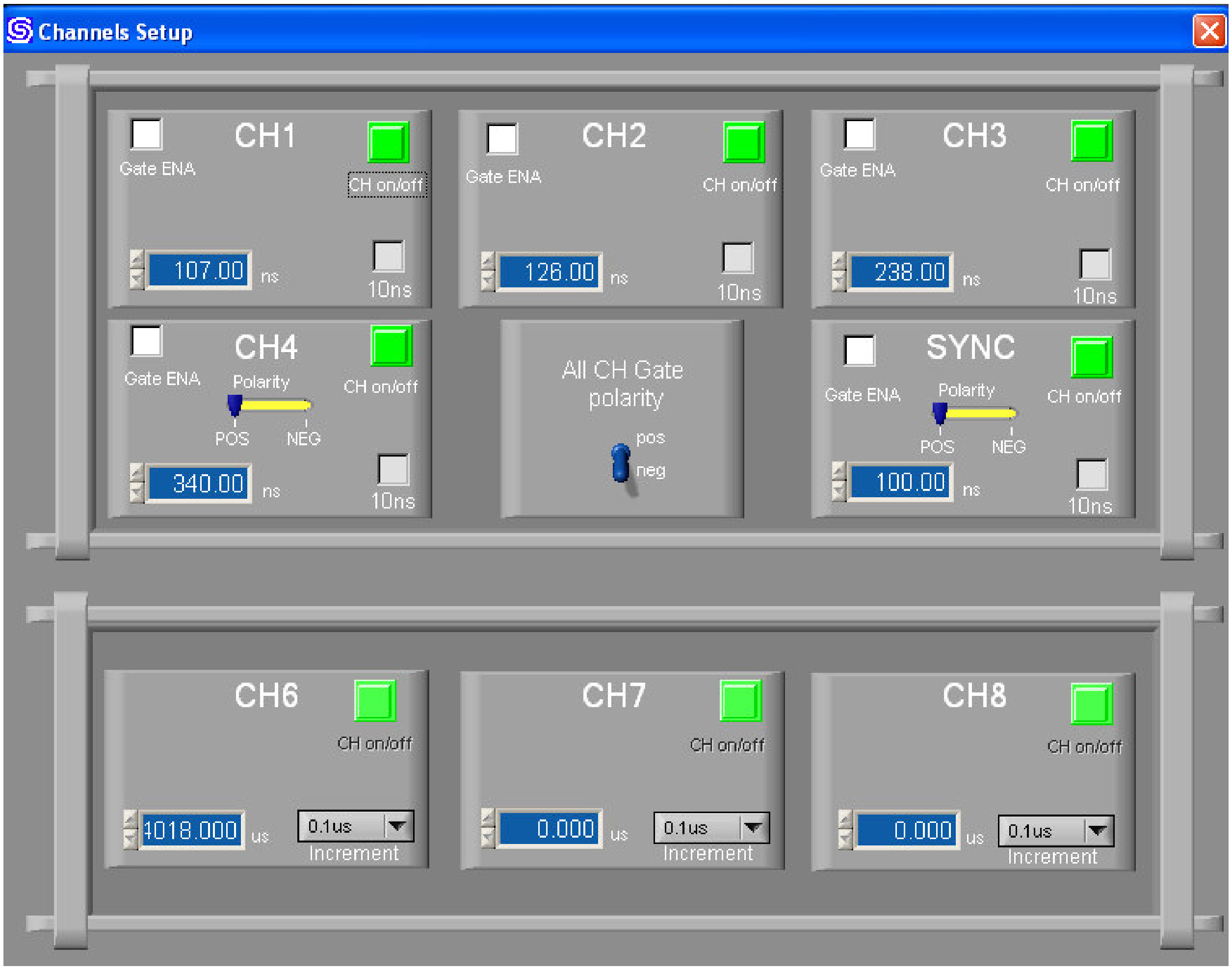

CH1 107.00 ns

CH2 126.00 ns

CH3 238.00 ns

CH4 340.00 ns

SYNC 100.00 ns

CH6 4018.000 us 0.1us

CH7 0.000 us 0.1us

CH8 0.000 us 0.1us

Figure 2—Spitfire Channels Setup window. Notice that all Pockels cells channels are currently turned on, as indicated by the depressed and illuminated green buttons to the right of each channel name.

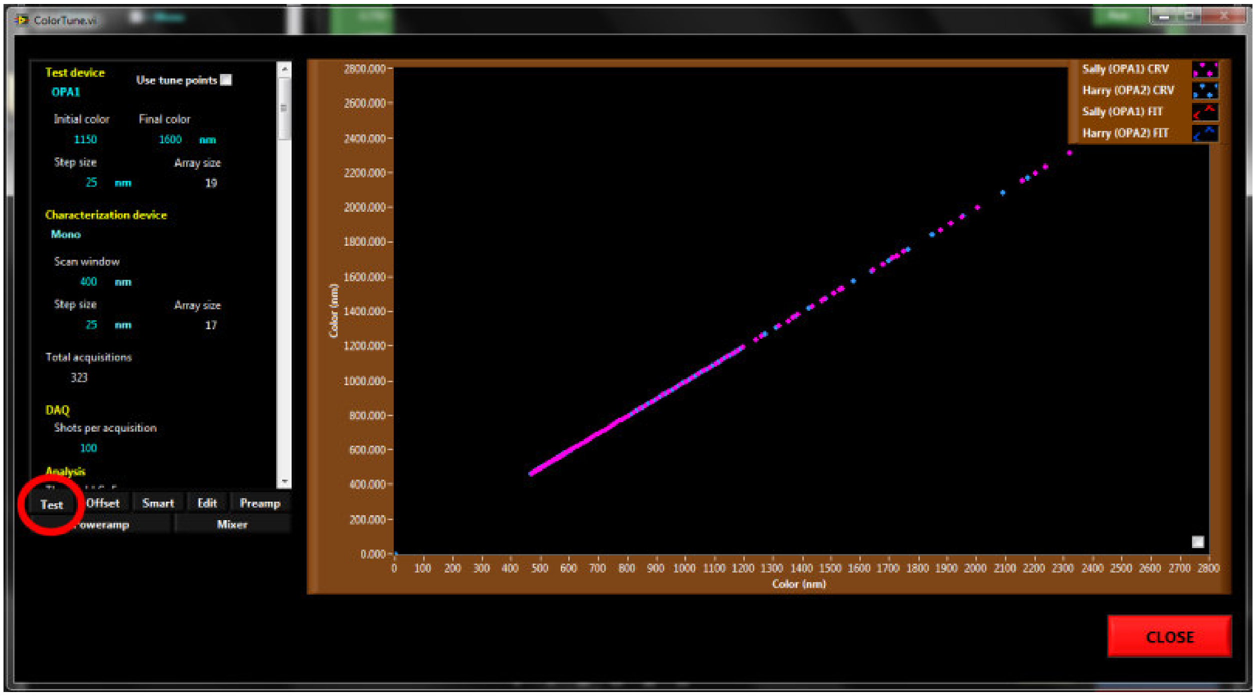

Test device
OPA1
Use tune points ☐
Initial color 1150
Final color 1600 nm
Step size 25 nm
Array size 19

Characterization device
Mono
Scan window 400 nm
Step size 25 nm
Array size 17

Total acquisitions 323

DAQ
Shots per acquisition 100

Figure 3—Running a TuneTest from the ColorTune window "Test" tab (indicated by the red oval).

	Affix	Geometric	Microsteps	New	Scan motor	500 step window
Crystal 1	-16.904 deg	-4.271 deg	3032	3032	Off	CAL
Delay 1	0.000 mm	2.432 mm	7783	7783	Off	CAL
Crystal 2	-145.900 deg	8.325 deg	37014	37014	Off	CAL
Delay 2	-100.167 deg	-53.775 deg	11134	11134	Off	CAL
Mixer 1	0.000 deg	0.000 deg	0	0	Off	CAL

	OPA	Mixer1	Mixer2	Mixer3
Process	Signal (S)	None	None	None
Polz'n	V	V		

Figure 4—Topas "Advanced" controls. Common uses in alignment are described in the main text. To manually change an actuator, enter the desired microstep value in the appropriate row of the "New" column and press the "MOVE!" button. Alternatively, press the "CONT" button for continuous reading of the "New" column and either enter the desired new position or place the cursor after any digit in the existing entry and use the up and down arrows on the keyboard to change the values. In each case, the change will have taken place by the time the value shown in the "Microsteps" updates. The "Geometric" column is the physical position or angle of the corresponding OPA element. The "Affix" is a static offset. The geometric angle is calculated by multiplying the Microsteps value and a conversion constant, then adding the affix.

Topas Advanced

OPA1

OPA1 WinTOPAS config file C:\Users\John\Desktop\COLORS\Topas\
OPA1 IR tuning curve file C:\Users\John\Desktop\COLORS\Topas\
OPA1 Mixer 1 tuning curve file C:\Users\John\Desktop\COLORS\Topas\
OPA1 Mixer 2 tuning curve file
OPA1 Mixer 3 tuning curve file

OPA2

OPA2 WinTOPAS config file C:\Users\John\Desktop\COLORS\Topas\
OPA2 IR tuning curve file C:\Users\John\Desktop\COLORS\Topas\
OPA2 Mixer 1 tuning curve file C:\Users\John\Desktop\COLORS\Topas\
OPA2 Mixer 2 tuning curve file
OPA2 Mixer 3 tuning curve file

Motor affixes				Filter limits		(Set limits=0 to disable a filter)			
C1	0.00000(	-16.904(	deg	F0	1110	1110	1600	1600	nm
D1	0.00000(	0.00000(	mm	F1	955	955	1150	1150	nm
C2	0.00000(	-145.90(	deg	F2	720	720	970	970	nm
D2	0.00000(	-100.161	deg	F3	530	530	730	730	nm
M1	0.00000(	0.00000(	deg	F4	410	410	540	540	nm
					Lower		Upper		
C1	0.00000(	-12.000(	deg	F0	1110	1110	1600	1600	nm
D1	0.00000(	0.00000(	mm	F1	955	955	1150	1150	nm
C2	0.00000(	-145.90(	deg	F2	720	720	970	970	nm
D2	0.00000(	0.00000(	deg	F3	530	530	730	730	nm
M1	0.00000(	0.00000(	deg	F4	410	410	540	540	nm

Figure 5—Topas Advanced Advanced window. When adjusting tuning curve files, this window can be used to reload the curves into LabVIEW. Simply press the appropriate RELOAD button. If the file path still appears on the left-hand side of this window, then the reload was successful.

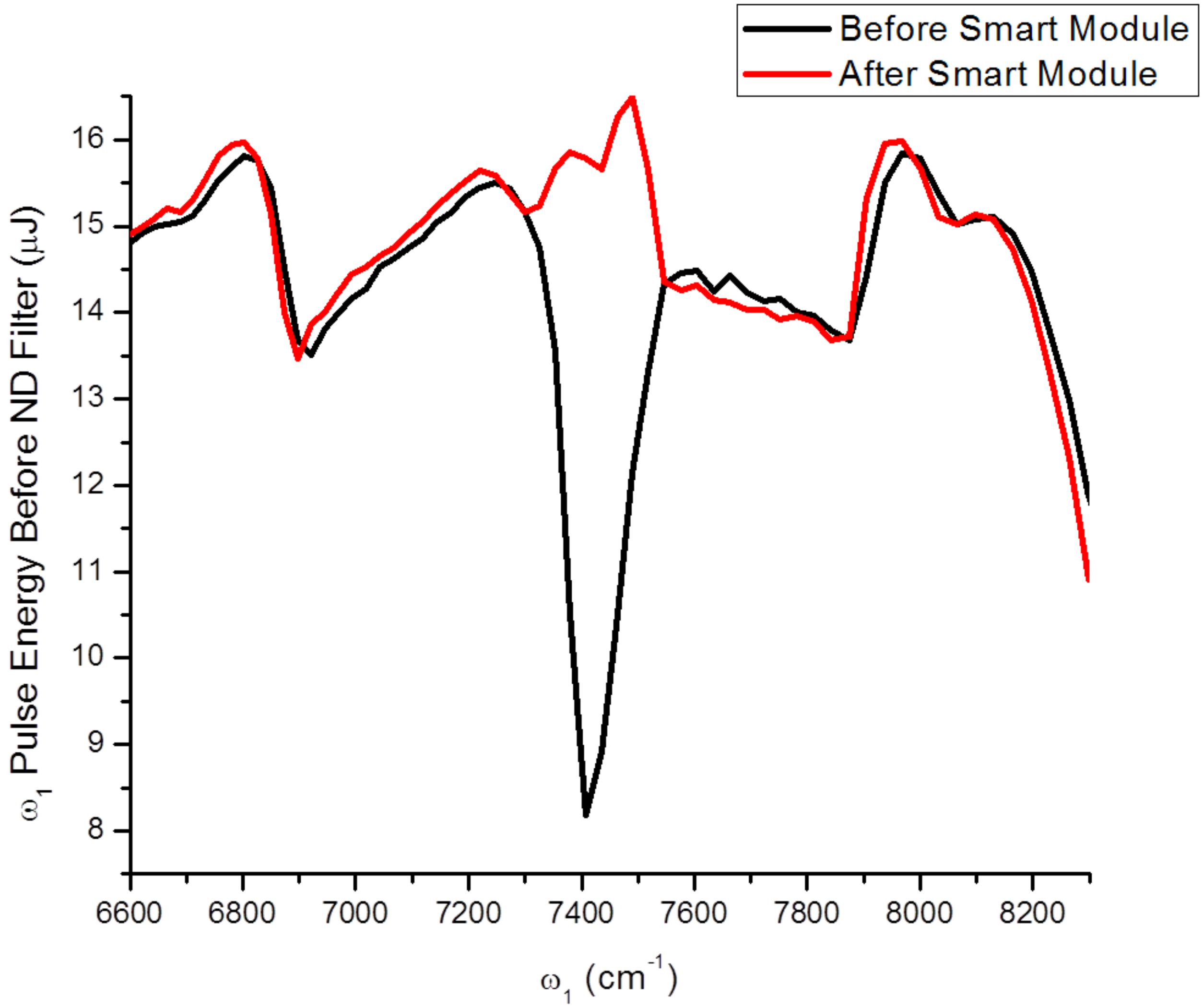

Figure 6—The influence of the Smart module correction. Shown above is the pulse energy at the output of OPA1. Before applying the correction algorithm, the output power profile (black) shows an abysmal dip near 7400cm^{-1}. After actuator optimization, the profile (red) has been smoothed nicely.

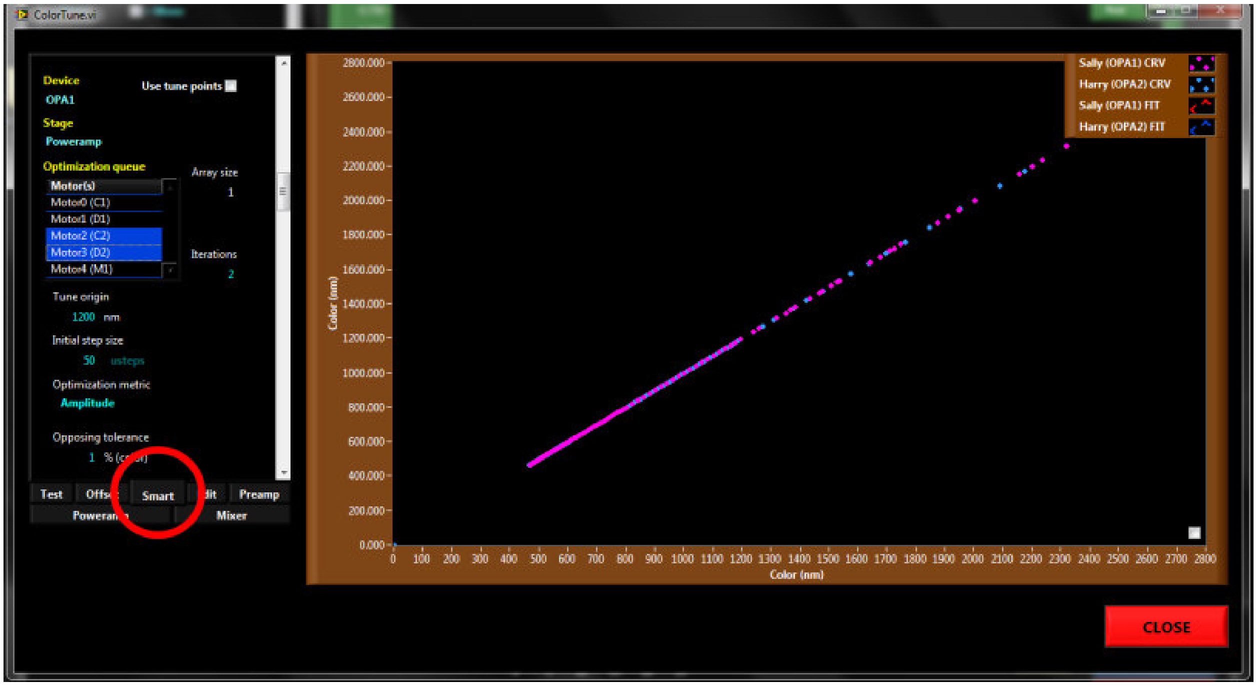

Device
OPA1

Use tune points ☐

Stage
Poweramp

Optimization queue

Motor(s)
Motor0 (C1)
Motor1 (D1)
Motor2 (C2)
Motor3 (D2)
Motor4 (M1)

Array size
1

Iterations
2

Tune origin
1200 nm

Initial step size
50 usteps

Optimization metric
Amplitude

Opposing tolerance
1 % (color)

Figure 7—Running the Smart module from the ColorTune window “Smart” tab (indicated by the red oval).

Figure 8—Boxcar averager. Notice in particular the output cable (shown with red tape) connected to the "AVERAGED OUTPUT" BNC, used when active background subtraction

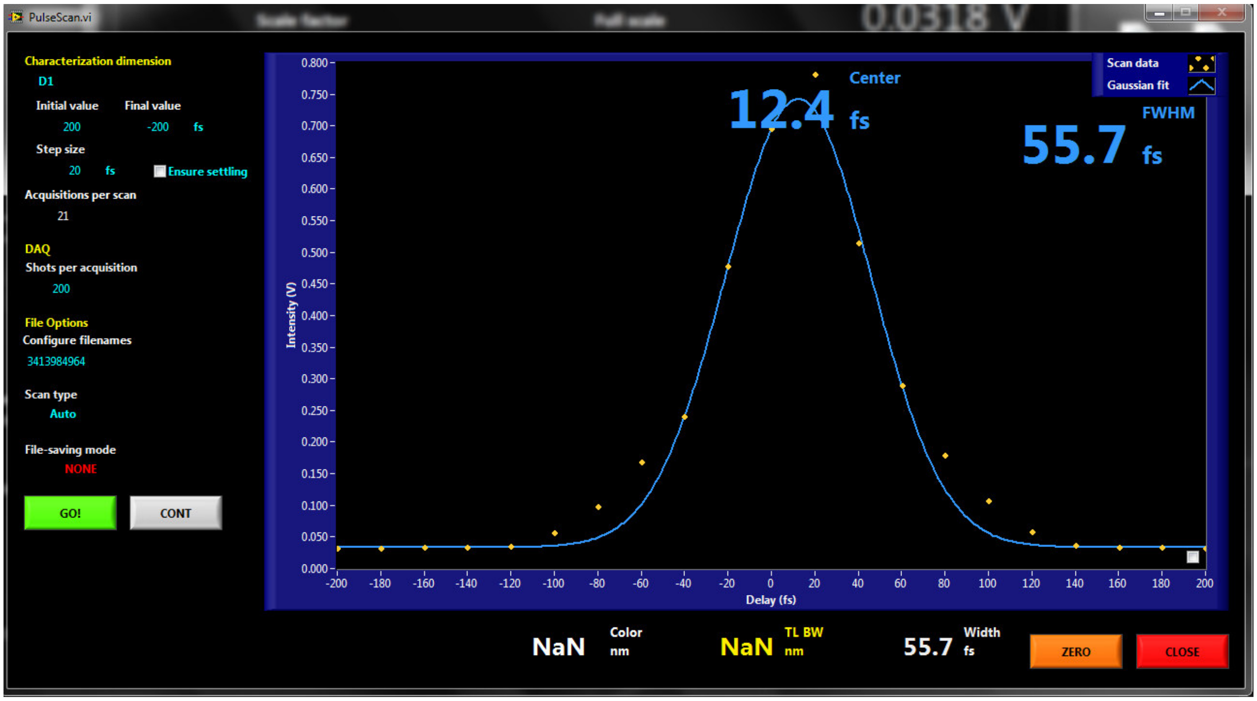

PulseScan.vi

Characterization dimension
D1
Initial value: 200
Final value: -200 fs
Step size: 20 fs
☐ Ensure settling
Acquisitions per scan: 21

DAQ
Shots per acquisition: 200

File Options
Configure filenames: 3413984964

Scan type: Auto

File-saving mode: NONE

Center: 12.4 fs
FWHM: 55.7 fs

NaN Color nm
NaN TL BW nm
55.7 Width fs

functionality is enabled. In experiments without a chopper, the LAST SAMPLE output (two rows below AVERAGED OUTPUT) is used.

Figure 9—PulseScan module, shown after a delay calibration scan. Notice the Gaussian fit and the displayed Center and FWHM values.

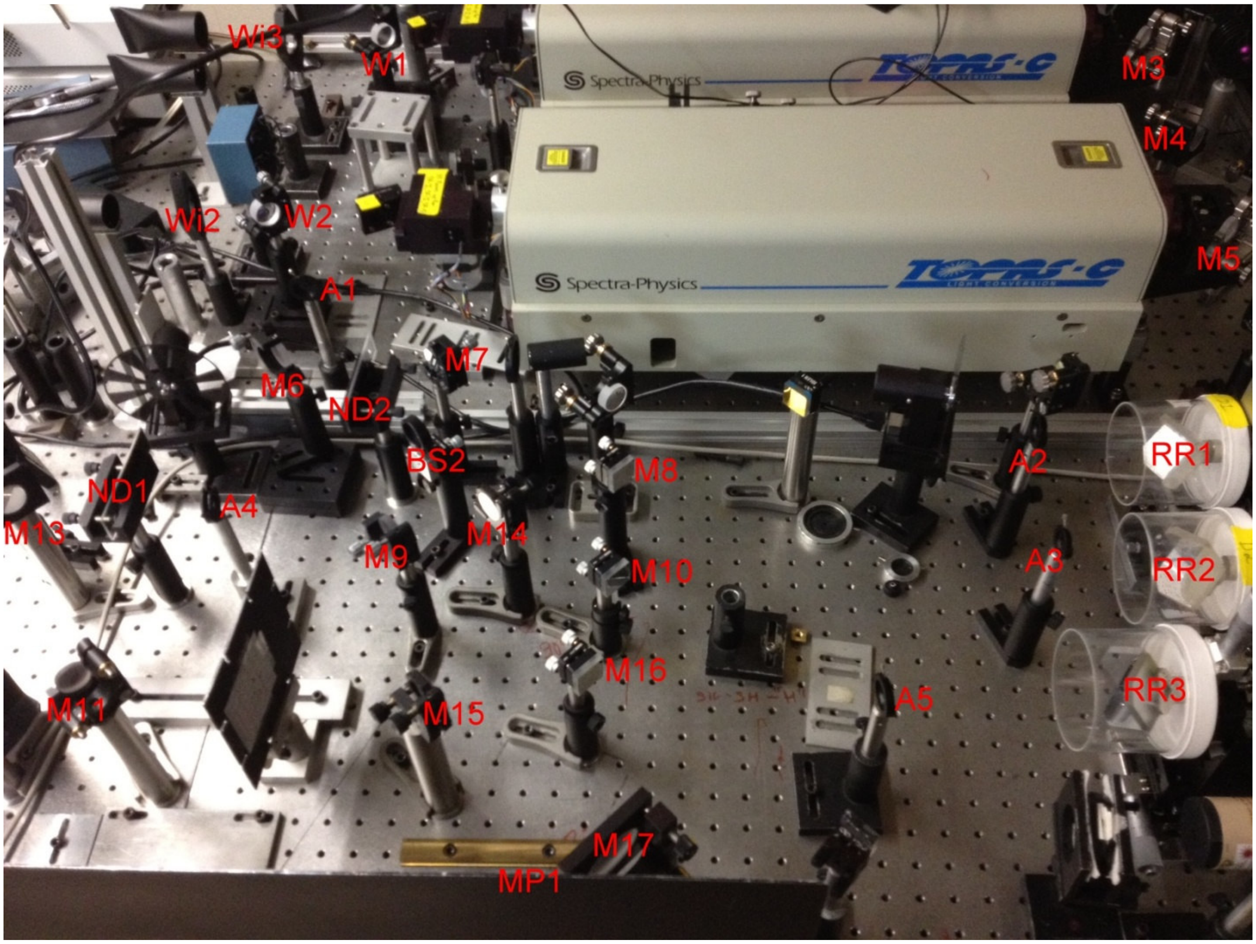

Figure A1—Optical table arrangement with element labels.

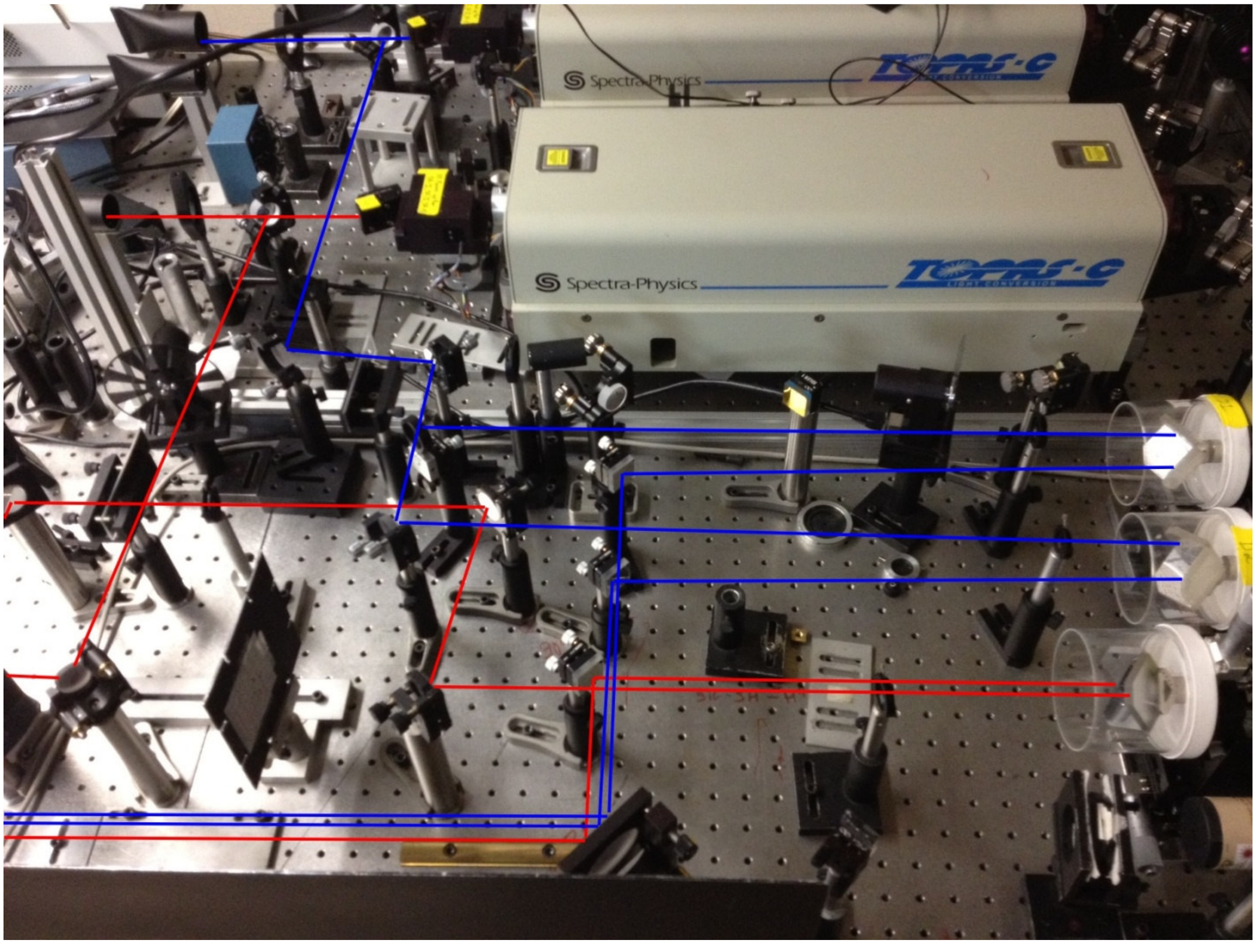

Figure A2—Optical table arrangement with beam traces. Blue traces show the paths of ω_2 and $\omega_{2'}$. Red traces show the path of ω_1.

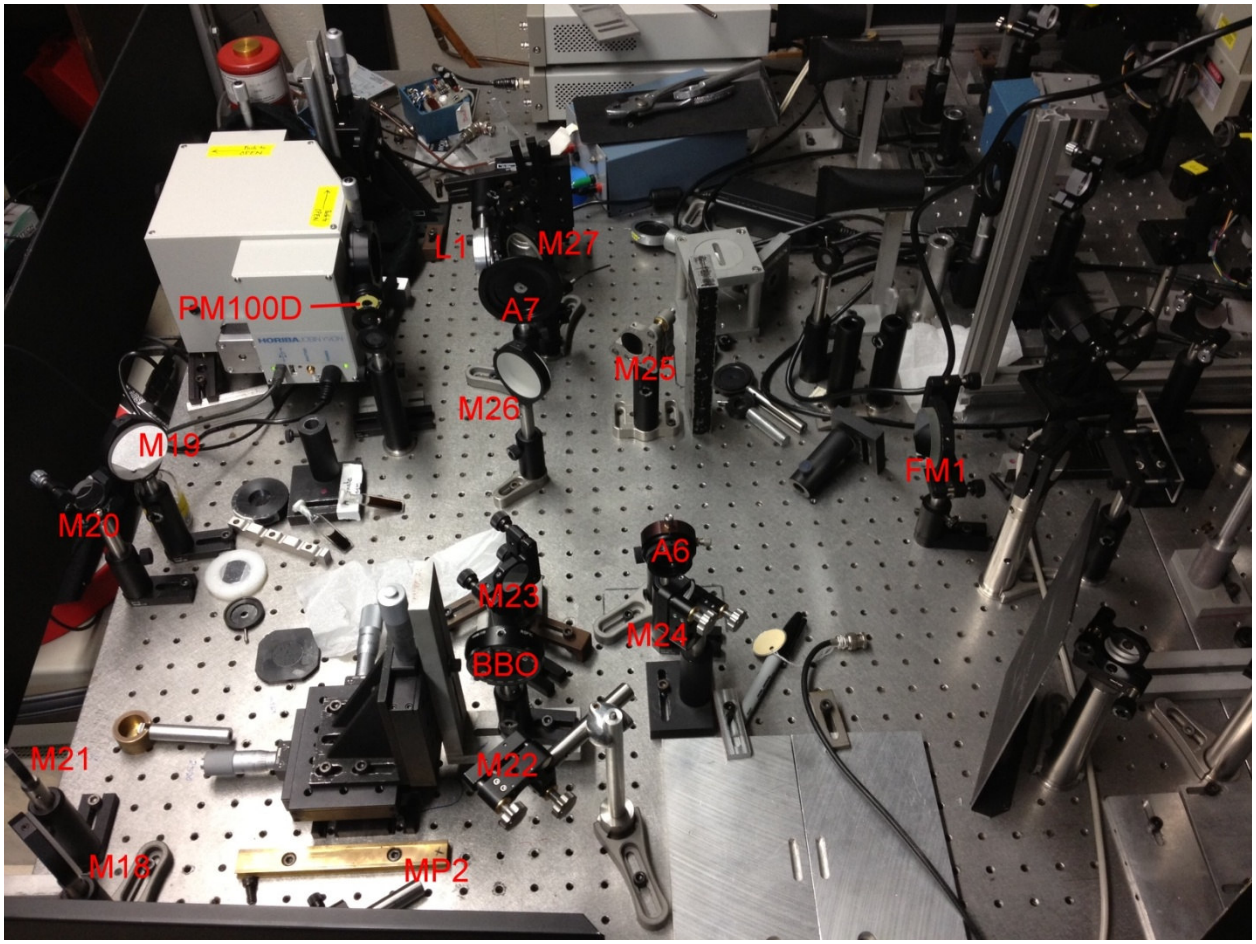

Figure B1— Optical table arrangement continued down-stream. The PM100D is shown out of beam paths. The BBO is shown in the sample cell position.

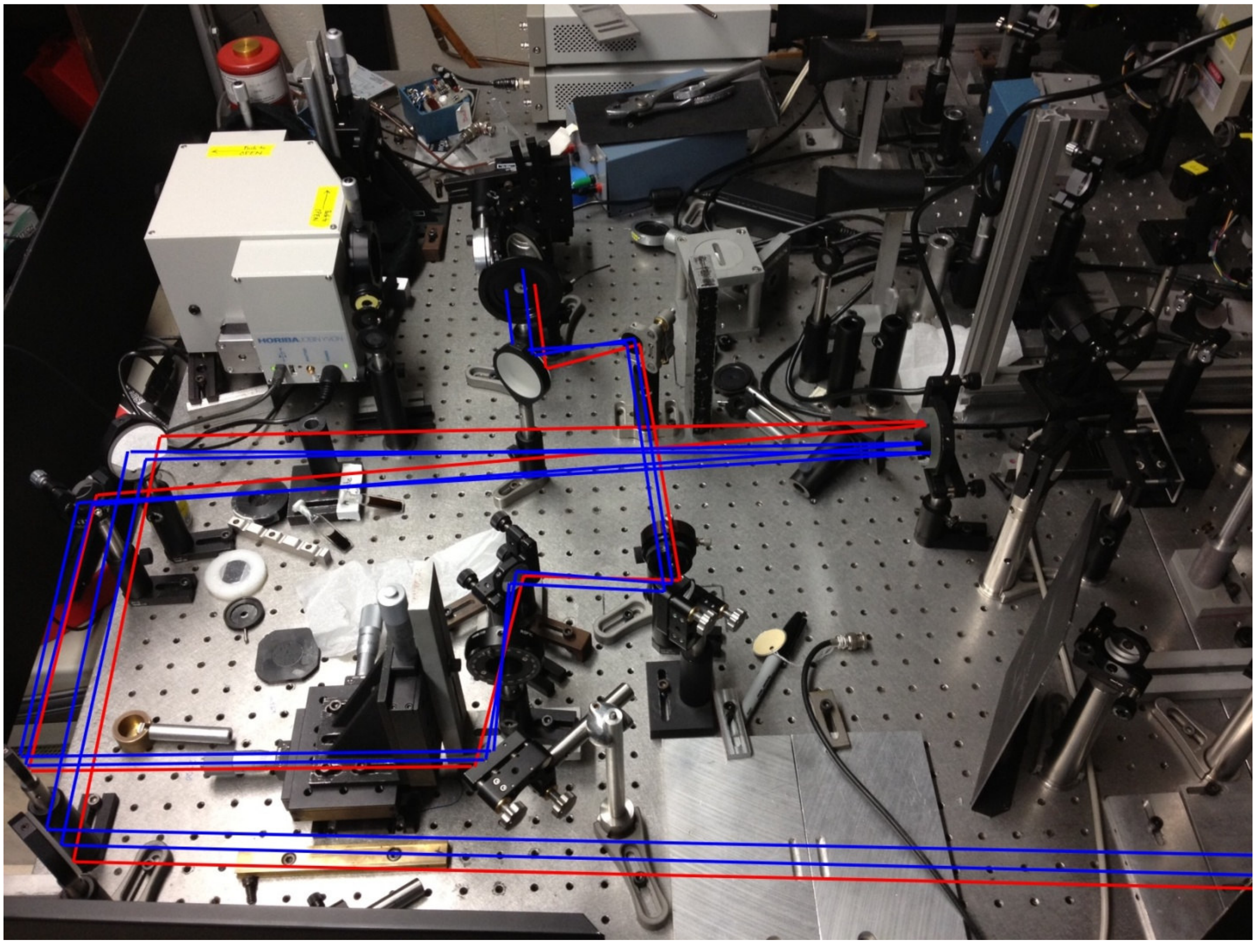

Figure B2— Optical table arrangement continued down-stream with beam traces. Blue traces show the paths of ω_2 and $\omega_{2'}$. Red traces show the path of ω_1.

Figure C1— Optical table near the OPAs with element labels. The figure shows the area after the OPA area enclosure was completed and the chirp compensation window (Wi1) was placed before OPA2.

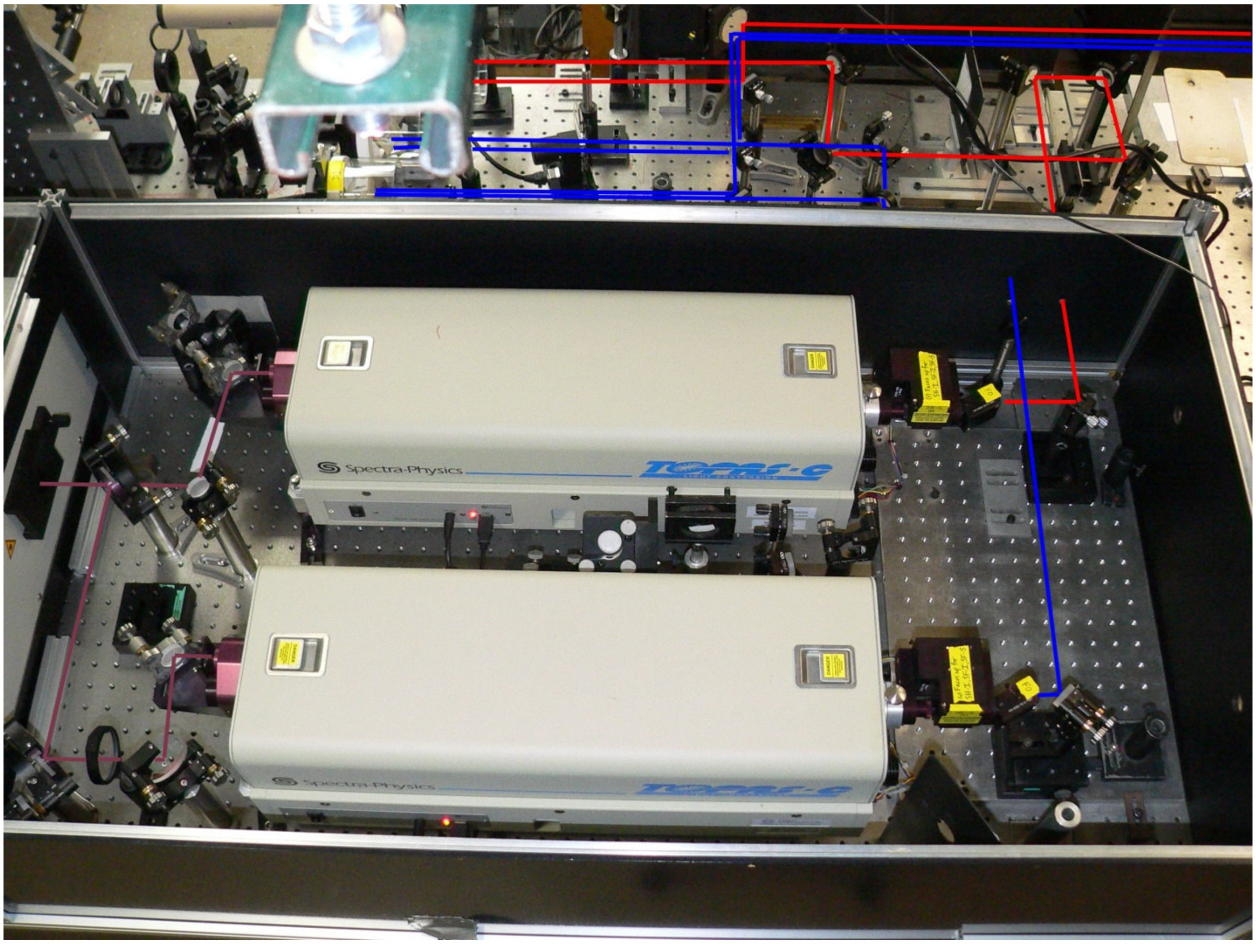

Figure C2—Optical table near the OPAs with beam traces. Blue traces show the paths of ω_2 and $\omega_{2'}$. Red traces show the path of ω_1. Violet traces show the amplifier output as it pumps the OPAs.

COLORS v0.93b (beta25).vi

Color dimension

Mono ☑ + Mono

Initial color 8500 Final color 6350 cm-1

Step size 25 cm-1

Total acquisitions 87

DAQ

Shots per acquisition 2000

Estimated time 0.00 min

File Options

Configure filenames 3413979628

Elapsed time

OPAs

	Shutter	Polz'n	Output color	
OPA1		V	1300.00	1300.00
OPA2		V	1300.00	1300.00 nm

OPA1 No error

OPA2 No error

Delays

D1 Relative position 0.00000 0.00000 fs

D2 Relative position 0.00000 0.00000 fs

D1 READY from MOVING mode: @ No error

D2 READY from MOVING mode: @ No error

Monochromator: JY microHR

Central color 1299.99 1300.00 nm

Grating #1 (150 gr/mm, 1200 nm blaze)

Bandpass 0

0

Figure D—COLORS main window. Scan parameters are set in the upper left corner. Simple OPA, monochromator, and delay controls are shown at the bottom of the window. ColorTune and PulseScan modules are accessed by the TUNE and PULSE buttons in the lower right corner. An active report of voltages for various channels is shown across the top. The tabs below this voltage screen also provide the option of watching the scan in progress (“Current Scan”) or plotting and processing existing data (“Post Processing”).

Appendix D: Power Measurement With "The Pig"

Calibrating pyroelectric detectors can be fun and educational, but before you decide to do so, there are a few things you should know.

First of all, the voltmeter requires that two leads find their way from the meter to the pig. The pig, however, has plugs for four tails, so you must choose wisely. In this case, the two black plugs are the signal plugs; connect the pig to the voltmeter by plugging the two leads into the two black plugs. Just leave the red ones alone. I know… but leave them alone anyway. The appropriate sockets have been labeled. Are you happy now? The other two plugs were simply used for calibrating the pig—run a known current through a known resistor… produce a known heating.

Next, verify that the 9V batteries still have sufficient charge for effective use. Switch the voltmeter box to the "battery check" setting. If the needle passes into the green region when the setting is on volts, then life is good (~9V is very good).

To ensure that you and the voltmeter are on good terms, switch the voltmeter to "zero check" and verify that it is reading zero when everything is shorted out inside. Once that is done, you're ready to step into the world of pyro calibration.

Line up the opening to the pig without actually letting the tracer beam hit the detector much. The detector in the pig takes a long time to cool down, so minimizing the amount of energy it gets is key. This alignment may require shorter legs or use of various stands; be creative if need be. When the pig is aligned such that the beam travels down the cavity of the pig perpendicular to the detector, turn off the HeNe and get the OPAs ready.

To calibrate pyros, it is important to make use of two polarizers—one to provide continuous adjustment of power and one to make sure that the polarization running through the system is always vertical by the time it reaches the beam splitters (it will be horizontal coming out of the OPAs, and rotated by periscopes). For more information as to why this is the case, look up information about Brewster’s angle and/or reflected and transmitted energy as it relates to polarization. See pp73-78 in Guenther’s Modern Optics text (John Wiley, 1990) for some explanation. Anywho, leave the pig blocked for a bit as you get the polarizers set up; you’ll use the pyros to find the initial setting of these polarizers. Put the last polarizer (last meaning the one that encounters the beam last) into place. Adjust the polarization angle to allow the maximum amount of light through possible. Now put in the second polarizer and set it to block out all light entirely.

If any light was allowed into the pig, it may still be warm. Make sure that it is allowed plenty of time to stop its decline (often 30 minutes or more if you gave it a good zap with the HeNe). Once it seems to have stopped moving (as visible on the 3 or 1 microvolt scale), set the zero level. Now is the time to open up the OPA to be used for pyrocalibration. Your initial reading should be close to zero, both on the voltmeter and in Labview (reading the setting for the appropriate pyro). Record data points at intervals as you slowly rotate the polarization of the first polarizer (according to beam path, again). Once you’ve reached the maximum in this manner, take another datum by removing the first polarizer. The last datum should follow by removing the last polarizer (the setting angle of which should not have been changed throughout this process). If done correctly, a linear plot of pyro voltage vs. pig signal should follow. Note pig voltage-to-power conversion factors. Sample data handling can be found in the TRIVE folder “pyro calibration” (at the time of this writing).

Appendix E: Fluence Calculations

$E_1 := 1000$ $E_2 := 700$ $E_{2p} := 450$

Values (in nJ) pulled from chart, accounting for neutral density attenuation

$\nu_1 := 6950$ $\nu_2 := 6950$ $\nu_{2p} := 6950$

Beam frequencies in wavenumbers

$$E_a(E) := E \cdot .972^6 \cdot .96$$

$E_{1a} := E_a(E_1)$ $E_{2a} := E_a(E_2)$ $E_{2pa} := E_a(E_{2p})$

$E_{1a} = 809.597$ $E_{2a} = 566.718$ $E_{2pa} = 364.319$

Adjusted pulse energy accounting for losses from the last 6 mirrors and quartz cuvette surface

$E_{1s} := \dfrac{7060}{8065}$ $E_{1s} = 0.875$

The central energy of the 1S absorption distribution, converted into eV (see table at right)

$s := \dfrac{263.5}{8.065}$ $s = 32.672$

the standard deviation of the Gaussian fit to the 1S absorption peak, converted to meV (see right)

$x := E_{1s} - 0.278$

For convenience only

$$d := \frac{-0.209 \cdot x + \sqrt{(.209 \cdot x)^2 - 4 \cdot .016 \cdot x \cdot (.45 \cdot x - 1)}}{2 \cdot .016 \cdot x}$$

diameter calculation adapted from formulation in Moreels

$d = 4.385$

in nm

$\varepsilon star := 3.1 \cdot d^{.9}$

$\varepsilon star = 11.724$

Integrated molar absorptivity in meV/(cm*μM) from Moreels paper

$$\varepsilon := \frac{\varepsilon star}{s \cdot \sqrt{2 \cdot \pi}}$$

$\sigma := \dfrac{\varepsilon}{6.022} \cdot 10^{-14}$ $\sigma \cdot 10^{16} = 2.377$

Absorptive cross section in cm^2 (conversion factor adjusts from moles to molecules and liters to cubic centimeters)

$F := \dfrac{6.626 \cdot 10^{-25} \cdot 3 \cdot 10^{10} \cdot E_{1s} \cdot 8065}{\sigma}$ $F = 5.903 \times 10^5$

Fluence (nJ/cm^2) required to average one photon (at 1S energy) per dot

$F \cdot .025^2 \cdot \pi = 1.159 \times 10^3$

Pulse energy (nJ) required to average one photon per dot (500μm beam)

$$F_1 := \frac{E_{1a}}{\pi \cdot .0315^2} \quad F_2 := \frac{E_{2a}}{\pi \cdot .0245^2} \quad F_{2p} := \frac{E_{2pa}}{\pi \cdot .0235^2}$$

$$F_1 = 2.597 \times 10^5 \quad F_2 = 3.005 \times 10^5 \quad F_{2p} = 2.1 \times 10^5$$

Pulse fluences (nJ/cm^2) using measured beam FWHM values from Dec 2011

$$\mathrm{flux}(\nu, F) := \frac{F \cdot \sigma}{6.626 \cdot 10^{-25} \cdot 3 \cdot 10^{10} \cdot \nu}$$

Converting fluence to photons/dot

$$\mathrm{flux}_1 := \mathrm{flux}(\nu_1, F_1) \qquad \mathrm{flux}_1 = 0.447$$

$$\mathrm{flux}_2 := \mathrm{flux}(\nu_2, F_2) \qquad \mathrm{flux}_2 = 0.517$$

$$\mathrm{flux}_{2p} := \mathrm{flux}(\nu_{2p}, F_{2p}) \qquad \mathrm{flux}_{2p} = 0.361$$

$$f(k, \lambda) := \frac{\lambda^k \cdot \exp(-\lambda)}{k!}$$

Poisson Distribution probability density

$$\mathrm{ratio}(\lambda) := \frac{f(3, \lambda)}{f(1, \lambda)}$$

$$\mathrm{ratio}(\mathrm{flux}_1) = 0.033$$

$$\mathrm{ratio}(\mathrm{flux}_2) = 0.045$$

Ratios of three-photon events to one-photon events for each pulse

$$\mathrm{ratio}(\mathrm{flux}_{2p}) = 0.022$$

Quantum Dot Sample Characteristics and Parameters

$$\begin{pmatrix} \text{BatchNumber} & \text{Center} & \text{StandardDeviation} \\ \text{fs1} & 7027 & 221.6 \\ \text{fs2} & 6378 & 208.1 \\ \text{fs3} & 6277 & 202.6 \\ \text{fs4} & 6912 & 253.6 \\ \text{fs8} & 7060 & 263.5 \\ \text{fs10} & 7828 & 308.5 \\ \text{▮} & \text{▮} & \text{▮} \end{pmatrix}$$

Appendix F: Ultrafast Coherent Multidimensional Spectroscopy of Quantum Dots for a Non-Technical Audience

The Wisconsin Initiative for Science Literacy (WISL) has established a program that provides incentives for graduating PhD students to include a non-technical description of their research in their dissertations. As much of the work done in doctoral programs interacts only indirectly with participants outside the individual sub-fields, the WISL objective is admirable. I welcome their invitation to include such content in this document and am grateful for the award WISL offers for participation in this part of their programming. The research I have conducted over the course of the past few years under the direction of John Wright is fundamental research—a step or two (if I'm generous) removed from commercial or industrial applications. Such foundational research, however, feeds into the growing body of knowledge possessed by the scientific community and is essential for the development of new technologies. Over the course of this overview, I intend to provide you with a general description of both my research and some of the connections these insights have and may come to have within the broader technological and scientific world. In a nutshell, I (and the members of the Wright group with whom I have worked) have developed a technique that uses pulsed lasers to interrogate the energetic structure and behavior of molecules and have adapted that technique so that it can be used to study semiconductor materials that are of potential use in solar energy collection devices.

Introduction to Spectroscopy

Spectroscopy is the study of the interaction between light and matter. Any discussion of why a substance reflects, absorbs, or emits a certain color of light stems from an understanding of spectroscopic phenomena. For example, the ozone layer is known to absorb harmful ultraviolet radiation, which has a shorter wavelength, and thus more energy per photon, than visible light or infrared light. Ozone accomplishes this task because light in that range of wavelengths matches the separation between energy levels in the ozone molecules (we would say that the light is resonant with the transition) and the probability of the molecule absorbing the right-colored light that happens to hit it is high (we would say that the transition dipole moment is large). A blue shirt contains molecules that absorb light in the red and green ranges of the spectrum, but still reflect and transmit blue. A microwave oven works because the long wavelength microwaves emitted by the device are absorbed by molecules in the food. That transfer of energy causes the food to heat up. The wavelengths of light absorbed by a substance are characteristic of the components of the substance—its atoms and their bonding arrangement. With the right tools, it is possible to learn about an unidentified substance by measuring the colors of light it absorbs.

Spectroscopy studies not only the energetic structure of a molecule, but also how each of its high energy states behaves. Consider a car left in the sun on a summer day. Sunlight is absorbed by the upholstery in the car because it is less than perfectly reflective; in fact it is often dark, which means that it absorbs light very effectively. The light that is absorbed doesn't just leave the molecules in their excited states forever. The molecules bump into their neighbors and have a chance of transferring some of their energy. Over the course of these collisions, energy is often dispersed from high energy states to many low energy states, such as molecular vibrations and bends. Given enough time, any of these states can relax back down to its initial state (the ground state) by emitting light again. Excited vibrational states tend to live longer than the higher excited electronic states. If any excited state has enough interactions with its surroundings, or even other parts of the molecule, then it doesn't emit light of the same color it absorbed. Rather it emits at the lower energy wavelengths of the vibrational modes (infrared instead of visible, for example). In the case of the car, the infrared light, which our skin detects as heat, rather than our eyes detecting it as light, is not transmitted by the windows of the car. Hence, visible light passes through the windows and is absorbed by molecules that relax to molecular vibrations before they can reemit at the same color they absorbed. The molecules then emit infrared radiation that is reflected by the windows and stays trapped in the car. Over time, the infrared radiation builds up and the car's interior temperature rises to an uncomfortably high level. Spectroscopy studies not only the color the upholstery absorbs (and hence the high energy states present in the molecules), but also the color it emits (the low energy states present), as well as how long it takes for a molecule to relax down from high to low energy and any states that the molecule may have passed through on its way down.

Why Use Lasers for Spectroscopy?

In order to learn about the structure and dynamics of molecules with certainty, a great deal of precision is required, and there is frequently no better source of well-defined light than lasers. Laser beams can be made to travel with very little divergence so you can direct all of the energy of the beams to the specific destinations desired. Lasers can be tuned to access wavelengths across the infrared, the visible, and the ultraviolet regions of the spectrum. Further, laser systems can be constructed so that they are not continuous beams, but rather pulses that are short enough in time to be used to measure phenomena as brief as the movement of an electron from one part of a molecule to another (this is the attosecond time scale—one billionth of a billionth of a second). Lasers also have well-defined phase, which is important for any experiments that need to observe phenomena that can only be described with the wave functions of quantum mechanics.

Spectroscopy in the Wright Group

The particular brand of spectroscopy used in my research is a type of non-linear spectroscopy. Linear spectroscopies are techniques that study interactions with a single light source. Our experiments use three laser pulses to gain a more complete picture of the structure and dynamics of the system. A schematic of the systems we use is shown in Figure 1, along with a photograph of one of the optical tables, at the end of this document. The schematic starts at a part of our laser system after the main laser pulse is created. That main pulse is split into two paths and directed into the boxes labeled “Optical Parametric Amplifier” (OPA). OPAs are devices that allow the wavelength of light to be changed. Once we’ve chosen the color of light that we want to use, we split one of them again and focus all three beams into the sample.

In order to observe and measure any behavior that is time-dependent, it is important to control the sequence and separation in time between the pulses. The schematic also shows a couple of delay stages. These stages have retroreflectors (a combination of mirrors that send incoming beams out exactly parallel to their angle of entrance) and precise motors that control their positions. By changing the position of a stage, we control the length of the path that each pulse takes to the sample. As we shorten the path, the pulse arrives earlier. I mentioned above that precision is required. The phenomena we wish to observe take place on time scales between ten femtoseconds (ten millionths of a billionth of a second) and ten picoseconds (ten millionths of a millionth of a second). To change the relative timing of something slow-moving by such a small amount of time, you would have to change its path by an absurdly small amount.

Conveniently, light is fast. Still, the 93 million mile journey from the sun to Earth takes light only eight minutes. If we want the light pulses to arrive at the sample one picosecond earlier, we have to make the path just 300 microns shorter (less than a third of a millimeter). To measure some of the faster dynamics, we need reliable control over delay stage position down to a few microns—about the spacing between the grooves on a CD.

The Basics of Non-Linear Spectroscopy Investigated in the Wright Group

I mentioned above that our type of spectroscopy is a non-linear spectroscopy, which means that we measure sample behavior as it interacts with multiple light sources. In particular, the three beams we focus into our samples each interact with the sample, and the effects produced by each beam interfere with each other to produce the complicated effects we measure. To get a feel for this kind of interference, consider dropping small rocks into a perfectly still pond. A single rock will create a ripple pattern that spreads out from the place it landed. If two rocks were dropped into the pond next to one another, their ripple patterns would interfere with each other—in some locations the waves they create would combine to make larger waves (constructive interference); in other places they would cancel each other out (destructive interference). If the second rock was dropped into the pond a short while after the first, the overall pattern would be the same, but the locations of each type of interference would be shifted.

The pond is similar to our sample and each rock dropped is like the interaction between a laser pulse and a molecule. As the pulses travel through the sample, it's as if they're dropping rocks across stretches of the pond. Connecting to an earlier idea, working with either a more intense laser or a larger transition dipole moment is like dropping a heavier rock in the pond.

Working with a resonant transition is like dropping rocks in the same location with timing set to make the ripple larger with every drop. So choosing resonant transitions with large dipole moments makes large waves. If the beam angles and wavelengths are chosen well, then the interference from multiple beam lines will cooperate to create large waves that travel out in certain directions. This process of cooperation is called phase matching. The red beam coming out of the sample in Figure 1 is one such “large wave” direction. It only appears when each beam’s interaction with the sample is strong and they all cooperate with each other. We block the portions of each other beam that are transmitted through the sample after they’ve interacted with it so that we only measure this one phase-matched output.

The non-linear output beam we choose is directed into a monochromator before reaching the detector. The monochromator spreads the incoming light into its component colors in an effect that appears like a prism separating sunlight into a rainbow. The mechanics of this spectral dispersion are more like the interference effects described in the pond analogy (or letting a shaft of sunlight reflect off a CD) than they are like a prism, but the final effects are similar. By adjusting the angles of a grating inside the monochromator (like changing the angle of the CD relative to the beam of light), we choose which color of light reaches the detector.

Experimental Overview and Technique Development on RDC

I have now summarized the primary variables used in each of our experiments—the two colors of light generated by the OPAs, the relative pulse timing (controlled by the pair of delay stages), and the color observed by our detector as selected by the monochromator. By changing one or two of these variables and fixing the rest we generate the spectra that give us insight into the structure and dynamics of our system. Additionally, we can change the intensity of the beams or rotate their polarization (loosely like swishing water back and forth instead of dropping a rock into the water from above) to study additional effects. The technique was developed over the course of a couple graduate student generations of investigation on molecules with interesting vibrations. I'll tell you about some of the primary capabilities of the technique using some of those experiments as examples.

Rhodium Dicarbonyl Acetylacetonate (RDC) was one of the molecules we studied when developing our technique. A picture of this molecule is shown in Figure 2a. We studied the behavior of this molecule's vibrational modes, specifically those involving the stretching and compressing of bonds in the carbonyl groups (carbon/oxygen pairs that aren't in the ring structure) connected to the rhodium atom. The two stretching modes of interest were the symmetric stretch and the antisymmetric stretch, as cartooned in Figure 2b. For RDC to start vibrating in these modes, the molecule must absorb infrared light that is resonant with the transitions. The simple linear absorption scan for RDC in this range of the infrared is shown in Figure 2c. These scans provide little more than the basic energetic structure of the molecule and the relative strengths of the transitions, but they also tell us the frequency ranges to use for our more complex experiments. The frequency of light is simply the multiplicative inverse of the wavelength, so the higher frequency corresponds to higher energy and shorter wavelengths.

The result of one of these more complex experiments is shown in Figure 3. Here the axes are the frequencies of the two lasers, as chosen by the OPAs. The relative delay between the pulses is fixed such that what are called ω_{-2} and $\omega_{2'}$ (the two beams that come from the same OPA output) arrive at the sample first. (Note that ω_{-2} is shown as ω_2 in Figure 1; the added negative sign reminds us how this pulse interacts in the particular alignment scheme used in these experiments.) They create an interference pattern (like the two different sequences of rocks dropped in the pond). Where the electric field intensity is high (where the waves are the strongest), these two beams can together put the molecule in an excited vibrational state, but only if their frequency/wavelength is resonant with a transition. That frequency—the frequency of the pulses that can be used to put the molecule into an excited state—is shown along the vertical axis. The horizontal axis is the ω_1 frequency (the beam that is not split again after being produced by the OPA). This laser interacts with the population states created by the other two beams, either triggering relaxation (stimulated emission) or adding to the molecular vibrations. To the left of the plot and above it, I've juxtaposed the linear absorption spectrum from Figure 2c for comparison.

It is immediately apparent that the spectrum in Figure 3 has more information than the spectrum in Figure 2c. When both lasers are tuned to the same frequency (along the diagonal), peaks appear at the same frequencies as appear in the linear absorption plot. On these peaks, all pulses interact with the same vibrational mode, either putting the molecule in its fundamental excited state or stimulating emission of light from that mode. The peaks that are *not* along the diagonal start to provide new information. When one laser is resonant with one transition and the other laser is resonant with the other transition (when $\omega_2 = 2015\text{cm}^{-1}$ and $\omega_1 = 2084\text{cm}^{-1}$, for example), a peak may appear, but only if the two modes are coupled. In this case, a peak does appear, indicating that the vibrational modes are coupled (which isn't surprising, given that they involve the same atoms). To say that the two modes are coupled simply means that one mode behaves differently when the other mode is populated. When the symmetric stretch of the molecule is excited, the amount of energy required to also get the molecule in the excited antisymmetric stretching mode decreases. Consider an analogy of two people in a room. Each person can be put into a good mood if they hear a certain amount of good news. Suppose one of the two hears enough good news for him/her to become rather giddy. If the other person in the room can be made happy more (or less) easily because the other person is in a good mood, then their moods are coupled like these two vibrational modes are coupled. If the second person is perfectly indifferent to the mood of the first, then their moods are not coupled. In this spectroscopy, no peak would appear on the cross peak of their moods.

For each of the four fundamental peaks visible in Figure 3 (peaks for which both lasers are resonant with one of the transitions visible in the linear absorption plot), there is also a second peak shifted to the left. These red-shifted peaks appear at the frequency required to create an overtone (the same type of vibration, but roughly two-times faster) or a combination band state (both types of vibration active at the same time). The peaks appear at lower energies than the fundamental transitions because it takes less energy to make the molecule vibrate more than it did to get it vibrating in the first place. An imperfect spring can be imagined to work the same way. When you first try to stretch a really tight spring, it takes a lot of force. If that spring is already loosened up, it's easier to stretch it more because the metal starts to get a little bent out of its original shape. Here as the bonded atoms vibrate more, the increase of energy means that the bond is getting closer and closer to breaking, so it isn't holding the atoms together as tightly. So each of the additional peaks in this spectrum appear when ω_1 can jump from the excited state created by ω_{-2} and $\omega_{2'}$ to an even higher excited state. From scans like this one, then, we can learn which modes interact with each other and we can start to learn about higher energy modes than just the fundamental transitions. In some cases, a linear absorption scan can have many peaks next to each other so that it is hard to identify which modes are present and what their energies are. When cross peaks only appear for coupled modes, it is much easier to resolve complicated portions of an absorption spectrum.

Dynamics and Coherences

Figure 3 shows one way that we access more energetic structure information. To study the behavior of any of these combinations of modes, we keep the frequencies of the lasers fixed, but scan the delays between them, producing plots like the one shown in Figure 4. Here the origin of the plot corresponds to all three pulses being overlapped in time. As ω_{-2} and $\omega_{2'}$ arrive at the sample before or after ω_1, the axis value becomes negative or positive, respectively. An example pulse ordering is shown above the plot; the timing corresponds to the delay values indicated in the plot by the black circle. Any type of molecular behavior in time can be shown in plots like this, but this one shows plainly a couple of important basic types of information. The signal stays bright (the red color on the plot) the furthest away from (0,0) when the two delay values are equal and negative. These values correspond to pulse sequences where ω_{-2} and $\omega_{2'}$ arrive at the sample simultaneously and create a population state. As we travel away from the origin in other directions, we instead measure the coherence lifetimes.

Coherences are quantum-mechanical superpositions between two different states. Being able to selectively create these superpositions and watch their behavior gives this technique a lot of its specificity. When populations relax (as in the case of a high-energy state dispersing its energy to low-energy states as a car heats up in the sun), the third pulse we send in to explore the state can still generate signal, even if the state we created with the first two pulses isn't the same as the state present when the third arrives. When we work with coherences only, any disruption of the energy level of the participating states either makes the signal disappear entirely or in certain circumstances makes it appear at a different wavelength, which we choose for or against with the monochromator setting.

As with many concepts in quantum mechanics, the nature of coherences isn't immediately intuitive. One way to think about a coherence is by considering a light with a dimmer switch. For the purposes of this analogy, suppose lights are normally thought of as either off or fully illuminated—those settings would correspond to population states. Coherences could be any of the partially illuminated settings from very dim (mostly "off" character) to rather bright (mostly "on" character). Signal from coherences is short lived because it is easy to disrupt. Unlike populations, coherences oscillate. When one thinks about molecular vibrational modes on a quantum mechanical level, they are regarded as stationary states—the probability of finding electrons in certain locations doesn't change for as long as the molecule is in that state. The probability of finding electrons in certain locations when the system is in a coherent superposition state does change in time. It's as if the light on the dimmer switch also flickered at a well-known rate whenever it was set to something other than "off" or "on". The signal from coherences disappears so quickly because while not every collision may be able to rearrange the energy of the molecule (like the collisions in the upholstery of the car on a summer day), collisions *are* able to easily disrupt the phase of the oscillation, making the molecules get out of sync with each other. So if many lights on dimmer switches are blinking in time with each other, it is easy to see the flicker. If they are out of sync with each other, then they all average out and you don't really see the flickering at all.

The added complexity of coherences may seem needless for research studying the behavior of excited states, but there are some very important phenomena that can only be described at the quantum mechanical level of coherences. Though this topic will arise in later descriptions, an example of behavior that can only be described on a quantum mechanical level is the energy transfer from light-absorbing molecules in plants to the parts of the cells that use the energy to convert carbon dioxide to sugars and oxygen. In order to have a detailed understanding of the molecules we study, it is important for us to be able to watch both population- and coherence-based phenomena. Coherent and incoherent behaviors create different effects in our data. Figure 4 shows a basic picture of lifetime measurements. Figure 5 shows the same type of scan, but then we changed the monochromator settings to watch output from a different state—a type of result that can only be observed when coherences retain their phase, but change to a different state. It's as if those blinking lights all changed from flickering at one rate to another rate, but did so in sync. The take-home message from scans like the one shown in Figure 5 is that we can detect coherent energy transfer, and the pattern that appears in scans detecting it tells us the energy separation between the initial and final states of that transfer.

Semiconductors and Quantum-Confinement

All of the research described above relates to vibrational transitions and modes. Over time, it became clear that the techniques developed provided a powerful and unique way to learn about different molecules. Our attention turned, then, to systems that have become of interest to the field of materials science—quantum-confined semiconductors. Before explaining the specifics of our results, I'll explain what quantum-confinement is and the aspects of semiconductors to which quantum-confinement is relevant. I will also provide something of an explanation of one (of many) important possible applications of these materials—dye-sensitized solar cells.

Semiconductors are given their designation because they can be electrical insulators or conductors, depending on their energetic condition and elemental composition. Instead of discussing individual states, such as the symmetric and anti-symmetric stretching modes of RDC, the identifying features of semiconductors revolve around two collections of electronic states—each of which blur into an effective continuum of states called the valence and conduction bands. The valence band is comprised of electronic states that are localized on the atoms in the material. Any electrons in the conduction band are in energetic states that are delocalized across the lattice of the material, like the electrons in metals that are free to flow around a wire. The energetic separation between the valence and conduction bands is called the bandgap, and can be changed by changing the composition of the semiconductor or, in some interesting cases, by changing the physical size and shape of the material.

If all electrons in a semiconductor structure are in the valence band, then the structure does not conduct electricity. If by injection of energy (be it in the form of light or voltage or another) equal to or greater than the bandgap, an electron is promoted to the conduction band, then the material will conduct… at least a little. When that electron is promoted, however, it is leaving its ground state localized orbital behind. The absence of the negative charge of the electron leaves a positive charge behind. This vacancy carries the positive charge and is called a hole. (I say that it carries the charge because the actual positive charge is in the nucleus of the atom, but if another electron fills in the hole, then the vacancy is associated with a different orbital, possibly on a different atom.) Even though the electron is now free to roam about the lattice, it still feels attraction to the positive charge it left behind, so it never wanders far. The electron/hole pair is called an "exciton". How far the electron will wander is a function of the atoms and bonds that make up the semiconductor, so each different material has a native exciton size, called the "Bohr radius".

Semiconductors can be synthesized in such a way that the actual lattice of atoms is smaller than the exciton Bohr radius of the material in at least one dimension. In this situation, the semiconductor is said to be quantum-confined and starts to take on new properties. First, an exciton has a native size in the first place because that size is the lowest energy configuration. By making the material smaller than the lowest energy exciton Bohr radius, the system can no longer access the lowest energy configuration and is forced to be in a higher energy state. This manifests as an increase in the bandgap energy. As the exciton container size decreases further, the bandgap energy increases further. With enough synthetic customizability, materials can be made with tunable bandgaps. Another effect of reducing the number of atoms (and hence also reducing the container size) in the semiconductor is that the number of electron states decreases. Quantum-confined materials tend to have a few clumps of states at low energies before the continuous band structure of the bulk material reappears. Because these are the quantum-confined excitonic states, the exciton fills the container and hence takes on the shape of the material.

Figure 6 shows a number of the characteristics of quantum-confined semiconductors described above. In Figure 6a, the band structure of a generic bulk semiconductor is shown next to the energetic structure of a hypothetical quantum-confined structure of the same material. The quantum-confined structure has a larger bandgap and discrete states. A diagram of a quantum dot—a spherical semiconductor that is smaller than the Bohr radius in all three dimensions—is shown in Figure 6b with a partially-transparent sphere representing the exciton Bohr radius. Data showing the effect of different amounts of confinement are shown in Figure 6c. Here a series of linear absorption scans shows the increasing energy of the first absorption peak of lead selenide (PbSe) quantum dots of decreasing radius.

Solar Cells and Quantum-Confined Semiconductors

I have described how changing the size of a semiconductor can change its energetic properties and that the ability to change those properties is important, but I have not yet explained why this flexibility is so important. Before I do, it is important to note that these structures can be made from very abundant and inexpensive materials. Some semiconductors have rare elements in the composition like indium or gallium; others require a great deal of energy to purify—silicon is ubiquitous in the form of silicon dioxide (glass, sand, quartz), but requires processing to reduce to pure silicon. Alternatively, iron oxide (rust, hematite) and titanium dioxide (TiO_2, present in such luxurious consumer products as white paint and sunscreen) can gain additional high tech uses when their energetic structure is tuned to meet a particular need. One such need is the development of devices that can be used to efficiently harvest solar energy.

Dye-sensitized solar cells make use of a molecule that can efficiently absorb some portion of the solar spectrum and transfer an electron into a conducting material. Figure 7 shows a basic schematic of such an assembly at a molecular level. TiO_2 is shown as the electron acceptor because it is well-suited to the task—it has a large bandgap so it is statistically unlikely for enough collisions to cooperate to get it to relax down to distant vibrational modes and it has many vacant electronic states in its conduction band, so there's always room for donation of electrons. With the right dye molecule attached to the surface of the electron acceptor, solar cells with low efficiencies can be constructed. The dyes, though, require some means of binding to the TiO_2 and have to be able to move an electron across that additional assembly before relaxing back down to their own ground state. Additionally these molecules must absorb as much of the solar spectrum as possible in order to avoid wasting the energy in the transmitted/reflected wavelength ranges.

It is in the creation of a donor/acceptor assembly that the use of quantum-confined materials is anticipated to shine. Quantum dots can be grown to sizes that absorb light all across the solar spectrum; in a full solar cell, if one size of dot only absorbs a portion of the spectrum, another size can absorb much of the rest. These dots can be grown directly onto the surface of an electron accepting material (and have been—see Figure 8a), meaning that there is no need for additional bridging assemblies. Additionally, as the exciton already wants to be larger than the quantum dot, the electron will already be stretching into the acceptor (diagrammed in Figure 8b), making transfer all the faster and more efficient. If both the donor and acceptor can be adapted to match energetically, then the transfer itself shouldn't require significant loss in energy. The alignment shown in Figure 8c, for example, would waste a lot of energy in the transfer.

The synthetic flexibility and energetic properties of quantum-confined materials already make their use for prototype dye-sensitized solar cells appealing. The question remains how to optimize their creation, and the answer lies in understanding the details of the charge transfer. What states are involved in the transfer? Are there additional electronic states formed at the interface between the two material types? What kind of synthesis produces the least disruptive interfaces? These are the types of questions that our type of spectroscopy can address.

Coherent and Incoherent Electron Transfer

Before providing an overview of our progress toward answering the questions above, there is one additional line of distinction I would like to draw regarding the nature of the change transfer. Earlier I discussed coherent energy transfer and said that the distinction between incoherent and coherent dynamics would be important; it is in this discussion that the distinction becomes critical. One way to think about this distinction is to consider a swimming pool with a shallow end and a deep end. If a bunch of water is added to the empty pool, it rather quickly ends up in the deep end. The water spreads out under the influence of gravity until it finds that it can continue to drop down until none of the water is in the shallow end of the pool. This scenario is like coherent electron transfer. The electron orbit is larger than the quantum dot (remember Figure 8b), and the electron acceptor has lower energy states for the electron to fall into, so the electron cloud just flows right into the proverbial deep end. Incoherent energy transfer is more like putting a beach ball in the same pool—it will roll into the deep end and stay there, but it may bounce around for a while first; how quickly it gets to the deep end depends on the slope of the shallow end of the pool (or how much other pull there may be to the deep end), and one could definitively say “now it’s in the shallow end; now it’s in the deep end”. Because coherent energy transfer happens by spreading out and simultaneously exploring the options, the fastest charge transfer phenomena end up being describable in only this way.

Most non-linear spectroscopy techniques (pump-probe and transient absorption are the names of the two most common) establish an excited state population and observe where that energy is at a later time. These techniques can be very good at determining initial and final states of a system, but they usually cannot provide any information about short-lived intermediate states and they cannot discriminate between different paths the system had taken to reach its final state. Experiments like the one that produced the plot in Figure 5 show the states involved in the transfer, and any intermediate state would contribute to the interference pattern created. So if we are able to measure coherence lifetimes and selectively excite different states, then we can explore every possible situation that could lead to charge transfer. But there's a lot of tailoring and development that must be done first.

Initial Wright Group Spectroscopy of Quantum Dots

Our first forays into the spectroscopy of quantum-confined semiconductor systems focused on PbSe quantum dots. PbSe dots have exciton states that are in an easily accessible wavelength range for our lasers, their synthesis is well-known, and other spectroscopy techniques have already been used to study them, so there is a body of work in existence for comparison. After making some changes to our OPAs to allow them to access the correct ranges, we collected frequency scans (see Figure 9) from a few different batches of dots. We found that we could resolve the peaks and gain some decent structural information about the system. We could confirm coupling between two different quantum-confined exciton states by noting the presence of a cross-peak. When we tried to study dynamics, however, we found that our one-picosecond pulses were too long to measure any coherent phenomena. Figure 10 shows a delay scan like the one in Figure 4. The population lifetimes are certainly long enough for us to measure (along the negative portion of the x = y diagonal and along the positive x-axis of Figure 10), but as soon as the pulses that create the population state aren't overlapped, we have no non-linear signal light at all. To confirm, we tried simulating our data from quantum mechanical calculations and we found that we could recreate the data with a wide range of coherence lifetimes—only the laser pulse duration mattered. Frequency scans can be matched in a similar way and yield lifetime information with some analysis and processing, but without the ability to select fully coherent processes with our pulses, much of the technique that was available to studies of molecular vibrations was no longer usable.

Quantum Dot Spectroscopy With Femtosecond Pulses

At the end of the line of picosecond system experiments, it became clear that we needed to use much shorter pulses if we wanted to observe any coherent phenomena. The next step, then, was to assemble a laser system that could give us tunable 40-femtosecond pulses—25 times shorter than one picosecond. (That duration was selected to be a match to the coherence lifetimes calculated from the frequency scans on the older system, which are also in accord with measurements from around the scientific community.) We used an experimental setup functionally the same as the one shown in Figure 1. Pulses this short are difficult to create and keep stable, so the optical table had to be designed with all high-end reflective optics on mounts that would dampen any vibrations that might run through the heavy steel table. As of late Spring 2012, we confirmed that we can collect the frequency scans that were available from the picosecond system (Figure 11 provides an example) and measure coherence lifetimes. Figure 12 shows a delay scan that seems similar to the one shown in Figure 10 (with picosecond pulses), but here the width of the peaks is larger than the pulses, which means that we are measuring coherence lifetimes directly. To confirm that we could generate signal from pulse sequences that did not create an intermediate population, we did another frequency scan at a different time ordering. Figure 13a shows the data next to two simulations (13b and 13c) that include and exclude signal from the fully coherent processes. The fact that the main peak area has a shape that appears more like the simulation with fully coherent contributions than the one without means that we are able to suppress the processes that have intermediate populations in favor of those that do not.

The signs that we have restored our technique's functionality are subtle. For example, Figure 12 (femtosecond system, quantum dots) still looks more like Figure 10 (picosecond system, quantum dots) than Figure 4 (picosecond system, RDC), even though it contains the same information as Figure 4 and more than Figure 10. Even so, the results are conclusive—we can once again selectively measure both energetic structure and excited state dynamics, be they coherent or incoherent. This restoration means that we are now positioned to start characterizing the types of charge transfer events that are essential for any efficient quantum-dot-sensitized solar cell cores. Future Wright group research directions include investigation of charge transfer systems and improvements to the technique, including cryogenic cooling (which increases the coherence lifetimes, making resolution of fully coherent dynamics easier) and OPA tuning range extension (which allows the investigation of a wider range of energy levels and materials).

Acknowledgments

Thank you for taking the time to read this addendum to my dissertation. I am pleased to have been able to see this project evolve over the course of the past few years. Though my formal dissertation acknowledgments are more thorough, I really must provide some additional recognition of the folks who were involved with the work discussed here. Doctors Andrei Pakoulev, Mark Rickard, Kathryn Kornau, and Nathan A. Mathew led the project through the entirety of the RDC work and associated vibrational studies. Dr. Lena Yurs joined the research group when I did and worked on vibrational studies and on the picosecond quantum dot experiments. Dr. Rachel Selinsky (from the research group of Song Jin) either made or trained the person who made all of the quantum dot samples shown in this research. The quantum dot samples studied on the femtosecond system were synthesized by Dan Kohler, who also helped devise and run many of the corresponding spectroscopy experiments. Doctors Igor Stiopkin and Andrei Pakoulev worked with Schuyler Kain to build the femtosecond laser system. Schuyler also developed the software that integrated and controlled the hardware that allowed us to run our experiments. Doctors Song Jin and Robert Hamers collaborated with our group, providing us with the opportunity to work with nanomaterials with much less blindness than might otherwise have been the case. Dr. John Wright provided direction, connections, recommendations, encouragement, analysis, and perspective throughout each of these projects. The US populace, by way of the National Science Foundation and Department of Energy, provided our group with the funding required to acquire and maintain the elaborate experimental setups used. I am grateful to each of these individuals and groups for their contributions and assistance, just as I am, again, grateful to you for the time you have taken to read this document.

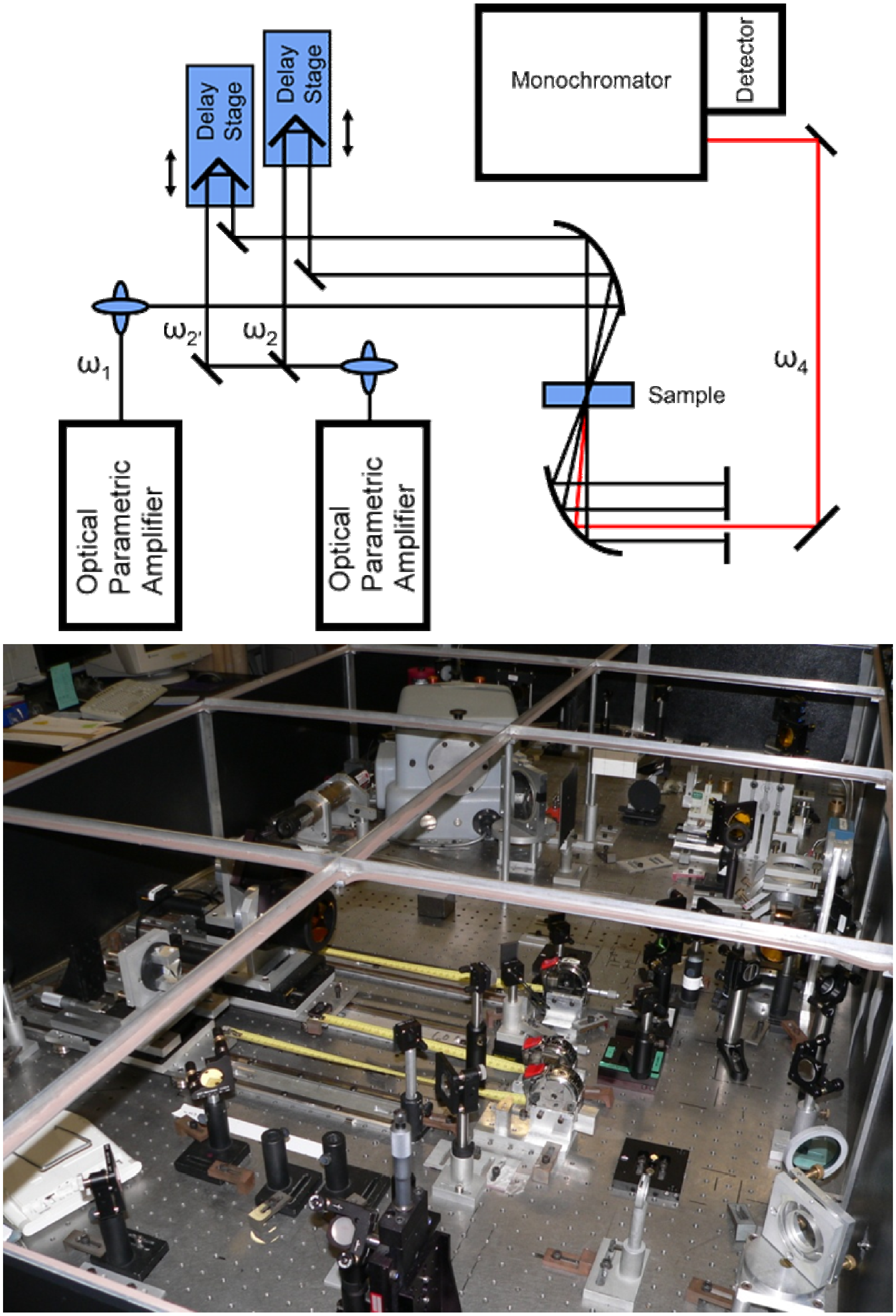

Figure 1—Diagram and photograph of the optical table used in non-linear spectroscopy experiments. OPAs change laser pulse color. Delay stages change the relative timing of the pulses at the sample cell position. The red line traces the path of the non-linear signal whose intensity we measure.

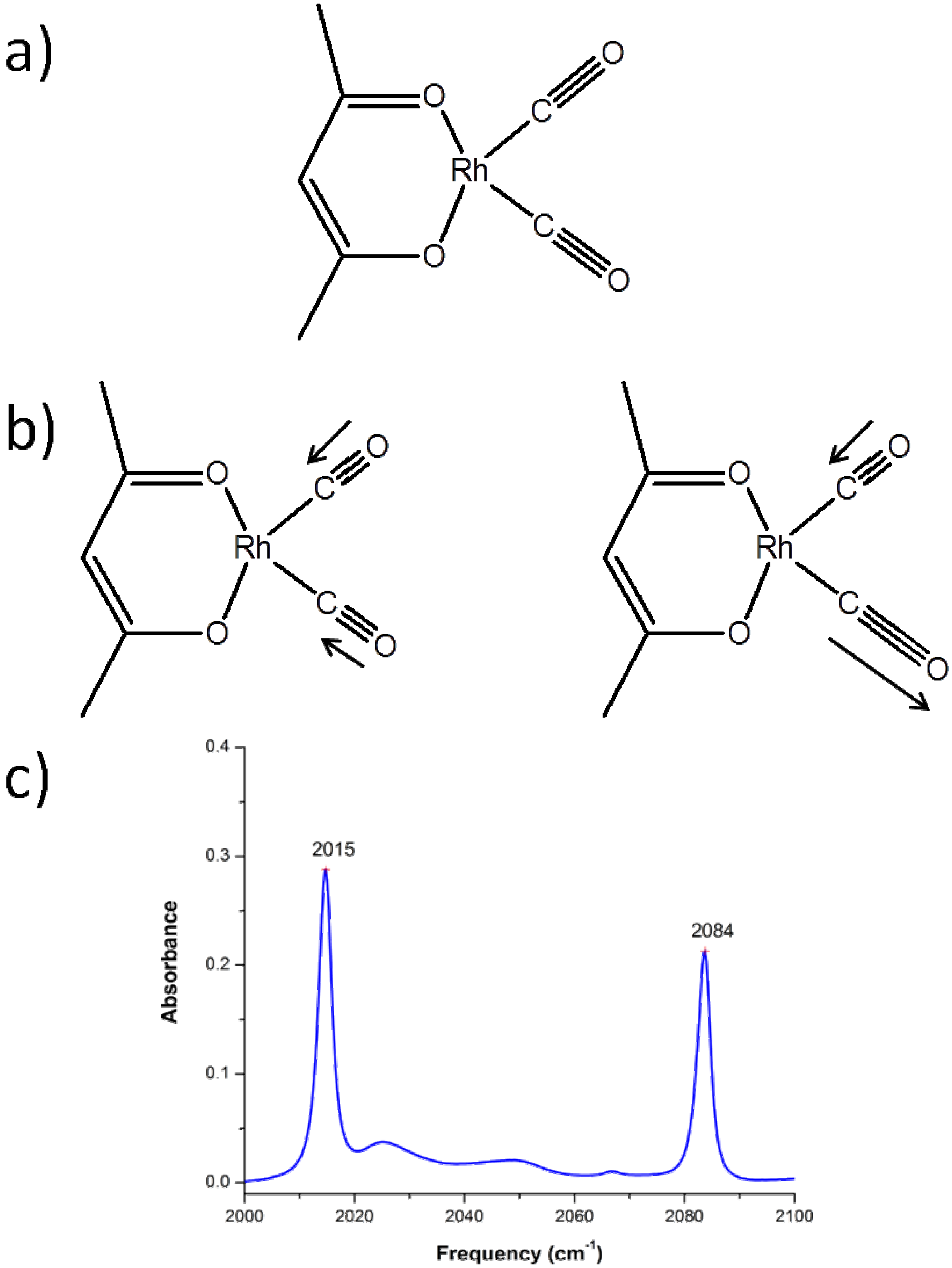

Figure 2—(a) Rhodium dicarbonyl acetylacetonate (RDC) molecular structure. Bonds are indicated by straight lines. (b) The symmetric (left) and anti-symmetric (right) stretching modes of the carbonyl groups. (c) The linear absorption profile of RDC carbonyl stretches. The absorption increases at the frequencies of light that are resonant with the two stretching modes.

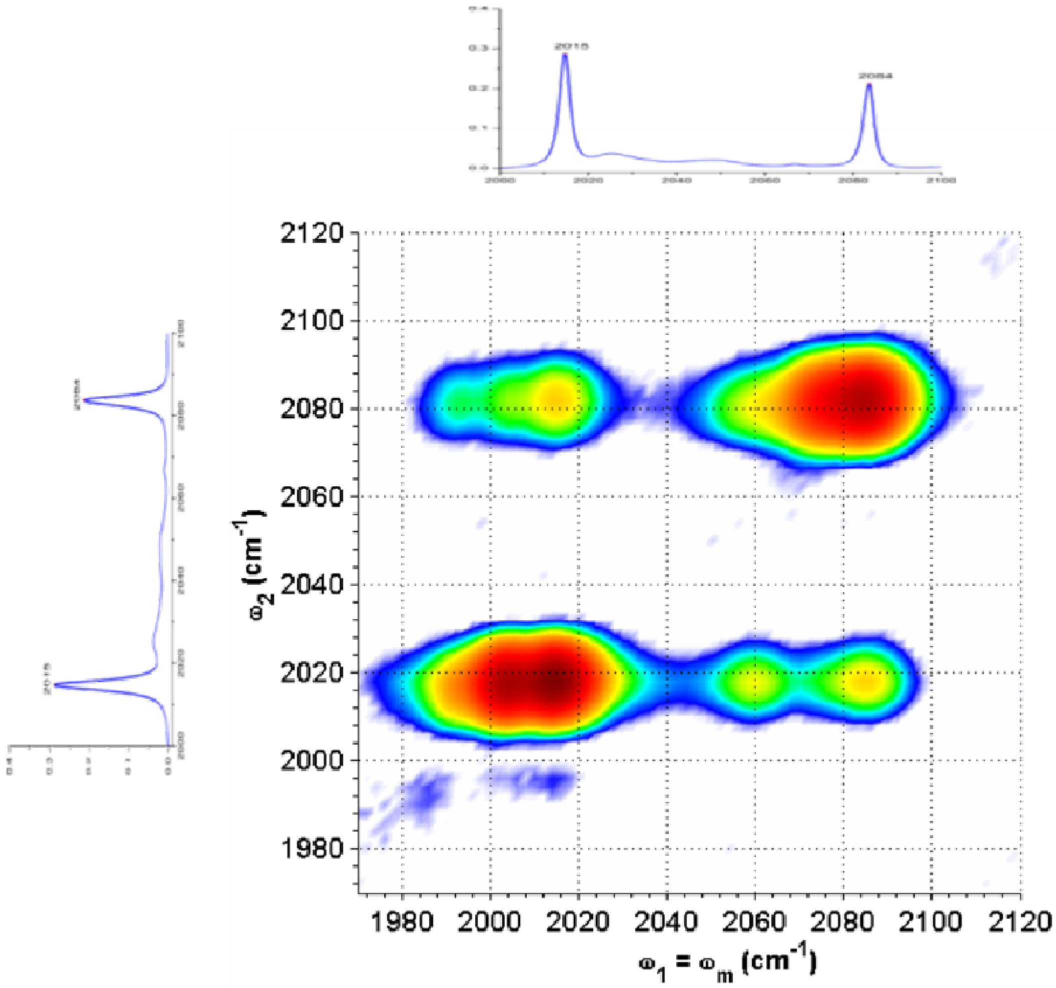

Figure 3—A multi-dimensional frequency scan of RDC with linear absorption scans juxtaposed for comparison. ω_2 and $\omega_{2'}$ create an excited state at the frequency shown on the y-axis. ω_1 (x-axis) interacts with that population. Signal appears when each laser is resonant with an available transition. The z-axis (see color bar to the right) shows the intensity of signal light; this plot shows a logarithmic scale. The presence of off-diagonal peaks indicates coupling between the modes. Peaks that are shifted to the left of primary peaks appear at frequencies matching the transition to overtones (same mode, vibrating faster) and combination bands (both modes vibrating).

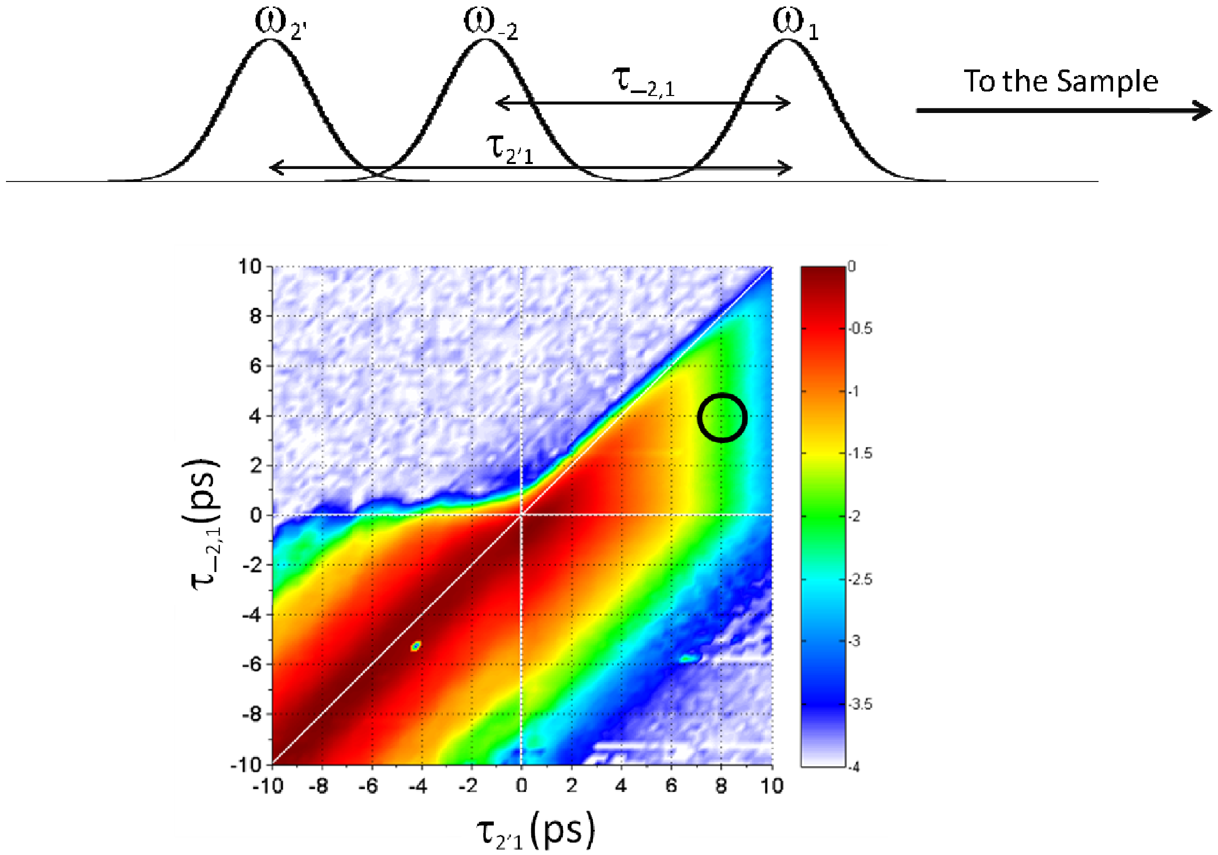

Figure 4—A multi-dimensional delay scan of RDC on a logarithmic scale. Here the laser frequencies correspond to the lower-rightmost peak in Figure 3. At the origin all the pulses are overlapped in time. The black ring shows the time-ordering shown in the diagram above the scan. Interpretation of x-axis and y-axis values is also available pictorially in the diagram. The decrease in signal in such directions as the positive x-axis traces out coherence relaxation (explained later in the main text). The steady signal along the negative x = y diagonal shows the long-lived population lifetime.

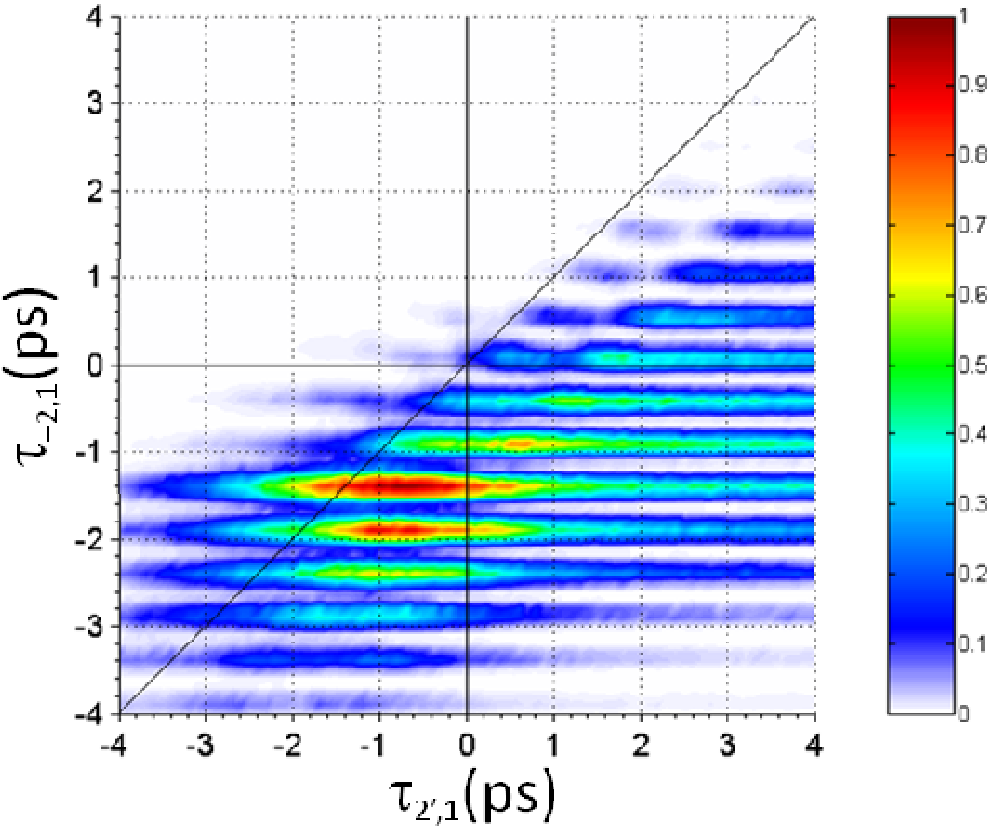

Figure 5—A multidimensional delay scan with all lasers tuned to the same frequencies as those used in Figure 4, but with the monochromator set to pass a different wavelength of light. Here signal only appears when there is coherent energy transfer from one mode to another. The beating pattern has a frequency corresponding to the different between the initial and final states of the transfer.

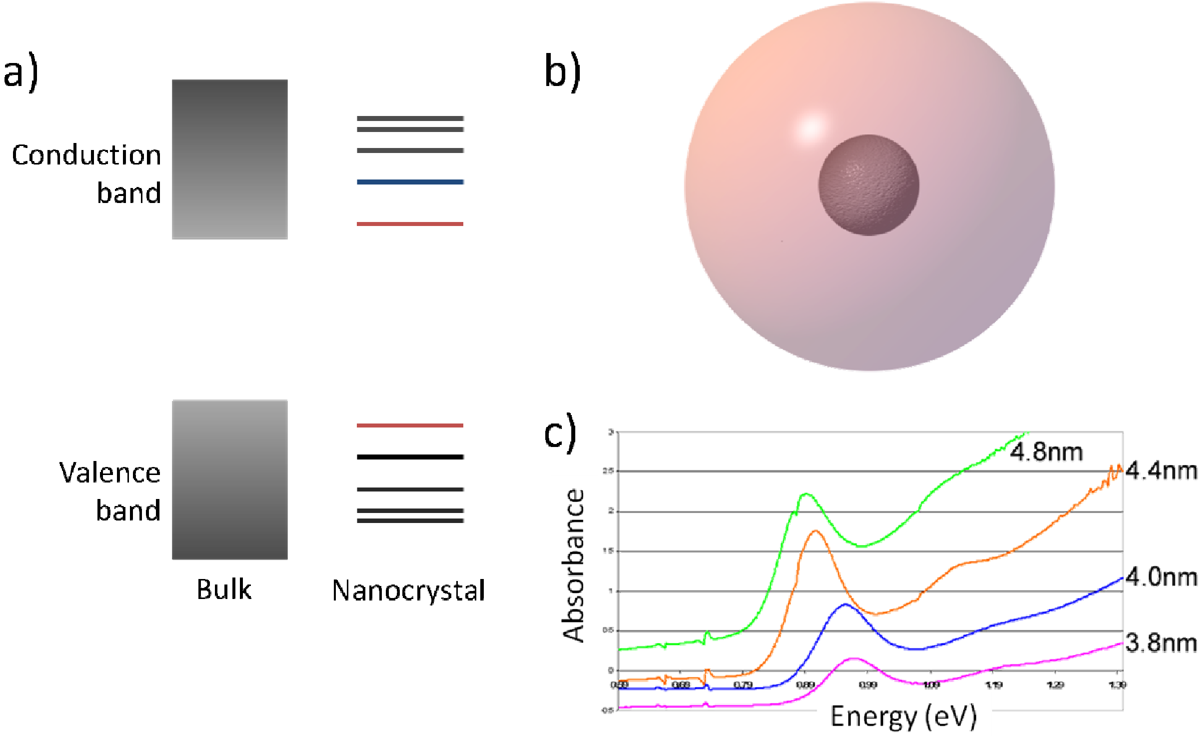

Figure 6—Depicting the effects of quantum-confinement. (a) The energetic structure of a non-confined semiconductor (bulk) and a quantum-confined structure (nanocrystal) of the same material. Notice in particular (1) the development of discrete states and (2) the increased separation between highest energy valence and lowest energy conducting states in the confined structure. (b) A graphical depiction of a quantum dot (inner sphere) compared to the native exciton orbital size (partially-transparent larger sphere). (c) Absorption scans of PbSe quantum dots of different diameters, collected by Rachel Selinsky. Notice that as the dots get smaller, the absorption profile shifts to higher energy. Greater confinement leads to higher energy states.

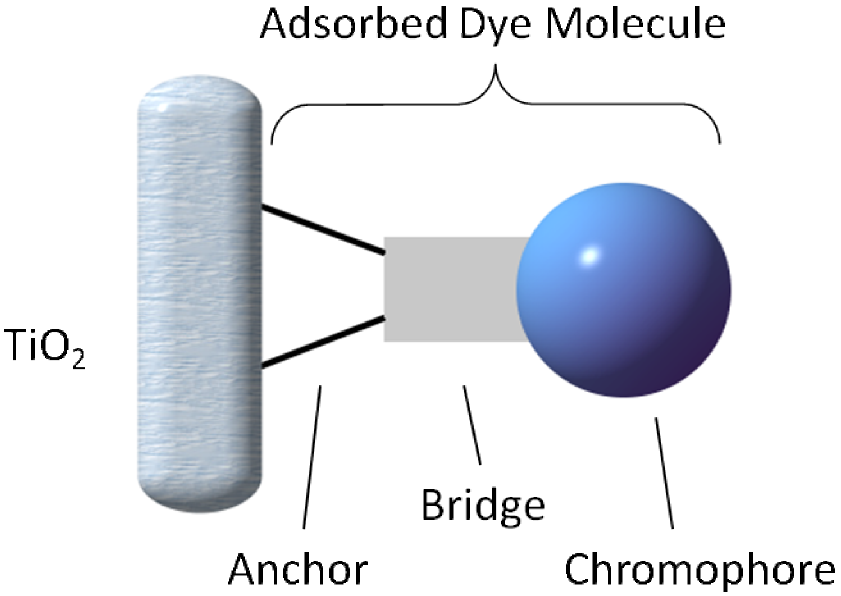

Figure 7—A simplified schematic of a dye-sensitized solar cell core. Here the chromophore absorbs incident sun light. The excited state electron transfers into the conduction band of the electron-accepting titanium dioxide (TiO_2). To make the transfer, the electron must pass the anchor that holds the dye molecule on the surface of the TiO_2. The transferred electron then moves through the TiO_2 to a device and completes the circuit by eventually replenishing the chromophore.

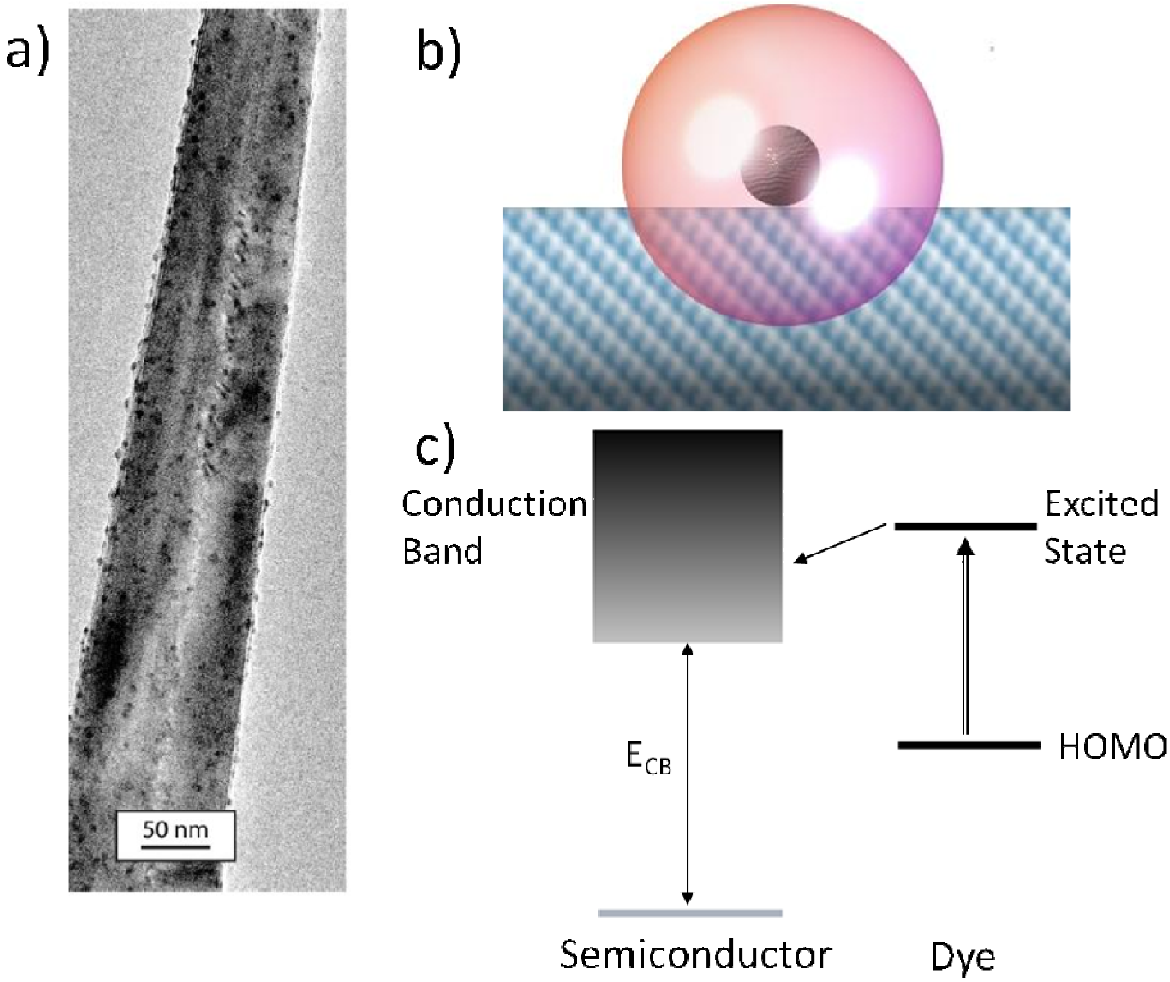

Figure 8—Using quantum dots as the "dyes" for solar cells. (a) A microscope (transmission electron microscope) image of PbSe quantum dots grown onto the surface of iron (III) oxide, Fe_2O_3 (image taken from the work of Rachel Selinsky and Mark Lukowski). (b) Conceptual image of a quantum dot on the surface of an electron-accepting material. Recall the exciton size relative to the quantum dot and consider the ease with which an electron might relocate into the TiO_2 (the blue solid). (c) An energy level diagram corresponding to the electron transfer event. An incident photon moves an electron from the highest occupied molecular orbital (HOMO) into an excited state. The excited electron then relaxes into the conduction band of the electron-acceptor.

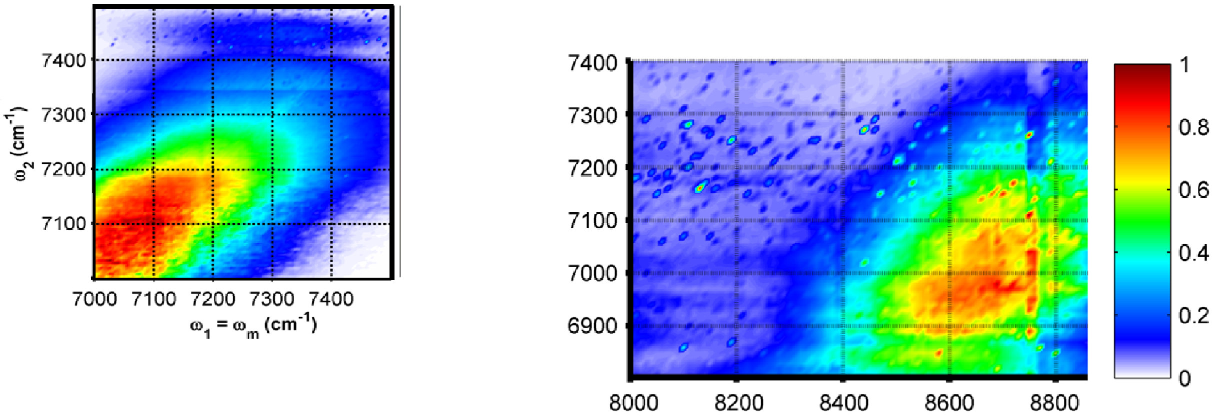

Figure 9—Multidimensional frequency scans taken of PbSe quantum dots with the picoseconds laser system. These two scans have been aligned to show their relative locations. Together they are analogous to the lower half of the scan of RDC shown in Figure 3. The peak on the left appears when all lasers are tuned to the lowest energy feature in Figure 6c (called the 1S exciton). The peak on the right is a cross peak between the lowest energy exciton feature and the higher energy hump (called the 1P exciton) on the rising hill in those absorption scans. The rising hill itself does not appear in this scan because those states are not coupled to the low energy feature, but the 1P exciton is.

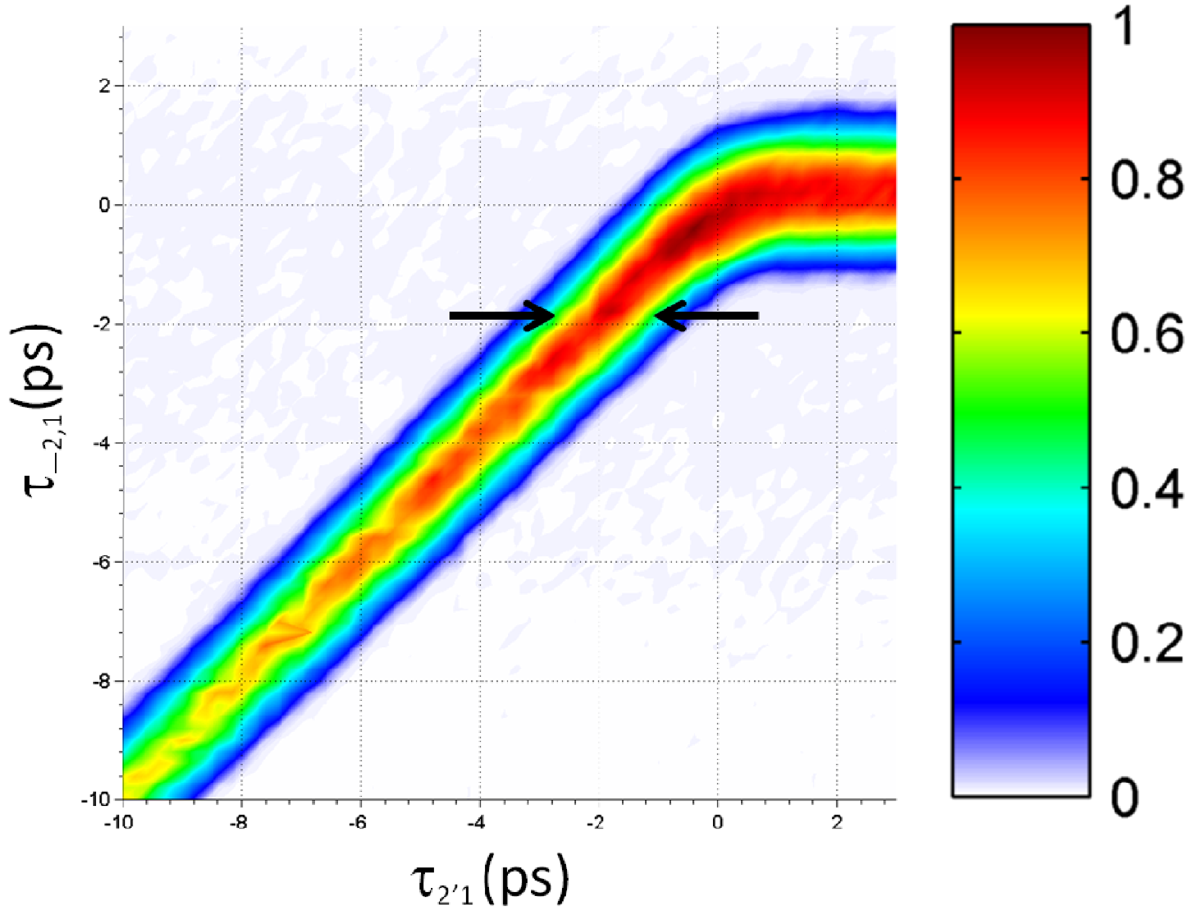

Figure 10—Multidimensional delay scan of PbSe quantum dots collected with picosecond pulses. All lasers are tuned to the wavelength of the 1S exciton (see Figure 9 caption for explanation). The population lifetime traces (here shown along the negative x = y diagonal and the positive x-axis) show long-lived signal, but coherence dephasing processes cannot be measured because the pulses are too long. The width of the peak indicated by the two black arrows should depend on the coherence dephasing rate, but instead it corresponds only to the width of the pulses.

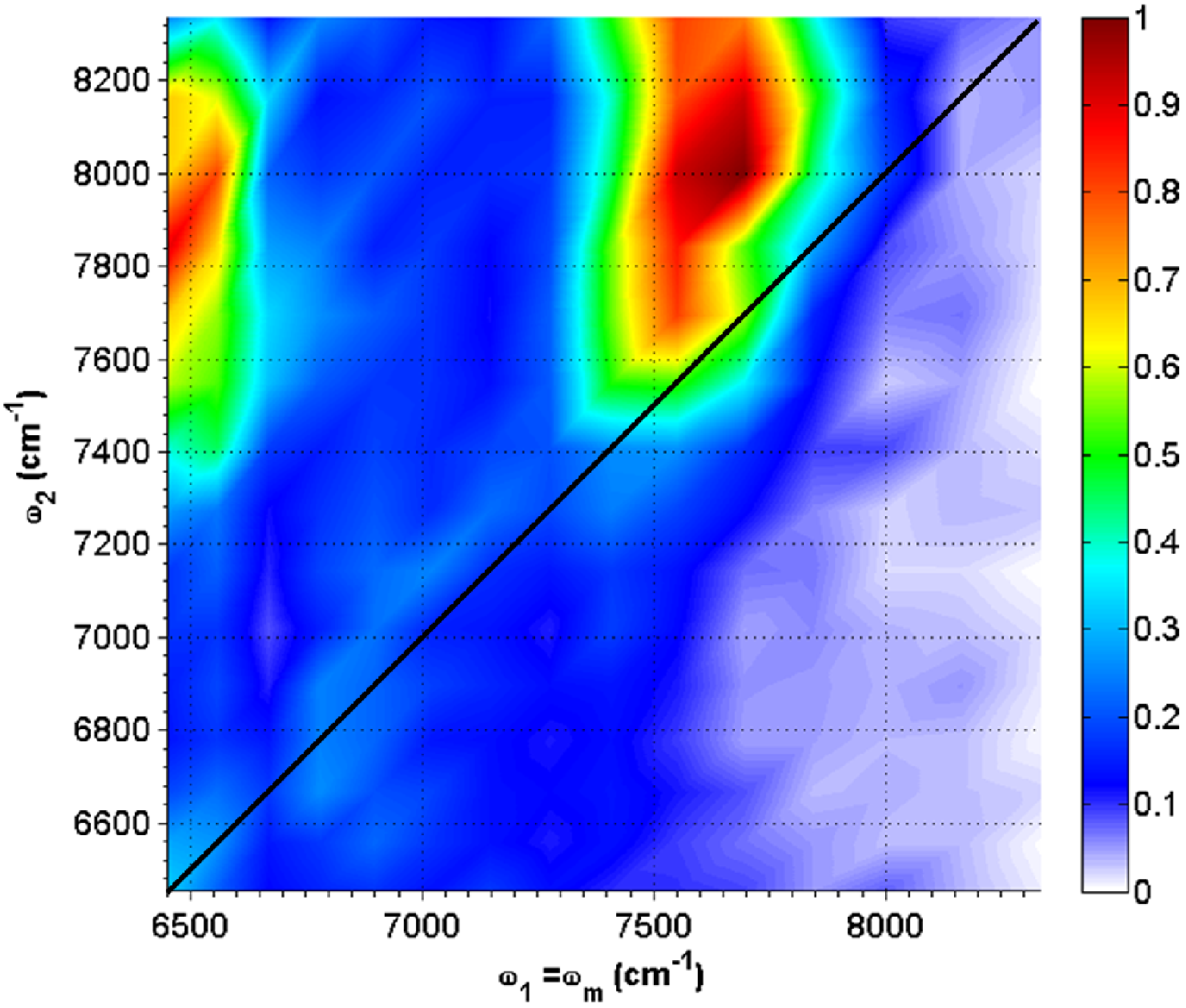

Figure 11—A multidimensional frequency scan of PbSe quantum dots collected on the newer femtosecond laser system. The two peaks shown would match the top half of the scan shown in Figure 3. The feature near the diagonal appears when all lasers are tuned to the 1P exciton (see Figure 9 caption for explanation). The upper left peak appears when a population is created in the 1P exciton and the 1S exciton is coupled to the state that exists when it reaches the sample (which was 600fs later in this scan).

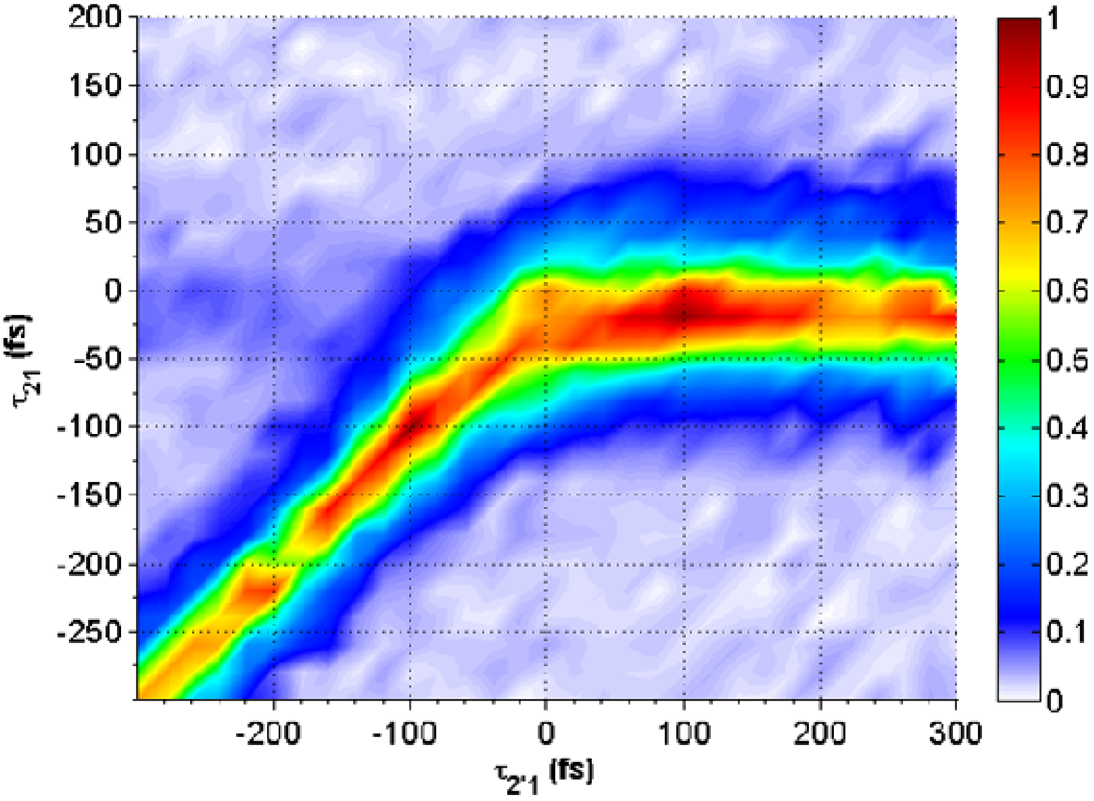

Figure 12—A multidimensional delay scan of PbSe quantum dots collected with 45fs pulses. As in Figure 10, lasers are tuned to the 1S exciton transition. The long population lifetimes are still apparent, but now the widths of these features can measure the coherence lifetimes—they are sufficiently wider than the excitation pulses.

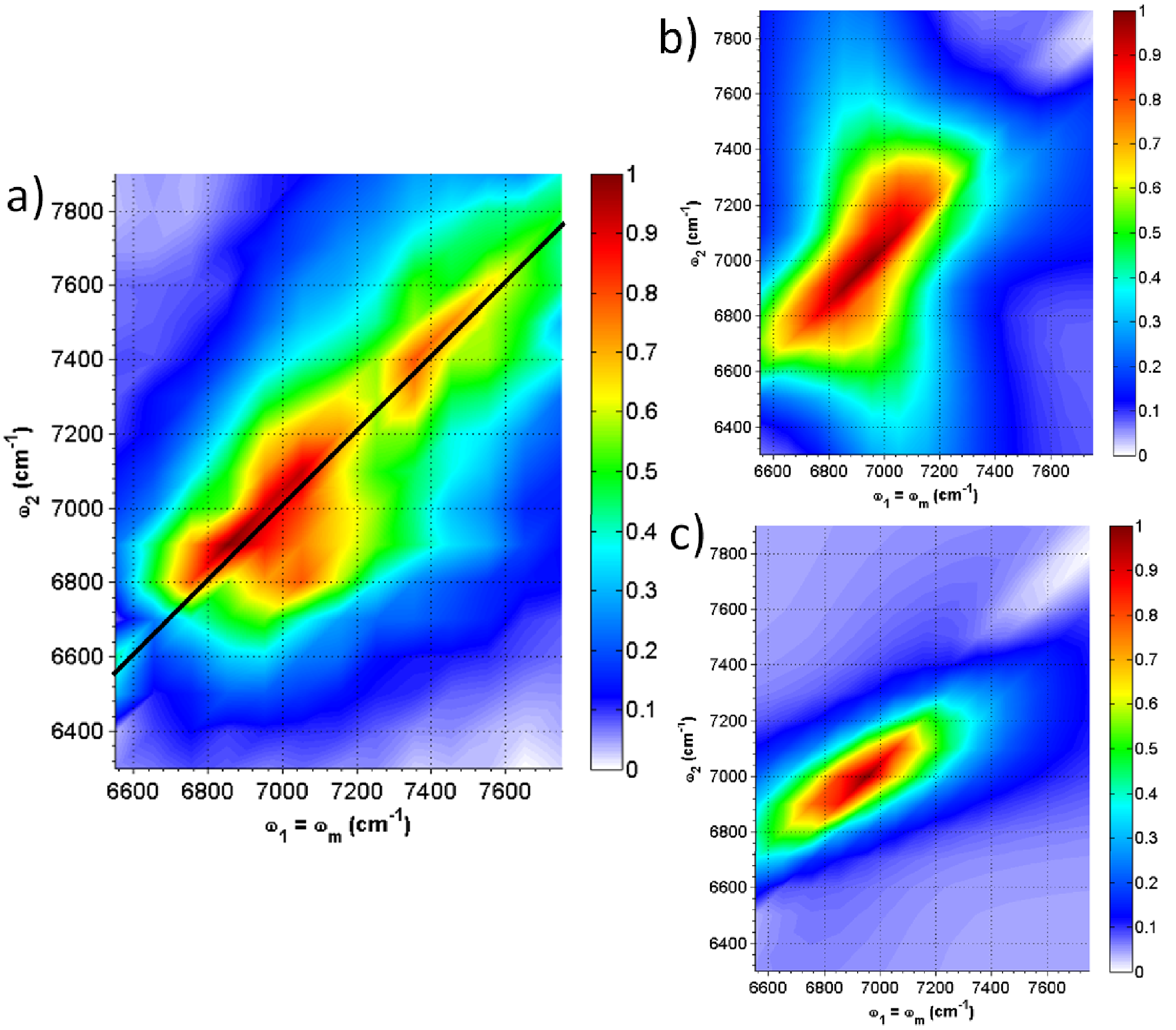

Figure 13—Multidimensional frequency scans verifying the measurable contribution of fully-coherent processes. (a) The data collected. (b) A simulation of (a) with signal contributions from fully-coherent processes. (c) A simulation of (a) without signal contributions from fully-coherent processes. The purpose of comparing the data to these two simulations is that the lobe in the spectral data located at (x,y) = (7050,6800) does not appear when no fully-coherent processes are allowed to contribute (c), but does appear when they are allowed (b). This subtle appearance confirms that we are able to once again access the full range of capabilities demonstrated in vibrational mode experiments like those of RDC.